

UNIVERSITÀ DELLA CALABRIA



UNIVERSITA' DELLA CALABRIA

Dipartimento di Ingegneria Meccanica, Energetica e Gestionale (DIMEG)

**Dottorato di Ricerca in
Ingegneria Civile e Industriale**

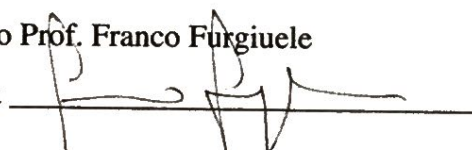
CICLO

XXIX

**DEVELOPMENT AND CHARACTERIZATION OF
ADVANCED CERAMIC MATERIALS**

Settore Scientifico Disciplinare ING-IND/14


Coordinatore: Ch.mo Prof. Franco Furgiuele

Firma 

Supervisore/Tutor: Ch.mo Prof. Leonardo Pagnotta

Firma 

Dottoranda: Dott.ssa Caterina Lamuta

Firma 

CONTENTS

Sintesi in lingua italiana	4
Introduction	7
Chapter 1. Nanostructured Yttria partially Stabilized Zirconia coatings	16
1.1 Thermally sprayed coatings	16
1.1.1 Coatings engineered for different applications	17
1.1.1.1 Thermal Barrier Coatings (TBCs)	17
1.1.1.2 Anti-wear coatings	20
1.1.1.3 Anti-corrosion coatings	21
1.1.1.4 Abradable coatings	22
1.1.1.5 Other thermally sprayed coatings	22
1.1.2 Thermal Spraying processes	23
1.1.2.1 Flame Spray	23
1.1.2.2 Wire Arc Spray	25
1.1.2.3 Plasma Spray	25
1.1.2.4 Other techniques	28
1.1.3 Nanostructured coatings	29
1.2 Materials and methods	31
1.2.1 Samples fabrication by APS	31
1.2.2 Microstructural characterization	35
1.2.3 Depth-sensing indentation tests	36
1.2.4 Tribological tests	47
1.3 Results and discussion	48
1.3.1 Microstructure	48
1.3.2 Mechanical properties	54
1.3.3 Tribological properties	63
1.4 Conclusions	65
1.5 References	67
Chapter 2. Advanced geopolymers	71
2.1 Geopolymers: structure and properties	71
2.1.1 Geopolymerization process	72
2.1.2 Aluminosicate precursors	73
2.1.3 Alkaline activators	75
2.1.4 Geopolymers chemical structure and microstructure	76
2.1.5 Important parameters	79
2.1.6 Metakaolin-based geopolymers	81
2.2 Experimental procedures	82
2.2.1 Samples production	82
2.2.1.1 Materials	82
2.2.1.2 Geopolymer synthesis and curing	83
2.2.2 Chemical characterization	85

2.2.3	Mechanical characterization	86
2.2.3.1	Macroscale characterization by Digital Image Correlation and Brazilian Disk Test	86
2.2.3.2	Micro and nano scale characterization by indentation tests	102
2.2.4	Piezoresistive Characterization	104
2.2.5	Piezoelectric Characterization	109
2.2.5.1	Piezoelectric effect and characterization methodologies	109
2.2.5.2	Direct piezoelectric characterization	121
2.2.5.3	Converse piezoelectric characterization	123
2.3	Results and discussion	123
2.3.1	Mechanical properties	123
2.3.1.1	DIC and Brazilian Disk Test results	123
2.3.1.2	Indentation tests results	127
2.3.2	Piezoresistive properties	132
2.3.3	Piezoelectric properties	134
2.4	Conclusions	147
2.5	References	149
Chapter 3. Geopolymers nanocomposites		162
3.1	Reinforced geopolymer composites: a review	163
3.2	Geopolymers/graphene nanocomposites	166
3.2.1	Graphene: properties and applications	166
3.2.2	Geopolymers reinforcement with graphene nano-sheets	175
3.2.3	Samples fabrication	177
3.2.4	Morphology and chemical characterization	182
3.2.5	Mechanical characterization	185
3.2.5.1	Indentation tests	185
3.2.5.2	DIC and Brazilian Disk tests	189
3.2.6	Electro-mechanical characterization	191
3.3	New potential nanofillers: “graphene like” materials	194
3.3.1	Topological insulators: properties and applications	194
3.3.2	Mechanical characterization of topological insulators by nanoindentation and DFT computations	199
3.3.2.1	Bi ₂ Te ₃	199
3.3.2.2	Bi ₂ Se ₃	224
3.3.2.3	SnSe	227
3.4	Conclusions	235
3.5	References	237
Annex		254
Acknowledgements		256

Sintesi in lingua italiana

Il presente lavoro di tesi è incentrato sullo sviluppo e la caratterizzazione di materiali ceramici avanzati. In particolare, tre diversi materiali sono stati prodotti e analizzati, e i risultati ottenuti sono stati presentati in tre differenti capitoli.

Il primo capitolo si focalizza sullo studio di rivestimenti ceramici nanostrutturati di zirconia parzialmente stabilizzata con yttria (YSZ), realizzati mediante un processo di Air Plasma Spray (APS). Tali rivestimenti sono stati prodotti presso il centro ricerche ENEA di Brindisi e sono stati caratterizzati nei laboratori del Dipartimento di Ingegneria Meccanica dell'Università della Calabria. L'obiettivo dell'attività di ricerca svolta è stato quello di analizzare l'influenza di alcuni parametri di processo sulle proprietà microstrutturali, meccaniche e tribologiche dei suddetti rivestimenti. È stato dimostrato che, modificando in maniera opportuna tali parametri, è possibile controllare la percentuale di aree nanostrutturate contenute all'interno del materiale e quindi conferire al rivestimento proprietà differenti. In tal modo si possono quindi ingegnerizzare tali rivestimenti in funzione dei diversi campi di applicazione, che spaziano dalla produzione di barriere termiche a quella di rivestimenti abrasibili, utilizzati per ridurre i flussi di bypass tra le pale e lo statore dei motori a turbina degli aerei. La microstruttura dei rivestimenti prodotti è stata analizzata mediante acquisizioni SEM (Scanning Electron Microscopy), mentre per la caratterizzazione meccanica e ad usura sono stati realizzati test di indentazione e test tribologici, rispettivamente.

Mentre la zirconia può essere considerata un materiale ceramico avanzato ben noto, il materiale analizzato all'interno del secondo capitolo, una malta geopolimerica a base di metacaolino, è presentato come materiale ceramico avanzato per la prima volta nel presente lavoro di tesi. Tale materiale è stato interamente prodotto e caratterizzato presso i laboratori di Ingegneria Meccanica e Chimica dell'Università della Calabria. I geopolimeri sono materiali ceramici consolidati a freddo, ottenuti dall'attivazione alcalina di precursori alluminosilicati. Tali materiali, sviluppati nel 1970 come alternativa al cemento Portland, pur essendo più ecosostenibili rispetto a quest'ultimo,

presentano proprietà meccaniche e applicazioni simili a quelle del comune cemento. Non trovando impiego nell'ambito di applicazioni *high-tech*, i geopolimeri sono sempre stati annoverati tra i materiali ceramici tradizionali. La scoperta di un effetto piezoelettrico diretto all'interno di tali materiali, proposta per la prima volta nella presente trattazione, ha però il potere di trasformare i geopolimeri in materiali ceramici avanzati. Nuove ed interessanti applicazioni derivano infatti da questa scoperta, sia nell'ambito della sensoristica che in quello dell' *energy harvesting*. In particolare, è stato proposto un nuovo modello chimico-fisico per la descrizione dell'effetto piezoelettrico osservato all'interno dei geopolimeri. Per la prima volta l'attività piezoelettrica è stata ricondotta ad un fenomeno di mobilità ionica anziché alla deformazione di una struttura cristallina non centro-simmetrica. Il coefficiente di carica misurato per le malte geopolimeriche prodotte varia da 4 pC/N a 40 pC/N, in base alla quantità di acqua contenuta all'interno del materiale. Oltre alla caratterizzazione piezoelettrica, sono state proposte anche una caratterizzazione piezoresistiva e meccanica. Quest'ultima in particolare, è stata condotta a diverse scale. Per la caratterizzazione alla nano e alla micro scala, sono state realizzate prove di indentazione, mentre per la caratterizzazione alla macroscale, è stata sviluppata ed ottimizzata una nuova metodologia, caratterizzata dalla combinazione della correlazione digitale delle immagini (DIC) e del Brazilian Disk Test.

Il coefficiente piezoelettrico misurato per le malte geopolimeriche prodotte risulta essere sufficientemente elevato per applicazioni sensoristiche; tuttavia, alcune applicazioni, soprattutto nell'ambito dell' *energy harvesting*, richiedono spesso coefficienti più elevati. Con lo scopo di incrementare le prestazioni elettro-meccaniche dei geopolimeri analizzati, si è deciso di utilizzare nanoplatelets di grafene (GNPs) come fillers all'interno delle malte prodotte. I risultati relativi alla produzione e alla caratterizzazione chimica, meccanica, ed elettromeccanica di tali nanocompositi sono stati presentati all'interno del terzo ed ultimo capitolo. Mentre l'aggiunta di GNPs sembra non aver modificato in maniera incisiva le proprietà meccaniche dei geopolimeri, sono stati misurati promettenti incrementi del gauge factor e del coefficiente piezoelettrico (pari al 20% e al 198%,

rispettivamente) in seguito all'aggiunta dell'1% in peso di grafene. Ulteriori analisi sono tuttavia necessarie per la formulazione di un modello fisico in grado di chiarire il ruolo del grafene nell'ambito dell'attività elettro-meccanica dei geopolimeri. Nella seconda parte del terzo capitolo, alcuni isolanti topologici (Bi_2Te_3 , Bi_2Se_3 e SnSe) sono stati proposti come nanofillers alternativi per l'incremento delle performances elettro-meccaniche dei geopolimeri. Gli isolanti topologici, noti anche come “graphene like materials”, pur essendo semiconduttori nel bulk, sono caratterizzati da un'eccellente conducibilità elettrica in superficie, paragonabile a quella del grafene. Rispetto a quest'ultimo inoltre, presentano una conducibilità priva di dissipazioni in presenza di difetti superficiali e possono essere prodotti tramite processi relativamente economici. La conoscenza delle proprietà meccaniche di tali materiali è tuttavia estremamente limitata e i pochi lavori presenti in letteratura sono quasi interamente di carattere teorico e computazionale. A tal proposito, il Bi_2Te_3 , il Bi_2Se_3 e lo SnSe sono stati caratterizzati mediante prove di indentazione strumentata e simulazioni DFT (Density Functional Theory), tenendo in considerazione l'anisotropia meccanica che tali materiali presentano. I risultati ottenuti sono di fondamentale importanza per tutti gli studi futuri incentrati sulla produzione e la caratterizzazione di nanocompositi geopolimerici rinforzati con nanofillers di Bi_2Te_3 , Bi_2Se_3 e SnSe .

“Ingegnerizzare”, “concepire” e “migliorare” un materiale ceramico avanzato sono quindi i tre differenti approcci proposti all'interno dei tre differenti capitoli del presente lavoro di tesi.

Introduction

Ceramics are commonly defined as inorganic and nonmetallic materials, complementary to metals and polymers. They exhibit interesting properties such as high strength and hardness, high melting temperatures, chemical inertness, low thermal and electrical conductivity, but they also display some deficiencies such as brittleness and sensitivity to microstructural defects [1]. "Ceramic" comes from the Greek word *keramos*, which means "burnt earth". The first ceramics materials were in fact produced by heating at high temperatures natural materials such as clay. High temperatures drive out water and foster the formation of strong chemical bonds between the flakes of clay. Ceramic functional objects such as pots, dishes, and storage vessels, were manufactured from clay since ancient Greece. White porcelain was later produced in China from natural kaolin, and it showed less brittleness if compared to clay-based ceramics. The two typologies of materials mentioned above are usually classified as traditional ceramics, in order to distinguish them from advanced ceramics, a new class of materials developed at a later stage in the historical development of ceramic materials. A detailed definition of advanced ceramics was proposed in 1933 by the Versailles Project on Advanced Materials and Standards (VAMAS). Such definition describes advanced ceramics as "an inorganic, nonmetallic (ceramic), basically crystalline material of rigorously controlled composition and manufactured with detailed regulation from highly refined and/or characterized raw materials giving precisely specified attributes" [2]. Several key features can be extracted from such definition. The microstructure of advanced ceramics tends to lack a glassy component (it is in fact "basically crystalline") and is highly engineered. Characteristics such as the grain size and shape, the phase distribution, or the amount of porosity, are strictly planned and controlled. Such control can be performed by carefully choosing the raw materials, which, contrary to traditional ceramics, are usually synthetic compounds rather than natural materials. Also the manufacturing process is deeply engineered in order to confer to advanced ceramics unique properties. Examples of advanced ceramics are binary oxides such as alumina (Al_2O_3), magnesia (MgO) and zirconia (ZrO_2), or

ternary oxides such as the spinels (MgAl_2O_4 -based compounds) and the perovskites (CaTiO_3 -based). There are also more complex oxides such as the ionically conducting material $\text{Na}_{3.1}\text{Zr}_{1.55}\text{Si}_{2.3}\text{P}_{0.7}\text{O}_{11}$, or groups of non-oxide ceramics such as the carbides (e. g., SiC), the nitrides (e. g., Si_3N_4), the borides, the suicides, the halides and many other solid compounds [3]. The variety of advanced ceramics becomes very wide by mixing the materials mentioned above.

“Advanced” is not the only adjective used to define such category of materials. The terms "technical," "special," "engineering," "fine" are also widely used, and practically, their definition is not as strict as that proposed by VAMAS. Advanced ceramics are usually distinguished from traditional ceramics according to their properties and application fields. While traditional ceramics applications include consumer products like dinnerware or ovenware and construction products like tile or windows, advanced ceramics are usually used in high-tech fields such as automotive, aerospace, chemical/petrochemical, and electrical/electronic. In particular, advanced ceramics can be divided into three main categories [3]: materials with electrical and electronic functions, those with high mechanical performances at ambient temperatures and those with high mechanical properties at high temperatures. Concerning electrical and electronic properties, electrical insulation is surely the most known feature of ceramic materials. However, the discovery of unique properties such as ferroelectricity and piezoelectricity [4] (ceramic perovskites are the most widespread piezoelectric materials) revolutionized the design, the manufacturing and the development of some advanced ceramics. The second category involves materials which provide high mechanical performances, such as wear resistance, hardness and corrosion resistance, at ambient temperature. Alumina and silicon carbide lie in such category and typical applications include wear parts in the medical engineering field (such as hip joints prosthesis), in industry (valves, components of pumps, or coatings for pipeworks) and in mechanical engineering (such as valves and bearings). Whereas such ceramic components display great strength, their main defect is the high brittleness. In the last category instead lie ceramic materials with high hardness, stiffness, wear and corrosion resistance,

and relatively low density at high temperatures. The refractoriness (i.e., the combination of high melting point and retention of mechanical strength to high temperature) is however the most attractive property of such materials. Alumina, zirconia and silicon carbides, show a melting point of 2054, 2770, and 2650 °C respectively, which is four times higher than that of commonly used metals such as aluminum [3]. These properties are very attractive for the production of ceramic tool tips for the highspeed machining of metals (aluminas and sialons are usually used), or the manufacturing of components and coatings for heat engines (diesels and turbines). Brittle fracture, usually caused by thermal shock, is however common in such applications.

Researchers' effort is continuously devoted to engineer and improve the performances of advanced ceramics by overcoming deficiencies usually related to the material's brittleness and porosity. Two different methodologies are usually adopted to reach such goals [3]: to act on the manufacturing process or to act on raw materials. In the first case, new sintering processes can be developed or the parameters of existing processes can be controlled in order to engineer the microstructure of the produced materials. In the second case, the chemical composition of well-known raw materials can either be carefully designed, or special fillers, characterized by unique properties, can be added to a known ceramic matrix.

The present thesis is a collection of research works carried out during a three-year PhD activity, pursued at the University of Calabria, Italy. Such works aim to propose a valuable research contribution in the advanced ceramics field, under different perspectives. In particular, the dissertation is divided into three chapters and each chapter describes a different approach to study an advanced ceramic material: how to engineer an advanced ceramic by acting on its production process; how to transform a traditional ceramic into an advanced material; how to improve an advanced ceramic by adding special nanofillers. While the second and the third approach (developed in Chapter 2 and Chapter 3, respectively) focus on the same material, the first approach (described in Chapter 1) deals with a different material.

In particular, in Chapter 1, nanostructured Yttria partially Stabilized Zirconia (YSZ) ceramic coatings are engineered for different applications by acting on some parameters of their manufacturing process. YSZ coatings were produced at ENEA Brindisi Research Centre, Italy, by means of Air Plasma Spraying (APS) and they were characterized at the Mechanical Engineering Laboratory of the University of Calabria.

As mentioned above, zirconia is a well-known advanced material, and it is widely used as thermal barrier coating for hot-sections components of aircrafts and land-based gas turbine engines. Such material is in fact notoriously characterized by high thermal expansion coefficient, low thermal conductivity, phase stability to relatively high temperatures, high strength, high thermal shock resistance and high fracture toughness [5, 6]. Nanostructured zirconia coatings were recently developed by partially melting the powder feedstock which is characterized by nanosized particles. Due to the partial melting, the final microstructure is composed by a melted phase (with the same morphology of conventional coatings) and a nanostructured phase (composed by microclusters of nanosized particles). A few studies [7, 8, 9] showed that nanostructured coatings can significantly improve the characteristics of different coatings typologies if compared to conventional coatings. Nanostructured coatings in fact showed higher creep rate, higher fracture toughness, lower elastic modulus, and higher thermal shock resistance.

In this dissertation it is shown how YSZ coatings can become suitable for different applications (which span from thermal barrier coatings to those requiring abradable seal coatings) by properly setting some APS process parameters in order to control the amount of retained nanostructured areas into the material microstructure, which influences the mechanical properties (such as hardness and Young's modulus). In particular, the influence of the process parameters on the material properties is analyzed by means of Scanning Electron Microscopy (SEM), indentation and wear tests. The obtained results were published in [10], where further details can be found.

Whereas zirconia is a well-known advanced ceramic material, a new advanced ceramic is instead proposed in Chapter 2. Such material was entirely produced and characterized at the Departments of Mechanical and Chemical Engineering of the University of Calabria. As a matter of fact, such material, i.e. a metakaolin-based geopolymer, is a well-known material. Geopolymers are inorganic ceramic materials obtained by the alkaline activation of natural aluminosilicate precursors such as fly ash, slag, or metakaolin [11]. They were developed in 1970s as substitutes of Ordinary Portland Cement (OPC). Even if geopolymers are more ecofriendly than OPC, their characteristics and applications are almost similar to those of ordinary cement [11]. According to the definition of advanced ceramics proposed above, geopolymers, produced from natural raw materials, and used for low-tech applications, have been considered traditional ceramics to date. However, the discovery of a direct piezoelectric effect in metakaolin-based geopolymer mortars [12], described in Chapter 2, completely changes the consideration of geopolymers into the portfolio of known materials. Piezoelectricity paves the way for interesting and high-tech applications in several fields such as self-sensing or energy harvesting, by transforming geopolymers from traditional to advanced ceramic materials. As previously specified in fact, the definition of advanced ceramics is mostly related to the application fields rather than the microstructure or chemical composition. A new chemical-physical model is proposed to explain the occurrence of the direct piezoelectric effect into geopolymers. Such model ascribes piezoelectricity to ionic mobility, by demonstrating that the piezoelectric effect is not necessarily related to the deformation of a non-centrosymmetric structure (as for all the piezoelectric materials known to date). More details can be found in [12].

Moreover, an anisotropic behavior of the effect was observed and the measured charge coefficient in the prevalent direction was found to lie in the range (4÷40) pC/N, depending on the water content. In addition to piezoelectric characterization, a piezoresistive characterization [13] and a multiscale mechanical characterization of the produced geopolymer mortars are also proposed in Chapter 2. While indentation tests were performed for the mechanical characterization at the nano

and micro scale, the macroscale characterization was carried out by means of a new proposed methodology which combines Digital Image Correlation (DIC) and Brazilian Disk Test. Details about the development and optimization of such methodology can be found in [14].

The charge coefficient measured for geopolymers is quite large and allows the application of such materials as a sensor. However, some applications, such as those in the energy harvesting field, sometimes require higher piezoelectric coefficients. In order to increase the piezoelectric activity, graphene nanoplatelets (GNPs) were added to the geopolymeric matrix and results about the production and characterization of such nanocomposites (carried out, also in this case, at the Departments of Mechanical and Chemical Engineering of the University of Calabria) are proposed in Chapter 3. Graphene, the monoatomic layer of graphite, is the thinnest, stiffest, and strongest material in the world [15]. It has also unique electric properties, and it is a promising filler for composites due to its high surface/volume ratio [15]. For such reason, graphene has been selected as nanofiller for the enhancement of the electro-mechanical properties of metakaolin-based geopolymer mortars. A chemical, mechanical (at different length scales) and electro-mechanical characterization of the produced geopolymer/GNPs nanocomposite is proposed in Chapter 3. Whereas no significant influences of GNPs on the mechanical properties of geopolymers were observed, high increases of piezoelectric and piezoresistive coefficient were recorded (198% and 20% respectively) with a graphene content of 1% wt.

Some topological insulators (i.e., Bi_2Te_3 , Bi_2Se_3 , and SnSe) are finally proposed as alternative nanofillers in the second part of Chapter 3. Topological insulators (TIs), also known as “graphene like materials”, are characterized by a high surface charge carriers mobility, comparable to that of graphene [16, 17]. Moreover, in TIs the electronic charge propagates in only one direction, and since it cannot be reflected back or scattered, the electronic propagation is dissipationless [18]. TIs are also characterized by reliable, large-scale, and low-cost production. All such properties make TIs a promising nanofillers for the improvement of the electro-mechanical performances of

metakaolin-based geopolymers. The knowledge of the mechanical properties of the filler is essential for the design, the production, and the characterization of a composite material. While the mechanical properties of graphene are well known, there is a lack of research efforts devoted to the mechanical characterization of TIs. Very few studies were in fact proposed on this topic and they are mostly computational [19-21].

In Chapter 3, a joint experimental and theoretical investigation (carried out by means of nanoindentation tests and DFT computations) of the mechanical properties of Bi_2Te_3 , Bi_2Se_3 , and SnSe is proposed, by taking into account the anisotropy of such layered materials. The obtained results can be also found in [22-24] and they represent an important starting point for all the ambitious future works devoted to the development and characterization of TIs/geopolymers nanocomposites.

References

- [1] Barsoum, Michael W. (1996). *Fundamentals of Ceramics*. New York: McGraw-Hill.
- [2] VAMAS, Technical Working Area 14, *Classification of Advanced Technical Ceramics*, Ed. Jamuel Schneider Jr., July 1993.
- [3] *Concise encyclopedia of advanced ceramic materials*, Ed. R. J. Brook, 1991, Pergamon Press
- [4] K. Uchino, *Advanced piezoelectric materials*, (Woodhead Publishing, 2010).
- [5] X. Q. Cao, R. Vassen, S. Stöver, *Ceramic materials for thermal barrier coatings*, *J.Eur.Ceram.Soc.*24(2004)1–10.
- [6] G. Di Girolamo, L. Pagnotta, *Thermally sprayed coatings for high temperature applications*, *Rec.PatentonMater.Sci.*4(2011)173–190.
- [7] R. Soltani, E. Garcia, T. W. Coyle, J. Mostaghimi, R. S. Lima, B. R. Marple and C. Moreau, *Thermodynamical behavior of nanostructured plasma sprayed zirconia coatings*, *J. Therm. Spray Technol.* 15(4) (2006) 657-662.
- [8] B. Liang and C. Ding, *Thermal shock resistance of nanostructured and conventional zirconia coatings deposited by atmospheric plasma spraying*, *Surf. Coat. Technol.* 197 (2005) 185-192.

- [9] W. Q. Wang, C. K. Sha, D. Q. Sun and X. Y. Gu. Microstructural feature, thermal shock resistance and isothermal oxidation resistance of nanostructured zirconia coating, *Mater. Sci. Eng. A* 424 (2006) 1-5.
- [10] Lamuta C, Di Girolamo G, Pagnotta L, Microstructural, mechanical and tribological properties of nanostructured YSZ coatings produced with different APS process parameters, *Ceramics International* 41(2015) 8904–8914.
- [11] John L. Provis and J annie S. J. van Deventer, *Geopolymers Structure, processing, properties and industrial applications*, First published 2009, Woodhead Publishing Limited and CRC Press LLC.
- [12] Lamuta C, Candamano S, Crea F, Pagnotta L, Direct piezoelectric effect in geopolymeric mortars, *Materials & Design* 107 (2016) 57–64.
- [13] Lamuta C, Bruno L, Candamano S, Pagnotta L, Piezoresistive characterization of graphene/metakaolin based geopolymeric mortar nanocomposites, XXV International Materials Research Congress, Cancun, Mexico, August 14-19, 2016.
- [14] Sgambitterra E, Lamuta C, Candamano S, Pagnotta L, Brazilian Disk Test and Digital Image Correlation: a methodology for the mechanical characterization of brittle materials (in review).
- [15] Nihil A. Koratkar, *Graphene in Composite Materials: Synthesis, Characterization and Applications*, DEStech Publications, Inc., Lancaster, Pennsylvania 17602, USA.
- [16] Orlita, M.; Faugeras, C.; Plochocka, P.; Neugebauer, P.; Martinez, G.; Maude, D. K.; Barra, A. L.; Sprinkle, M.; Berger, C.; de Heer, W. A. et al. Approaching the dirac point in high-mobility multilayer epitaxial graphene. *Phys. Rev. Lett.* 2008, 101, 267601.
- [17] Morozov, S. V.; Novoselov, K. S.; Katsnelson, M. I.; Schedin, F.; Elias, D. C.; Jaszczak, J. A.; Geim, A. K. Giant intrinsic carrier mobilities in graphene and its bilayer. *Phys. Rev. Lett.* 2008, 100, 016602.
- [18] T. Zhang, P. Cheng, X. Chen, J. F. Jia, X. Ma, K. He, L. Wang, H. Zhang, X. Dai, Z. Fang, X. Xie, and Q. K. Xue, *Phys. Rev. Lett.* 103, 266803 (2009).
- [19] S. Feng, S. Li, H. Fu, *Comput. Mater. Sci.* 82 (2014) 45–49.
- [20] Y. Tong, F. Yi, L. Liu, P. Zhai, Q. Zhang, *Comput. Mater. Sci.* 48 (2010) 343–348.
- [21] Z. Xiong, X. An, Z. Li, T. Xiao, X. Chen, *J. Alloys Compd.* 586 (2014) 392–398.
- [22] Lamuta C, Campi D, Cupolillo A, Politano A, Aliev ZV, Babanly MB, Chulkov EV, Pagnotta L, Mechanical properties of Bi₂Te₃ topological insulator investigated by density functional theory and nanoindentation, *Scripta Materialia* 121 (2016) 50–55.

- [23] Lamuta C, Cupolillo A, Politano A, Aliev ZV, Babanly MB, Chulkov EV, Pagnotta L, Indentation fracture toughness of single-crystal Bi₂Te₃ topological insulator, *Nano Research* 9 (2016) 1032–1042.
- [24] Lamuta C, Cupolillo A, Politano A, Aliev ZV, Babanly MB, Chulkov EV, Alfano M, Pagnotta L, Nanoindentation of single-crystal Bi₂Te₃ Topological Insulators grown with the Bridgman-Stockbarger method, *Phys. Status Solidi B* 253 (2016) 1082–1086.

Chapter 1

Nanostructured Yttria partially Stabilized Zirconia coatings

This chapter focuses on the study of the influence of some Air Plasma Spray process parameters on the microstructural, mechanical and tribological properties of nanostructured Yttria partially Stabilized Zirconia (YSZ) ceramic coatings.

A brief dissertation on thermally sprayed coatings engineered for different industrial applications, as well as on the different fabrication techniques used to their production, will be proposed. The difference between conventional and nanostructured coatings will be also discussed.

The experimental procedures followed for the samples fabrication and characterization will be described in detail and the obtained results will be finally presented and discussed.

1.1 Thermally sprayed coatings

Engineering components usually operate in severe conditions and are subject to several detrimental agents, such as high temperature, oxidation, corrosion, and wear, which are responsible for unexpected component failure and reduced lifetime. In order to overcome such issues, advanced materials, characterized by enhanced chemical and mechanical properties, need to be developed, as well as new manufacturing processes have to be studied. However, it is worth noting that for certain applications the use of structural materials with enhanced properties may be very expensive and sometimes technically unsatisfactory. Solid advanced ceramics, for example, could be suitable for the production of components subject to high temperatures such as gas turbine blades and vanes, but their brittleness limits their application. The use of a ceramic coating on a super alloy component can represent the most suitable and cost-effective application in this case. In general, the application of a surface coating is a smart solution to tailor the component

surface to withstanding in hard environments by enhancing its properties and without compromising the original characteristics. A great advantage of such technical solution consists also in the possibility of restoring a damaged coating without replacing the underlying component.

Within this framework, Thermal Spraying is an easy, reliable, cost-effective attractive technique to produce coatings with high quality and well-tailored microstructural and mechanical properties, suitable for different applications. Coatings with a thickness varying from few micrometers to some millimeters can be fabricated with such techniques and several typologies of materials (ceramics, metals, or cermet) can be processed [1]. Different kinds of Thermal Spraying techniques were developed from the early 1882, when the first equipment was patented by Schoop [1] and they are commonly used for a wide range of applications in several industrial fields such as aerospace, automotive, biomedical, glass manufacturing, fabrication of electronic devices, corrosion of marine and land-based infrastructures, petrochemical and paper industry. The interest in developing new coatings and new fabrication techniques by exploiting the advantages of Thermal Spraying is still growing.

1.1.1 Coatings engineered for different applications

Different coatings, of different materials and with different properties, can be produced by Thermal Spraying in order to cover a wide range of applications. Some examples are listed below.

1.1.1.1 Thermal Barrier Coatings (TBCs)

The production of TBCs is surely the most promising industrial application of thermally sprayed coatings. Hot-sections components of aircrafts and land-based gas turbine engines (such as first-stage turbine blades and vanes, transition pieces and combustion chamber tiles) are notoriously exposed to high temperature and operate in highly oxidizing and corrosive environments. Ni-based super-alloys are usually used for the fabrication of such components. Temperatures in the range of

900-1100°C are usually reached on the surface of actual turbines and may exceed the temperature capability of Ni-base super-alloys. Furthermore, aggressive agents, such as sulphates, chlorides and vanadates contained in low grade fuel, can cause hot corrosion by considerably reducing the lifetime of metal components. Figure 1.1 shows the improvements obtained in terms of thermal capability of gas turbine engine components from 1950 to 2010 by considering the evolution of Ni-super-alloys and the benefits related to the application of TBCs. It is worth nothing that, compared to the use of cast or single crystal alloys, the presence of a TBC on the metallic substrate allows to reach higher operating temperatures. Furthermore, TBCs provide also lower peak combustion temperatures and a decrease of CO₂ and NO_x emissions, with a consequent low environmental impact.

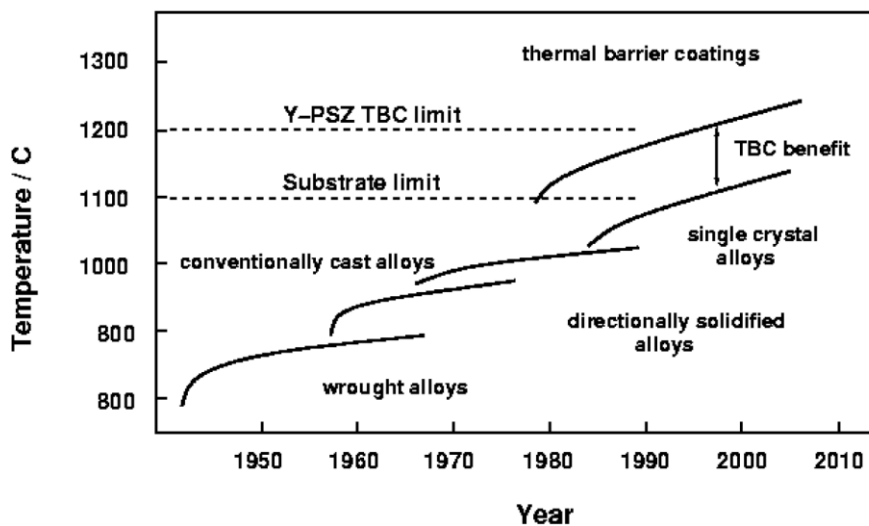


Figure 1.1: Historical evolution of the thermal capability of turbine engines hot components [1].

It is well known that gas turbine components need to be cooled down when operating. An internal cooling system is usually used in order to reduce metal surface temperature by up to about 150°C. However, such cooling system results very expensive and cheaper alternatives need to be developed. The application of a TBCs can significantly reduce the requirements for the cooling system. Thanks to TBCs in fact a lower cooling air flow is required and a higher efficiency can be

obtained. A TBC in fact allows to tolerate a ΔT through its thickness, maintaining the underlying component at lower temperatures, as shown in Figure 1.2 for a turbine blade. The blue line represents the temperature profile and one can observe that the temperature decreases from the hot gas zone to the super-alloy substrate thanks to the presence of the TBC (characterized by a top coat and a bond coat). The higher the TBC thickness the higher the ΔT produced by the coating. However, higher thickness cause higher stresses during deposition and during service and this could lead to an increase of cracks formation and a premature failure of the TBC. The optimum TBC thickness is then related to the specific operating temperature range of a specific application. As an example, the total thickness of a TBC applied on a stationary turbine blade is generally around 500 μm or less.

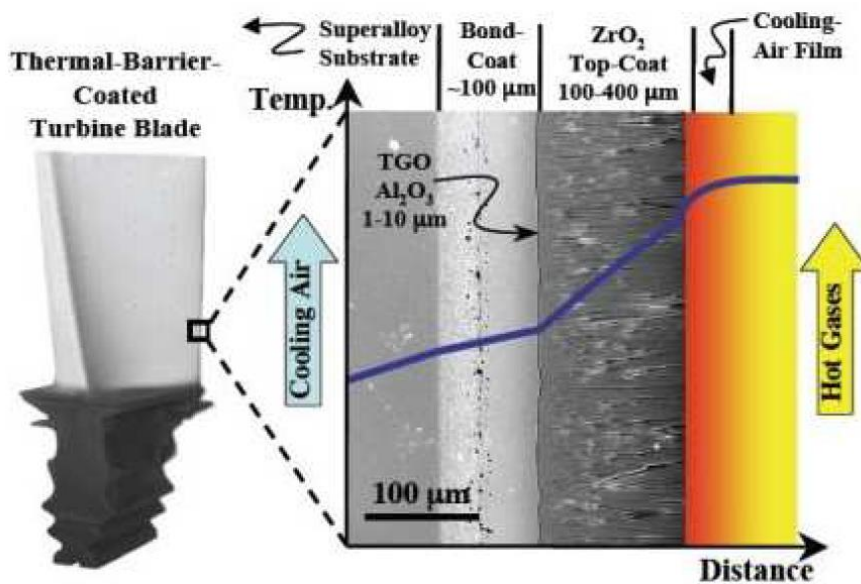


Figure 1.2: Temperature (blue line) decrease caused by a Thermal Barrier Coating deposited on a turbine blade.

Since ceramic materials are good thermal insulators, they are widely used for the production of TBCs. Among them, zirconia is an excellent candidate since it is notoriously characterized by high thermal expansion coefficient, low thermal conductivity, phase stability to relatively high temperatures, high strength, high thermal shock resistance and high fracture toughness. However, zirconia shows a phase transition from tetragonal to cubic phase for temperatures higher than

2370°C [2, 3] and such instability limits its application as a TBC since a phase transition causes a volume change and then the formation of cracks. Such issue is overcome by means of the addition of zirconia stabilizer oxides, such as CaO, MgO, Y₂O₃, CeO₂.

In general, the basic requirements that materials candidates for TBCs must satisfy are: low thermal conductivity, a thermal expansion coefficient similar to that of the metal substrate, high melting point, high temperature capability, phase stability between room temperature and operating temperature, low Young modulus, chemical compatibility with the substrate, low sintering rate of the porous microstructure at high temperatures. All these properties aim to thermally isolate the substrate by promoting high performances at elevated temperatures and guarantee the mechanical integrity of the coatings. Whereas in diesel engines the ceramic coating is directly deposited on the metal substrate, in the turbine engine components a metallic bond coat is deposited between the substrate and the ceramic coating (called top coat). Such metallic coating (MCrAlY, where M = Ni, Co) has to exhibit high chemical compatibility with the substrate material and it plays an important role on the lifetime of the TBC. The metallic substrate and the ceramic coating are in fact characterized by significantly different thermal expansion coefficients and such difference can generate high interfacial shear stresses during in-service thermal cycling, promoting the cracks growth and propagation which leads to the TBC spallation and failure [4, 5, 6]. The bond coat application provides a rough surface which fosters the mechanical bonding with the top coat and increases the adhesion between the substrate and the TBC. Furthermore, the metallic bond coat preserves the substrate from oxidation and hot-corrosion.

1.1.1.2 Anti-wear coatings

Different wear modes, such as abrasive wear, adhesive wear, and surface fatigue wear, can affect a mechanical component. A functional coatings can then be engineered in order to protect the surface of the component from the wear mechanism mentioned above.

Abrasive wear occurs when hard particles (such as metal debris or dust), cause the abrasion of rubbing surfaces between which they are entrapped. Such phenomenon can also occurs at high temperatures. Among the materials used for the production of coatings able to counteract abrasive wear there are alumina (Al_2O_3), chromia (Cr_2O_3) and tungsten-carbide-cobalt (WC-Co) [7, 8].

Adhesive wear instead occurs between surfaces during frictional contact and it consists in the attachment of wear debris from one surface to another. This wear mechanism commonly occurs in mechanical components such as piston guides and bronze bearings, above all with inadequate lubrication. In such case, soft bearing coatings are applied to entrap abrasive fragments. For more severe applications, such as in piston rings and fuel pump rotors, hard coatings (usually Al_2O_3 - TiO_2 and WC-Co) are used.

Surface fatigue wear occurs when the surface of a material is weakened by repeated loading and unloading cycles which cause the crack growth and hence the detachment of wear particles. Fretting is a common example of fatigue wear which can occur in turbine engines sections, both in low and high temperature sections. High temperatures usually imply a more severe wear because the components can be hardly lubricated.

Cermet coatings usually offer good performances against wear. They can be used in both hot and cold sessions of engines and are able to extend the component life to several months or years. Chromium carbide in a matrix of nickel chromium (Cr_3C_2 -NiCr) and tungsten carbide-cobalt are commonly used to enhance the erosion resistance of components such as rocker arms, piston rings, cylinder lines, compressor air seals, exhaust fans and valve seats.

1.1.1.3 Anti-corrosion coatings

Hot components of gas turbines and diesel engines are commonly affected by hot corrosion and MCrAlY and ceramic coatings are usually used to protect such components. Several infrastructures (such as electrical conduits, bridges, ship holds and tanks, ship pylons, storage tanks for oils and

fuels, antennae, wind towers, offshore structures, petrochemical pumps and valves) need to be protected against atmospheric and water corrosion. Thermally sprayed coatings have been widely used since the 1930s in U.S. to this purpose. Such coatings, characterized by high effectiveness, low cost, predictable life and high abrasion resistance, can be considered as a valuable alternative to traditional metal paints or organic coatings. Typical anti-corrosion coatings include metal coatings made of aluminum, aluminum metal-matrix composites, zinc, molybdenum and nickel-chromium, chemically inert ceramics and polymers [1]. Since porosity does not offer a good resistance against corrosion, sealants are usually used to close the open porosity of coatings produced by thermal spray. These sealants (organic or not organic) may be applied by means of different deposition techniques such as Sol-Gel, Impregnation or Slurry Coating.

1.1.1.4 Abradable coatings

Abradable seals coatings are used in aircraft turbine engine components in order to reduce the bypass flow, of both hot combustion gases and cold compressor gases, which can occur between the rotating blade tips and the stator. The coating can improve the efficiency of the engine by providing a good sealing of the gas path [1]. An abradable coating accommodate high-speed blade tip rubs (induced during the start-up and the next operating conditions) and provide wear resistance to both stationary and rotating components. Such coatings have to counteract abrasion and spallation during rubbing but at the same time they cannot be too hard in order to avoid the damage of the blade tips. Abradable coatings are usually produced with polymers, soft metals and abradable ceramics.

1.1.1.5 Other thermally sprayed coatings

Environmental Barrier Coatings (EBCs) are an attractive technological solution to protect silicon-based ceramic matrix composites (CMC) components of turbine engines [9]. Mullite is a promising

material for EBCs due to its thermal expansion coefficient close to that of silicon carbide substrates [10].

Biomedical coatings are used for implant prostheses, orthopedic devices and dental implants. They can be divided into biocompatible and bioactive coatings. Whereas biocompatible coatings are usually porous titanium coatings compatible with the human bones and are used on titanium alloys prosthesis, bioactive coatings (including tricalcium phosphate and hydroxyapatite coatings) are applied before the implantation of the prosthesis in the human body and represent a dynamic interface between titanium alloy implants and osteoblast cells.

Electrically insulating and electromagnetic coatings are instead widely used in the electronic devices field.

1.1.2 Thermal Spraying processes

Thermal Spraying is a cost effective and easy technique to produce coatings of a wide variety of materials without causing a high thermal distortion of the substrate and without altering the mechanical properties of the component.

Different thermal spraying equipment, such as Flame Spray, Electric Arc Spray and Plasma Spray, are commercially available and they can differ for the heat source used, the input energy, the feedstock type (powder, wire or rod) and the spraying environment. Such processes allow to produce coatings with well-tailored characteristics, suitable for different applications.

1.1.2.1 Flame Spray

The Flame Spraying technique includes Flame Spray, Wire Flame, High Velocity Oxy-Fuel (HVOF) and Detonation Gun. The first two, Flame Spray and Wire Flame, differ only in the starting material they are able to process (i.e. powders or wires).

An oxy-fuel flame is used as heat source to melt the starting material in the Wire Flame process. A wire is introduced along the axial direction through the rear of the nozzle into the flame at the nozzle exit. Here it is then atomized by an expanding air stream and propelled toward the substrate. The flame can be made oxidizing or reducing (according to the material to be processed) by setting the fuel-oxygen ratio and the gas flow rate parameters. Wire Flame is a cheap system and coatings produced with such technique are usually characterized by low bond strength and high porosity [1]. In 1958 the Union Carbide (Praxair Surface Technologies, Inc.) invented HVOF. Such technique allows to obtain coatings with high bond strength and high density. The gas-particle stream is accelerated by an oxy-fuel burner with an advanced nozzle design technology which confers to particle a velocity of around 600 m/s. An internal combustion jet is produced by the reaction between oxygen and a gas fuel (usually propylene, propane or hydrogen) at temperature from 2500°C to 3000°C. A supersonic flame gas stream is generated through a confined cooled convergent-divergent nozzle into a high pressure chamber, where the combustion occurs. The powder particles are then injected into the gas jet and here heated and finally propelled toward the substrate [1]. Coatings with a porosity less than 1% can be obtained, suitable for anti-wear and anti-corrosion applications, but inappropriate for TBCs.

Detonation Gun confines the combustion between oxygen and fuel (acetylene) within a barrel, by producing high thermal and kinetic energy jets. The ignition of the gas mixture is realized by means of a spark plug. A controlled explosion is produced along the barrel, where the powder particles are injected [1]. Since high temperature and pressure are used to melt and accelerate the powder particles with high speed and kinetic energy, dense and hard coatings, with low oxidation level and high wear resistance, are produced with such technique.

1.1.2.2 Wire Arc Spray

Wire Arc Spraying was discovered by M. Schoop in 1910. During such process two conductive wires are connected to a DC power source and are driven to meet each other at the same time. When wire tips are in contact into the gun, they melt due to the presence of the electric arc which they generate. A high velocity air jet behind the wire tips atomizes the molten material and creates fine droplets which are propelled toward the substrate. When the droplets reach the substrate they impact, flatten and solidify [1]. Since the wires are directly melted by the electric arc, the thermal efficiency and the deposition rate are higher in Wire Arc Spray if compared to those of other thermal spraying techniques. Moreover, also the heating of the substrate can be limited because the particles are already molten when they are propelled toward the substrate. This allows to deposit coatings on substrates characterized by a low melting point, such as polymer or glass. However, Wire Arc Spraying is limited to conductive materials that may be formed into wires, such as aluminum, copper, steel and zinc (widely used for the protection of buildings from atmospheric or sea-water corrosion).

1.1.2.3 Plasma Spray

Plasma Spray includes **Atmospheric Plasma Spray (APS)**, Vacuum Plasma Spray (VPS) and Radio-Frequency Plasma Spray (RFPS).

In Figure 1.3 the coating formation mechanism of APS is shown. In such process a plasma is used to create an heat source which melts a powder feedstock which is subsequently accelerated toward the substrate. The plasma is produced by means of the ionization of a primary gas, usually argon. Such gas flows between an anode and a cathode and is ionized when an electric arc is struck between the electrodes. When the plasma is produced, the powder feedstock is injected into the plasma jet in order to be melted and it is then driven toward the substrate, where it solidify and forms the coating.

When the powder to be melted is a ceramic material, a secondary gas, usually hydrogen, is generally added to argon to increase the power of the plasma. The plasma gun is characterized by an axially aligned thoriated tungsten cathode and a water-cooled copper anode-nozzle. The high melting point of tungsten allows the cathode to survive the high-temperature arc while the water cooling system prevents melting and minimizes the erosion of both cathode and nozzle.

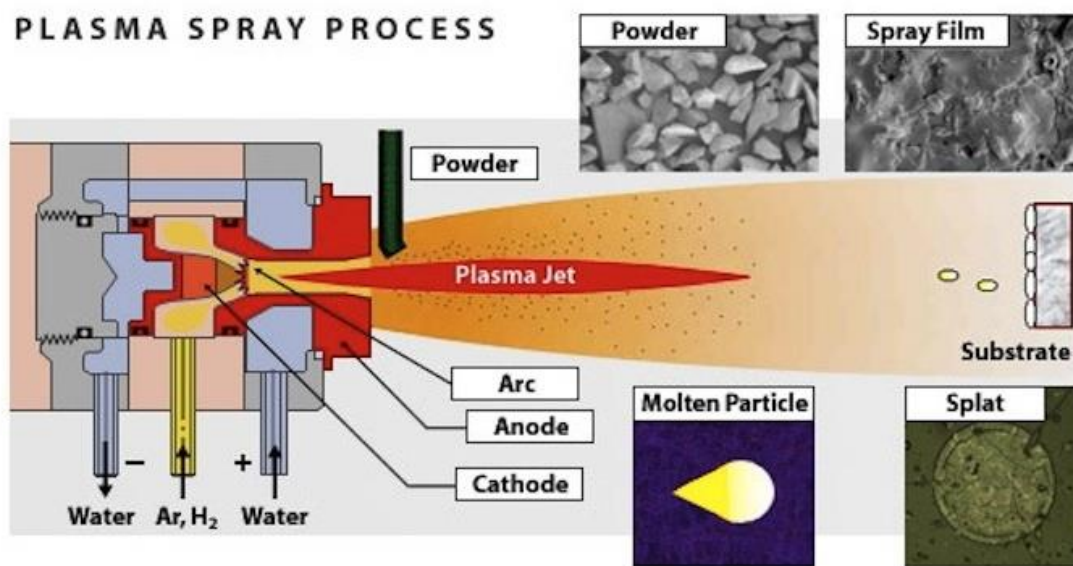


Figure 1.3: Coating formation mechanism for Atmospheric Plasma Spray.

When the melted particles impact the substrate, they are flattened and form splats which solidify at high cooling rate. The resultant coating is characterized by a lamellar structure with lamellae parallel to the coating-substrate interface. Figure 1.4 shows the typical microstructure of a plasma sprayed coating.

Thermally sprayed coatings are usually characterized by typical microstructural defects, such as pores (with different shape and size), interlamellar or horizontal microcracks and vertical microcracks. Porosity can be related to several causes such as unmelted or partially melted particles, voids not filled by the spreading particles, poor wetting onto adjacent splats, or intrinsic porosity of the feedstock particles. Interlamellar cracks are perpendicular to the spraying direction and are due

to the rapid cooling. Their presence can affect significantly affect the cohesive strength between lamellae. Vertical microcracks instead are produced by solidification, thermal stresses and relaxation of tensile quenching stresses.

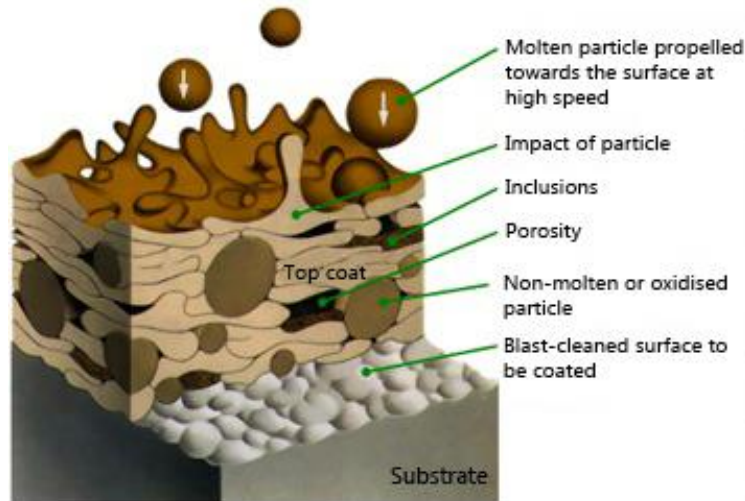


Figure 1.4: Microstructure of a plasma sprayed coating.

Coatings with well-tailored properties and suitable for different applications can be obtained by acting on several spraying parameters. Plasma spraying parameters include: torch type and diameter nozzle, arc current intensity, plasma power, process gas or gas mixture, process gas flow rate, carrier gas flow rate, standoff distance between torch and substrate, power injector diameter, power feed rate and traverse speed. The influence of some of these parameters on the mechanical properties of the produced coatings will be analyzed in the present dissertation.

VPS or LPPS (Vacuum Plasma Spray or Low-Pressure Plasma Spray) was proposed in 1974. Such process uses a modified plasma torch which operates in a chamber at low pressure (in the range between 0.1 and 0.5 atm). This configuration increases the expansion of the plasma. In this case the plasma jet is broader and more extended if compared to that of Air Plasma Spray, and the resultant spray pattern is large and uniform [1]. Denser coatings can be hence produced with such technique. However, VPS system is very expensive and it is not suitable for ceramic powder

feedstocks, due to their shorter dwell time and less degradation degree than that produced in atmospheric plasma spraying process.

Radio-Frequency Plasma Spray (RFPS) is commercially available since 1960s. In this case the torch uses an induction coil to produce an oscillating RF field (in the 450 kHz - 4 MHz range) in a reactor tube. Such field couples to the plasma arc gas stream by inductively heating such stream [1]. RFPS is suitable to melt coarser particles in atmospheric environments with high dwell times.

1.1.2.4 Other techniques

Cold Spray is a technology developed for particular applications and it is mainly used to produce coatings of high purity materials (such as pure metals, cermet and composites). In such process a pressurized gas is heated (at a temperature typically up to 700°C) in order to produce a high sonic flow speed. After its expansion into the spray nozzle, the gas flows out of the gun at a temperature usually below the ambient temperature. The powder feedstock is introduced into the high-pressure side of the nozzle and then accelerated toward the substrate. The peculiarity of such process is that both the gas and particles temperature are much lower than those reached in other thermal spraying techniques and some detrimental effects, such as high temperature particles oxidation and evaporation or the amount of residual stresses, are consequently minimized.

Electron Beam Physical Vapor Deposition (EB-PVD) is a quite widespread technique. In EB-PVD a ceramic source ingot is melted and evaporated in a vacuum chamber by a high energy electron beam. Such technique shows some shortcomings if compared to other thermal spray processes such as APS. It is in fact characterized by low deposition rates and the deposition of thick coatings can be really expensive. Furthermore, due to the limited dimensions of the vacuum room, large components with a complex shape and geometry cannot be coated.

Chemical Vapor Deposition (CVD) is a valid alternative recently proposed. During CVD a gaseous precursor is thermally decomposed into a vacuum chamber and its reaction at the substrate

surface forms a coating. Since the process is omni-directional, samples with complex geometries can be coated. Coatings with high density and bonding strength can be produced because the bonding is guaranteed by the diffusion of the coated material to the substrate. Interfacial stresses are consequently very low.

1.1.3 Nanostructured coatings

Nanostructured coatings were recently developed and their interesting properties revolutionized the performances of coated components. They can be produced by partially melting a powder feedstock characterized by nanosized particles in order to retain nanosized areas within the coating. The final coating will be characterized by two phases: a melted phase, with the same microstructure of conventional coatings (produced by means of a complete melting of the feedstock); and a nanostructured phase, composed by microclusters of nanosized particles. Plasma spray is suitable for the fabrication of nanostructured coatings because the melting degree can be controlled by an accurate choice of the spraying parameters during deposition. By controlling the amount of retained nanozones embedded into the microstructure, nanostructure ceramic coatings can be engineered for a given application [11]. It is worth noting that a low melting degree can also lead to coatings with a low cohesive strength. The melting degree is related to the temperature of the particles into the plasma jet and both plasma temperature and enthalpy need to be carefully controlled in order to melt only the outer surface of the microclusters and leave their nanosized particles core unmelted.

A few nanostructured powder feedstock for thermal spraying ($\text{ZrO}_2\text{-}7\text{Y}_2\text{O}_3$, $\text{Al}_2\text{O}_3\text{-}13\text{TiO}_2$, TiO_2 , WC-Co) are commercially available to date. However, such powders are produced in small quantities due to the high manufacturing costs and the lacking scientific results on this topic.

A few studies showed that nanostructured coatings can significantly improve the characteristics of different coatings typologies if compared to conventional coatings. Higher creep rate was observed for nanostructures zirconia coatings with the advantage of a more rapid stress relaxation at high

temperatures [12]. Nanostructured coatings exhibit also higher fracture toughness thanks to the presence of nanozones which are able to arrest crack propagation. Furthermore, they possess a lower elastic modulus by promoting a better stresses accommodation during high temperature service. Higher thermal shock resistance was also measured, in comparison to conventional coatings [13, 14].

However, a long term exposures at temperatures higher than 1300°C can promote sintering of the porous microstructure and the growth of the grain size, by counteracting all the advantages of the nanosized structure. Lima et al [15] observed that nanostructured coatings can be properly engineered to prevent the sintering effect, due to their bimodal microstructure characterized by areas with different sintering rate.

Nanostructured alumina-titania coatings were proposed for anti-wear applications, due to their high abrasion and sliding wear resistance, significantly higher than those of conventional coatings [11]. The high wear resistance can be ascribed to the presence of the nanozones, able to arrest cracks propagation. Also nanostructured Tungsten Carbide-Cobalt coatings are promising for anti-wear applications [16, 17].

The presence of porous and friable nanozones can be also useful for the production of abradable coatings for high temperature applications in turbine engines and can also favor the bioactivity level of biomedical coatings via biomimetism.

The blend between the promising properties of nanostructured coatings, the lack of studies about their characterization, the possibility offered by Air Plasma Spray to produce coatings with well-tailored characteristics, and the excellent properties of zirconia which make such material suitable for different applications, represents then the motivation of the work presented in this Chapter.

1.2 Materials and methods

1.2.1 Samples fabrication by APS

The nanostructured YSZ ceramic coatings analyzed in the present dissertation were deposited on Ni superalloy disks (IN738, $\phi = 25$ mm, thickness = 4 mm) by means of an APS process. The substrates were sand blasted using an alumina abrasive powder to increase their surface roughness and to improve the mechanical interlocking between coating and substrate. The substrate roughness, measured using three dimensional optical surface profilometer, was found to be 6.9 ± 1.1 μm . A metallic CoNiCrAlY coating (Amdry 995C, Sulzer Metco) with thickness of 150 μm was previously applied as bond coat on the substrate surface.

Figure 1.5 shows the Air Plasma Spray equipment used for the production of the samples.

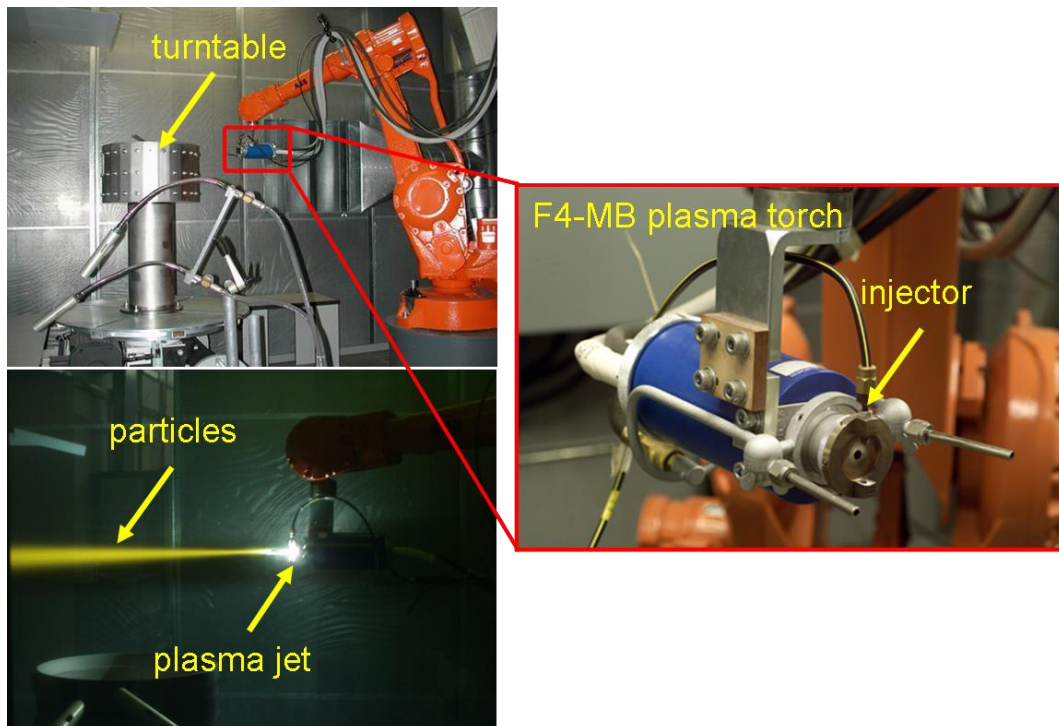


Figure 1.5: APS system installed at ENEA Brindisi Research Centre. [18]

Such equipment is installed at ENEA Brindisi Research Centre, Italy, and it is able to deposit coatings with thickness varying from tens of microns to few millimeters. The system is equipped with a F4-MB plasma torch with a 6 mm internal diameter nozzle (Sulzer Metco, Wolhen,

Switzerland). As shown in Figure 1.5, the plasma gun is moved by an industrial robot (model IRB 2400 M98A, ABB Ltd, Zurich, Switzerland) with six external axes, whereas the samples to be coated are fixed on a turntable with two external axes. An operator controls the motions of both the plasma torch and the turntable. Such configuration allows to coat substrates with complex geometry and different sizes.

The electric components of the APS system include a direct current (DC) PT-820E (800 A, 100 V) power source, a high frequency RF spark ignition source, and the electric controls for arc current and voltage. The plasma gun contains the cathode and the anode. This latter is shaped as a constricting nozzle and is water-cooled. An argon-hydrogen gas mixture was pumped into the gun in order to create the plasma from the high-voltage discharge which produces a localized ionization and a conductive path for a DC arc to form between the electrodes. The electric arc causes a resistance heating and increases the gas temperature, by inducing its ionization and then the formation of a high-energy plasma. Since the cold gas around the surface of the water-cooled anode nozzle is electrically non-conductive, it constricts the plasma arc and increases its temperature and velocity. A nanostructured ZrO₂-7wt% Y₂O₃ powder feedstock (Nanox S4007, Inframat, US) was used. It was first placed in a powder feeder (model Twin-120-A) in order to be stirred by a stirrer vibrator. During stirring, the powder particles precipitate on the upper surface of a rotating disk and herein they are collected by an argon gas and carried up to the injector through a carrier tube. The injector, placed at a distance of 5 mm from the exit of anode nozzle, introduces the powder particles into the high-temperature plasma flame which superheats, partially melts and accelerates the raw material toward the cold substrate. Herein, the particles impact and finally cool down to room temperature by producing a coating characterized by irregular thin lamellae.

The final thickness of the coatings was of about 300 μm whereas their roughness was equal to $8.3 \pm 1.0 \mu\text{m}$ (no significant changes were appreciated for the samples produced using different process parameters). Two sets of six different samples were produced for indentation and tribological tests

respectively. The six samples of each set (shown in Figure 1.6) differ for the process parameters employed: the arc current was varied on three levels (500 A, 565 A and 630 A) and the substrate-torch distance on two levels (80 mm e 100 mm). The other parameters were kept constant as summarized in Table 1.1.

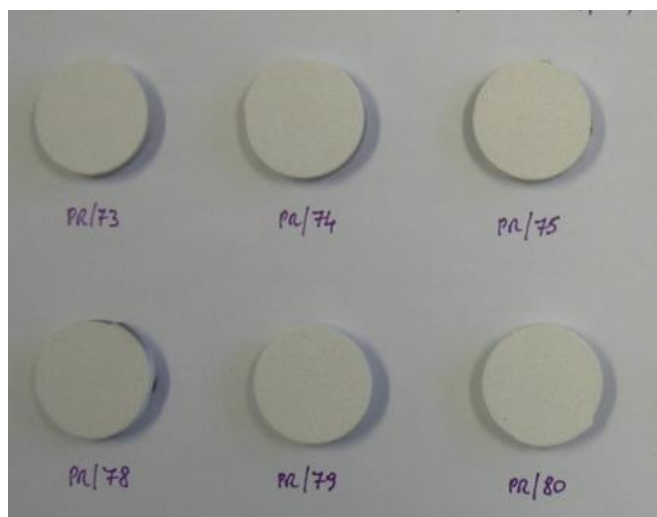


Figure 1.6: set of YSZ coated samples produced by APS with different process parameters.

Table 1.1: APS process parameters used for the production of nanostructured YSZ coatings.

Arc Current (A)	500, 565, 630
Substrate-torch distance (mm)	80, 100
Primary gas (Ar) flow rate (slpm)	40
Secondary gas (H ₂) flow rate (slpm)	12
Powder flow rate (g/min)	28,5
Substrate tangential speed (mm/s)	2086

Whereas the set of samples for the tribological characterization was tested after the APS process, the set addressed to microstructural characterization and indentation tests was subject to a further processing. Indeed, in order to analyze all the microstructural features of plasma sprayed coatings, such as pores, splat boundaries, and microcracks, the coating cross section has to be properly prepared. Grinding and polishing steps are needed to produce a cross section suitable for SEM observations at both low and high magnifications. Such procedure is also needed for indentation tests, since a flat surface is required.

The samples were cut by means of a low-speed precision saw (Isomet, Buelher Ltd, Lake Bluff, Illinois, U.S.) in order to obtain the cross sections. In particular, the saw was equipped with diamond wafering blades recommended for precise sectioning of thermally sprayed coatings. After cutting, the samples were cleaned and cold-mounted in vacuum in a bi-component epoxy resyn. The specimens were subsequently evacuated in a vacuum desiccator (Vacuum Impregnation Pump, Buelher, Lake Bluff, Illinois, U.S.) in order to fill the open pores and the microcracks of the materials. Such filling procedure was performed to preserve the starting size and the shape of the pores and to minimize the pull-out effect caused by grinding and polishing procedures. Moreover, the microstructure of the material can be more clearly observed by SEM analysis after the filling process. The grinding procedure was carried out by means of a grinder-polisher machine (Motopol 2000, Buelher Ltd, Lake Bluff, Illinois, U.S.), SiC abrasive papers (35 and 26 μm), and special diamond discs (20 and 10 μm). Water was used during grinding in order to remove abrasion debris. The specimens were ultrasonically cleaned in demineralized water at the end of each step. The polishing process was performed by using texmet cloths and diamond abrasive pastes and suspensions (6 μm , 3 μm and 1 μm , respectively). An alumina suspension was finally used to finish the samples up to 0.25 μm . During polishing the surfaces were cooled and lubricated with an ethanol and oil suspension. The rotation speed of the disc and the contact pressure were set according to the values recommended for thermally sprayed coatings in order to avoid the pull-out

of particles and the generation of large pores. After polishing, cross sections were ultrasonically cleaned in ethanol and dried at 100 °C in oven (Ghibli Plus, Carlo Erba Reagenti, Milano). A very thin gold film (thickness ~ 20 nm) was finally sputter-deposited on the polished cross section to prevent surface charging during SEM observations. Figure 1.7 shows the set of samples at the end of the grinding and polishing procedure described above. As shown in Figure 1.7, two cross sections were cold-mounted and polished for each sample in order to have a bigger amount of material to be analyzed.



Figure 1.7: cold-mounted and polished cross sections prepared for the microstructural analysis and the indentation tests.

1.2.2 Microstructural characterization

The phase composition of nanostructured zirconia powder and coatings produced using different processing parameters was investigated by x-ray powder diffraction (XRD). XRD is an experimental technique which allows to obtain informations about the structure of crystalline materials. In particular, an incident beam of monochromatic X-rays interacts with the tested

material and, according to the obtained diffraction pattern, information such as the sample purity, or the unit cell dimensions, can be obtained.

In particular, an x-ray powder diffractometer (XRD PW 1880, Philips, Almelo, Netherlands), operating with CuK α radiation ($\lambda = 0.154186$ nm), produced at 40 kV and 40 mA, was used. The analyzed range of the diffraction angle 2θ was between 20 and 80°, by a step width of 0.02° and a time per step equal to 5 s.

The morphology and the microstructure of powder feedstock and as-sprayed YSZ coatings were analyzed by scanning electron microscopy (SEM). A scanning electron microscope scans the surface of a sample with a focused beam of electrons. When electrons interact with the atoms of the sample they produce different signals containing informations about the topography and the composition of the sample's surface.

In particular, the SEM-LEO 438 VP, Carl Zeiss AG (Oberkochen, Germany) microscope was used. The SEM pictures were then processed by image analysis software (Image J, U.S. National Institutes of Health, Bethesda, MD, USA) to measure the percentage of molten and semi-molten areas embedded in coating microstructure, and the distribution of the nanostructured areas. The size of the regions used for porosity measurements was 350 x 250 μm^2 .

1.2.3 Depth-sensing indentation tests

An indentation test allows the evaluation of the mechanical properties of a material of interest by touching such material with another material of known properties. Such concept was introduced in 1822 by Friedrich Mohs, who proposed an empirical criterion for the evaluation of the hardness of materials. He defined an hardness scale (i.e., the Mohs' scale) consisting of a list of minerals enumerated from 1 to 10 in which each material is able to scratch to previous one and it is scratched by the following one. The maximum value of 10 was assigned to diamond. Such approach leads to a qualitative estimation of the hardness and the indentation technique was subsequently refined with

the introduction of the Brinell, Rockwell, Knoop, and Vickers tests. These tests consist of performing a permanent imprint on the tested materials by means of an indenter (the shape of the indenter varies from one test to another) and the hardness of the material can be numerically evaluated by knowing the value of the indentation load and the area of the imprint. This latter is obtained from direct measurements of the dimensions of the impression left on the surface of the sample and observed by means of optical acquisitions. The conventional indentation tests mentioned above are characterized by consistent limitations. Since extremely small imprints (in the range of few micrometers or nanometers) are hard to be observed with common optical microscopes, only large volumes of material can be tested at high indentation loads and the analysis of thin films or nanostructured materials cannot be carried out. Furthermore, the measurement of mechanical properties different from hardness cannot be performed by conventional indentation.

The introduction of depth-sensing indentation (also known as instrumented indentation) overcame the limitations mentioned above since the area of the imprint can be estimated by knowing the penetration depth of the indenter and its geometry. Besides, due to the real time acquisition of the indentation load and the penetration depth, several mechanical properties, such as the Young modulus or the creep behavior, can be estimated.

Figure 1.8 schematically shows the working principle of depth-sensing indentation. By means of a load actuator and a displacement sensor, the system records real time the applied load, P , and the penetration depth, h , while the indentation is performed and the indentation curve (shown in Figure 1.9) is obtained. A reference ring detects the sample surface which needs to be perfectly flat.

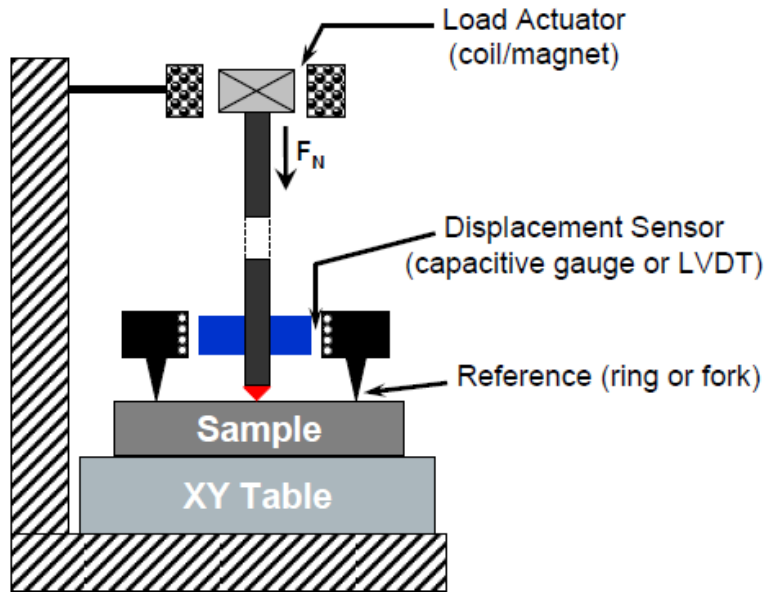


Figure 1.8: instrument principle for depth-sensing indentation [19].

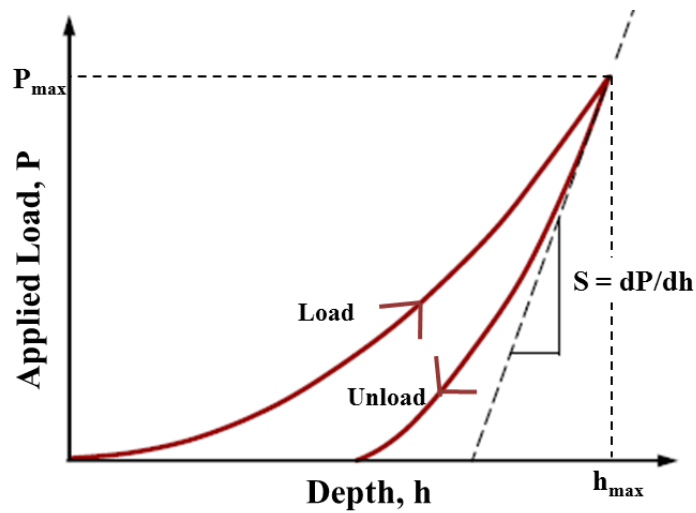


Figure 1.9: indentation curve (Load versus penetration depth).

In order to understand how mechanical properties can be evaluated by means of depth-sensing indentations, basic principles of contact mechanics need to be considered [20]. Figure 1.10 shows the schematic representation of the contact between a rigid sphere and a flat surface with modulus E .

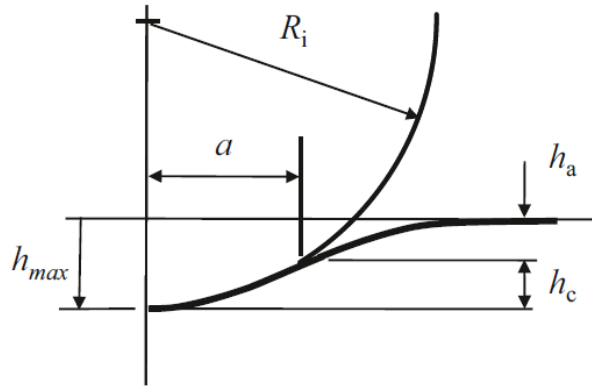


Figure 1.10: Schematic representation of contact between a rigid indenter and a flat specimen, where a is the radius of the circle of contact, h_{max} the total depth of penetration, h_a the depth of the circle of contact from the specimen surface, and h_c the contact depth (the distance from the bottom of the contact to the contact circle) [20].

Hertz proposed the following relation [21, 22] for the radius of the contact circle a , the indentation load P , the relative radius R , and the indentation modulus E_r :

$$a^3 = \frac{3 PR}{4 E_r} \quad (1.1)$$

The indentation modulus E_r , also called “reduced modulus” or “combined modulus” is defined as follow:

$$\frac{1}{E_r} = \frac{(1 - \nu^2)}{E} + \frac{(1 - \nu_i^2)}{E_i} \quad (1.2)$$

where ν and E are the Poisson ratio and the Young modulus of the flat specimen, ν_i and E_i the Poisson ratio and the Young modulus of the tip (usually $E_i = 1141$ GPa and $\nu_i = 0.07$ for a diamond tip). The relative radius R is instead given by:

$$\frac{1}{R} = \frac{1}{R_s} + \frac{1}{R_i} \quad (1.3)$$

where R_i is the indenter radius and R_s the specimen radius. In particular, while the indenter radius is set to be always positive, the sample radius is considered positive if its center of curvature lies in the opposite side of the lines of contact.

It is worth noting that the Hertz's equations refer to localized deformations in the region of contact and not to bulk deformations and stresses of the contacting bodies. The profile of the deflection h of the specimen surface in the vicinity of the indenter is given by the following equation:

$$h = \frac{1}{E_r} \frac{3}{2} \frac{P}{4a} \left(2 - \frac{r^2}{a^2} \right) \quad r \leq a \quad (1.4)$$

The mean contact pressure p_m , is defined as the ratio between the indentation load P and the contact area:

$$p_m = \frac{P}{\pi a^2} \quad (1.5)$$

Combining Equation 1.5 with Equation 1.1, the following relationship can be obtained:

$$p_m = \left(\frac{4E_r}{3\pi} \right) \frac{a}{R} \quad (1.6)$$

Equation 1.6 is considered a kind of constitutive stress-strain relation of indentation, where p_m is the “indentation stress” and a/R the “indentation strain”. However, it is worth noting that although in Equation 1.6 a fully elastic condition yields a linear response like in conventional uniaxial tension tests, the localization of the stress field confers to the “indentation stress-strain relationship” the ability to give information about the elastic-plastic properties of the indented materials, which are not available by means of a classic uniaxial tension tests. Considering a conical indenter instead of a spherical one, Equation 1.1 and 1.4 can be written as follow, respectively:

$$P = \frac{\pi}{2} a^2 E_r \cot \alpha \quad (1.7)$$

$$h = \left(\frac{\pi}{2} - \frac{r}{a}\right) a \cot\alpha \quad r \leq a \quad (1.8)$$

where α is the semi-angle of the cone, as illustrated in Figure 1.11. The term $a \cot\alpha$ is the effective contact penetration h_c , as shown in Figure 1.11.

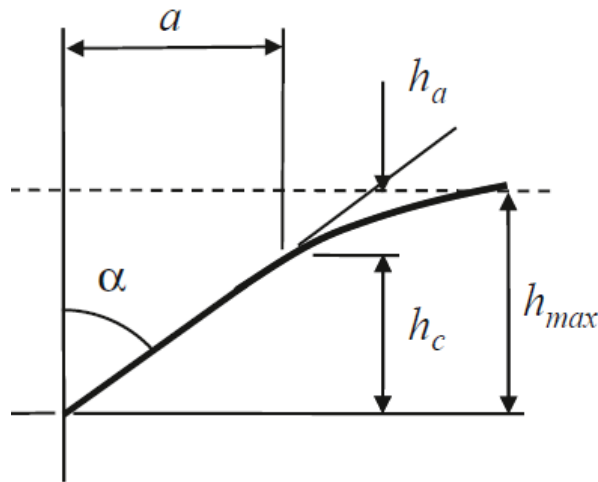


Figure 1.11: Illustration of the contact with a conical indenter [20].

The relationship between the indentation load P and the maximum penetration depth h_{max} can be obtained by substituting Equation 1.7 into Equation 1.8 with $r = 0$:

$$P = \frac{2}{\pi} E_r \tan\alpha h_{max}^2 \quad (1.9)$$

The most commonly used indenters are usually characterized by a spherical shape (in this case the Hertz's equations can be directly applied) or pyramidal shape. The four-sided Vickers indenter and the three-sided Berkovich indenter are the most common pyramidal indenters.

As mentioned before, the peculiar characteristic of depth-sensing indentation is related to the possibility of calculate the area of the imprint by avoiding direct measurements and optical acquisitions. The contact area is in fact related to the geometry of the indenter and to the effective

penetration depth. For a spherical indenter, the radius of the contact circle can be simply obtained as follow:

$$a = \sqrt{2R_i h_c - h_c^2} \approx \sqrt{2R_i h_c} \quad (1.10)$$

The approximation of Equation 1.10 is the same one applied in the Hertz's equations (Equations 1.1 and 1.4) and it is suitable for small deformations ($h_c \ll R_i$).

For a conical shape indenter, the radius of the circle of contact is instead given by:

$$a = h_c \tan \alpha \quad (1.11)$$

Pyramidal indenters are usually considered as conical indenters with a cone angle able to provide the same relationship between the contact area and the penetration depth. Due to this assumption, Equations 1.7-1.9, which refer to axial-symmetric elastic problems, can be used also for contact problems involving non-axial-symmetric indenters such as the pyramidal ones.

Table 1.2 shows the formula for the projected area and the intercept factor (whose meaning is described below) for different types of indenters, as well as the semi-angles and the effective cone angles values given for pyramidal tips, while Figure 1.12 shows the geometry of some of the indenters commonly used.

Table 1.2: Projected areas and intercept factors for various types of indenters. The semi-angles given for pyramidal indenters are the face angles with the central axis of the indenter [20].

Indenter type	Projected area	Semi-angle θ (deg)	Effective cone angle α (deg)	Intercept factor ϵ
Sphere	$A \approx \pi 2R h_c$	N/A	N/A	0.75
Berkovich	$A = 3\sqrt{3}h_c^2 \tan^2 \theta$	65.27°	70.3°	0.75
Vickers	$A = 4h_c^2 \tan^2 \theta$	68°	70.3°	0.75
Knoop	$A = 2h_c^2 \tan \theta_1 \tan \theta_2$	$\theta_1 = 86.25^\circ$, $\theta_2 = 65^\circ$	77.64°	0.75
Cube corner	$A = 3\sqrt{3}h_c^2 \tan^2 \theta$	35.26°	42.28°	0.75
Cone	$A = \pi h_c^2 \tan^2 \alpha$	α	α	0.727

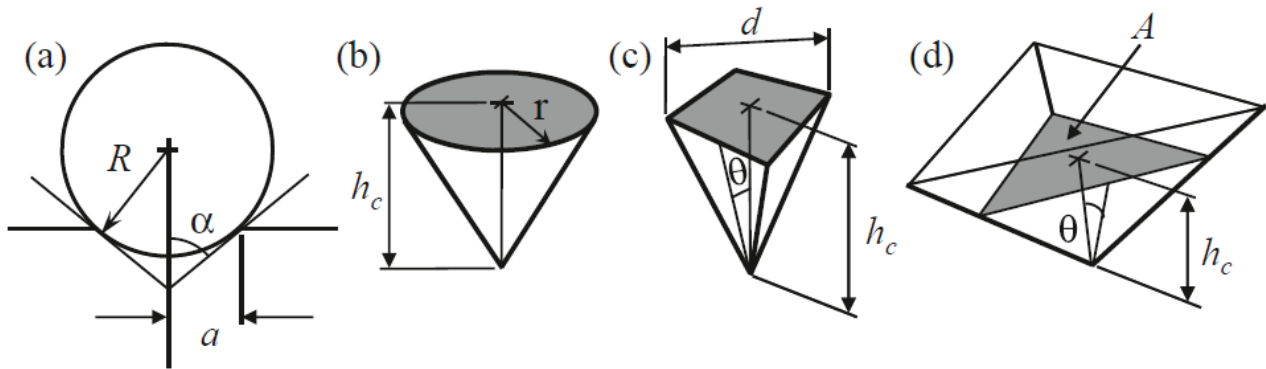


Figure 1.12: indentation parameters of commonly used indenters: a) spherical, b) conical, c) Vickers, d) Berkovich [20].

Fundamental equations can be obtained by deriving the indentation load P with respect to the penetration depth. Considering the case of a conical indenter, from Equation 1.9, one can obtain:

$$\frac{dP}{dh} = 2 \left(\frac{2}{\pi} E_r \tan \alpha \right) h \quad (1.12)$$

Considering $r = 0$ in Equation 1.8 and inserting into Equation 1.12, we obtain:

$$\frac{dP}{dh} = 2 E_r a \quad (1.13)$$

Finally, considering the relationship between the radius of the circle of contact a and the projected area A , the basic equation of the depth-sensing indentation technique can be obtained:

$$E_r = \frac{\sqrt{\pi}}{2} \frac{S}{\sqrt{A}} \quad (1.14)$$

where $S = dP/dh$ is the contact stiffness evaluated at the beginning of the unloading curve, as shown in Figure 1.9. Equation 1.14 can be applied for the elastic contact with any axis-symmetric indenter with a smooth profile and, combined with Equation 1.2, it allows to calculate the Young modulus E of a tested materials. As described before, the projected area of the imprint can be calculate by

using formula in Table 1.2, by knowing the geometry of the tip and the effective penetration depth h_c . However, only the maximum penetration depth h_{max} can be experimentally measured by means of displacement sensors (shown in the schematic representation of Figure 1.8) and such value differs from the effective penetration depth h_c , which refers to the real contact between the tip and the specimen, due to the deflection of the surface of this latter (such phenomenon is known as “sink-in”). Oliver and Pharr [23, 24] proposed the following equation for the calculation of the effective penetration depth, h_c :

$$h_c = h_{max} - \varepsilon \frac{P_{max}}{S} \quad (1.15)$$

where ε is the intercept factor, whose values, for different types of indenters, are listed in the last column of Table 1.2.

From depth-sensing indentation tests also the indentation hardness can be easily calculated. Although there are different definitions of hardness [20], the most commonly used definition of indentation hardness is that one proposed by Meyer, consisting in the following equation:

$$H = \frac{P_{max}}{A} \quad (1.16)$$

where P_{max} is the maximum indentation load and A the projected area of contact, as described above. According to Equation 1.16, the indentation hardness is then defined as the mean contact pressure at full load and it must be measured in conditions of full plasticity in order to obtain a load-independent value.

The evaluation of the indentation area A is strictly related to the geometrical parameters of the indenter and when this latter is subject to wear after several tests, its geometry changes by causing significant errors in the estimation of the mechanical properties of the tested materials. For such reason, a periodic calibration of the indenter tip is usually required. During such procedure, the

relationship between the projected area A and the effective indentation depth h_c is experimentally obtained by means of a fitting procedure, according to the following formula:

$$A_p = C_0 h_c^2 + C_1 h_c + C_2 h_c^{\frac{1}{2}} + C_3 h_c^{\frac{1}{4}} + \dots \quad (1.17)$$

The mechanical properties of YSZ coatings were determined by depth-sensing Micro and Nano Indentation tests. A measuring system of CSM Instruments SA, Peseux, Switzerland, was used. As shown in Figure 1.13, such system is equipped with a Micro Indenter and a Nano Indenter head, an Optical Microscope with three objective lenses (with magnitude of 5x, 20x and 100x), a ConScan, an XY motor which moves the sample holder and an anti-vibration table.

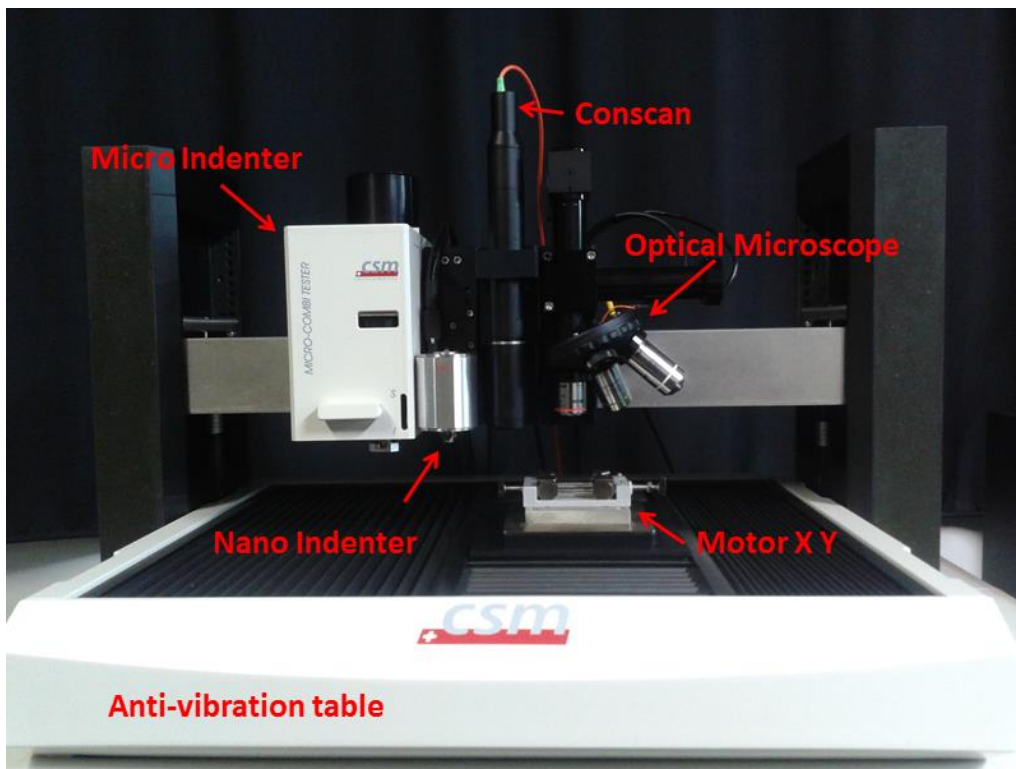


Figure 1.13: Equipment for indentation tests.

The indentations were performed on a portion of the ceramic top coat containing areas with different melting degree and were equally spaced (40 μm for NI and 60 μm for MI) in order to avoid the mutual influence of consecutive indentations [20]. In depth-sensing indentation tests, an

Adjust Depth Offset (ADO) operation must be performed at the beginning in order to find the height position of the sample surface, which represents the zero for the penetration depth parameter. Since the surface of the tested YSZ coatings is quite heterogeneous due to the presence of nanostructured zones, melted areas, and microstructural defects such as pores or macrocracks, one ADO at the beginning of a series of indentations is not sufficient because the height position of the sample surface changes from one point to another due to the high roughness. When the indenter tip does not find the sample surface in a certain tolerance range established during the ADO, the indentation cannot be performed and no output data are recorded. Ideally, a solution could be to perform an ADO every indentation, but such strategy implies a too long testing time when several indentations are performed. Considering the roughness of the tested samples and the ADO height range tolerance, it was found that an ADO operation every ten indentations (acronym ADO in Figure 1.14) was sufficient to obtain sufficient output data (very few indentations did not started because of ADO issues).

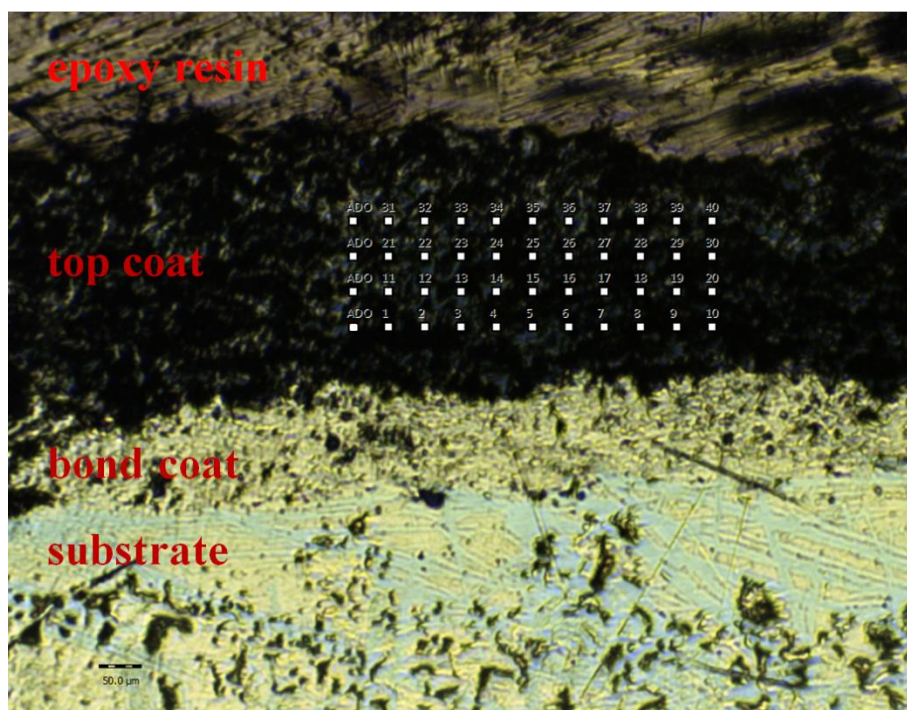


Figure 1.14: Disposition of NI on the topcoat cross section. Starting from the top: epoxy resin, topcoat, bondcoat and metallic substrate (magnitude5x).

NI tests were performed according to a 4x10 matrix (with lines parallel to the substrate) by using a Berkovich tip, a loading and unloading speed of 3 mN/s, a hold time of 10 s and two different values for the maximum load: 8 and 100 mN. MIs, distributed according to a 3x10 matrix, were also performed by using a Vickers microindenter with maximum loads of 50 gf and 100 gf and a hold time of 10 s. The values of the indentation loads reported above were chosen to cover a sufficiently large range, from the nanoscale to the microscale, in order to analyze the mechanical properties of the coatings at different length scales and observe the contribution of both the melted and nanostructured areas to the final performances of the material.

The experimental data were analyzed by assuming a two-parameters Weibull statistical distribution, suitable to study the behavior of ceramic materials characterized by different phases [25].

1.2.4 Tribological tests

The second set of specimens was addressed to wear tests. For the tribological characterization ball-on-disk tests were carried out using a CSM Instrument Tribometer, shown in Figure 1.15. The tests were performed in dry mode with a sintered α -Al₂O₃ ball (6 mm in diameter), a wear track radius of 5 mm, a normal load of 10 N, a linear speed of 0.1 m/s and a cycle number of 20,000. The wear rate was calculated according to the Equation (1.18):

$$WR = \frac{V}{Fl} \quad (1.18)$$

where WR is the wear rate [mm³/(Nm)], V is the worn volume [mm³], F is the normal applied load [N] and l the sliding distance [m]. The track profile was determined by means of a Taylor-Hobson Surtronic 25 profilometer (Rand Taylor Hobson Ltd., Leicester, UK) and as the maximum depth of the worn area exceeded the full scale of the profilometer (300 μ m) the CSM Instrument ConScan (shown in Figure 1.13) was used. Ten randomly located profile measurements were performed on

each tested sample after removing wear scraps by an air jet. The wear tracks were finally analyzed by scanning electron microscopy.

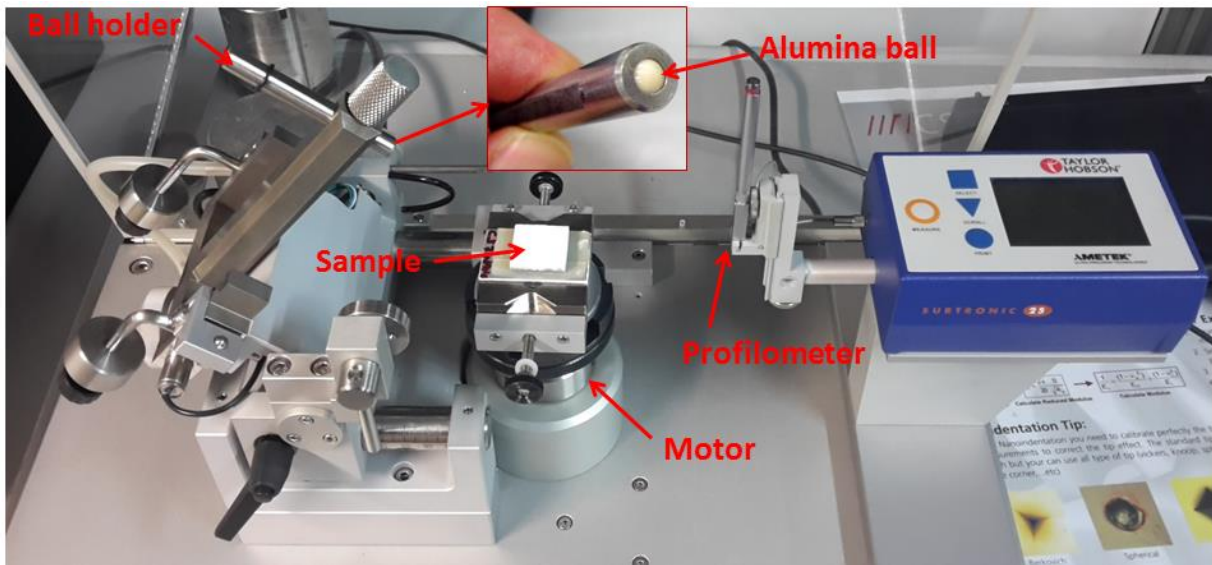


Figure 1.15: Equipment for tribological tests.

1.3 Results and discussion

1.3.1 Microstructure

X-ray diffraction patterns of YSZ powder and coatings produced using different processing parameters are shown in Figure 1.16: the high-angle ($72-75^\circ$) region of the diffraction patterns showing (400) zirconia reflections is drawn. The powder feedstock is mainly composed of tetragonal t zirconia phase with smaller amounts of cubic and monoclinic zirconia phases, according to Joint Committee on Powder Diffraction Standards (JCPDS) available at International Centre for Diffraction Data (no. 81-1544 for tetragonal, no. 49-1642 for cubic and no. 37-1484 for monoclinic zirconia). All the coatings are composed of a mixture of metastable t' zirconia phase and tetragonal t phase. The metastable t' phase is associated to the molten part of the powder agglomerated particles, whereas the tetragonal t phase is associated to their retained nanostructured unmelted nanostructured part. No monoclinic phase was detected in the coatings. The calculation of the

percentage of t' and t zirconia phases cannot be properly performed by XRD spectra because of the overlapping between the related peaks. As reported below, more reliable estimation can be obtained by studying the distribution of retained nanostructured areas in the coating microstructure using scanning electron microscopy.

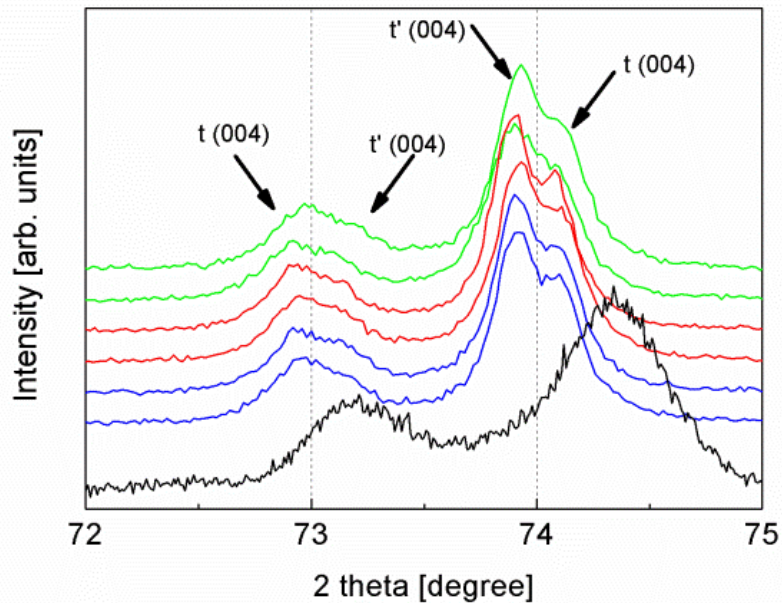


Figure 1.16: High-angle region of XRD spectra for YSZ (a) powder and coatings produced using different process parameters: (b) 500 A and 80 mm, (c) 500 A and 100 mm, (d) 565 A and 80 mm, (e) 565 A and 100 mm, (f) 630 A and 80 mm, and (g) 630 A and 100 mm.

Figure 1.17 shows the cross sectional SEM microstructure of nanostructured YSZ coatings produced at the spraying distance of 80 mm and using different values of plasma current (500, 565 and 630 A).

The plasma current is proportional to the plasma power and to the temperature of the sprayed particles, so that it can be used to have a good control on the degree of melting of the particle agglomerates. All the coatings exhibited a bimodal microstructure composed of well melted splats (dark grey dense areas in the pictures) and partially melted nanostructured areas (light grey areas) possessing an intrinsic porosity derived from their pre-agglomeration, as shown in Figure 1.18 (a). The nanostructured areas are composed of loosely bound nanostructured particles.

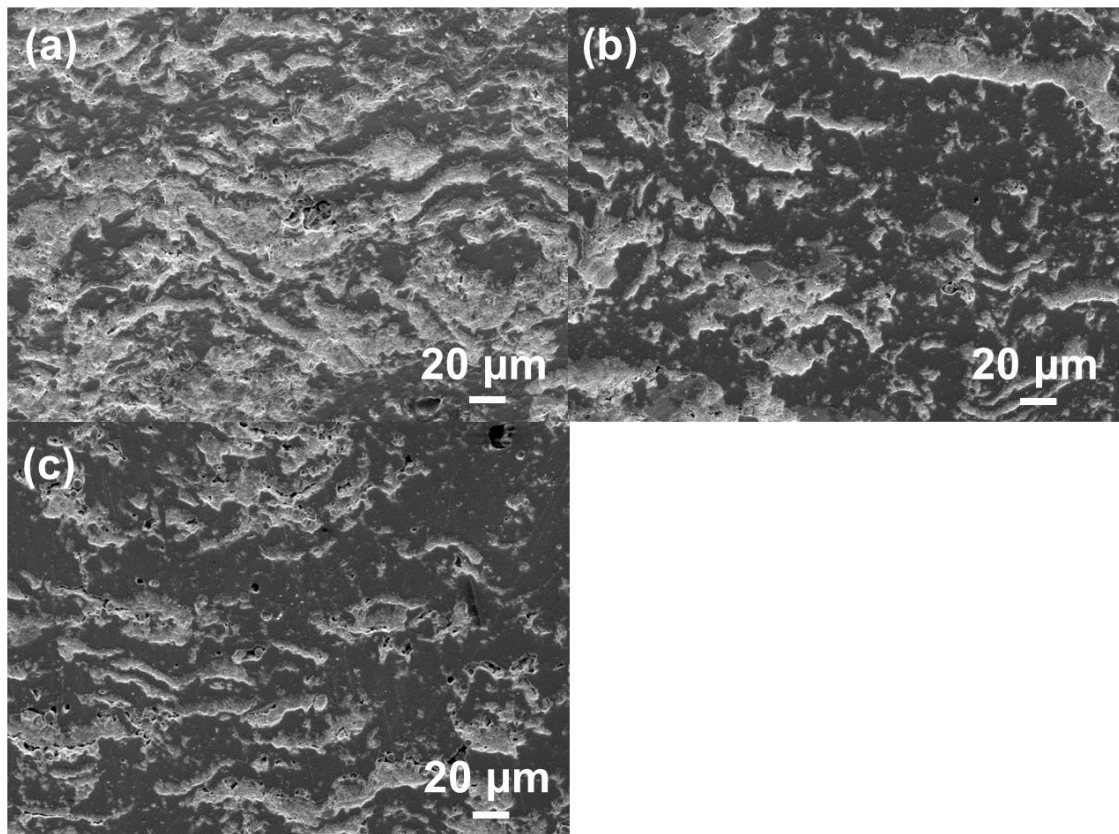


Figure 1.17: cross sectional SEM microstructure of nanostructured YSZ coatings deposited at spraying distance of 80 mm and various plasma current levels (a) 500 A, (b) 565 A and (c) 630 A.

Figure 1.18 (b) shows the morphology of the related powder particles, so that it can be deduced that the nanostructured zones retained in the final coatings were not affected by complete melting during processing. The inset shows some clusters of nanograined particles with size close to 100 nm. During processing the hot plasma gas penetrated inside the agglomerated particles of the powder feedstock, melting their surface, while their core remained unmelted. The low heat transfer associated to their intrinsic porosity, the short residence time of the same sprayed particles in the plasma jet and the high quenching rate of the solidified splats at the substrate surface were able to reduce the mechanism of grain growth and nucleation, thus preserving great part of the starting nanostructure in the final coating.

As well displayed in Figure 1.17, the well melted areas cement the loose microstructure, providing good mechanical integrity. The distribution of the nanostructured areas is more uniform for lower

values of plasma current. For increasing values of this parameter the melting degree of the powder particles enhances, thus leading to denser coating with lower content of nanostructured areas. The flight path and the temperature history of the agglomerated particles in the plasma jet affect their distribution in the final coatings. The melting process is strongly related to the temperature distribution in the plasma jet and to the heat transfer to the porous agglomerates.

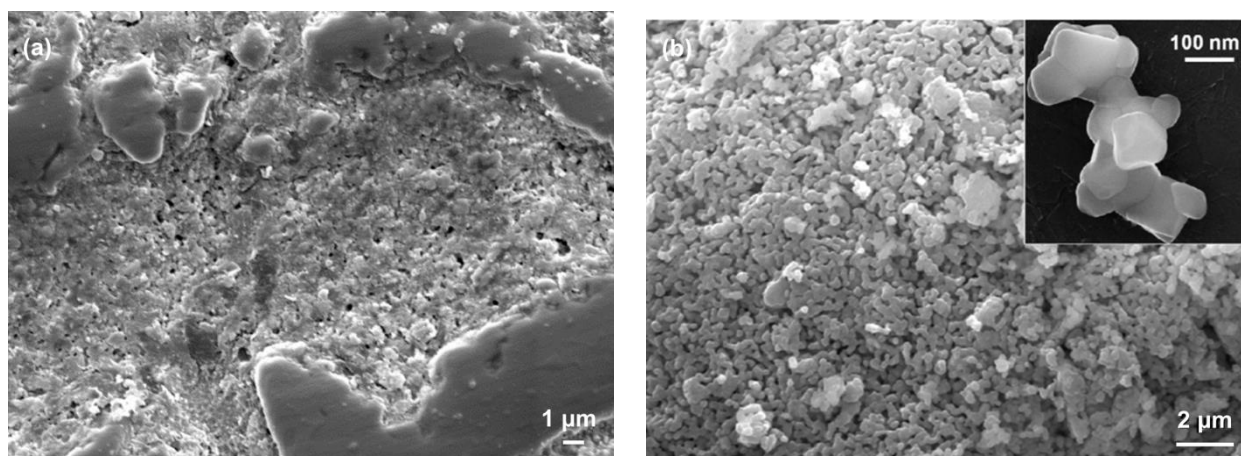


Figure 1.18: (a) cross sectional SEM microstructure showing the morphology of retained nanostructured areas; (b) a view of agglomerated nanoparticles in the powder feedstock with detail of zirconia clusters

Table 1.3 reports the amount of retained nanostructured areas measured by image analysis along the cross section of nanostructured YSZ coatings produced using different process parameters. At constant spraying distance the percentage of nanozones decreases with increasing the plasma current, due to the better melting of the particle agglomerates, so that denser coatings are produced. This effect is more pronounced at 80 mm. The effect of spraying distance is more pronounced at the lowest value of plasma current. Higher spraying distance involves higher residence time of the sprayed particles in the plasma jet, better melting and thus higher deposition efficiency and higher coating thickness.

It is worth noting that the percentage of nanostructured areas embedded in coating cross section can be properly optimized based on the application the coating is addressed to. High retention of

nanozones (30-40%) is particularly desired for manufacturing of abradable coatings with relatively low mechanical integrity [1]. These coatings can be used in turbine engines to minimize the bypass flow of hot combustion or cold compressor gases through the spaces between the rotating blade tips and the walls of the shroud, in order to provide seal and improve the efficiency.

Table 1.3: fractions (%) of retained nanostructured areas measured in YSZ coatings produced using different process parameters (plasma current and spraying distance)

Distance/current	500 A	565 A	630 A
80 mm	36 ± 4	23 ± 1	20 ± 4
100 mm	31 ± 2	25 ± 4	21 ± 1

On the contrary, lower retention of nanostructures (20%) is preferable for development of thermal barrier coatings with low thermal conductivity, high structural integrity and resistance to the infiltration of oxygen and molten salts in severe working environments (stator turbine blades and vanes). The presence of nanostructured areas with low sintering rate can counteract the high-temperature densification of YSZ coatings, which negatively affects the compliance and the thermal property, thus retarding extended microcracking and TBC delamination [11].

Nanozones play a significant role on the thermal shock resistance and durability of TBCs, because they act as crack arresters in the case of microcracking promoted by thermal stresses produced by thermal expansion mismatch between overlapped layers, thus increasing the fracture toughness [11]. For this reason a Vickers indentation at very high load (5000 gf) was performed on one of the produced samples in order to induce cracks (white circles in Figure 1.19). In the detailed micrograph taken at higher magnification it can be observed as cracks that propagate in the molten phase are arrested by nanozones.

Columnar grains with diameter in the range from 50 to 300 nm are detectable within coating microstructure (Figure 1.20). They are oriented along the direction of the grain growth and derived

from heterogeneous nucleation at splat boundary produced by the heat flow released by the crystallization of the previous deposited splats. Some equiaxed grains can be also observed at splat boundary. They are produced by homogeneous nucleation, occurring when the heat loss promoted by cooling at the substrate is higher than the heat released by the crystallization [26].

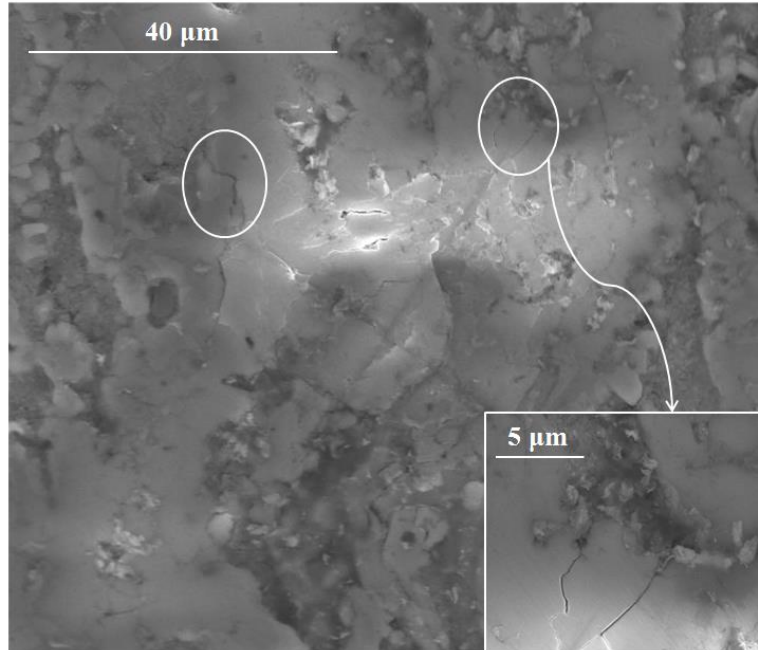


Figure 1.19: Crack arrest produced by nanozones in plasma sprayed nanostructured YSZ coating.

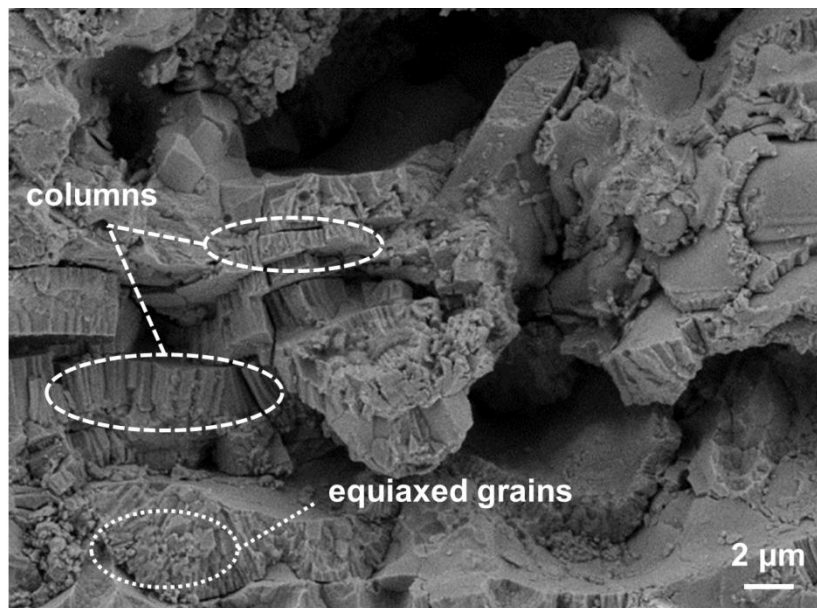


Figure 1.20: Fractured coating crosssection showing the morphology of the melted splats, composed of columnar and equiaxed grains.

1.3.2 Mechanical properties

Tables 1.4 and 1.5 summarize the values of Young's modulus, nano and microhardness measured on the cross sections of nanostructured YSZ coatings, deposited at spraying distance of 80 and 100 mm, respectively, and using different values of plasma current parameter. The measured values magnitude is in good agreement with that of results in literature [27, 28].

Table 1.4: mean values and standard deviations of the mechanical properties for YSZ coatings sprayed at 80 mm and using different values of plasma current, measured by Micro and Nano Indentation tests using various loads

Load	Current (A)	Er (GPa)	H (GPa)
8mN (NI)	500	151 ± 47	11.1 ± 5.4
	565	170 ± 33	11.8 ± 4.9
	630	174 ± 42	13.7 ± 4.8
100mN (NI)	500	100 ± 37	6.3 ± 3.9
	565	121 ± 37	8.3 ± 4.7
	630	125 ± 41	7.9 ± 4.3
50gf (MI)	500	76 ± 20	4.2 ± 2.4
	565	114 ± 28	6.1 ± 3.2
	630	123 ± 31	8.7 ± 5.0
100gf (MI)	500	80 ± 19	3.4 ± 1.4
	565	100 ± 26	4.4 ± 2.5
	630	125 ± 21	7.2 ± 2.7

Table 1.5: mean values and standard deviations of the mechanical properties for YSZ coatings sprayed at 100 mm and using different values of plasma current, measured by Micro and Nano Indentation tests using various loads

Load	Current (A)	Er (GPa)	H (GPa)
8mN (NI)	500	159 ± 68	9.9 ± 5.8
	565	177 ± 54	11.7 ± 5.1
	630	170 ± 60	12.1 ± 6.2
100mN (NI)	500	108 ± 37	7.1 ± 4.3
	565	124 ± 53	9.1 ± 6.2
	630	135 ± 36	9.5 ± 4.0
50gf (MI)	500	78 ± 40	4.4 ± 3.3
	565	125 ± 40	10.3 ± 6.3
	630	158 ± 73	19.6 ± 12.9
100gf (MI)	500	76 ± 20	3.3 ± 1.9
	565	113 ± 29	5.9 ± 2.9
	630	109 ± 22	5.5 ± 2.6

It should be noted that the mechanical properties tend to increase with increasing the plasma current and the spraying distance. Specifically, at constant spraying distance, for increasing values of current, an average increase of 9% and 30% for Er and 13% and 60% for H, was observed, from nanoscale to microscale, respectively. Instead, the influence of the spraying distance is less prominent. At constant current value, for increasing values of torch-substrate distance, an average increase of 4% and 7% for Er and 3% and 34% for H was recorded, from nanoscale to microscale. It should also be noted that the values of the mechanical properties exhibited large scattering.

Figure 1.21 shows the load-depth (P-d) curves obtained by nanoindentations performed in the melted areas (continuous line) and in partially melted ones (dashed line), respectively. The curves refer to coatings produced at 500 A and 100 mm, but similar behavior was noticed for all the other samples. The parameters used for NI were: maximum load 100 mN, loading and unloading speed 3 mN/s, hold time 10 s.

It is possible to observe that in the melted phase lower maximum penetration was noticed (709 nm versus 2056 nm in the partially melted phase) as well as higher unloading curve slope. This suggests that the melted phase is characterized by higher stiffness and hardness in comparison with the partially melted area [22, 23].

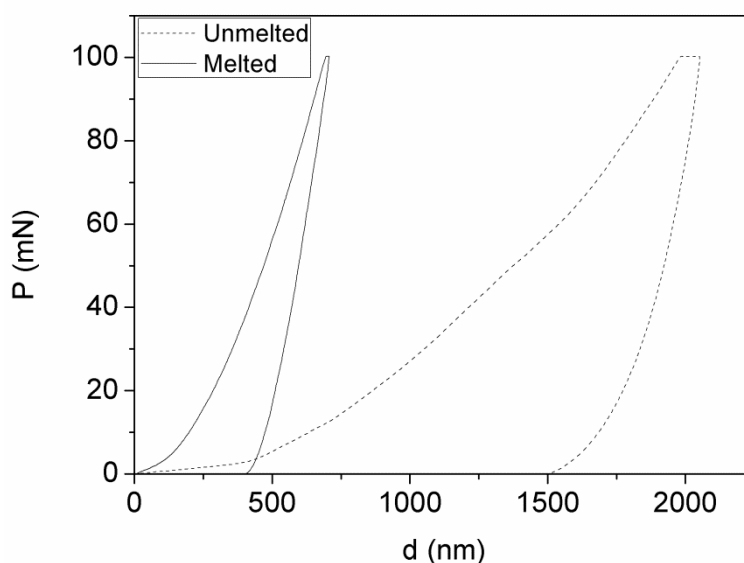


Figure 1.21: Load–depth (P–d) curves corresponding to melted and partially melted phases.

Indeed, as shown in Figure 1.22, the size of the imprint is bigger in partially melted area. The nanostructured areas are characterized by porosity at nanoscale which reduces the cohesion between the agglomerated nanostructured particles. In addition, the curves in Figure 1.21 show that the melted phase reveals a weak creep phenomenon, whereas the unmelted one is quite affected by it. Creep can be observed in the indentation load-depth curve as an increase of the penetration depth during the holding time at the maximum load [20] and in Figure 1.21 one can be clearly observe that such increase is almost absent in the melted area curve whereas it is quite evident in the curve related to the unmelted zone. Based on the observations herein reported, one can conclude that the increase of the mechanical properties, observed in Tables 1.4 and 1.5, is related to the increase of the melted fraction in YSZ coatings when higher values of current and distance are employed (Table 1.3).

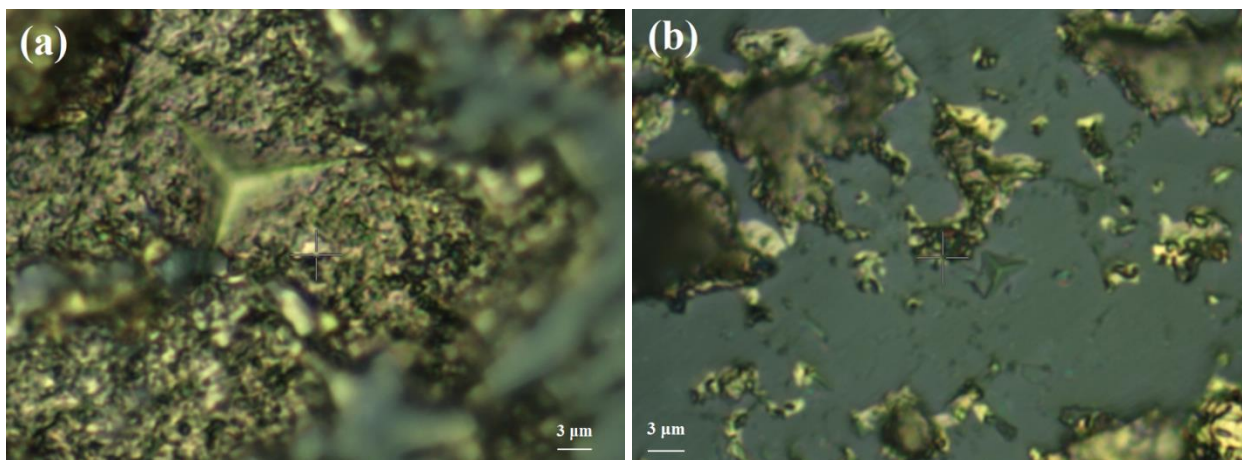


Figure 1.22: Indent of NI (Berkovich) in (a) partially melted and (b) melted phase (magnitude100x).

The usage of increasing current values involves higher plasma power, higher temperature of the sprayed particles and therefore lower retention of nanostructured areas and higher coating density. As previously reported, higher distance involves higher residence time of the sprayed particles in the plasma jet and better degree of melting, even if the effect of distance on the experimental trend of the mechanical properties was not always consistent, probably because of a kind of mutual

influence with current. This aspect could be analyzed in future works by performing an experimental plan that provide a third level of torch-substrate distance and more in-depth analysis.

As clearly observed in Tables 1.4 and 1.5, the values of the mechanical properties measured at microscale are lower than those obtained at nanoscale, because of the larger analyzed volume and the higher influence of typical defects embedded in coating microstructure, such as coarse pores, splat boundaries and microcracks.

Moreover, for each indentation technique employed, as the indentation load rises the analyzed volume grows and the same microstructural defects become more significant, enough to bring down the mechanical properties, that result always more averaged and far from those of bulk stabilized zirconia [29,24].

Further analysis showed that the mechanical properties don't change across coating thickness and their variation is so small to be covered by the high scattering of the results (related to the different characteristics between melted and partially melted phases). In order to understand the reasons of this high scattering, two series of NIs were performed on the areas with different morphology, by using a maximum load of 8 mN and a time for loading and unloading of 10 s, without any hold time. A low indentation load was chosen in order to avoid averaged results and analyzed the single contribution of the different areas present in the material microstructure. Figure 1.23 shows some of the load-depth curves obtained.

It is interesting to notice that the curves related to the melted area (continuous lines) are very close and repeatable, whereas the curves acquired during indentation in the unmelted area (dashed lines) are somewhat different and scattered. The well melted area is, in fact, characterized by lower scattering in the mechanical properties, whereas the second one exhibits widely scattered data (Table 1.6), typical of structures produced by nanostructured agglomerates assembly and characterized by intrinsic porosity. Table 1.6 summarizes the mean values and the standard deviations of the elastic modulus and hardness for both these areas.

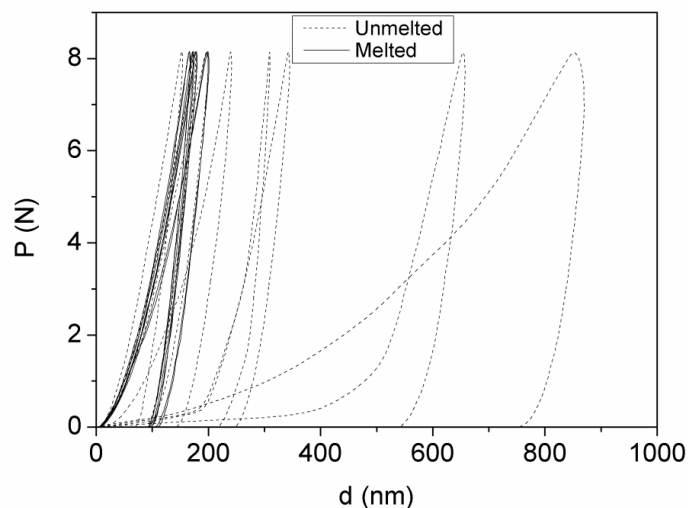


Figure 1.23: Load–depth (P–d) curves corresponding to melted and unmelted fractions and measured by NI at 8mN.

Table 1.6: elastic modulus and hardness of melted and unmelted phases

Mechanical properties	Melted area	Unmelted area
E_r (GPa)	196 ± 29	131 ± 61
H (GPa)	$15,8 \pm 2.3$	9.0 ± 7.8

Figure 1.24 shows the distribution of E_r and H , in a bilogarithmic scale [23], for the well melted and unmelted areas, by assuming a two parameters Weibull distribution for the mechanical properties.

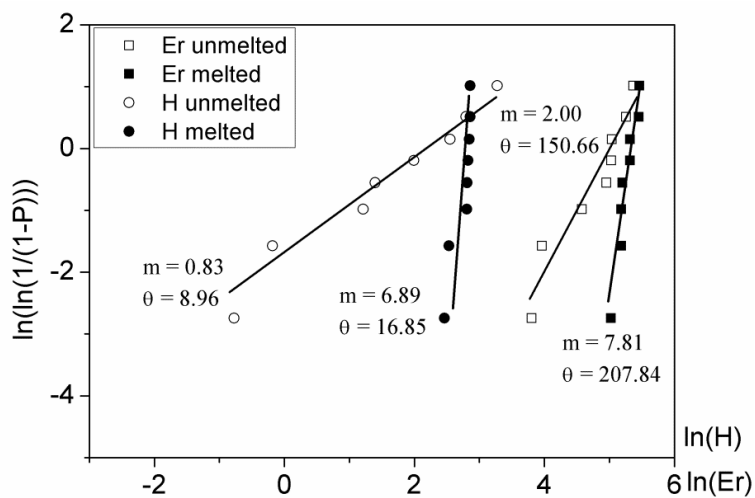


Figure 1.24: Weibull plot of E_r and H for melted and unmelted phases; the shape (m) and the scale (θ) parameters are also reported.

The data can be approximated with a linear regression curve. On the same graph, the values of shape and scale parameters are reported. According to the previous assertions, the melted phase, characterized by less scattered data, presents greater values of m . The probability density functions of Er and H are plotted, respectively, in Figs. 1.25 (a) and (b), in grey for the melted area and in black for the partially melted one. The sample obtained by merging the experimental data related to melted and unmelted areas can be considered like a coating with the 50% of the two phases. The analysis of the distributions concerning this kind of sample can be very useful for the prediction of the mechanical properties of any other nanostructured coating. For this purpose, in Figure 1.26, Er and H Weibull plot of this simulated coating are shown, while Figs. 1.25 (a) and (b) show (dashed lines) the related probability density function (obtained as a weighted average of the probability density of the data referred to single zones).

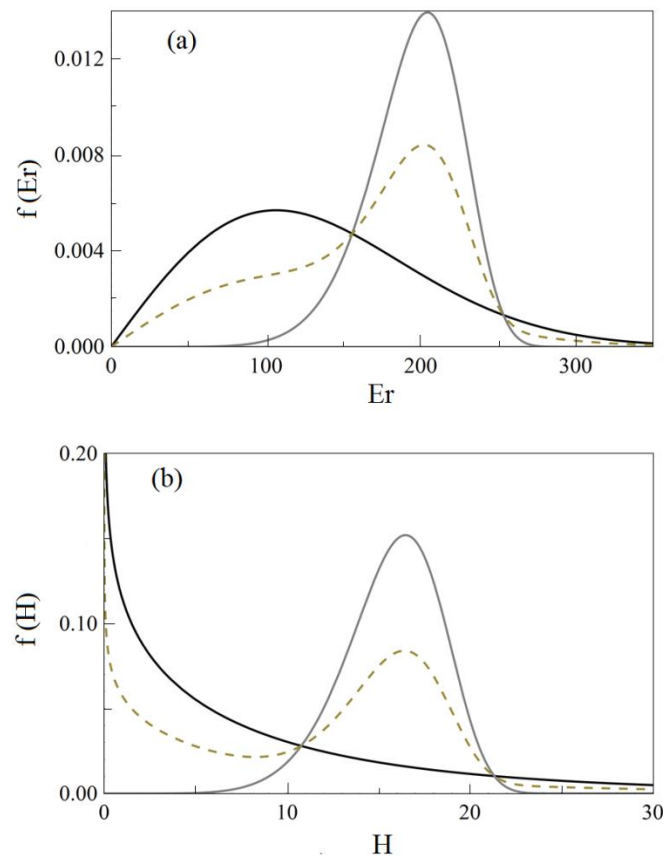


Figure 1.25: Probability density function of (a) Er and (b) H for melted (gray) and unmelted (black) phases and of the resultant bimodal distribution (dashed).

It can be noted that the points related to partially melted phase are so scattered that they contaminate the data of the second section, concerning the melted area, and go also beyond this region (in this example it is just a point). The slope of the mixed section (the second one) increases by decreasing the level of contamination. Despite the data merging, the bimodal behavior of the coating can be clearly observed, due to the change in the slope of the Weibull plot. In order to find the transition point between the two regions the R^2 statistics analysis can be used [29]. It should be noted that the presence of points above the mixed zone may generate incorrect interpretations of the data distribution, by suggesting, erroneously, the existence of a third phase, and then a trimodal distribution. Figure 1.27 shows the trends of the mechanical properties for the coatings produced in this work and tested by Nano Indentation at 8 mN.

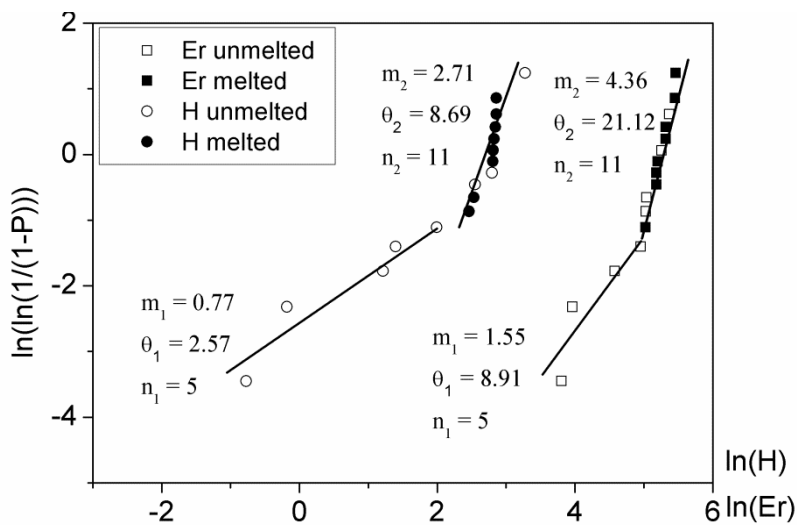


Figure 1.26: Weibull plot of H and Er data for the sample obtained by merging the data arising from melted and unmelted areas.

In all the cases a bimodal Weibull distribution can be noticed, as also observed in any previous works [27,29]. The zone in the graph characterized by lower values of H or Er reflects the mechanical behavior of the partially molten phase and it is characterized by lower slope, owing to greater scattering, whereas the second one is characteristic of the mixed area. It is interesting to notice that, at constant torch-substrate distance, as current value rises the slope of the second

regression line increases: this is caused by the increase of the degree of melting of the sprayed particles which results in lower probability of contamination of the data pertaining to the molten zone. Note that, at constant current level, the increase of the torch-substrate distance produces different trend, but the results are in good agreement with the volume fractions of nanostructured areas listed in Table 1.3.

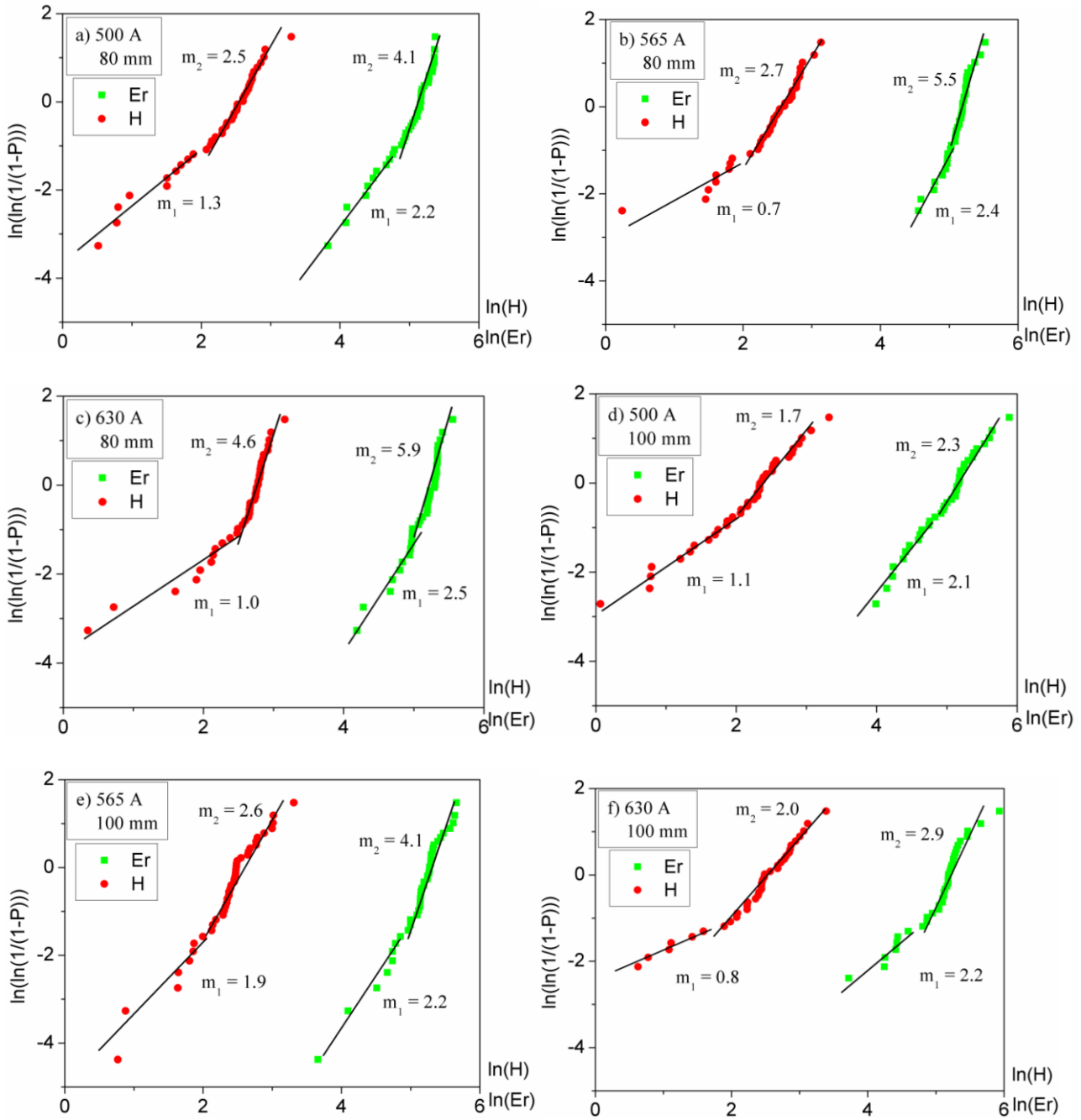


Figure 1.27: Weibull plot of H and Er for nanostructured YSZ coatings fabricated using different process parameters (plasma current and spraying distance) and tested by NI at 8mN.

The results obtained by NI tests performed at maximum load of 100 mN showed similar behavior, but less noticeable changes in slope between the interpolating sections were detected. This effect is the consequence of the greater size of the volume involved during NI at higher load, which mediates the local properties and makes the bimodality of the distributions more difficult to be observed.

In turn the results obtained by Micro Indentation for the coatings produced at 500 A and 100 mm are shown in Figure 1.28. The second region of the distributions of MI data exhibits lower slope with respect to the first one, unlike NI tests, and in agreement with the data reported in literature [27,29].

This behavior can be addressed to the scale effect for which microcracks and globular pores embedded in the molten areas are responsible of data scattering, since higher volume of material was under analysis [29].

Therefore at higher indentation loads the data distribution is almost single-mode, as shown in Figure 1.28 (b). Similar behaviors was observed for the other five specimens produced with different values of current and torch-substrate distance.

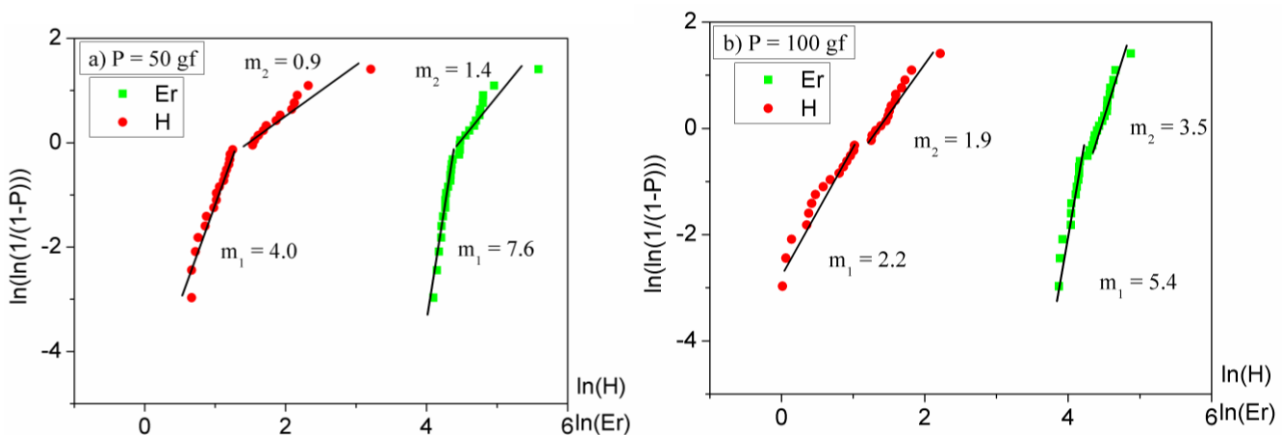


Figure 1.28: Weibull plot of H and Er for nanostructured YSZ coating produced at 500 A and 100 mm and tested by MI at (a) 50 gf and (b) 100 gf.

1.3.3 Tribological properties

Figure 1.29 shows result about wear rate of the second set of samples tested by the ball-on-disk test. By comparing the wear behavior of nanostructured coatings to that of a conventional one (characterized by the same initial roughness of about $8\ \mu\text{m}$ and tested with the same parameters listed in Section 1.2.4) it can be noted that just the sample with the lowest nanozones percentage (20%) has a higher wear resistance and that the wear rate increases with increasing the values of nanozones percentage (values in Table 1.3). For specimens with 31% and 36% of nanozones the coating was completely worn until the appearance of the superalloy substrate during the test.

Many researchers have reported superior wear performances for nanostructured ceramic coatings when compared to that of conventional coatings [11]. In this kind of coatings in fact the wear mechanism is a combination of brittle fracture and abrasive wear (promoted by delamination and detachment of small fragments or particles from the surface) and the presence of dense nanozones limits both of these phenomena. The brittle fracture is confined by the crack arrest effect whereas the abrasive wear is reduced by the wear scars of the nanostructured coating that are finer and smoother than those of the conventional coatings and form an adherent layer which limits wear [30].

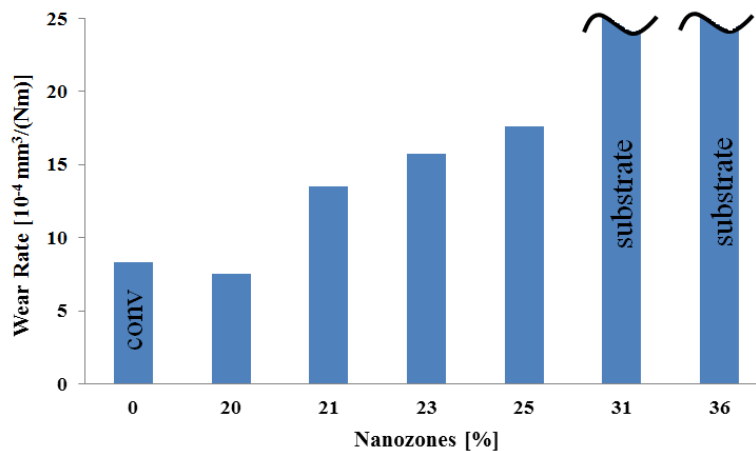


Figure 1.29: Wear rates of nanostructured YSZ coatings (produced with different process parameters and characterized by different percentages of nanozones (Table 1.3)) and conventional YSZ coatings.

These anti-wear performances refer to coatings with relatively low nanozones percentage (less than about 20%). When the amount of nanozones is higher (as observed for the samples analyzed in this work) the molten part of the semi-molten agglomerates can't fully infiltrate into the capillaries of their non-molten core during thermal spraying by causing the formation of porous and friable nanozones, typical of abradable coatings [11].

Therefore by varying process parameters the percentage of retained nanozones can be controlled in order to produce abradable coatings with different wear degrees or thermal barrier coatings with higher mechanical integrity.

Figure 1.30 shows the wear tracks of the three samples produced at torch-substrate distance of 100 mm and using different current values.

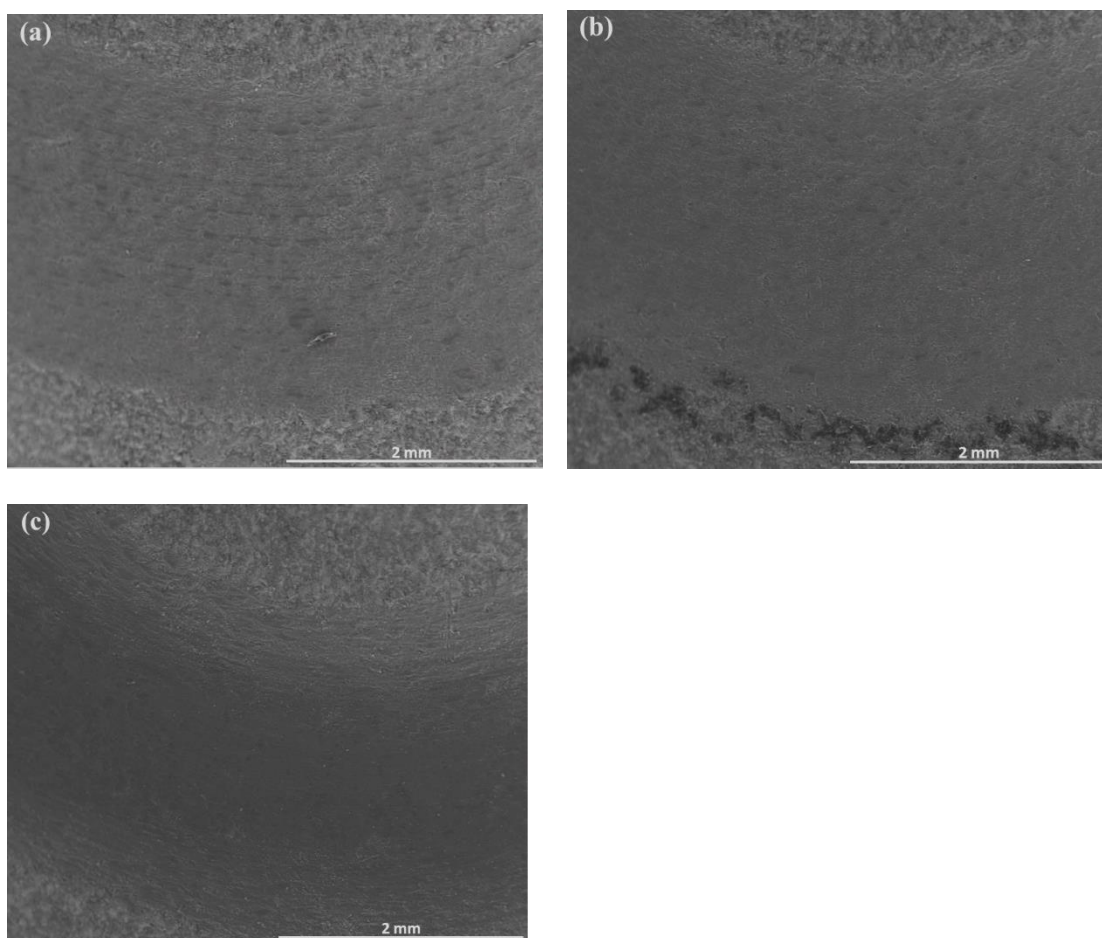


Figure 1.30: Wear tracks of samples produced with a distance of 100 mm and different current values: (a) 630 A (21% of nanozones); (b) 565 A (25% of nanozones); and (c) 500 A (31% of nanozones).

It can be observed that the track becomes more pronounced with decreasing the values of the current and increasing the percentage of retained nanozones. The dark zone in the middle of the track in Figure 1.30 c) represents the metallic substrate by confirming the results showed in Figure 1.27.

The morphology of the wear area is the same for all the nanostructured coatings produced and it is shown in Figure 1.31. In the magnification of Figure 1.31 (b) the white holes highlight the cracks caused in the molten zones during the wear test that indicate the occurrence of a brittle fracture. However, the observed cracks are very few and the dominant wear mechanism of the analyzed nanostructured coatings, characterized by a high percentage of friable nanozones, comes from abrasive wear. Indeed, the darker areas in the worn zone (observable in Figure 1.30 and Figure 1.31) may represent not only the molten zones, but also the compaction of the fine debris produced during the wear test.

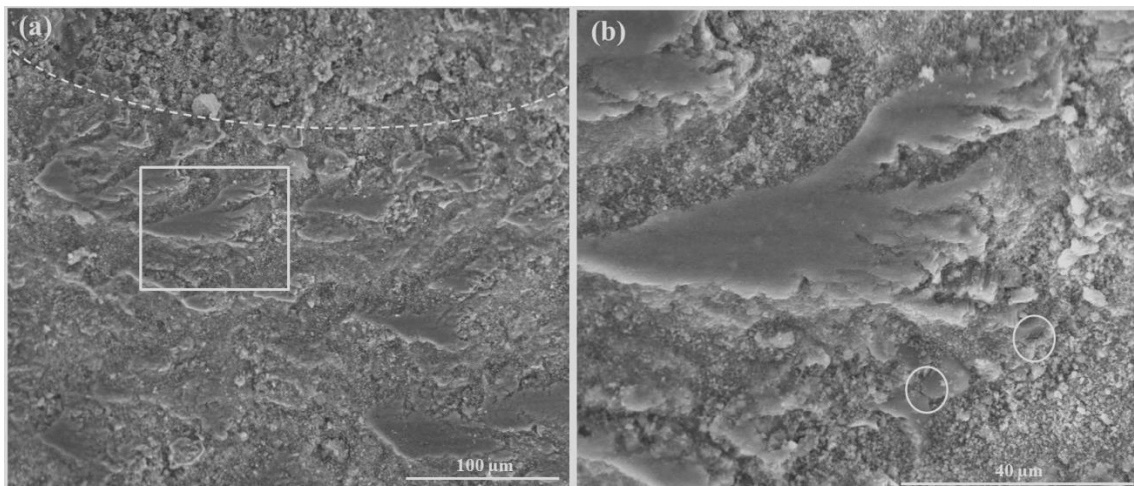


Figure 1.31: (a)Wear zone morphology of the nanostructured coatings: the dashed curve presents the inner edge of the wear track; (b) magnification of the area in the white box of (a).

1.4 Conclusions

In this Chapter the influence of some process parameters (plasma current and stand-off distance) on the microstructural, mechanical and tribological properties of plasma sprayed nanostructured YSZ

coatings was investigated. The partial melting of the nanostructured particle agglomerates produced the formation of a bimodal microstructure composed of well melted splats and semimolten areas. Columnar and equiaxed grains were observed in the melted splats, while the partially melted areas did not suffer grain growth and retained porosity at nanoscale. An increase of plasma current promoted the increase of the particle temperature, improving the melting degree and the density of the coatings.

The reduction of the retained nanostructured areas produced significant increases of Young's modulus, hardness and wear resistance. The effect of the torch-substrate distance was more significant at lower current values.

The Nano and Micro Indentation tests, performed at various loads, in conjunction with Weibull statistical approach, revealed that the bimodal microstructure involved a bimodal distribution of the mechanical properties, which tended to disappear with increasing the indentation load. The elastic modulus and the hardness decreased with increasing the indentation load, because of higher analyzed volume and stronger influence of the microstructural defects.

The ball-on-disk tests performed revealed that the nanostructured coatings produced with the APS process parameters set in this work were mostly abradable coatings, characterized by wear rate higher than that of the conventional coatings due to a high presence of nanozones.

The SEM images of the wear area showed that the morphology is the same for all the produced nanostructured coatings and that the dominant wear mechanism comes from abrasive wear rather than a brittle fracture.

The analysis of the influence of APS process parameters on coatings properties is really useful in order to engineer nanostructured YSZ coatings for different applications.

The development of a reliable procedure allowing a proper control of the percentage of the nanostructured areas embedded in coating microstructure is not easy to be achieved and will require a more detailed plan of experiments with the introduction of other process parameters and further

investigations. However, the results presented in this first chapter and published in [31], have been extremely useful for the understanding of nanostructured coatings properties and inspired several literature works [32-41].

1.5 References:

- [1] J. R. Davis, Handbook of Thermal Spray Technology, ASM International 2004, Materials Park, OH, USA, 2004, pp. 1-338.
- [2] R. Ruh, K. S. Mazdigasni, P. G. Valentine and H. O. Bielstein, Phase relations in the system ZrO_2 - Y_2O_3 at low Y_2O_3 contents, J. Am. Soc. 67(9) (1984) 190-192.
- [3] H. G. Scott, Phase relationship in the zirconia-yttria system, J. Mater. Sci. 10 (1975) 1527-1535.
- [4] A. Rabiei and A. G. Evans, Failure mechanism associated with the thermally grown oxide in plasma-sprayed thermal barrier coatings, Acta Mater. 48 (2000) 3963-3976.
- [5] A. G. Evans, M. Y. He and J. W. Hutchinson, Mechanics-based scaling laws for the durability of thermal barrier coatings, Prog. Mater. Sci. 46 (2001) 249-271.
- [6] A. G. Evans, D. R. Mumm and J. W. Hutchinson, Mechanism controlling the durability of thermal barrier coatings, Prog. Mater. Sci. 46 (2001) 505-553.
- [7] H. Liao, B. Normand and C. Coddet, Influence of coating microstructure on the abrasive wear resistance of WC/Co cermet coatings, Surf. Coat. Technol. 124 (2000) 235-242.
- [8] Y. Qiao, Y. R. Liu and T. E. Fischer, Sliding and abrasive wear resistance of thermal-sprayed WC-Co coatings, J. Therm. Spray Technol. 10(1) (2001) 118-125.
- [9] D. Zhu, N. P. Bansal and R. A. Miller, Thermal conductivity and stability of HfO_2 - Y_2O_3 and $La_2Zr_2O_7$ evaluated for 1650°C thermal/environmental barrier coating applications, NASA/TM-2003-212544. ARL-TR-3093.
- [10] K. N. Lee, Current Status of environmental barrier coatings for Si-based ceramics, Surf. Coat. Technol. 133-134 (2000) 1-7
- [11] R. S. Lima and B. R. Marple, Thermal spray coatings engineered from nanostructured ceramic agglomerated powders for structural, thermal barrier and biomedical applications: A review, J. Therm. Spray Technol. 16(1) (2007) 40-63.

- [12] R. Soltani, E. Garcia, T. W. Coyle, J. Mostaghimi, R. S. Lima, B. R. Marple and C. Moreau, Thermodynamical behavior of nanostructured plasma sprayed zirconia coatings, *J. Therm. Spray Technol.* 15(4) (2006) 657-662.
- [13] B. Liang and C. Ding, Thermal shock resistance of nanostructured and conventional zirconia coatings deposited by atmospheric plasma spraying, *Surf. Coat. Technol.* 197 (2005) 185-192.
- [14] W. Q. Wang, C. K. Sha, D. Q. Sun and X. Y. Gu. Microstructural feature, thermal shock resistance and isothermal oxidation resistance of nanostructured zirconia coating, *Mater. Sci. Eng. A* 424 (2006) 1-5.
- [15] R. S. Lima and B. R. Marple, Nanostructured YSZ Thermal barrier coatings engineered to counteract sintering effects, *Mater. Sci. Eng. A* 485 (2008) 182-193.
- [16] Y. C. Zhu, K. Yukimura, C. X. Ding and P. Y. Zhang, Tribological properties of nanostructured and conventional WC-Co coatings deposited by plasma spraying, *Thin Solid Films* 388 (2001) 277-282.
- [17] P. H. Shipway, D. G. McChartney and T. Sudprasert, Sliding wear behavior of conventional and nanostructured HVOF sprayed WC-Co coatings, *Wear* 259 (2005) 820-827.
- [18] G. Di Girolamo, Development and testing of plasma sprayed coatings for high-temperature applications, PhD Thesis, University of Calabria, IT, 2010.
- [19] "Introduction on INSTRUMENTED INDENTATION", CSM instrument Manual, CSM Instruments SA, Peseux, Switzerland.
- [20] A. C. Fischer-Cripps, *Nanoindentation*, 3rd edn. (Springer, New South Wales, Australia, 2011).
- [21] H. Hertz, "On the contact of elastic solids," *J. Reine Angew. Math.* 92, 1881, pp. 156–171. Translated and reprinted in English in Hertz's *Miscellaneous Papers*, Macmillan & Co., London, 1896, Ch. 5.
- [22] H. Hertz, "On hardness," *Verh. Ver. Beförderung Gewerbe Fleisses* 61, 1882, p. 410. Translated and reprinted in English in Hertz's *Miscellaneous Papers*, Macmillan & Co, London, 1896, Ch. 6.
- [23] W.C. Oliver, G.M. Pharr, An improved technique for determining hardness and elastic modulus using load and displacement sensing indentation experiments, *J. Mater. Res.* 7 (1992) 1564-1583.
- [24] W.C. Oliver, G.M. Pharr, Measurement of hardness and elastic modulus by instrumented indentation: Advances in understanding and refinements to methodology, *J. Mater. Res.* 19 (2004) 3-20.
- [25] W. Weibull, A statistical distribution function of wide applicability, *J. Appl. Mech.* 18 (1951) 293-297.

- [26] G. Di Girolamo, F. Marra, C. Blasi, E. Serra, T. Valente, Microstructure, mechanical properties and thermal shock resistance of plasma sprayed nanostructured zirconia coatings, *Ceram. Int.* 37 (2011) 2711-2717.
- [27] L. Wang, Y. Wang, X.G. Sun, J.Q. He, Z.Y. Pan, C.H. Wang, Microstructure and indentation mechanical properties of plasma sprayed nano-bimodal and conventional ZrO_2 -8wt% Y_2O_3 thermal barrier coatings, *Vacuum* 86 (2012) 1174-1185.
- [28] M. Saremi, A. Keyvanimahmoud, H. Sohi, Hot corrosion resistance and mechanical behavior of atmospheric plasma sprayed conventional and nanostructured zirconia coatings, *Int. J. Modern Phys. Conf. Series* 5 (2012) 720–727.
- [29] R.S. Lima, A. Kucuk, C.C. Berndt, Bimodal distribution of mechanical properties on plasma sprayed nanostructured partially stabilized zirconia, *Mater. Sci. Eng. A* 327 (2002) 224-232.
- [30] B. Liang, G. Zhang, H.L. Liao, C. Coddet, C.X. Ding, Structure and tribological performance of nanostructured ZrO_2 -3 mol% Y_2O_3 coatings deposited by air plasma spraying, *J. Therm. Spray Technol.* 19(6) (2010) 1163-1170.
- [31] Lamuta C, Di Girolamo G, Pagnotta L, Microstructural, mechanical and tribological properties of nanostructured YSZ coatings produced with different APS process parameters, *Ceramics International* 41(2015) 8904–8914.
- [32] Dan Chen, Fa Luo, Xufei Lou, Yuchang Qing, Wancheng Zhou, Dongmei Zhu, Comparison of thermal insulation capability between conventional and nanostructured plasma sprayed YSZ coating on Ni_3Al substrates, *Ceramic International*, Volume 43, Issue 5, 1 April 2017, Pages 4324–4329.
- [33] Lei Guo, Mingzhu Li, Sixian He, Chenglong Zhang, Qi Wang, Fuxing Ye, Preparation and hot corrosion behavior of plasma sprayed nanostructured $Gd_2Zr_2O_7$ - $LaPO_4$ thermal barrier coatings, *Journal of Alloys and Compounds*, Volume 698, 25 March 2017, Pages 13–19.
- [34] Fang Shao, Huayu Zhao, Chenguang Liu, Xinghua Zhong, Yin Zhuang, Jinxing Ni, Shunyan Tao, Dense yttria-stabilized zirconia coatings fabricated by plasma spray-physical vapor deposition, *Ceramics International*, Volume 43, Issue 2, 1 February 2017, Pages 2305–2313
- [35] H. R. Bakhsheshi, E. Hamzah, S. Bagheriyan, M. Daroonparvar, M. Kasiri-Asgarani, A. M. Shah, M. Medraj, Preparation and Performance of Plasma/Polymer Composite Coatings on Magnesium Alloy, *J. of Materi Eng and Perform* (2016) 25: 3948.
- [36] Wang, Y., Zhou, C., Microstructure and thermal properties of nanostructured gadolinia doped yttria-stabilized zirconia thermal barrier coatings produced by air plasma spraying, *Ceramics International*, Volume 42, Issue 11, 15 August 2016, Pages 13047–13052.
- [37] Yixiong Wang, Chungeng Zhou, Effect of Gd_2O_3 on the microstructure and thermal properties of nanostructured thermal barrier coatings fabricated by air plasma spraying, *Progress in Natural Science: Materials International*, Volume 26, Issue 4, August 2016, Pages 362–367.

- [38] H.R. Bakhsheshi-Rad, E. Hamzah, A.F. Ismail, M. Daroonparvar, M.A.M. Yajid, M. Medraj, Preparation and characterization of NiCrAlY/nano-YSZ/PCL composite coatings obtained by combination of atmospheric plasma spraying and dip coating on Mg–Ca alloy, *Journal of Alloys and Compounds*, Volume 658, 15 February 2016, Pages 440–452.
- [39] Daroonparvar, M., Yajid, M.A.M., Yusof, N.M., Bakhsheshi-Rad, H.R., Hamzah, E., Microstructural characterisation of air plasma sprayed nanostructure ceramic coatings on Mg–1%Ca alloys (bonded by NiCoCrAlYTaN alloy), *Ceramics International*, Volume 42, Issue 1, Part A, January 2016, Pages 357–371.
- [40] Bumgardner, C. & Li, X., Unveiling Ultra-High Temperature Wear and Indentation Damage Mechanisms of Thermal Barrier Coatings, *JOM* (2015) 67: 2921.
- [41] H.R. Bakhsheshi-Rad, E. Hamzah, A.F. Ismail, M. Daroonparvar, M. Kasiri-Asgarani, S. Jabbarzare, M. Medraj, Microstructural, mechanical properties and corrosion behavior of plasma sprayed NiCrAlY/nano-YSZ duplex coating on Mg–1.2Ca–3Zn alloy, *Ceramics International*, Volume 41, Issue 10, Part B, December 2015, Pages 15272–15277.

Chapter 2

Advanced geopolymers

This chapter deals with the production, the mechanical, and the electro-mechanical characterization of metakaolin-based geopolymer mortars. In the first part of the chapter, the properties and applications of geopolymers will be described. Geopolymers are ceramic materials developed in 1970s as a substitute of Ordinary Portland Cement and they have been considered ordinary materials to date. However, the discovery of excellent electro-mechanical properties, such as piezoresistivity and piezoelectricity, proposed for the first time in this dissertation, makes geopolymers advanced materials, suitable for a wide range of applications. In this chapter, all the experimental procedures related to the fabrication and characterization of geopolymers, as well as the results of the mechanical and electromechanical characterization, will be described. In particular, a new physical-chemical model of piezoelectricity will be proposed.

2.1 Geopolymers: structure and properties

The increasing emphasis on the environmental protection and energy conservation involved also the building materials in the last decades and lead researchers toward the development of alternative materials, able to reduce the gas emissions and minimize the energy required for their production. Ordinary Portland Cement (OPC) is currently the most widely used construction material and it fulfills a demand of over 1.5 billion tons annually. However, the OPC production requires high energy (very high temperatures, 1400-1500°C, are involved) and releases a large amount of carbon dioxide (CO₂) to the atmosphere that intensely contributes to greenhouse gas emissions. The production of one ton of OPC causes the releasement one ton of CO₂.

In 1978 Joseph Davidovits developed a green material called geopolymer [1], able to reduce the carbon dioxide emission by 80-90% compared to OPC [2]. Geopolymer is an inorganic ceramic material obtained by the alkaline activation of aluminosilicate precursors. Such material is characterized by a wide range of properties that are superior to OPC and it can be used to produce concrete with higher strength and durability.

Geopolymer is essentially composed by two components: the first one is the source material, which can be any material mainly composed of alumina and silicate; the second one is the alkali-activating solution, which can be composed of any alkali silicate, hydroxide, carbonate, sulfate and their mixtures. Sodium silicate (NaOH) or potassium silicate (KOH) solutions are the most used [3]. However, it is worth noting that geopolymers cannot be defined alkali-activated materials and a great confusion still remains on this definition. Geopolymer is based on the use of friendly alkali solution (usually sodium, or potassium silicates dissolved in water) and it can be produced at ambient temperatures. Alkali-activated materials instead, usually use strong activators and requires heat curing. Moreover, geopolymerization process produces a stable durable product whereas alkali activation usually produces unstable products. In this latter case in fact, the alkali remains free and out of the structure, and can be leached out with a certain easiness.

2.1.1 Geopolymerization process

The geopolymerization process can be divided into three different steps. The first step is the dissolution. During this stage the alkali solution dissolves the aluminosilicate precursors and the aluminum and silicon species are released in the mixture. These dissolved species hydrolyze and deprotonated in order to produce the $[Al(OH)_4]^-$ and $[Si(OH)_4]^-$ monomers, respectively. This process generates rapid and intense heat which is directly proportional to the pH level of the alkali solution. The second step is the condensation and during this process the aluminate and the silicate monomers produce oligomers and generate a larger network by adjoining together and co-sharing

the oxygen atoms. During condensation, the water consumed during the hydrolysis processes is driven out of the microstructure. In the last stage, the mixture becomes oversaturated with the aluminosilicate gel, which is Al-bonds rich at the beginning. The connectivity of the network increases and the geopolymer gel starts to harden when more silicates are dissolved by fostering the rearrangement of the structure [4, 5]. Figure 2.1 schematically shows the geopolymerization process described above, proposed by Duxson.

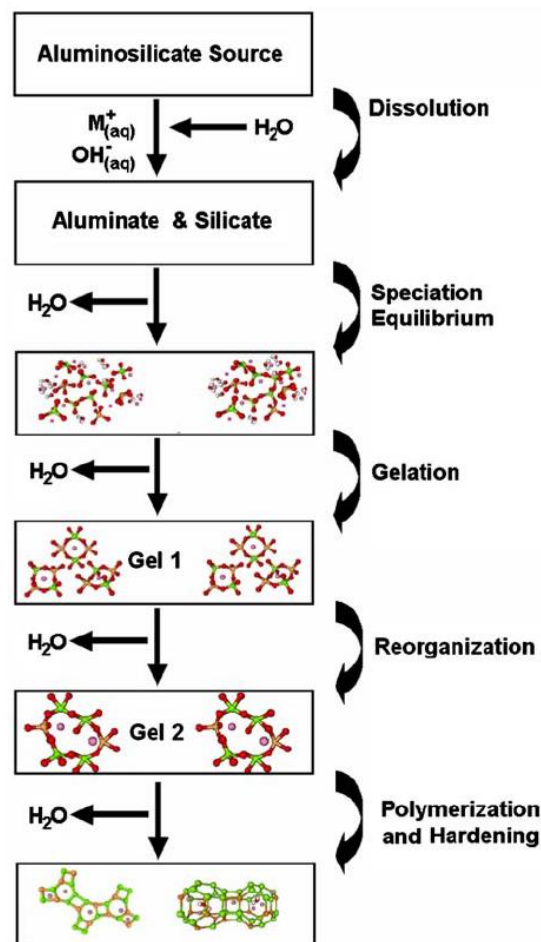


Figure 2.1: Geopolymerization model proposed by Duxson [4].

2.1.2 Aluminosilicate precursors

The primary requirement for the aluminosilicate precursors of geopolymers is that they must be materials rich in silicon or aluminum.

Fly ash are silicon rich materials and they are widely used for the production of geopolymers. Such material is usually obtained from the burning of anthracite and bituminous coal and contains acidic oxides such as Al_2O_3 , SiO_2 and Fe_2O_3 which foster alkali reactions [6]. Fly ash produced from the combustion of coal are characterized by an inhomogeneous mix of aluminosilicate and silica glasses, with a low content of crystalline materials such as mullite, quartz, hematite and magnetite [7]. The high degree of inhomogeneity makes the design and the fabrication of a dense final product more difficult [8]. The key parameters that must be taken into account for the production of fly ash base geopolymers are: the fly ash particles size distribution and finess, the percentage of unburned material, the liquid/solid ratio, and the content of its vitreous phase. Fernandez-Jimenez derived a fly ash-based geopolymer with optimum binding properties [9].

Ground granulated blast furnace slag is another aluminosilicate precursor rich in silicon. It is an industrial by-product derived from the rapid water cooling of molten steel. Such material is characterized by excellent thermal properties, high resistance to chemical attack and low production costs.

Among the aluminosilicate materials rich in aluminum, the calcined **metakaolin** is surely the most widely used. Metakaolin is a dehydroxylated pozzolanic product obtained from the high temperature firing of raw kaolin. Kaolin, or kaolinite [$\text{Al}_2\text{Si}_2\text{O}_5(\text{OH})_4$], widely used in the manufacture of porcelain, is a clay mineral with an high content of layered tetrahedral silicon atoms, connected to octrahedral aluminum atoms via oxygen. When the raw kaolin is heated at a temperature above 550°C the atomic structure, characterized by hydroxyl ions that are strongly bonded to the aluminosilicate framework, rearranges to form a partly ordered system with a high reactivity to alkaline solutions [10]. The metakaolin is then obtained. It was found that the optimum process to convert kaolin into metakaolin consists in heating at a temperature of 600°C for two hours [11]. After such procedure, metakaolin is highly reactive. Chareerat et al. [11] showed that high compressive strength values (in the range of 30–50 MPa) can be obtained by replacing

traditional fly ash material with metakaolin by up to 30 percent (by mass). Unlike fly ash, metakaolin doesn't contain contaminants which affect the final product and it allows to obtain a geopolymer with a more homogeneous microstructure and a higher level of predictability of the curing process [8].

Concerning the geopolymerization process, Provis has proposed a detailed model for metakaolin and fly ash based geopolymers [5]. Such model is shown in Figure 2.2. Compared to Duxson's model, this model includes more details concerning the silicate oligomers, which can be incorporated into the alkali solution. Such oligomers have been divided into amorphous and nanocrystalline phases, according to the Si/Al ratio. Provis introduced also a different reaction pathway for the direct formation of the aluminosilicate gel in addition to the zeolite phase.

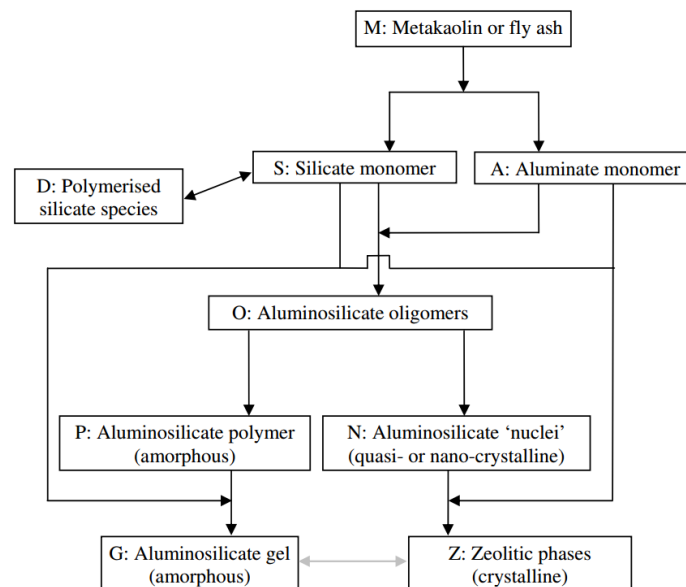


Figure 2.2: Geopolymerization model proposed by Provis [5].

2.1.3 Alkaline activators

The alkaline activator role is fundamental for the realization of the geopolymerization process. The activators foster the precipitation and crystallization of the siliceous and aluminous species

contained within the solution. In particular, whereas OH^- acts as a catalyst for reactivity, the metal cation (usually K^+ or Na^+) forms a structural element and balances the negative framework produced by the presence of tetrahedral aluminum [8]. The alkaline solution drives the initial stage of the geopolymerization by dissolving the aluminosilicate precursor and releasing reactive silicon and aluminum into solution.

The most used alkaline activators for geopolymers are a mixture of sodium or potassium hydroxides (**NaOH, KOH**) and sodium silicate (**Na₂SiO₃**).

Since K^+ is more basic than Na^+ , potassium hydroxides possesses a greater potential for polymeric ionization in solution, resulting in high reactivity of the aluminosilicate precursor, a denser final product, with a higher compressive strength [12]. On the other hand, sodium cations are smaller than potassium cations and can easily migrate throughout the material network, promoting better zeolitization [8]. Furthermore, it was observed that geopolymers activated with NaOH develop greater crystallinity and are characterized by a greater stability in aggressive environments [13].

Sodium silicate it is commonly mixed with NaOH or KOH as a fortifying agent. It in fact enhances alkalinity and increases the material strength [14]. It is produced by fusing sand (SiO_2) with sodium or carbonate (Na_2CO_3) at temperatures in excess of 1100 °C. The product is dissolved into a semi-viscous liquid with a high pressure steam [15]. Researchers found that geopolymers produced with a high content of sodium silicate show higher compressive strength compared to geopolymers produced with a low content of silicate or with the base activator (NaOH, KOH) only.

2.1.4 Geopolymers chemical structure and microstructure

The chemical structure of geopolymers can be described as a phase of aluminosilicate gel, composed by aluminate and silicate 3D-tetrahedral units which are covalently bonded and share oxygen atoms. The alkali cations (usually K^+ or Na^+) balances the negative charge of the aluminate groups [16]. Davidovits proposed the following structural formula [17] to describe geopolymers:



where M represents any alkali cations (K^+ , Na^+ , ...), z (usually equal to 1, 2, or 3) is a lattice index, w is the number of water molecules, and n the degree of polycondensation. Three different types of monomeric -Si-O-Al- structure can define geopolymers, according to the different Si/Al ratio [18]. The poly-sialate unit, where Si/Al=1 [-Si-O-Al-O] is the basic monomer unit. When the Si/Al=2 it is called poly(sialate-siloxo) and contains two Si atoms [-Si-O-Al-O-Si-O-], while when the Si/Al ratio is equal to 3 it contains three Si atoms [-Si-O-Al-O-Si-O- Si-O-].

The drawing of a 3D schematic diagram of the geopolymers structure is very challenging, due to the disordered nature of such material. Davidovits proposed the model shown in Figure 2.3 (a). It is based on metakaolin as a source material using the poly(sialate-siloxo) monomers as a base unit. Since the Davidovits' s model does not take into account the presence of water, Barbosa et al. [19] proposed a new model, shown in Figure 2.3 (b).

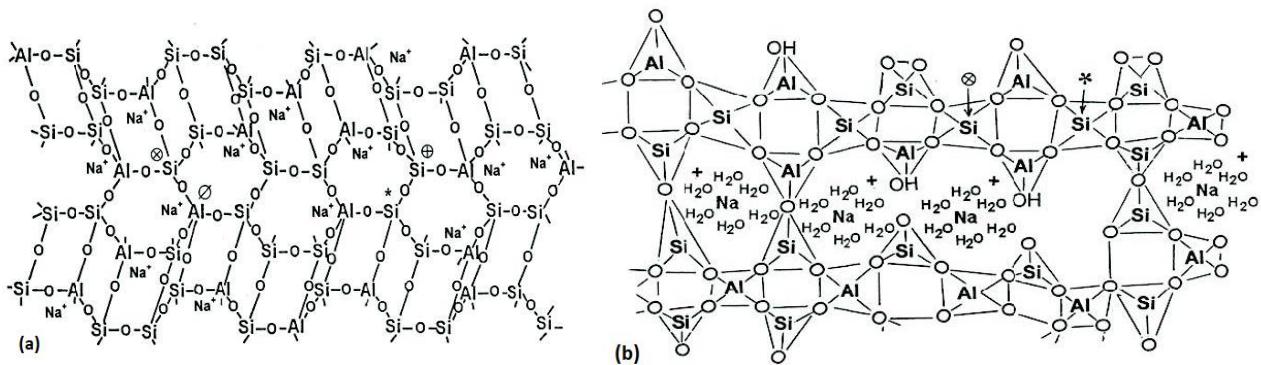


Figure 2.3: (a) Davidovits's model [17], (b) Barbosa et al.'s, model [19] proposed for the geopolymer structure.

Concerning geopolymer microstructure, it is mainly composed of three phases: the aluminosilicates gel phase (considered the main phase of geopolymers), the unreacted or partially reacted particles phase, and the pore water phase [17, 5]. Figures 2.4 (a-d, f) shows the SEM micrograph for fly ash based geopolymer, whereas Figure 2.4 (e) refer to metakaolin based geopolymer. Points 4 and 5 of

Figure 2.4 (a) indicate the aluminosicate gel, which represents the main composition of the material microstructure. It is worth noting that a big amount of unreacted or incompletely reacted round fly ash particles (points 2 and 3, respectively) is present. Point 6 of Figure 2.4 (b) and points 7 and 8 of Figure 2.4 (d) indicates crystalline phases which could be new crystals generated at the last stage of the geopolymerization process or crystal initially present in the source material (such as quartz and hematite). In Figure 2.4 (c) one can observe that some fly ash particles are incompletely covered by the reaction products and this is due to an incomplete or weaker geopolymerization process. The microstructure of fly ash based geopolymers is then highly heterogeneous and the prediction of the degree of geopolymerization is quite difficult for such materials.

The metakaolin based geopolymer microstructure (Figure 2.4 (e)) is instead more homogeneous and it presents a less amount of unreacted or partially unreacted phases if compared to the fly ash based geopolymer microstructure (Figure 2.4 (f)).

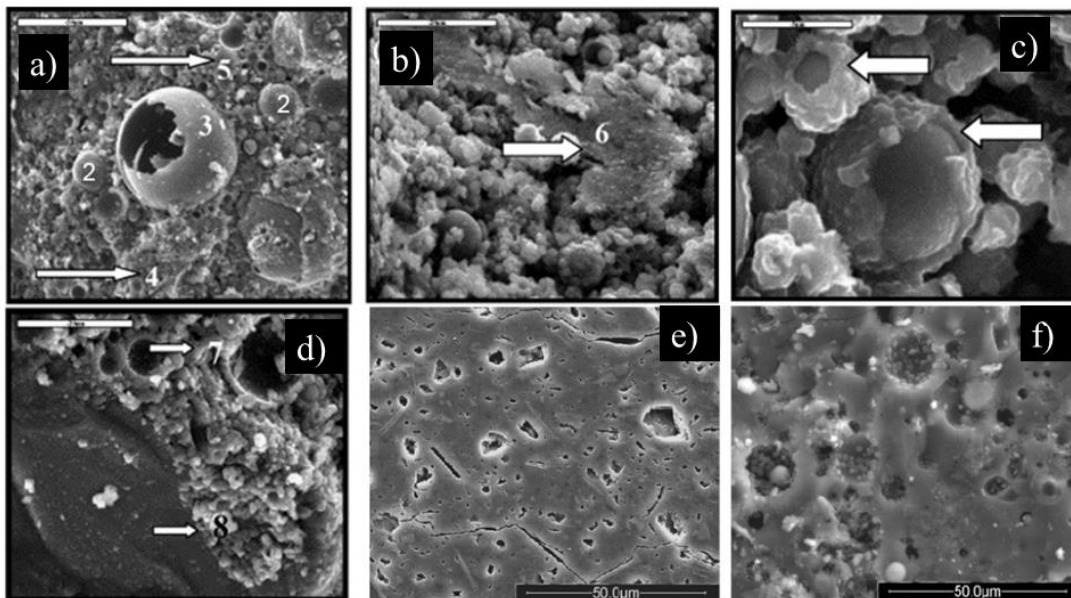


Figure 2.4: SEM micrographs of (a-d) fly ash and (e, f) metakaolin-based geopolymers [5].

The higher reaction degree of metakaolin is related to the morphology of the source material. Whereas the fly ash particles are spherical and the dissolution reaction products deposit on the outer

surface, the metakaolin particles are in form of layered sheets (alumina and silica sheets) and dissolution products peels off the surface layers. In this latter case additional layers of metakaolin are exposed to the reactions and a greater amount of material reacts.

2.1.5 Important parameters

Geopolymers with different properties, suitable for different applications, can be produced by acting on several parameters.

One of the most influent parameters whose variation can significantly change the chemical and mechanical properties of geopolymers is the Si/Al ratio. In Table 2.1 different applications are listed according to the different Si/Al ratios.

Table 2.1: Applications of geopolymer materials according to the different Si/Al ratios [4]

Si:Al Ratio	Applications
1	<ul style="list-style-type: none"> ● Bricks ● Ceramics ● Fire Protection
2	<ul style="list-style-type: none"> ● Low CO₂ Cements and Concretes ● Radioactive and Toxic Waste Encapsulation
3	<ul style="list-style-type: none"> ● Fire Protection Fiberglass Composites ● Foundry Equipment ● Heat Resistant Composites, 200°C to 1000°C ● Tooling for Aeronautics Titanium Process
>3	<ul style="list-style-type: none"> ● Sealants for Industry, 200°C to 600°C ● Tooling for Aeronautics SPF Aluminum
20-35	<ul style="list-style-type: none"> ● Fire Resistant and Heat Resistant Fiber Composites

The alkaline activator concentration is also a critical factor to be considered. It is generally assumed that a higher concentration produces a higher mechanical strength. However there is an optimum limit for each activator type, and to cross such limit can cause detrimental effects. A significant decrease of the compressive strength was observed when a 10M KOH concentration rises to 15 M

[12]. With an excessive KOH concentration in fact, the mixture exceeds its saturation point and there is a high content of unreacted K^+ ions which cause a decrease of the material strength.

Mechanical strength is also influenced by the aluminosilicate precursor/activator ratio. Figure 2.5 shows the combined effect of the Liquid /Fly Ash ratio (L/FA) and activator solution concentration on compressive strength of a fly ash based geopolymer. Significantly high values were obtained by using an L/FA ratio of 0.4 and a 5M activator concentration [20].

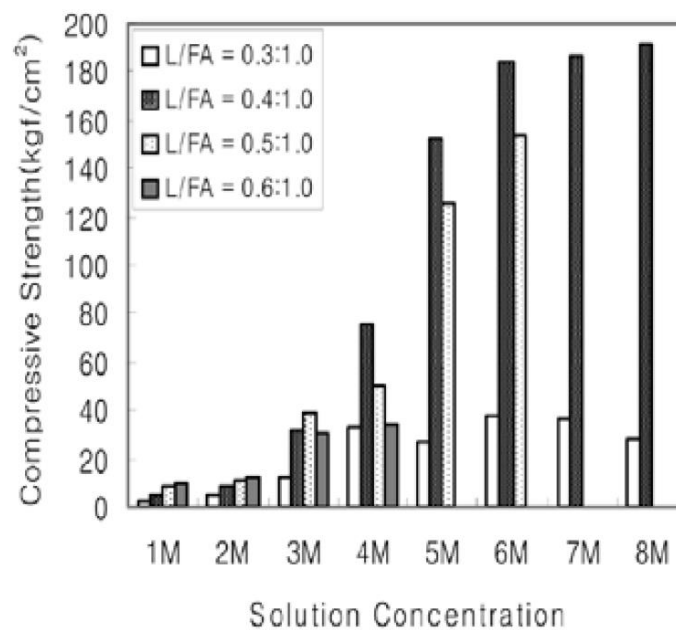


Figure 2.5: Effect of Liquid /Fly Ash ratio (L/FA) and activator solution concentration on compressive strength [20].

As described above, the addition of sodium silicate to the hydroxide activator increases the mechanical performances of geopolymers. However, the sodium silicate/hydroxide ratio must be also controlled. Laboratory experience suggests that good results can be obtained by setting such ratio (by mass) to an approximate value of 2.5 [21].

Since geopolymers are characterized by a capillary porosity, a great amount of water is lost during the curing process and such dehydration causes a material shrinkage with the consequent generation of cracks. Fillers such as quartz sand are usually added to the geopolymer paste as a dimensional

stabilizer in order to avoid cracks generation or arrest their propagation [22]. Geopolymer mortars (defined as geopolymers pastes with the addition of sand fillers) are characterized by higher mechanical properties if compared to pastes and they are more suitable for structural applications. The presence of sand fillers is then another important parameter to be considered in the geopolymers production, according to the different application field.

2.1.6 Metakaolin-based geopolymers

Geopolymers, similar to Portland cement, can be considered quite conventional ceramic materials with prevalent application in the production of structural components. However, their unique structure, characterized by hydrated and mobile cations, as shown in Figure 2.3, can pave the way to interesting electro-mechanical properties, by significantly enlarging the application fields of such materials. This initial intuition was the main motivation to carry out the work presented in this chapter, since the presence of unexplored properties such as piezoelectricity can transform geopolymers from traditional to advanced materials. In particular, metakaolin-based geopolymers were chosen for such investigation because they are characterized by high homogeneity [5], contrary to most of geopolymer materials, such as fly ash-based ones, in which the presence of impurities and unreacted particles is very high, as shown in Figure 2.4. A non-homogeneous microstructure could in fact make difficult the understanding of the physical-chemical model which drives the electro-mechanical activity observed into a material. Furthermore, since the piezoelectric performances of geopolymers are related to the ionic mobility, as explained in the following sections, NaOH was chosen as alkaline activator because, as described in section 2.1.3, sodium cations are smaller than potassium cations and can easily migrate throughout the material network. Lots of studies were focused on the production and characterization of metakaolin-based geopolymers. Chemical and production aspects such as the hydration process [23-27], the $\text{SiO}_2/\text{Al}_2\text{O}_3$ ratio [28-35], solid/liquid ratio [36-43], or the effect of curing conditions [44-46], were

deeply studied. The mechanical properties of such materials were also investigated, with particular attention to the resistance to aggressive solutions [47, 48] or the resistance at elevated temperature and fire [49-61]. Several fiber reinforced metakaolin-based geopolymers composites were also proposed [62-67], as well as different blends with fly ash [68-73], slag [74-84], calcium hydroxide [85-87] and other materials [88-102]. However, no studies were focused on the electro-mechanical properties of metakaolin-based geopolymers. In the following sections the electro-mechanical characterization of the produced metakaolin-based geopolymers mortar samples will be then proposed for the first time. The sample production and the mechanical characterization at different length scales will be also described.

2.2 Experimental procedures

2.2.1 Samples production

2.2.1.1 Materials

Metakaolin having a D10 of 0.51 μm , a D50 of 1.59 μm and a D90 of 9.74 μm , based on a volume distribution, was provided by Doldes Massara S.r.l. Sodium silicate solution was provided by Condea Augusta S.P.A. The weight composition of metakaolin, as determined by X-ray fluorescence, and sodium silicate solution are listed in Table 2.2.

Table 2.2: weight composition of metakaolin and sodium silicate solution

Component	Metakaolin (%wt)	Sodium Silicate solution (%wt)
Al ₂ O ₃	42.0	–
SiO ₂	53.2	29.5
K ₂ O	0.3	–
Na ₂ O	0.1	13.8
Fe ₂ O ₃	1.5	–
TiO ₂	1.9	–
LOI*	1.0	–
H ₂ O	–	56.7

*Loss of Ignition at 955°C;

Quartz sand passing 500 μm was used as filler. Deionized water was used throughout the experiments to avoid the effects of unknown contaminants in water. Na(OH) 99.9% pure was purchased by Sigma-Aldrich.

2.2.1.2 Geopolymer synthesis and curing

Geopolymers were synthesized by activating metakaolin with the alkaline silicate solution [17]. In order to guarantee good mass transfer and dissolution rate, the maximum extent of metakaolin reaction and aluminium incorporation in geopolymer matrix, the following molar ratios $\text{SiO}_2/\text{Na}_2\text{O}=1.62$ and $\text{H}_2\text{O}/\text{Na}_2\text{O}=12.25$ have been used to prepare the alkaline silicate solution. Firstly, the sodium hydroxide solution was obtained by dissolution of NaOH pellets in ultrapure water, with container kept sealed wherever possible to minimize contamination by atmospheric carbonation and prevent water evaporation. The solution was stirred until the NaOH pellets had dissolved and the solution became clear. Once cooled down it was poured into sodium silicate solution. The so obtained alkali activator solution was covered, sealed, stirred and allowed to cool back down to room temperature. Finally, the activator solution was added to metakaolin powder and the slurry was mechanically vigorously mixed for 10 minutes. The last step involved sand addition and mechanically mixing for 5 min. The slurries were, afterwards, rapidly casted (as shown in Figure 2.6) into open and dismountable molds, properly designed and produced (see Figure 2.7).



Figure 2.6: casting of geopolymeric mortar into open and dismountable molds.

In particular, cubic samples of dimension 20 mm and 40 mm (see Figure 2.8) were produced for the piezoelectric and piezoresistive characterization respectively, disks of 55 mm diameter and thickness/diameter ratio of 0.16 for the Brazilian tests, and a brick shape samples of dimensions 135 x 12 x 9 mm³ for the bending tests.

All samples were placed on the vibration table to remove entrained air. In order to prevent the moisture loss, the moulds were sealed from the atmosphere and cured for 24 h at 50°C. The sealed specimens were then stored at ambient temperature and pressure for four weeks to complete curing.

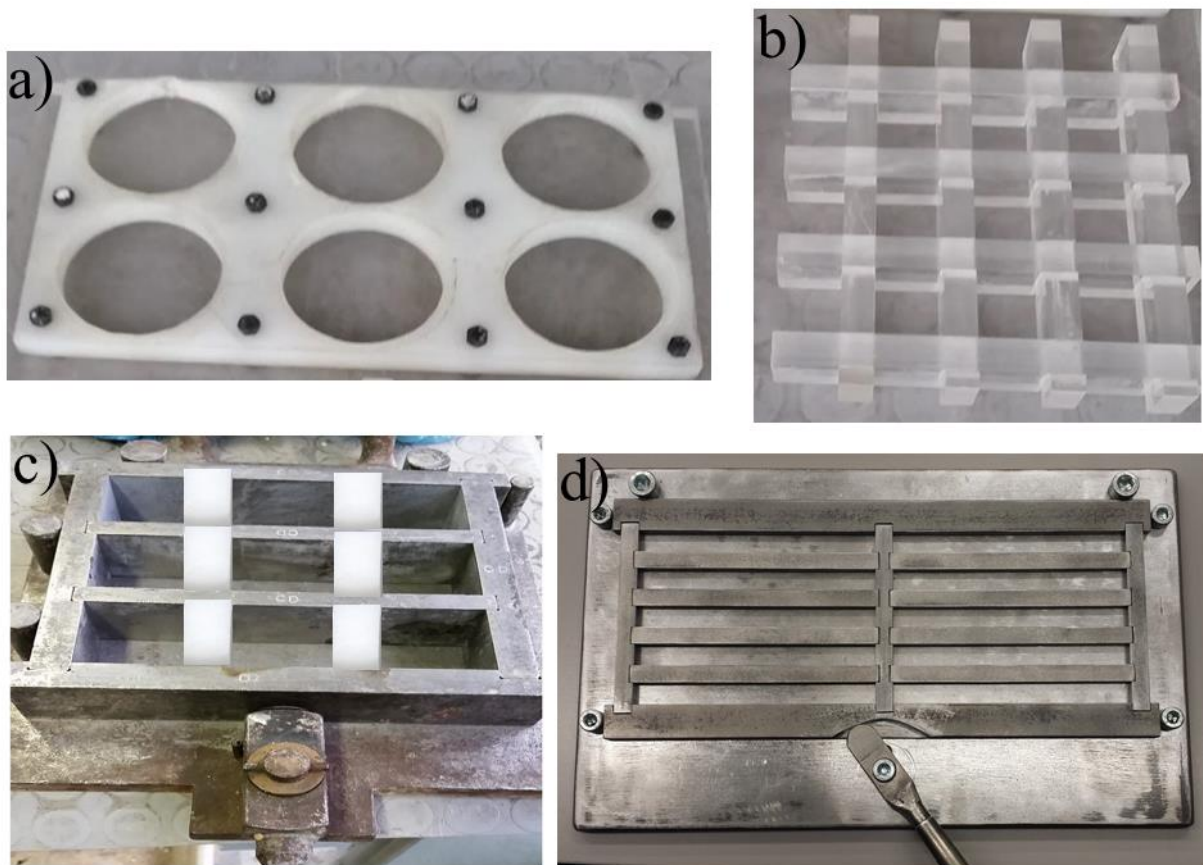


Figure 2.7: Open and dismountable molds for geopolymeric samples casting: a) teflon mold for the production of disks of 55 mm diameter and 8.8 mm thickness, screwed on a flat plexiglass sheet; b) plexiglass mold for cubic samples of dimension 20 mm placed on a flat plexiglass sheet; c) steel molds of dimensions 16mm x 4 mm x 4mm with teflon inserts in order to obtain cubic samples of dimension 40 mm; d) steel molds for brick shape samples of dimensions 135 x 12 x 9 mm³.



Figure 2.8: cubic samples of dimension a) 40 mm and b) 20 mm produced for the piezoresistive and piezoelectric characterization respectively.

The final theoretical composition of geopolymers, in terms of oxides, is equal to $\text{Na}_2\text{O}-3.86\text{SiO}_2-\text{Al}_2\text{O}_3-5.22\text{H}_2\text{O}$. Al/Na molar ratio was fixed equal to one because sodium balances the negative framework charge carried by tetrahedral aluminium, thus acting as structure forming agent. $\text{SiO}_2/\text{Al}_2\text{O}_3$ molar ratio was fixed to 3.86 in order to minimize geopolymer porosity thus increasing mechanical performance [103]. The Water/Binder (W/B) weight ratio was fixed at 0.56 to obtain a good mortar workability. Sand/Binder (S/B)=1.5 has been used to prevent microcracks due to shrinkage [22].

2.2.2 Chemical characterization

Phase identification of prepared geopolymeric pastes was carried out recording X-Ray diffractograms, using $\text{CuK}\alpha$ radiation in $2\theta = 5^\circ - 50^\circ$ range (Philips PW 1730/10 generator equipped with a PW 1050/70 vertical goniometer, $\lambda = 1.5404 \text{ \AA}$), with step of 0.02° and a scan rate of $1^\circ/\text{min}$.

Nuclear magnetic resonance spectroscopy (NMR) was also performed to study the chemical environment of the produced samples. During NMR analysis, the sample is subject to an external magnetic field that changes the resonance frequency of atoms. By recording such changes, it is possible to obtain information about the electronic structure of a molecule and its individual functional groups. In particular, ^{29}Si MAS-NMR, ^{27}Al MAS-NMR and ^{23}Na MAS-NMR analysis were performed on a Bruker 600 spectrometer. For ^{29}Si (119.2 MHz), at $3 \mu\text{s}$ ($\theta = \pi/4$) pulse was used with a repetition time of 30 s, for ^{27}Al (156.37 MHz), at $2 \mu\text{s}$ ($\theta = \pi/4$) pulse was used with a

repetition time of 1 s, for ^{23}Na (158.74 MHz), at 4 μs ($\theta = \pi/4$) pulse was used with a repetition time of 1 s.

The porosity of the produced material was studied by means of thermogravimetric and N_2 adsorption/desorption analysis. With thermogravimetric analysis the mass loss was measured as a function of increasing temperature. In particular, a Netzsch STA 409 analyzer was used and the samples were heated at a rate of $10^\circ\text{C}/\text{min}$ in air from 20°C to 820°C . The mass loss was measured to confirm the presence of water into the material pores and its evaporation at high temperatures. The study of the physical absorption of gas molecules on a solid surface is useful for the measurement of the specific surface area of materials and consequently, for the analysis of the porosity morphology. Probing gas that do not chemically react with material surfaces must be used and nitrogen is one of the most commonly employed. In such dissertation, N_2 adsorption/desorption plots of powdered geopolymer paste were carried out in micromeritics ASAP 2020 instruments. Before the analysis, all samples were pretreated in vacuum condition at 200°C for 12 h. The specific surface area was calculated using the Brunauer–Emmet–Teller method. Mesopore diameter distributions was determined with the Barret–Joyner–Halenda (BJH) method using the desorption data.

2.2.3 Mechanical characterization

2.2.3.1 Macroscale characterization by Digital Image Correlation and Brazilian

Disk Test

For the macroscale mechanical characterization of the produced geopolymeric mortar an optimized and reliable approach was developed combining Brazilian Disk Test (BDT) and Digital Image Correlation (DIC). The Brazilian test was introduced in 1943 [104, 105] as a promising technique to evaluate the tensile strength of brittle materials like concrete or rocks. The experiment consists in compressing a thin circular disk along its vertical diameter in order to induce tensile failure at the

center of the disk. The standardized procedure, together with the suggested dimensions of the samples, to well calculate the tensile strength of brittle materials was proposed by the ASTM C496 Standard [106]. However, it is important to underline that the identification of the correct size of the sample, as well as the shape of the loading platens and the type of failure during a Brazilian test is still an open issue. In fact, several studies were devoted to evaluate the failure mechanisms [107-111] and it was demonstrated that they are highly dependent upon the loading method used. In particular, it was shown that for small angles of load contacting area failure occurs far away from the center of the disk, as a consequence of the high local stress induced by the contact loading platens [107].

The ASTM adopts the use of flat platens with recommended thickness/diameter (t/D) ratios ranging between 0.2 and 0.75 [106] but it was widely criticized because failure occurs at the loading points rather than at the center of the disk, which is critical in ensuring the validity of the test [109, 112]. In contrast, the ISRM recommends the application of load through a curved platen of radius 1.5 times that of the sample whose t/D ratio should be 0.5 [113], whereas a modified flattened Brazilian disk that ensures failure from the center of the disk was proposed in [112].

Brazilian test was also proposed as a valid alternative for measuring the elastic mechanical properties of brittle materials [114, 115]. In particular, the inverse method [114] and an over-deterministic approach [115], was implemented to fit the experimentally displacements, calculated by means of the Moiré interferometry, to the theoretical solution for the simultaneous determination of two elastic constants, Young's modulus, E , and Poisson's ration, ν . However it is worth noting that the application of interferometric optical techniques for in-plane displacement and deformation measurements requires special equipment, longtime preparation and stringent stability requirements.

Therefore, most recently, DIC technique was used in supporting the mechanical characterization of brittle materials during Brazilian test. In fact, compared with the most common interferometric

optical methods, the DIC offers special and attractive advantages like simple experimental setup and specimen preparation, low requirements in measurement environment and wide range of measurement sensitivity and resolution. Therefore it results more suitable for experiments in conventional testing laboratories.

The implementation of the DIC method is based on simple steps: (i) specimen and experimental preparations; (ii) recording images of the specimen surface under investigation before and after loading and, finally, (iii) processing the acquired images using a computer program to obtain the desired displacement and strain information.

However, only few studies [116, 117] were devoted in evaluating the elastic constants of materials by using the DIC technique during a Brazilian test.

In this context, a novel, optimized and reliable approach to obtain the elastic tensile properties of brittle materials by combining BDT and DIC technique is proposed.

The digital image correlation (DIC) technique was used to obtain the full displacement field on a geopolymeric disk surface and a numerical procedure, based on an over-deterministic method and the least square regression, was used for determining the elastic constants from the measured displacement field. In order to perform automatic and accurate evaluation, not only the elastic properties but center of the disk location and rigid body motions are also determined simultaneously in the present study. Three different loading platens were adopted in all the experiments in order to evaluate their effect on the elastic properties calculation, on the failure mechanisms and strength of the investigated material. Results were also compare with data obtained from a 4 points bending test. All the guidelines to well perform this kind of characterization are reported and discussed and suggestions, in terms of loading platens to use and specimen dimensions, are proposed.

A. Methodology description

A.1 Displacement Fields of a Brazilian Disk

The horizontal (u_x) and vertical (u_y) displacement field experienced by a generic point Q located on the surface of a disk loaded in plane stress condition (see Figure 2.9), can be expressed as follow [118]:

$$u_x = \frac{1}{E}A_x + \frac{\nu}{E}B_x \quad (2.2)$$

$$u_y = \frac{1}{E}A_y + \frac{\nu}{E}B_y \quad (2.3)$$

Where E is the Young's modulus and ν is Poisson's ratio. A_x , A_y , B_x and B_y are load P , dimensions (thickness t and diameter D), and location (x and y coordinate) dependent parameters and they can be expressed as follow:

$$A_x = -\frac{P}{\pi t} \left[(\theta_1 + \theta_2) - \frac{1}{2} \sin(2\theta_1) - \frac{1}{2} \sin(2\theta_2) - \frac{2x}{D} \right] \quad (2.4)$$

$$A_y = -\frac{P}{\pi t} \left[2 \ln \left(\frac{r_2}{r_1} \right) + \frac{1}{2} \cos(2\theta_1) - \frac{1}{2} \cos(2\theta_2) - \frac{2y}{D} \right] \quad (2.5)$$

$$B_x = \frac{P}{\pi t} \left[(\theta_1 + \theta_2) + \frac{1}{2} \sin(2\theta_1) + \frac{1}{2} \sin(2\theta_2) - \frac{2x}{D} \right] \quad (2.6)$$

$$B_y = -\frac{P}{\pi t} \left[\frac{1}{2} \cos(2\theta_1) - \frac{1}{2} \cos(2\theta_2) + \frac{2y}{D} \right] \quad (2.7)$$

Where

$$\theta_1 = \tan^{-1} \left(\frac{x}{D/2 - y} \right) \quad (2.8)$$

$$\theta_2 = \tan^{-1} \left(\frac{x}{D/2 + y} \right) \quad (2.9)$$

$$r_1 = \sqrt{x^2 + (D/2 - y)^2} \quad (2.10)$$

$$r_2 = \sqrt{x^2 + (D/2 + y)^2} \quad (2.11)$$

Figure 2.9 schematically shows the diametral compression of a disk and all the parameters used in the previous equations.

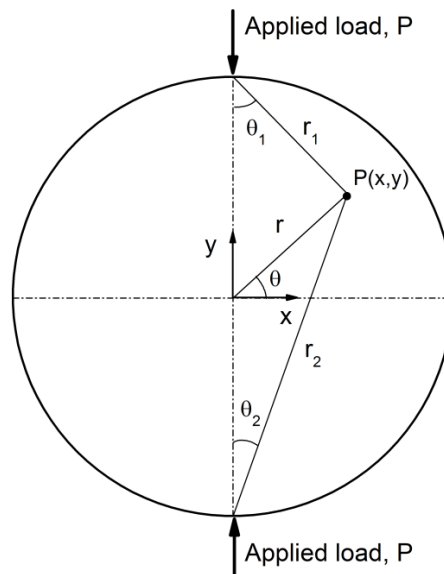


Figure 2.9: Schematic depiction of a Brazilian disk subjected to a compression load P .

A.2 Over-deterministic Inverse Approach for the elastic properties evaluation

Equations (2.2-2.3) show that $1/E$ ratio and ν are linearly coupled, therefore, they can be simultaneously obtained using either the u_x or the u_y displacement field or combining both of them.

In particular, if both the u_x and u_y displacement of a generic single point is known, equation (2.2)

and equation (2.3) can be easily solved to calculate Young's modulus and the Poisson's ratio parameter. Instead, if the only u_x displacement or the u_y displacement is known you need two points to evaluate both the elastic constants. If the latter is the case, these points must be selected in such a way that the obtained equations are linearly independent avoiding ill-conditioning that could significantly affect the final result.

To limit such mathematical problem a better way is to use an over-deterministic method which basically makes use of a large number of data points to calculate a small set of unknown coefficients from a large system of equations. Therefore, measuring the whole displacement field of the disk, many equations as much as the investigated points can be written and an overdetermined system of equations can be obtained. In this way ill-conditioning and unavoidable measurement errors are significantly reduced.

For the over-deterministic approach it is desired to use all the point of the disk, because more data can reduce random noise and provide more accurate results. However, it is worth noting that the theoretical solution is based on a point load, whereas experiments were performed using different load platens that generate a distributed pressure near the contact region. In the last years several studies were carried out in order to provide analytical solutions dependent on the load configuration [119, 120] and it was demonstrated that the displacement field, compared with the solution described in the equations (2.2-2.3), does not significantly change if a region, far away from the contact point, is considered. If the latter is the case, there is no need to use more complex equations [119, 120] to describe the displacement experienced by the disk during the experiment.

In order to verify this aspect, finite element simulations were carried out applying different load distributions [120], and results revealed that the proposed regression method, based on equations (2.2-2.3) is not affected by the load configuration.

Furthermore, it has to point out that the theoretical displacements near the loading area can be different from the experimental data because of the plastic deformations induced by high localized stresses.

For all of these reasons, the region located in the central part of the disk (light grey in Figure 2.12) was used for least-squares calculation.

A.3 Stress solution of an isotropic Brazilian disk for the tensile strength calculation

The stress solution for an isotropic 2D disk subjected to concentrated loads, Figure 2.9, is [121]

$$\sigma_x = \frac{2P}{\pi t} \left(\frac{\cos \theta_1 \sin^2 \theta_1}{r_1} + \frac{\cos \theta_2 \sin^2 \theta_2}{r_2} \right) - \frac{2P}{\pi D t} \quad (2.12)$$

$$\sigma_y = \frac{2P}{\pi t} \left(\frac{\cos^3 \theta_1}{r_1} + \frac{\cos^3 \theta_2}{r_2} \right) - \frac{2P}{\pi D t} \quad (2.13)$$

$$\tau_{xy} = \frac{2P}{\pi t} \left(\frac{\cos^2 \theta_1 \sin \theta_1}{r_1} + \frac{\cos^2 \theta_2 \sin \theta_2}{r_2} \right) \quad (2.14)$$

Considering the parameters reported in Figure 2.9, the following relationship can be written:

$$r_2^2 = r_1^2 + D^2 - 2r_1 D \cos \theta_1 \quad (2.15)$$

$$\cos \theta_2 = \frac{D^2 + r_2^2 - r_1^2}{2r_2 D} = \frac{D - r_1 \cos \theta_1}{r_2} \quad (2.16)$$

$$\sin \theta_2 \sqrt{1 - \cos^2 \theta_2} = \frac{r_1 \sin \theta_1}{r_2} \quad (2.17)$$

$$x = r_1 \sin \theta_1 \quad (2.18)$$

$$y = \frac{D}{2} - r_1 \cos \theta_1 \quad (2.19)$$

Manipulating and substituting equations (2.15-2.19) in equations (2.12-2.14) we get

$$\sigma_x = \frac{2P}{\pi t} \left[\frac{(R-y)x^2}{((R-y)^2+x^2)^2} + \frac{(R+y)x^2}{((R+y)^2+x^2)^2} - \frac{1}{D} \right] \quad (2.20)$$

$$\sigma_y = \frac{2P}{\pi t} \left[\frac{(R-y)^3}{((R-y)^2+x^2)^2} + \frac{(R+y)^3}{((R+y)^2+x^2)^2} - \frac{1}{D} \right] \quad (2.21)$$

$$\tau_{xy} = \frac{2P}{\pi t} \left[\frac{(R-y)^2x}{((R-y)^2+x^2)^2} + \frac{(R+y)^2x}{((R+y)^2+x^2)^2} - \frac{1}{D} \right] \quad (2.22)$$

The formula suggested by ASTM and ISMR standards for the calculation of the tensile strength, σ_T , can be obtained from equation (2.20) evaluated at the center of the disk ($x=0, y=0$), i.e. where σ_x stress reaches its maximum tensile value.

$$\sigma_T = -\frac{2P}{\pi Dt} \quad (2.23)$$

It is important to underline that in rock disk the tensile strength leads to the failure because its absolute value is much lower than the one recorded in compression.

B. Error sources analysis

Technical aspects have to be taken into account when the proposed method is implemented in order to reduce the effect of unavoidable source of errors: (1) meet plane stress conditions, (2) elimination of rigid body motions, (3) identification of the correct disk center location.

B.1 Meet plane stress conditions

The analytical solution of the displacement field reported in section A.1, is referred to plane stress condition. In order to evaluate the error committed in calculating the elastic properties by means of the over-deterministic inverse method, when plane stress condition is missed, finite element simulations were carried out. In particular, 3D analysis on a disk with linear elastic properties ($E=15$ GPa, $\nu=0.19$), diameter $D=55$ mm and different thickness/diameter ratio (t/D) were performed. Height-nodes brick elements were used and special care was done in order to guarantee a regular mesh on the central area of the disk, see Figure 2.10 a), where the proposed method is applied.

Figure 2.10 b) and 2.10 c) report the typical horizontal, u_x , and vertical displacement, u_y , respectively. In particular, results are referred to a disk with 1 mm of thickness subjected to 1000 N of compression load.

A least squares regression was performed on the FEM displacements measured at the surface of the disk. Equations (2.2-2.3) were used to fit the numerical data obtained from the simulations and the unknown elastic constant parameters, E and ν , were calculated. Results were compared with the elastic properties used in the simulation ($E=15$ GPa, $\nu=0.19$).

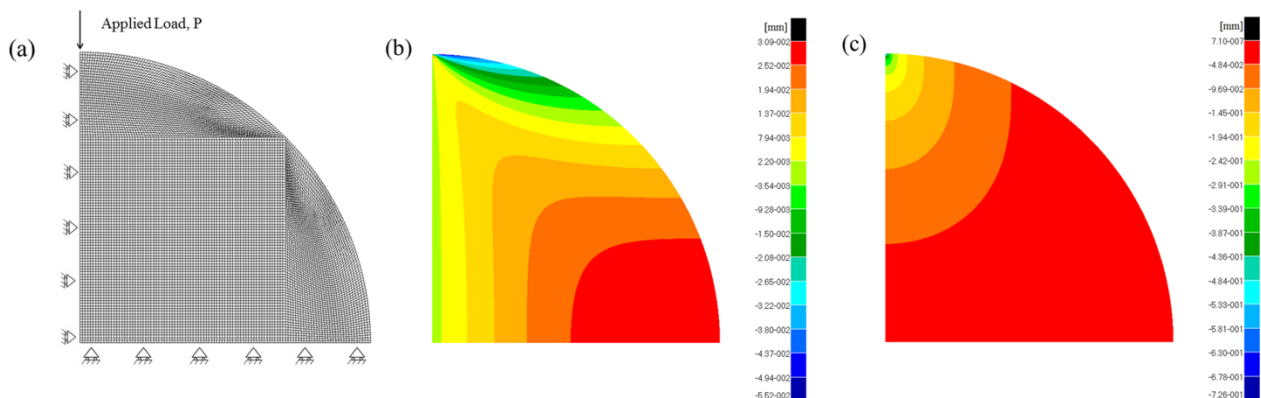


Figure 2.10: a) FEM model; b) horizontal displacement, u_x ; c) vertical displacement, u_y .

In particular, Figures 2.11 report the estimation errors for the Young's modulus, Figure 2.11 a), and for the Poisson's ratio (Figure 2.11 b) obtained for different thickness/diameter (t/D) ratios and for different displacement field adopted in the regression procedure, i.e. the only horizontal one, u_x , the only vertical one, u_y , and both u_x and u_y .

Results revealed that increasing the t/D ratio, i.e. approaching the plane strain condition, the errors increase. Furthermore, results showed that if the only u_y is used in the least square regression big errors occur in the Poisson's ratio estimation, whereas very good agreement is obtained if the only u_x [115] or both the displacement fields are used.

Based on these preliminary results, with the aim to reduce the errors when the over-deterministic method is applied, both the displacements were used. Furthermore, $t/D=0.16$ was chosen for the specimens preparation in order to get low estimation errors and to meet plane stress condition.

In addition, Equation (2.23), used for the tensile strength evaluation, is referred to plane stress conditions.

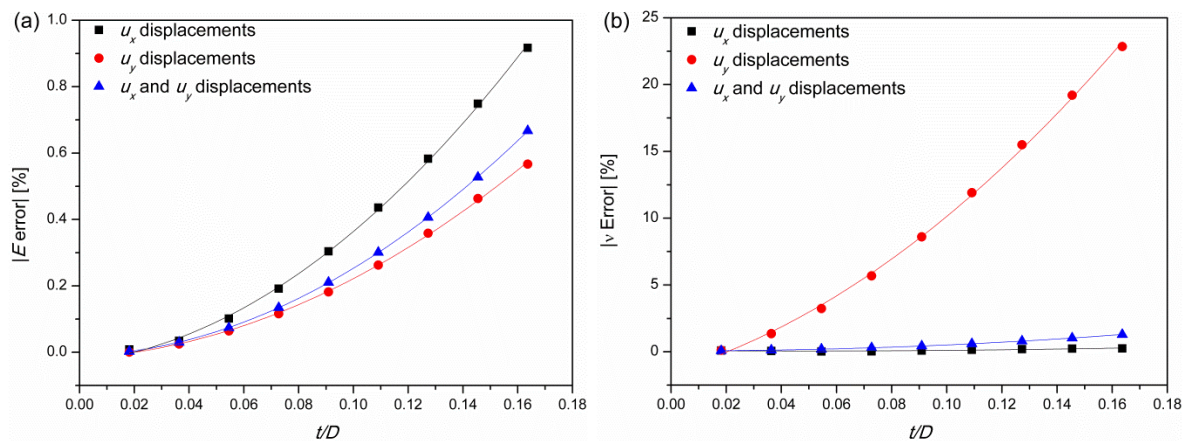


Figure 2.11: absolute error for different t/D ratios: a) Young's modulus, b) Poisson's ratio.

Yu et al [122] studied the relation between the rock specimen geometry and tensile strength and they proposed a correction of Equation (2.23) which considers higher values of t/D ratios, i.e. when the plane stress condition is not satisfied:

$$\sigma_T = \left(0.2621 \frac{t}{D} + 1\right) \frac{2P}{\pi Dt} \quad (2.24)$$

In order to calculate the correct value of the tensile strength for the chosen t/D ratio, Equation (2.24) was adopted in this work.

B.2 Elimination of rigid body motions

During the experiment the disk can be subjected to unavoidable rigid body motions that can significantly affect the elastic constant calculation. Therefore, it is of great interest to estimate their values and delete their influence on the final solution. To this aim, new terms have to be introduced in equations (2.2-2.3):

$$u_x = \frac{1}{E}A_x + \frac{\nu}{E}B_x - Ar \sin(\theta) + B_{ux} \quad (2.25)$$

$$u_y = \frac{1}{E}A_y + \frac{\nu}{E}B_y + Ar \cos(\theta) + B_{uy} \quad (2.26)$$

where B_{ux} and B_{vy} represent the horizontal and vertical rigid translation, respectively, A is the rigid body rotation, $r = \sqrt{x^2 + y^2}$ and $\theta = \tan^{-1}(y/x)$, see Figure 2.9.

It is important to underline that the introduction of the latter parameters does not represent an issue for the implementation of the over-deterministic method due to the high number of information provided by the correlation technique.

B.3 Identification of the disk center location

The correct position of the disk center has to be correctly identified in order to get a good fitting between the experimental and analytical data and to well estimate the elastic constants of the

material. In fact, the experimental displacements, provided by a commercial correlation software, are typically related to a reference system that is different from the disk center, see Figure 2.12. Therefore, it is mandatory identify such point and make a coordinate change.

To this aim, a proper numerical procedure, able to identify the correct location of the disk center, was implemented. It is based on the following steps: (1) calculation of the experimental displacements inside the investigation area (light grey in Figure 2.12); (2) identification of an area where the disk center is located with high probability (dark grey in Figure 2.12); (3) identification of the new reference system (x', y') after a trial location of the center (x_0, y_0) is fixed; (4) calculation of the elastic constants E and ν by regressing the experimental displacements.

It is important to underline that the calculated elastic parameters will be affected by an error if the selected point (x_0, y_0) does not match with the correct disk center and it can be expressed as follows:

$$e = \sum \left(\begin{bmatrix} u_{x \text{ experimental}}(x - x_0, y - y_0) \\ u_{y \text{ experimental}}(x - x_0, y - y_0) \end{bmatrix} - \begin{bmatrix} u_{x \text{ analytical}}(x - x_0, y - y_0) \\ u_{y \text{ analytical}}(x - x_0, y - y_0) \end{bmatrix} \right)^2 \quad (2.27)$$

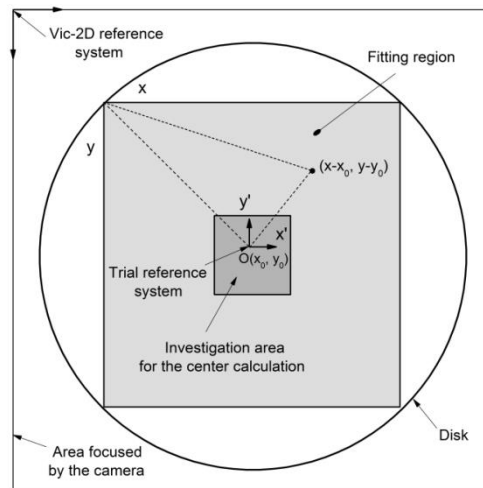


Figure 2.12: Reference system and coordinate change.

Where the summation is extended to all the points of the investigation area (dark grey in Figure 2.12), u_x experimental e u_y experimental are the experimentally measured displacements, u_x

analytical u_y analytical are the analytical displacements obtained for the regressed elastic constants. Finally the correct disk center location (x_0, y_0) is identified when the error function (equation (2.27)) reaches its minimum value. The latter procedure was numerically validated exploiting the displacement fields obtained from finite element simulations, see Figure 2.10 b) and 2.10 c). In particular, Figure 2.13 a) and 2.13 b) show that if the correct disk center location is missed, the numerical displacement contours plot (blue lines) does not match with the analytical one (red line), affecting the elastic constants calculation.

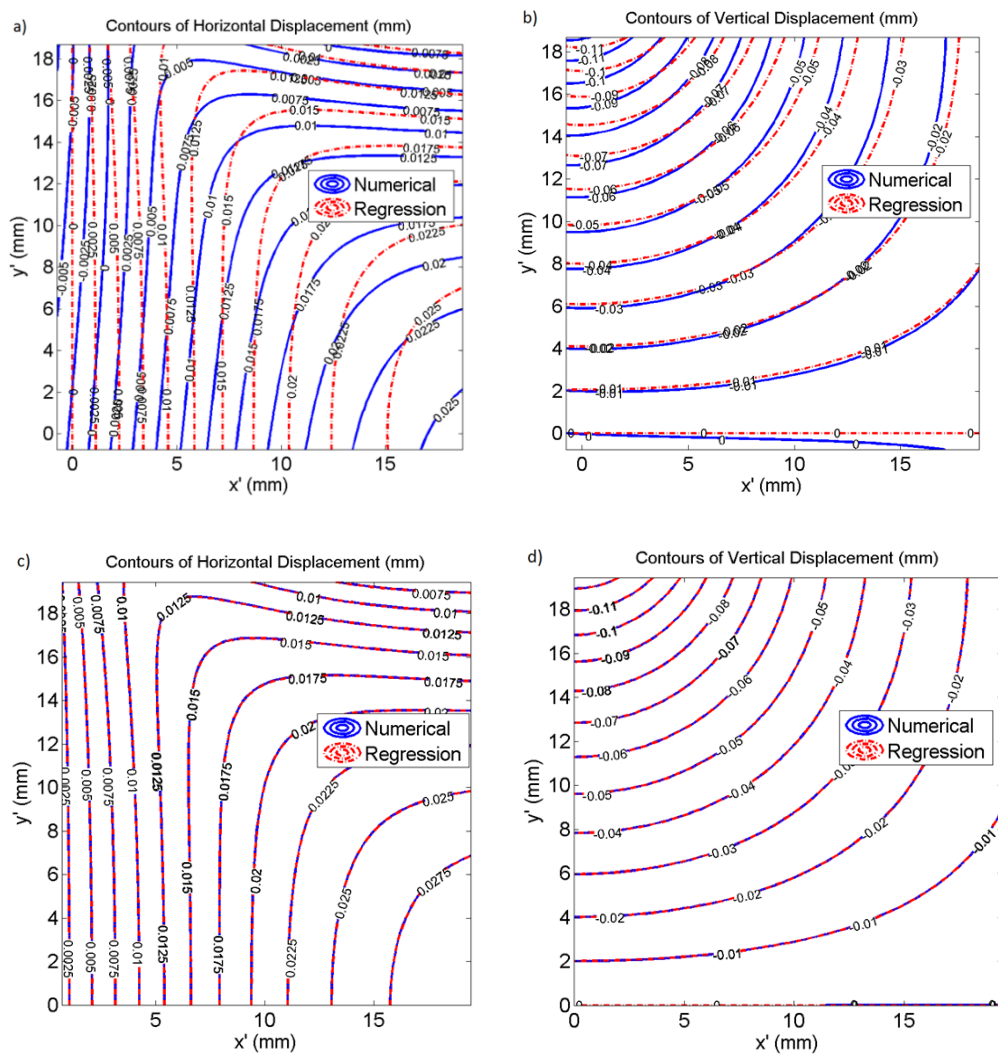


Figure 2.13: Effect of the disk center location: a) horizontal displacement u_x for a trial point (x_0, y_0) ; b) vertical displacement u_y for a trial point (x_0, y_0) ; c) horizontal displacement u_x when the correct center is located; d) vertical displacement u_y when the correct center is located.

Only when the correct disk center location is well identified, i.e. when the error function reaches its minimum value, displacements show good agreement and the regressed elastic constants are equal to the one used in the FEM model ($E=15$ GPa, $\nu=0.19$).

C. Experimental tests

C.1 Brazilian disk experiments and DIC measurements

Brazilian test experiments were performed using an electro-mechanical testing machine (MTS Criterion s42, USA) equipped with a 5 kN load cell. All the experiments were carried out in displacement control with a speed of 0.05 mm/min and three different loading platens were adopted, see Figure 2.14. A typical mechanical load-displacement response of a disk is reported in Figure 2.15.

Six samples for each load condition were investigated and all of them were painted with white and black paint (as shown in Figure 2.16) in order to get a proper pattern with a random grey scale distribution.

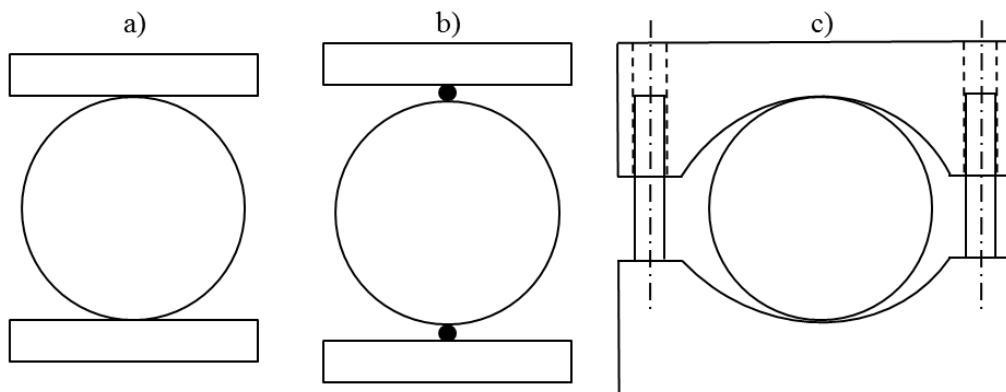


Figure 2.14: loading platens adopted during the experimental investigations.

A digital camera (Sony ICX 625- Prosilica GT 2450 model) with a resolution of 2448 by 2050 pixels of $3.45 \mu\text{m}$ was used to capture images throughout measurement tests. The focus of the images was performed using a Linos Photonics objective and a Rodagon lens f. 80 mm, which ensures, in conditions of correct illumination, a scale of approximately 50 pixels/mm.

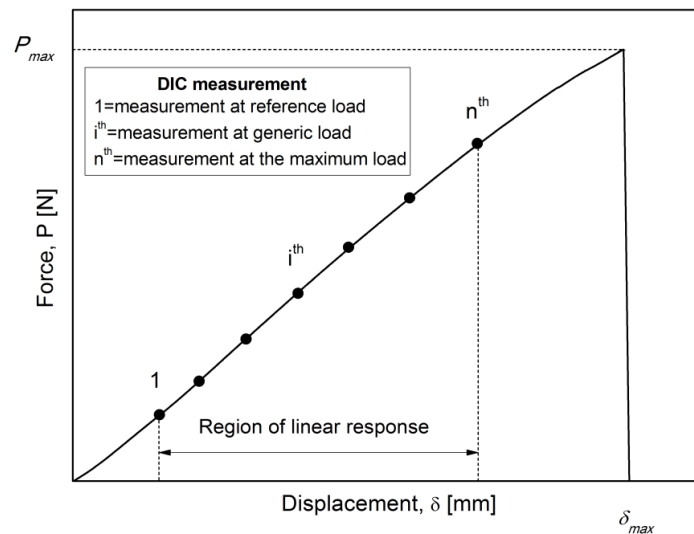


Figure 2.15: Typical force-displacement response of a Brazilian test.

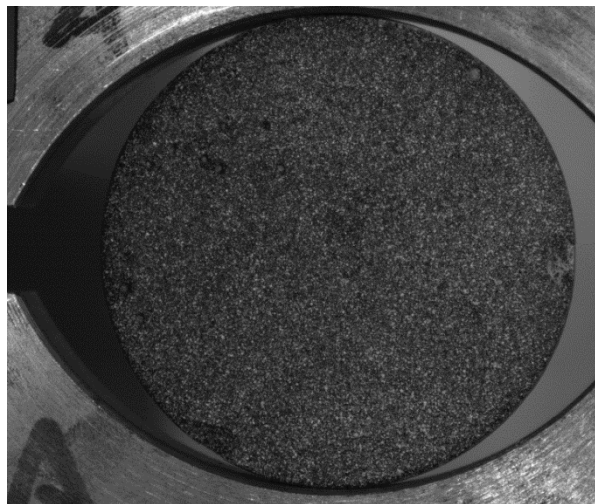


Figure 2.16: Speckle pattern on the sample's surface.

Digital image correlation was performed on images captured from each test using a commercially available image correlation software (Vic-2D). All the correlation measurements were performed in the region with linear response, see Figure 2.15; to this aim, the first image in the measurement test (point 1 in Figure 2.15) was used as the reference image, and terms up to first order displacement gradients were used in all correlations. Digital image correlation was used to obtain full-field displacements for each image throughout the test (n-points in Figure 2.15).

The whole experimental setup, see Figure 2.17, including the testing machine, was placed on an anti-seismic platform to avoid measurements errors due to unavoidable vibrations.

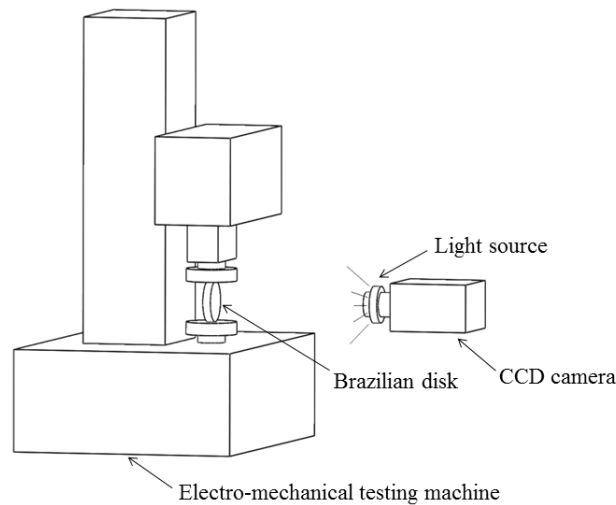


Figure 2.17: schematic depiction of the experimental setup.

C.2 Bending Test

Four points bending tests were performed according to the ASTM C 1161-02c [123] standard and using an electro-mechanical testing machine (MTS Criterion s42, USA), equipped with a 5kN load cell.

Six brick shaped samples with dimensions of 135 x 12 x 9 mm were used to perform these tests. Such dimensions are recommended by the ASTM C 1161 Standard for advanced ceramic materials. HBM K-XY3 strain gauges were glued at the center of the lower surface of the samples (i.e. where the maximum tensile stress is localized) and the HBM QuantumX MX1615B Strain Gauge Bridge Amplifier together with the Catman software was employed to record longitudinal and transverse strains during the test. The crosshead speed was set to 1 mm/min and the Poisson ratio ν was calculated by editing the measured strains according to the transverse sensitivity of the strain gauges and the Poisson ratio of the material adopted for their calibration [124]. The experimental setup is shown in Figure 2.18.



Figure 2.18: experimental setup for the four points bending tests. The red wires connect the XY strain gauge to the Strain Gauge Bridge Amplifier in order to record the strain signal.

2.2.3.2 Micro and nano scale characterization by indentation tests

Micro and nano indentation tests were performed on the produced geopolymers samples with the equipment described in Section 1.2.3.

Since the sample surface need to be perfectly flat when it is tested by depth-sensing indentation with a nanometric resolution, a proper grinding and polishing procedure has to be carried out. Samples shown in Figure 2.8 b) were firstly cold mounted by using a bi-component epoxy resin. A cold mounting procedure is the most suitable one for geopolymers. During the hot mounting procedure in fact a temperature of 180°C is usually reached and it can dehydrate such material and cause cracks formation which alter the mechanical properties evaluation process. After the bi-component resin polymerized, the sample was grinded and polished by using a Struers automatic, microprocessor controlled machine (Tegramin-25), shown in Figure 2.19. A dry grinding and polishing procedure was adopted since geopolymers properties are strongly influenced by the water

content present into the material. The mounted and polished geopolymer sample is shown in the inset of Figure 2.19.



Figure 2.19: Equipment used for the grinding and polishing of geopolymer samples. The inset shows the cold mounted and polished sample.

For micro indentations a pyramidal Vickers tip, a maximum load of 100 mN, a loading and unloading rate of 200 mN/min, and a holding time of 5 s were used, whereas for nanoindentation tests were employed a Berkovich tip, a maximum load of 15 mN, a loading and unloading rate of 30 mN/min, and a holding time of 5.

For both micro and nano indentation tests a set of 40 indentations were performed, the values of reduced Young's modulus E_r and hardness H were obtained by load–depth curves, according to Oliver and Pharr theory [125, 126] and then the experimental data were analyzed by assuming a two-parameters Weibull statistical distribution [127], as described in Chapter 1 for nanostructured ceramic coatings. Indentations were placed at a proper distance in order to avoid the mutual influence of close indentations and data were filtered in order to exclude the influence of impurities or macropores on the mechanical properties evaluation.

It is worth noting that different tips and indentation loads were selected in order to provide the characterization of the produced geopolymer mortar at different length scales and propose a comparison of the obtained results. In particular, the mechanical characterization at the nanoscale was carried out by performing indentations with the Berkovich tip and a maximum load of 15 mN, which involve the testing of a small volume of material. A larger amount of material is instead tested by using a Vickers tip and a higher load (100 mN), and a microscale characterization can be performed with such parameters. The results obtained at the nano and micro scale were compared with those obtained at the macroscale by means of DIC and Brazilian Disk tests.

2.2.4 Piezoresistive Characterization

The piezoresistive effect is defined as the variation of the electrical resistance into a homogeneous body when it is subjected to mechanical stress. According to experiments performed by Mildred on bismuth [128], a linear relationship is assumed in the most general case between the output resistance variation and the mechanical input. Contrary to the piezoelectric effect, the piezoresistive effect produces a change only in the electrical resistance and not in the electrical potential.

In particular, the coefficient that defines the piezoresistive performances of materials is called gauge factor and it is defines as follow:

$$G_f = \frac{\frac{\Delta R}{R_0}}{\varepsilon} \quad (2.28)$$

where R_0 is the initial electrical resistance, ΔR is the change in the electrical resistance and ε is the applied strain.

The piezoresistive effect was discovered by Lord Kelvin in 1856 and it represents the work principle at the basis of strain gauges, able to measure the strain of materials due to the resistance change, measured using a Wheastone bridge. Moreover, interesting and high-tech applications are related to piezoresistivity. In particular, focusing on structural materials such as cement-based

materials (herein we focus on the piezoresistive characterization of cement materials due to their similarity with geopolymers), the piezoresistive effect paves the way for several strain sensing applications such as damage monitoring, traffic monitoring, building evacuation monitoring, border monitoring.

The gauge factor can be obtained using Equation 2.28 by imposing a mechanical deformation on the sample and by measuring the output resistance variation. There are several experimental methods to measure the electrical resistance of a material. A big classification can be made between four-probes and two-probes methods. The two different configurations are illustrated in Figure 2.20. While in the four-probes method the outer electrodes are used to apply the input current and the inner electrodes are used to measure the output voltage (used to calculate the resistance of the material, according to the Ohm's law), in the two-probes methods the same electrodes are used to apply the current and to measure the voltage. As shown in Figure 2.20, whereas for the four-probes method the measured voltage is only that one related to the resistance of the tested material (R_M), the output voltage measured by the two-probes method is the sum between the voltage related to the resistance of the material R_M , the resistance of the electrodes R_E , and the contact resistance R_C .

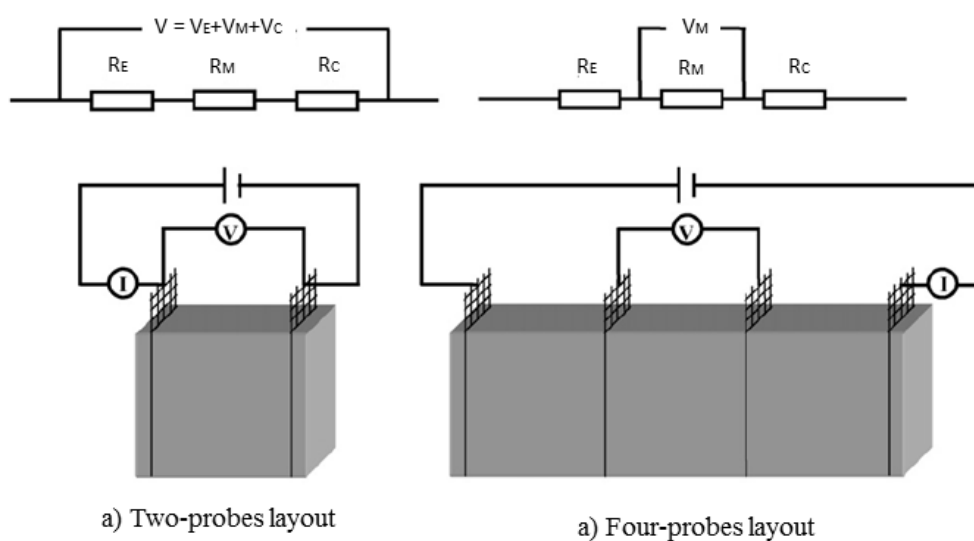


Figure 2.20: a) two-probes and b) four-probes configuration for the measurement of the electrical resistance.

The resistance of the electrodes is usually very low (the electrodes are made by conductor materials) and it can be neglected, but the contact resistance, related to the contact between the material and the electrodes, has a significant influence on the final measurement.

Figure 2.21 a) shows the typical trend of the electrical resistance measured by means of a two-probes method, on cement-based materials. One can observe a rapid initial increase, followed by a slow and steady increase. The resistance measured is in fact called apparent resistance since it does not represent the real electrical resistance of the tested material but it is influenced by the contact resistance, which is responsible of the increase mentioned above. Such increase is due to a polarization process that takes place at the interface between the cement-based material and the electrodes. As shown in Figure 2.21 b), during the electrical resistance measurement the ions present into the material move toward the electrodes (positive ions gather at the negative electrode and negative ions at the positive electrode). Such movement of charges causes the generation of a current which moves in the opposite direction of the external current applied for the measurement by causing an increase of the measured resistance [129].

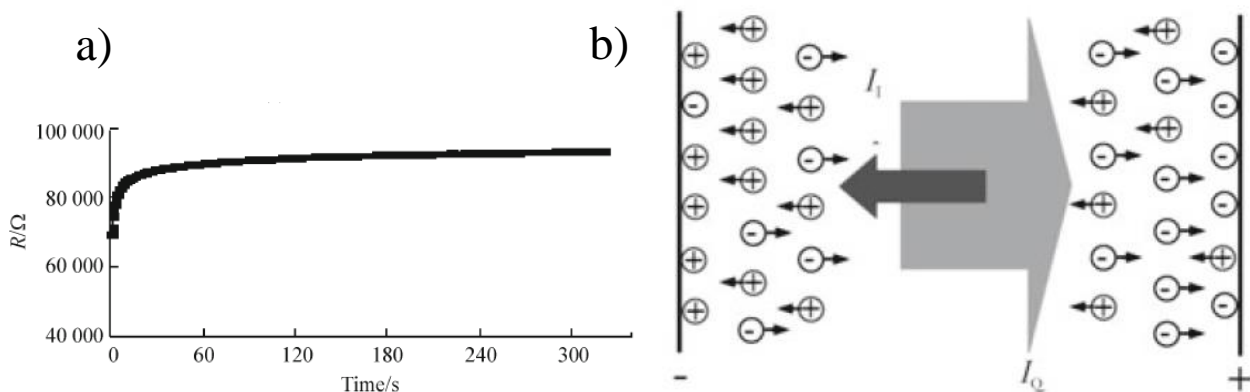


Figure 2.21: a) trend of the electrical resistance measured by means of the two-probes method on cement-based materials; b) schematic representation of the polarization process at the interface between the material and the electrodes [129].

The main goal of a strain-sensing device that exploits the piezoresistive effect is that the output resistance variation follows in real time the strain signal. It is clear that the polarization process that

takes place by using the two-probes method can significantly affect such goal, as testified by results of Figure 2.22, referred to the piezoresistive characterization of carbon fiber-reinforced cement [130]. It is worth noting that while for the four-probes method (Figure 2.22 b) the resistance variation curve (thick curve) accurately follows the strain signal (thin curve), in the case of two-probes measurements (Figure 2.22 a) there is a great difference between the two signals at the beginning of the measurement, due to the influence of the contact resistance, as explained above.

Due to the chemical-physical analogies between geopolymers and cement-based materials [22] and considering the observations reported above, the four-probes method was chosen for the piezoresistive characterization of the produced geopolymer mortar samples.

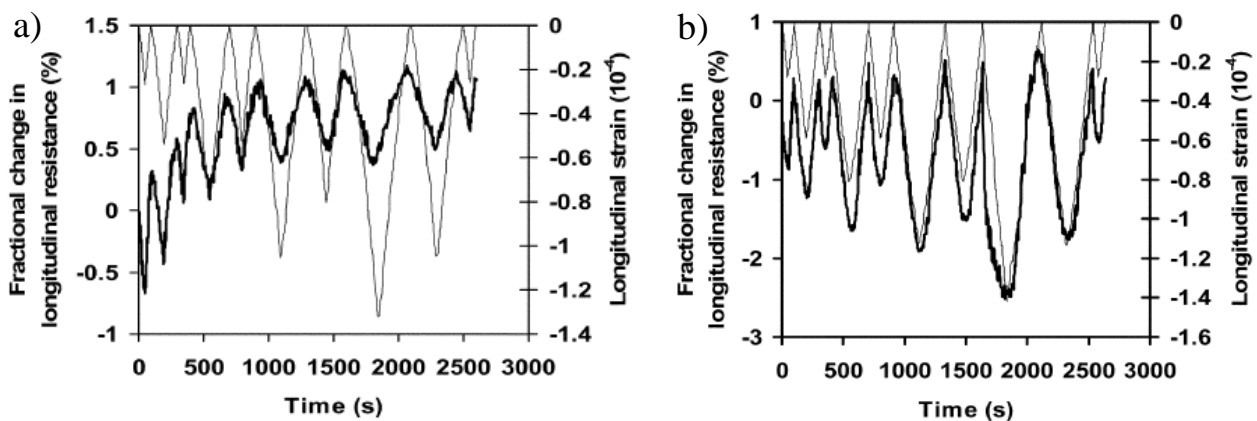


Figure 2.22: resistance variation (thick curve) and strain (thin curve) versus time using repeated compression at different strain amplitudes for a) two-probes and b) four-probes measurements performed on carbon fiber-reinforced cement [130].

In particular, silver electrically conductive paint was applied around samples perimeter at four interior planes which were parallel to the end surfaces and four copper wires were wrapped around each silver painted perimeter, in order to form four electrical contacts. The distance between the inner electrodes is equal to 10 mm whereas the distance between the outer electrodes is equal to 30 mm. Finally, an HBM strain gauge was glued on each sample between the inner electrodes for the strain measurements, as shown in Figure 2.23.

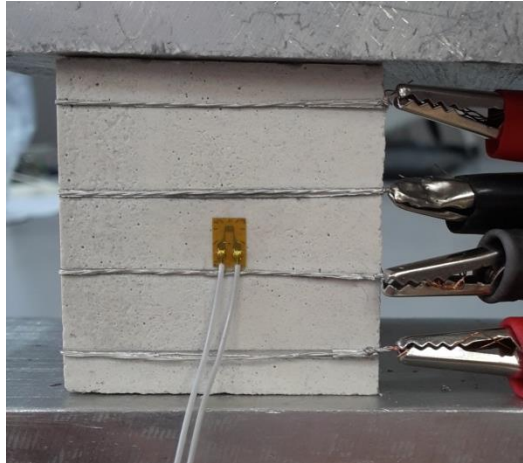


Figure 2.23: Geopolymeric sample with silver paint/copper wires electrodes and glued strain gauge.

The silver paint/copper wires configuration was adopted instead of that one which implies embedded foils as electrodes (shown in Figure 2.20) in order to reduce the contact area between the material and the electrodes and further avoid any polarization process at the interface. Furthermore, although the embedded electrodes are widely used [130, 131], they unavoidably cause a discontinuity into the tested material, by inducing stress concentration and damage initiation in such regions.

The electrical resistance was instead measured by means of a Parstat 2263 Potentiostat/Galvanostat (shown in Figure 2.24). The value of the amplitude of the input AC current was set to 2 mA and the frequency varied in the range $10 \div 100000$ Hz in order to find the maximum value of the gauge factor for each tested sample.

Samples were subjected to linear loading/unloading cycles of compression by means of an electro-mechanical Instron biaxial testing machine (ElectroPlus E10000) equipped with a 10 kN load cell. In particular, the lower and upper peaks of each cycle were respectively equal to 1 kN and 5 kN while the frequency was set to 0.008 Hz. This load range guaranteed the linear elastic mechanical behavior of the tested materials whereas the adopted static preload allowed to avoid any influence related to the high roughness of the ceramic samples surfaces.

An HBM QuantumX MX1615B Strain Gauge Bridge (set by means of Catman-Easy software) was employed to the real time recording of strain from the strain gauges.



Figure 2.24: Parstat 2263 Potentiostat/Galvanostat.

2.2.5 Piezoelectric Characterization

2.2.5.1 Piezoelectric effect and characterization methodologies

The direct piezoelectric effect was discovered in 1880 in single crystal quartz by Pierre and Jacques Curie, who noticed that under pressure quartz is able to generate electrical charge [132]. The word “piezo” in fact comes from the Greek and it means “pressure”, by suggesting that “piezoelectricity” (term proposed by W. Hankel in 1881) can be thought as “electricity produced by pressure”. Piezoelectric materials usually show also a converse piezoelectric effect, consisting in the production of a mechanical strain following the application of an external electric field. The converse piezoelectric effect was discovered by Gabriel Lippmann in 1881. Figure 2.25 shows a schematic representation of the direct (Figure 2.25 b and c) and converse (Figure 2.25 d-e) piezoelectric effect.

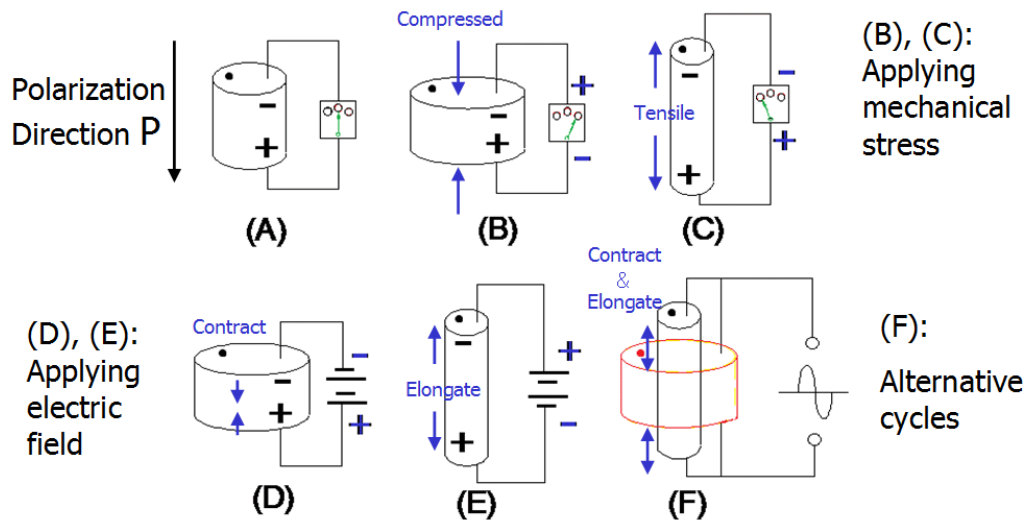


Figure 2.25: Schematic representation of the direct (b, c) and converse (d, e, f) piezoelectric effect.

Paul Langevin proposed the first practical application of piezoelectricity in 1917, during World War I, by developing a crystal quartz based ultrasonic submarine detector [132]. The real breakthrough in the piezoelectric research field came during World War II, when researchers from U.S, Soviet Union and Japan, independently discovered a new class of synthetic materials, the ferroelectric materials, characterized by piezoelectric constants several order of magnitude higher than those of natural piezoelectric materials. Barium titanate was the first ferroelectric material to be developed, in the 1940's, followed by lead zirconate titanate (PZT) in the 1950's. This latter in particular, is one of the most widespread piezoelectric material.

The piezoelectric materials known to date can be divided into three main categories: natural and synthetic crystals (quartz and Rochelle salt are an example of natural crystals whereas lithium sulfate and ammonium dihydrogen are synthetic crystals); polarized ferroelectric ceramics (such as PZT); piezo-polymers (Polyvinylidene fluoride (PVDF)). While crystal, due to their natural asymmetric structure, do not need additional processing to show piezoelectric properties, ferroelectric ceramics and piezo-polymers need to be polarized. In order to clarify such difference, a brief description of the physical phenomenon that characterizes piezoelectricity in the different categories mentioned above is reported below.

Figure 2.26 a) shows the typical shape of a natural quartz crystal with its characteristic axis. In particular, the Z axis is called optic axis and it is a three-fold symmetry axis, which means that the characteristics of the crystal are the same when it is rotated 120/240 degrees around such axis. The X axis, also called electric axis, and the Y axis, known as mechanical axis, are instead two-fold symmetry axis. As shown in Figure 2.26 b), each pair of $X_1 - Y_1$, $X_2 - Y_2$ and $X_3 - Y_3$ axes have the same characteristics and relationships to each other. The Curie brothers cut the crystal along the direction perpendicular to the X axis in order to obtain a plate and they observed the generation of an electric polarization in the direction of the thickness after pulling or compressing the plate. In order to understand the origin of such polarization, let's consider the atomic structure of the quartz crystal. Figure 2.27 a) shows the unit cell of α quartz where the small black circles represent the Si atoms while the large white circles are the O atoms. If we observe one unit of Si and O atoms viewed from the Z axis, as shown in Figure 2.27 b), it is clear that the electrical center of the structure lies in the origin of the X-Y plane and that there is a charge balance. When a mechanical pressure is applied along the X axis, the structure loses its charge balance and a polarization along the X axis is produced, as shown in Figure 2.27 c).

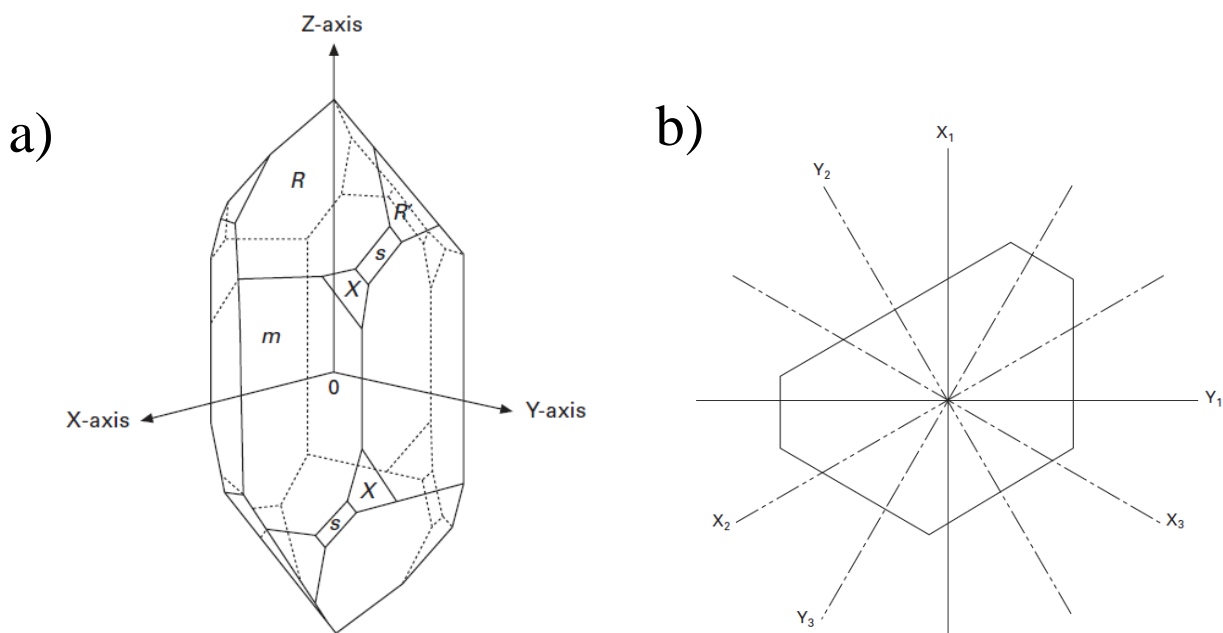


Figure 2.26: a) typical external form of natural quartz crystal; b) two-fold symmetry axis: X-axis (electric axis) and Y-axis (mechanical axis) [132].

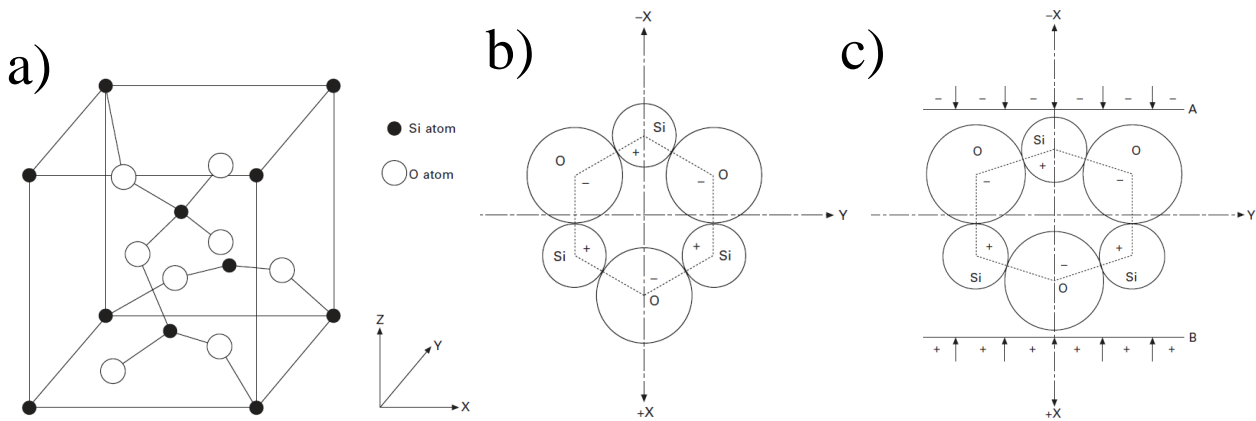


Figure 2.27: a) α quartz unit cell; b) one unit of Si and O atoms viewed from Z-axis; c) direct piezoelectric effect [132].

Ferroelectric ceramics such as barium titanate and PZT are instead based on the perovskite structure ABO_3 , shown in Figure 2.28. In such structure A-site cations form a cubic box while an oxygen octahedron lies within the box with one B-site cation in the middle. In the case of PZT the A-sites are filled by Pb ions, whereas the B-sites are randomly filled by Zr or Ti ions. Piezoelectric ceramics are synthesized from a powder feedstock, heated at high temperatures and subsequently cooled. Furthermore, a poling process is applied during synthesis in order to confer a piezoelectric behavior. Ferroelectric ceramics are characterized by a different atomic structure above and below the Curie temperature T_c , as shown in Figure 2.28. While there is a charge equilibrium above the Curie point (Figure 2.28 a), a non-centrosymmetric structure exists below the Curie temperature (Figure 2.28 b). This latter structure is characterized by electric dipoles and presents a spontaneous polarization even without an external electric field. Piezoelectric properties can then be found in ferroelectric ceramics below the Curie temperature.

In particular, the electrical dipoles present in the ferroelectric materials are organized in domains. A domain is defined as a homogeneous region in which all the dipoles moments have the same orientation and the different domains, with different orientations, are randomly distributed into the material, as shown in the first picture of Figure 2.29 a.

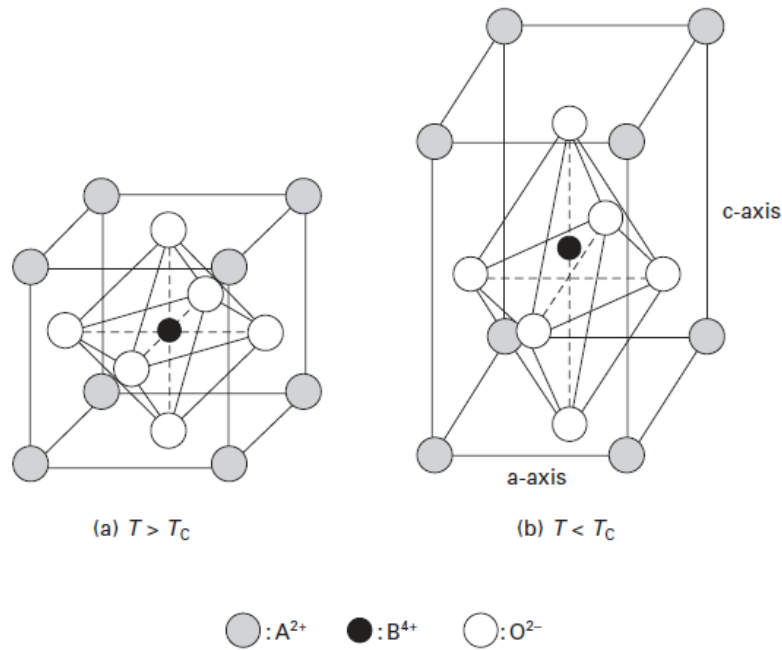


Figure 2.28: Atomic structure of perovskite [132]

However, with a such configuration a ferroelectric ceramic does not exhibits piezoelectric properties since, when a mechanical stress is applied, some domains experience an increase in dipole moment and some domains experience a decrease in dipole moment by causing no overall increase in polarization. For such reason, a poling process need to be applied. It consists in the application of an external electric field when the ferroelectric passes through its Curie temperature, in order to align in a single directions all the domains which spontaneously develop (see second picture of Figure 2.29 a). The dipoles are locked in the aligned configuration when the electric field is removed, due to a hysteretic behavior, as shown in Figure 2.29 b.

Figure 2.29 b shows the typical hysteresis curve obtained during the poling process. An electric field E is applied until a saturation polarization P_{sat} is reached. When the electric field is reduced to zero there is still a polarization, called remanent polarization P_r . Furthermore, it is worth noting that a negative polarization can be also obtained by reversing the electrical field. Finally, if the electric field is re-reversing, the initial positive polarization can be obtained again [133].

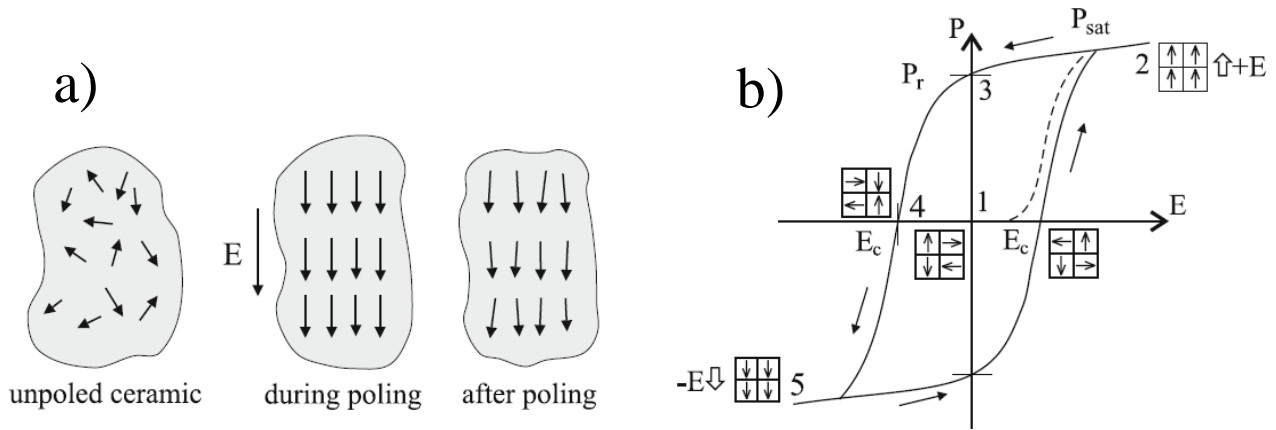


Figure 2.29: a) electrical domains distribution before and after poling; b) hysteresis curve obtained during the poling process of a piezoelectric ceramic [133].

Piezo-polymers, such as PVDF, are characterized by crystalline regions with internal dipole moments, that can be obtained by stretching the material during fabrication [134]. As for ferroelectric ceramics, such dipoles are randomly oriented and need to be aligned by means of a poling procedure.

The piezoelectric effect of all the known piezomaterials is always related to the presence of a non-centrosymmetric structure (as described above). However, in this dissertation a new piezoelectric model is proposed for the first time, by demonstrating that piezoelectricity is not always due to a non-centrosymmetric atomic structure.

The piezoelectric performances of a material can be evaluated by using piezoelectric coefficients which describe the interaction between the mechanical and the electrical behavior. The most common piezoelectric coefficient are the charge coefficient, d , and the voltage coefficient, g , whose definition is shown in Table 2.3 for both the direct and the converse effect.

Such coefficients are related by the following formula:

$$d = \epsilon^* \epsilon_0 g \quad (2.29)$$

where ϵ^* is the relative permittivity and ϵ_0 the permittivity of the free space (8.85 pF/m). In particular, while the constant d refers to short circuit conditions, the constant g is referred to open circuit conditions.

Table 2.3: definition of the charge coefficient, d , and the voltage coefficient, g , for both the direct and the converse piezoelectric effect [135]

Direct Effect	Converse Effect
$d = \frac{\text{charge density developed}}{\text{applied mechanical stress}}$	$d = \frac{\text{strain developed}}{\text{applied field}}$
$g = \frac{\text{electric field developed}}{\text{applied mechanical stress}}$	$g = \frac{\text{strain developed}}{\text{applied charge density}}$

Since piezoelectric materials are usually characterized by a great anisotropy in term of piezoelectric response, due to the existence of a polarization direction, the piezoelectric coefficients are usually defined as d_{ij} and g_{ij} , where the first subscript gives the "electrical" direction (field or dielectric displacement) and the second one gives the mechanical component (deformation or stress). The subscripts "i" and "j" can vary from 1 to 6, according to the reference system shown in Figure 2.30. In particular, direction 3 is the poling direction, while directions 4, 5 and 6 refer to shear strain associated to directions 1, 2 and 3, respectively.

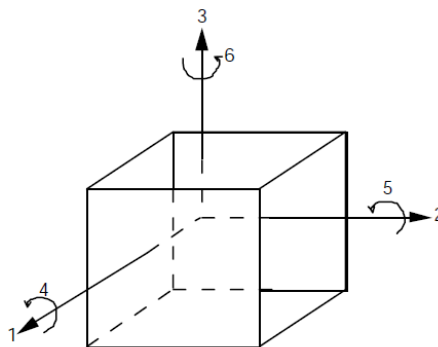


Figure 2.30: reference system for the definition of piezoelectric constants.

The piezoelectric constants can be evaluated by means of static, quasi-static, or dynamic methods. The static tests are seldom used because of the difficulty in controlling electrical boundary conditions. Piezoelectric material in fact, usually ceramic insulator materials, quickly loses the stored electrical charge if they are subject to static mechanical loads.

The dynamic characterization is considered the most reliable and it represents also the only standardized method [136]. By means of such method, also called resonance method, the piezoelectric constants can be evaluated by electrically exciting a resonance in a sample of known geometry. As for all bodies, also piezoelectric ceramics samples have a certain characteristic frequency, called resonance frequency f_r , at which they resonate freely with an amplitude greater than at other frequencies. An anti-resonant frequency f_a follows the resonance frequency and in correspondence of f_a the impedance of the body reaches its maximum value while the oscillation amplitude is at its minimum value. Figure 2.31 shows the typical resonance plot of a piezoelectric ceramic.

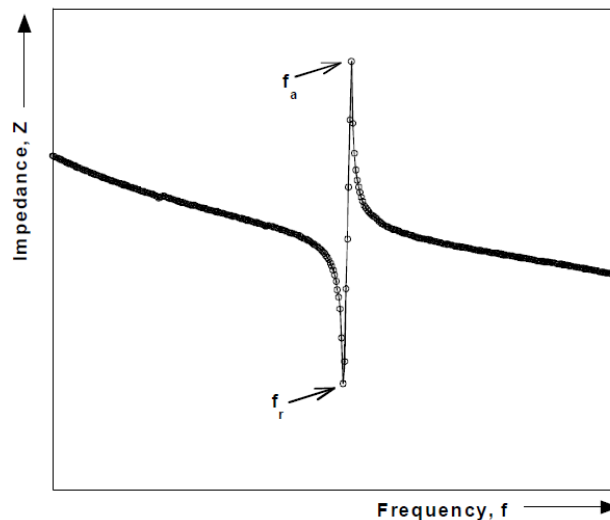


Figure 2.31: resonance plot of a piezoelectric ceramic (i. e., relationship between the impedance of the sample and the frequency of the applied electric field) [137].

By modeling the piezoelectric sample as an equivalent circuit (the most used circuit is that one proposed by the Van Dyke's Model and it is also recommended by the IEEE Standard [136]), the charge coefficient d_{33} can be calculated by using the following equation:

$$d_{33} = k_{33} \sqrt{\epsilon_0 K_3^T s_{33}^E} \quad (2.30)$$

were k_{33} is called coupling coefficient and it is related to the resonance and anti-resonance frequencies:

$$k_{33}^2 = \frac{\frac{\pi}{2}}{1 + \frac{(f_a - f_r)}{f_r}} \tan \left(\frac{\frac{\pi(f_a - f_r)}{2 f_r}}{1 + \frac{(f_a - f_r)}{f_r}} \right) \quad (2.31)$$

K_3^T is the free relative dielectric constant K^T under constant stress conditions (the superscript T indicates constant stress conditions) along direction 3 (the direction is specified by the subscript 3). In general, K^T can be calculated from the following:

$$K^T = \frac{t C}{\epsilon_0 A} \quad (2.32)$$

where t is the distance between electrodes, C the capacitance of the specimen, A the area of electrodes and ϵ_0 the permittivity of the free space.

The parameter s_{33}^E in equation 2.30 is the specimen compliance along direction 3 calculated in condition of constant electric field (short circuit) and it is given by:

$$s_{33}^E = \frac{s_{33}^D}{1 - k_{33}^2} \quad (2.33)$$

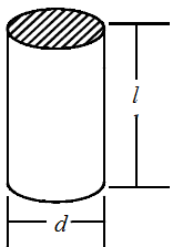
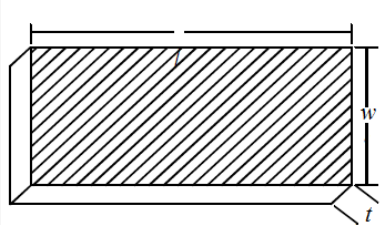
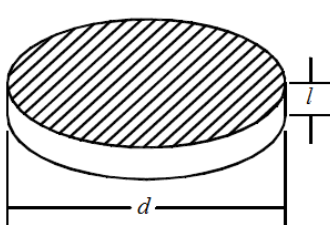
were s_{33}^D is the specimen compliance along direction 3 calculated in conditions of constant electric displacement D (open circuit) and it can be calculated as follow:

$$s_{33}^D = \frac{1}{4\rho f_a^2 l^2} \quad (2.34)$$

were ρ is the density of the material, l the distance between electrodes and w the width of the specimen. The resonance model is valid only near the resonance and the resonance needs to be

isolated from other modes in order to eliminate the influence of adjacent modes. Such isolation can be obtained by carefully choosing the geometry of the tested samples. Table 2.4 shows the most used geometry for the dynamic piezoelectric characterization.

Table 2.4: sample geometries typically used for the piezoelectric characterization by means of the resonance method [137].

			
Dimensional	long, slender, length	thin, flat plate, thickness poled;	thin flat disc, thickness poled
Requirements	poled rod; $l > 3d$	$l > 3.5 t, w$	$d > 10 t$

Although the dynamic method is highly reliable, it cannot be considered a flexible procedure, easy to be applied, since it needs a particular sample geometry (that must be such that only a pure fundamental resonance mode is produced) and a high excitation frequency (in the range of the resonance response).

The direct quasi-static piezoelectric characterization instead is more straightforward: a small oscillating mechanical load is applied to the sample and the output electric charge is recorded and divided by the applied load in order to obtain the piezoelectric coefficient. Such methodology is not standardized but it can be easily applied by anyone with a suitable measurement system.

Mathematically, the interaction between the electrical and mechanical behavior of the piezoelectric effect can be described as follow, considering a linear approximation:

$$S = s^E T + dE \quad (2.35)$$

$$D = \epsilon^T E + dT \quad (2.36)$$

where E is the electrical field strength, D the dielectric displacement, T the applied stress, S the strain, s the compliance and ϵ the permittivity. As described before, the superscripts E and T indicate constant field and constant stress condition, respectively. Equations 2.35 and 2.36 are written in the general form, without considering the directional notation. If we consider the poling direction 3, and we maintain a constant field condition (i. e., electric field equal to zero), Equation 2.35 can be written as follow:

$$d_{33} = [\delta D_3 / \delta T_3]_E \quad (2.37)$$

or, by considering the possibility of measuring d_{33} :

$$d_{33} = \left[\left(\frac{Q}{A} \right) / \left(\frac{F}{A} \right) \right] = \left(\frac{Q}{F} \right) \quad (2.38)$$

where F is the applied input force, A the area force applied over and Q the output electric charge.

Equation 2.38 is the basis of the application of the direct quasi-static method, since the charge coefficient can be evaluated by divided the value of the developed electric charge by the value of the applied mechanical load. The only requirement is that the measurements must be performed at constant field conditions, i. e. under short circuit conditions. Such conditions can be satisfied by using a virtual earth amplifier for the measurement of the electric charge, or by short circuiting the sample by means of a large enough capacitor (with a capacitance much greater than that of the tested sample). The charge coefficient can be also measured in the indirect mode, by applying an external field and by measuring the output mechanical strain, in condition of constant stress. In such case, the following equation must be considered (obtained from Equation 2.36):

$$d_{33} = [\delta S_3 / \delta E_3]_T \quad (2.39)$$

Piezometers testers able to measure the charge coefficient d_{33} are commercially available. Such testers use the quasi-static measurement method described above and, in particular, they consider

the direct piezoelectric effect. The direct quasi-static piezoelectric characterization is also known as “Berlincourt method”. Such name was proposed in “Piezoelectric Ceramics” by Jaffe et al [138] and it refers to Don Berlincourt, a scientist who worked for Channel Products on the development of one of the first d_{33} piezometer testers. In particular, a d_{33} piezometer is characterized by two main components, the force head and the control electronics. Figure 2.32 shows a schematic representation of the force head. The oscillating load is applied via a loudspeaker type coil. A PZT reference sample (red in Figure 2.32) is inserted in the load chain and it experiences the same load of the tested piezoelectric material (yellow in Figure 2.32). A static preload is usually applied in order to avoid that the sample rattles and to obtain stable measurements. The control electronics is characterized by an AC signal amplifier, a charge measurement system and a readout electronics. The frequency of the applied load lies in the range $10 \text{ Hz} \div 1\text{kHz}$. The lower limit is established in order to avoid thermal drift issues while the upper limit to avoid the resonance of the system. All the test is carried out in short circuit conditions, as described above. The charge coefficient d_{33} is obtained as the ratio between the charge of the reference PZT (the force) and the charge developed in the tested material.

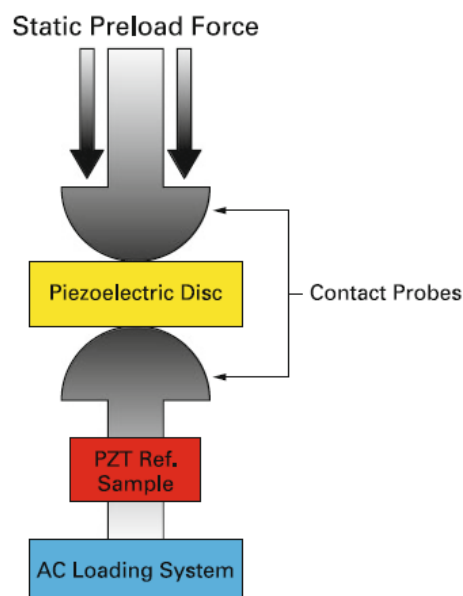


Figure 2.32: Components of the force head of a d_{33} piezometer tester [135].

Considering the flexibility and the easy application of the quasi-static characterization, such methodology was chosen for the piezoelectric characterization of the produced geopolymer mortars, for both the direct and the converse characterization. In particular, a suitable experimental setup was developed, as described in the following two paragraphs.

2.2.5.2 Direct piezoelectric characterization

A schematic representation of the setup realized for the direct quasi-static piezoelectric characterization with the adopted reference system, referred to the casting process, is reported in Figure 2.33. The mechanical input was imposed by means of an electro-mechanical Instron biaxial testing machine (ElectroPlus E10000) provided with a 10 kN load cell. Samples were tested under cycling compression load with a static pre-load of 1.25 kN and a frequency of 3 Hz. A light dependence of the charge coefficient from pre-load and frequency was observed and the chosen values of 1.25 kN and 3 Hz are those for which the higher coefficient was measured. The steel loading plates were electrically isolated by means of mika foils 300 μm thick and two copper foils, with the same dimensions of the sample surface and 200 μm thick, were used as electrodes. An HBM digital charge amplifier (CMD600), with a measuring range of 50-600000 pC, was used to measure the produced electric charge and a HBM Universal DAQ amplifier (QuantumX MX 840B) to real-time data recording. The HBM software catmanEasy-AP was used for data acquisition. After the acquisition of the sinusoidal signal of both of the applied load and the produced electric charge, the charge coefficient, d_{ij} (where i varies from 1 to 3, depending on the analyzed direction, according to the adopted reference system), was obtained as the ratio between the charge and the load amplitude. In particular, the charge amplitude was measured after the stabilization of the charge signal. In Figure 2.33 raw data referred to a test performed with a load amplitude of 250 N are reported.

The reliability of the measuring system was verified by testing commercial PZT piezoelectric ceramic materials of known charge coefficients, characterized by means of standard dynamic

procedures [136] by the supplier company. In particular, PZT piezoceramic samples (PIC181, hard) were purchased by Physik Instrumente (PI). The charge coefficient d_{33} declared by the supplier company, and measured by means of standard dynamic procedures, is equal to 265 pC/N.

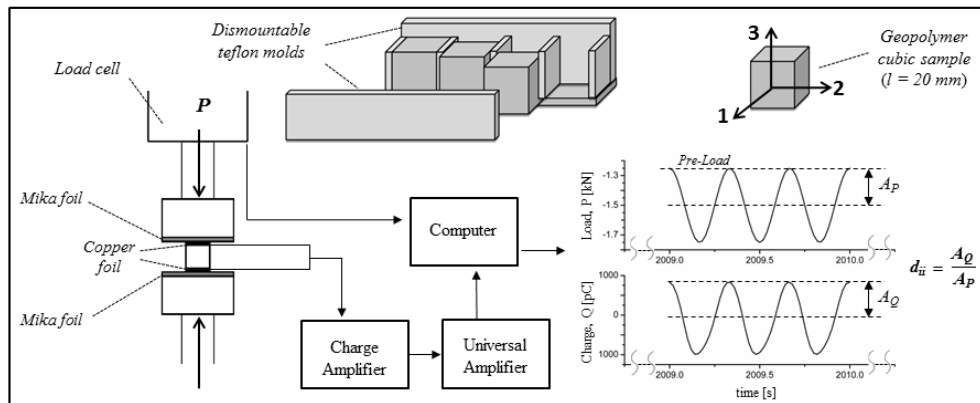


Figure 2.33: Schematic representation of the setup realized for the direct piezoelectric characterization with the adopted reference system.

In Figure 2.34 results about the direct quasi-static characterization carried out with the setup shown in Figure 2.33 on a PIC181 sample are shown. In particular, the sample was cyclically loaded (using a preload of 295 N and a frequency of 3 Hz) with different load amplitude and the charge amplitude was measured. It is worth noting that, as expected, the charge-load relation is linear and the slope is equal to 263.77 pC/N that is really near to the charge coefficient d_{33} declared by the supplier company, equal to 265 pC/N

The quasi-static characterization with the realized setup led to the same values of the charge coefficient declared by the supplier with the advantage that, compared to standard procedures, it is easier to implement. Contrary to dynamic procedures in fact it doesn't need of a particular sample geometry (that must be such that only a pure fundamental resonance mode is produced) and a high frequency (in the range of the resonance response).

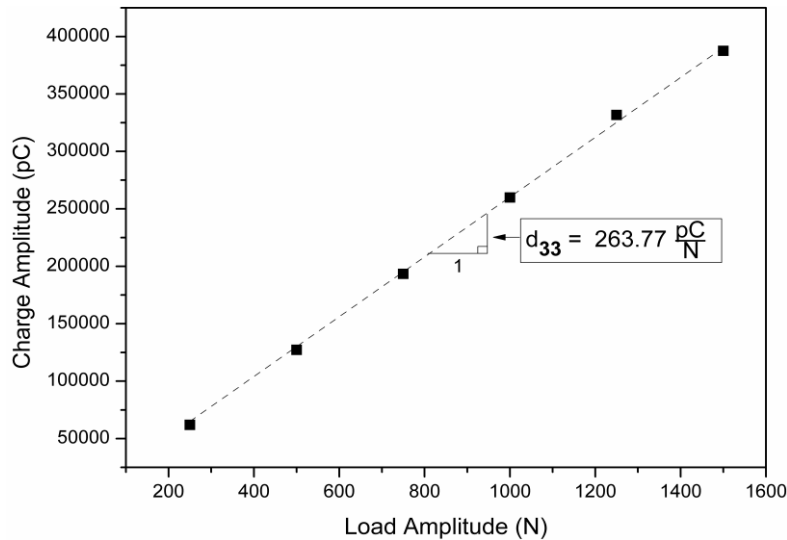


Figure 2.34: results of the direct piezoelectric characterization performed on commercial PZT of known charge coefficient.

2.2.5.3 Converse piezoelectric characterization

For the converse piezoelectric characterization samples were electrically excited with an AC voltage of 10 V amplitude at frequencies ranging from 50 mHz to 10 Mz by means of a function generator (HAMEG HM8030-6). Samples were clamped with a pre-load of 1.25 kN and electrically isolated by means of mika foils, whereas copper foils were used as electrodes. The output strain was measured by means of stain gauges glued on samples and a HBM strain gauge bridge amplifier (QuantumX MX 1615), with the catmanEasy-AP software, was used to real-time data recording.

2.3 Results and discussion

2.3.1 Mechanical properties

2.3.1.1 DIC and Brazilian Disk Test results

The methodology proposed in section 2.2.3.1 was used for the mechanical characterization of geopolymeric materials at the macroscale. In particular, the experimental displacements, recorded by means of the correlation software, were used as input parameters of the equations (2.2-2.3).

Figures 2.35 report the contours plot of the horizontal u_x , Figure 2.35 a), and vertical u_y , Figure 2.35 b), displacements. In particular, blue lines represent the experimental displacements after the rigid body motions, A , B_x and B_y , were deleted, whereas red lines are the analytical displacements calculated by using the regressed elastic constants, E and ν .

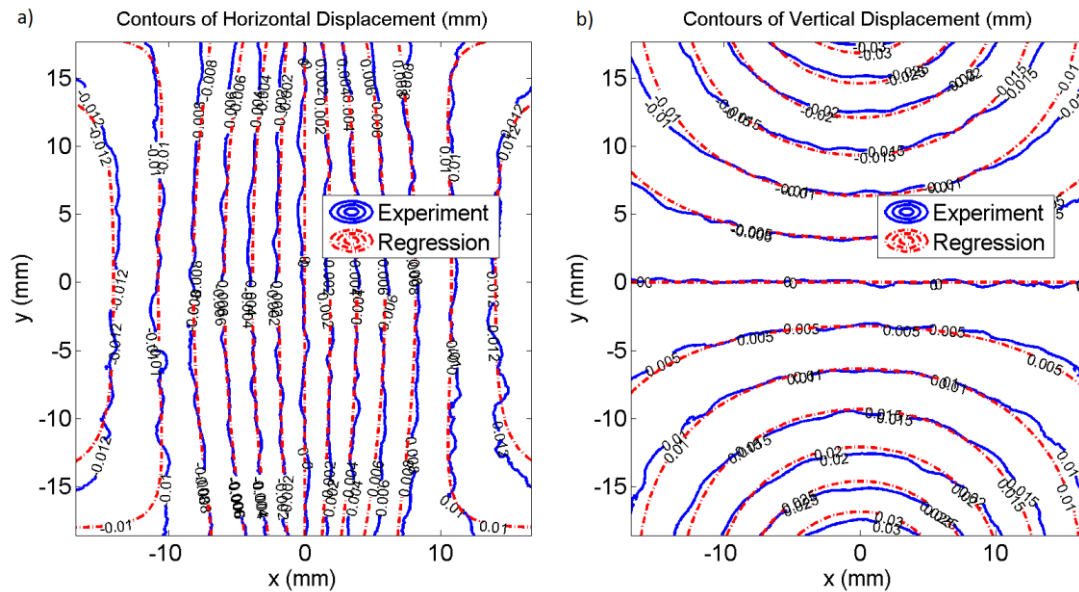


Figure 2.35: Comparison between the experimental and regressed displacement fields: (a) horizontal displacements u_x and (b) vertical displacement u_y .

Results revealed a very good match between the experimental and analytical data. Regressed elastic constants, for the three loading conditions, together with the ones obtained from the four points bending tests, are reported in Table 2.5.

Table 2.5: Tensile elastic constants obtained from four-point bending tests and least square regression.

	Four-point bending test		Least square regression flat platens (ASTM)		Least square regression rod platens		Least square regression curved platens (ISRM)	
	Average	Standard deviation	Average	Standard deviation	Average	Standard deviation	Average	Standard deviation
Young's modulus, E [GPa]	14.73	0.16	14.33	1.17	14.96	0.83	15.21	1.47
Poisson's ratio, ν	0.186	0.004	0.190	0.016	0.197	0.014	0.192	0.025

Results revealed that the proposed approach is well suitable in evaluating the elastic constants of brittle isotropic material. In fact no big difference between results obtained with the regression and the four points bending tests was observed.

Furthermore, it was demonstrated that loading conditions do not significantly affect the elastic constants calculation because the slight differences between calculated values can be ascribed to experimental errors.

As previously discussed, the shape of the loading platens for the evaluation of the tensile strength is still an open issue.

In order to better investigate such aspect three different loading platens (flat, rod and curved) were used for the experiments and the tensile strength, according to Equation (2.24), was calculated see Table 2.6. Results revealed that σ_T value increases for increasing angles of load contacting area between the disk and the loading platens, as also observed in [107]. The highest σ_T value was measured when curved platens, suggested by the ISMR standard, were used. In fact, these latter guarantee the highest contact area with the sample and the lowest stress concentration at loading points.

Further investigations were also done in order to investigate on the crack initiation and failure mechanisms during the Brazilian tests. According to the Griffith criterion, fracture should initiate from the central part of the specimen, where the maximum tensile stress is located. However, in some cases failure can occur far away from the center of the disk and, in particular, at the loading points due to the high stress concentration.

Table 2.6: Tensile Strength values measured with the three different loading conditions adopted.

	Flat platens (ASTM)		Rod platens		Curved platens (ISRM)	
	Average	Standard deviation	Average	Standard deviation	Average	Standard deviation
Tensile Strength, σ_T [MPa]	4.28	0.44	3.17	0.43	5.47	0.68

In this context, in order to understand which platen is able to guarantee the valid failure mode, the horizontal tensile strain (ϵ_{xx}) distribution was measured immediately prior to failure by means of DIC for each adopted loading condition. Results revealed that when flat and rod platens are used the maximum tensile strain is recorded near the loading points for all the specimens, whereas if curve platens are used the maximum ϵ_{xx} can be observed or near the center of the disk or near the loading points, as shown in Figure 2.36. These observations confirm that curve platens generate the lowest stress concentration at the loading points.

However, despite the different failure mode, the calculated tensile strength don't differ from one another (5.44 MPa was calculated for the disk of Figure 2.36 (a) and 5.73MPa for that one in Figure 2.36 (b)). One can conclude that the localization of the crack initiation point is not so important in the tensile strength evaluation of brittle materials if the loading platens don't cause excessive stress concentration at loading points. For the analyzed material and the adopted samples dimensions the curve platens represent then the most suitable loading condition for the evaluation of the tensile strength.

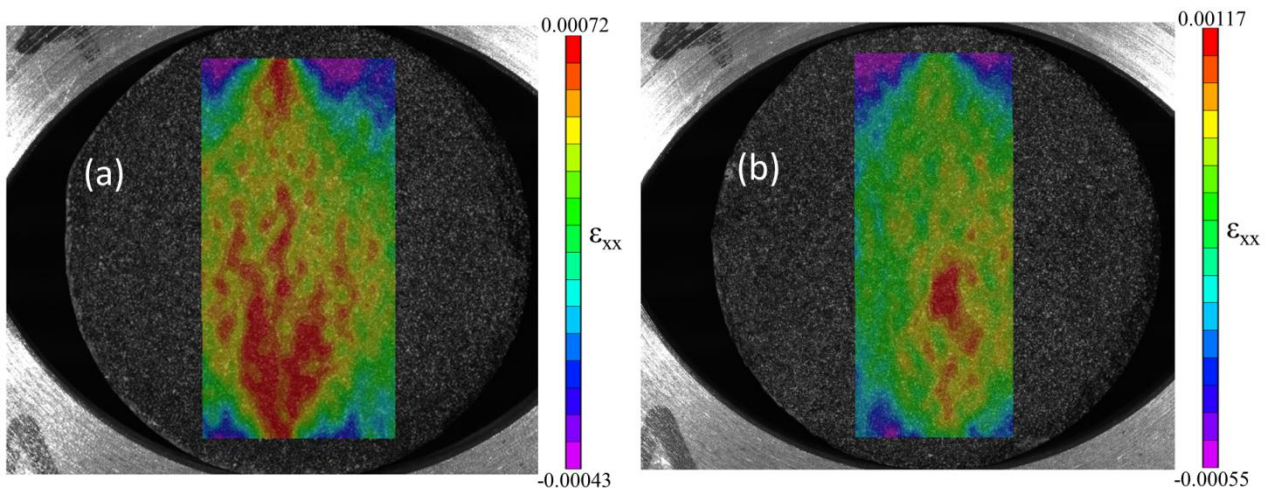


Figure 2.36: Tensile strain (ϵ_{xx}) distribution immediately prior to failure for two specimens loaded with curve platens: (a) the maximum ϵ_{xx} is located near the loading points and propagates toward the center of the disk; (b) the maximum ϵ_{xx} is located near the center of the disk.

2.3.1.2 Indentation tests results

A mechanical characterization at the micro and nano scale of the produced geopolymers was also carried out by indentation tests in order to understand the relationship of the material properties at different length scales. In Figure 2.37 an optical microscopy of the geopolymer mortar sample, mounted and polished as described in Section 2.2.3.2, is shown. One can observe that the material is characterized by two different phases. In particular, the quite homogeneous matrix represents the geopolymer paste whereas the lighter spots are the quartz sand fillers.

Micro indentations were firstly performed (by using the parameters described in section 2.2.3.2) only on the geopolymer paste matrix and the measured values of the indentation modulus, E_r , and hardness, H , are reported in the first row of Table 2.7.

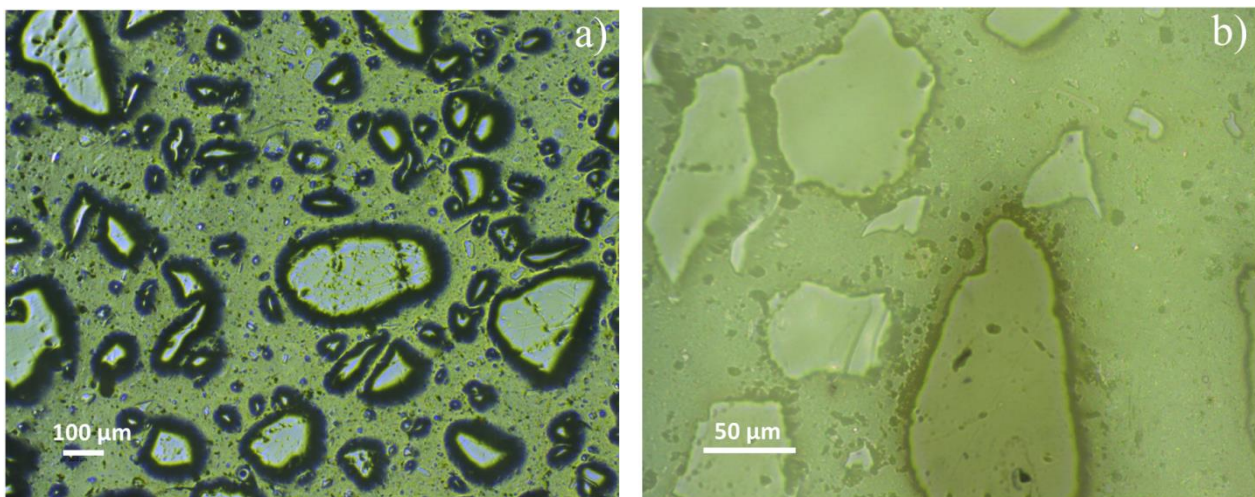


Figure 2.37: Optical microscopy of the produced geopolymer mortar performed with a) 5x and b) 20x magnitude.

A second set of micro indentations was then carried out by testing the entire surface of the sample and by randomly localizing the indentations, without excluding the quartz sand regions, and results are listed in the second row of Table 2.7. It is worth noting that the increase of mechanical properties caused by the quartz sand addition is extremely high: the increments recorded for E_r and H are 184 % and 591% respectively. The sand addition is then necessary to improve the mechanical

properties of the geopolymer paste and to enlarge the application fields spectrum of such materials, as discussed in Section 2.1.

Table 2.7: indentation modulus, E_r , and hardness, H , values measured by micro indentations performed only in the geopolymer paste matrix (Paste), and on the entire surface of the sample (Mortar), with a Vickers tip and a maximum load of 100mN.

	Er		H	
	[Gpa]	Incr%	[Mpa]	Incr%
Paste	11.43		468.98	
Mortar	32.45	184	3240.09	591

In Figure 2.38 and Figure 2.39 the Weibull distribution of E_r and H is shown for micro indentations performed into the paste and the mortar, respectively. In Figure 2.39 the first region (green square symbols) is related to the mechanical properties of the paste (mean values of $E_r = 15.91$ GPa and $H = 533.53$ MPa were measured) while the second region (red circle symbols) shows the higher mechanical properties of the quartz sand (mean values of $E_r = 44.13$ GPa and $H = 5331.51$ MPa were measured).

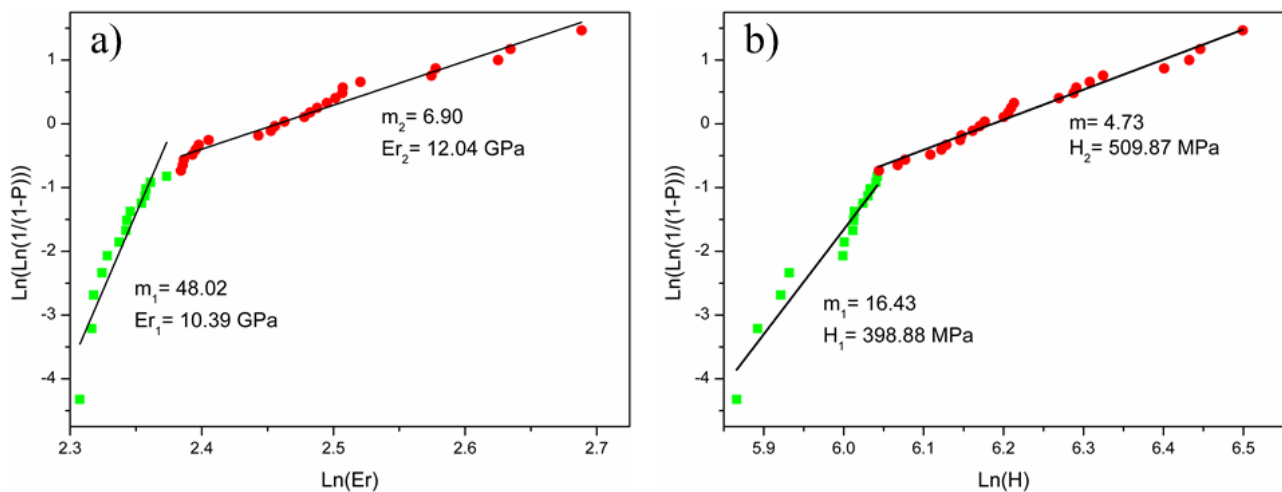


Figure 2.38: Weibull distribution of a) reduced Young modulus E_r and b) hardness H , for micro indentation performed only in the geopolymer paste matrix, with a Vickers tip and a maximum load of 100mN.

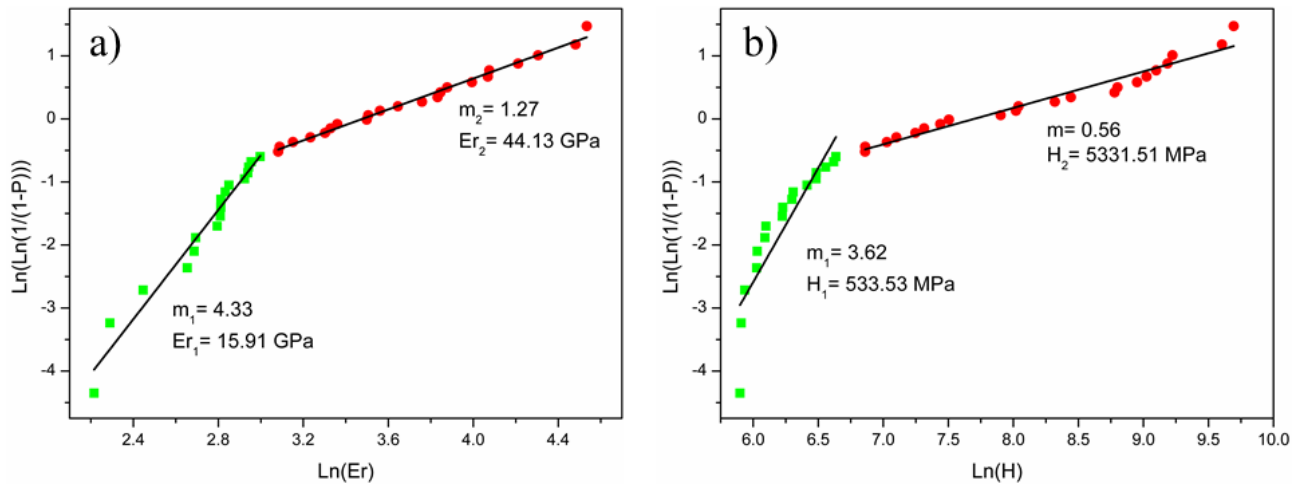


Figure 2.39: Weibull distribution of a) reduced Young modulus E_r and b) hardness H , for micro indentation performed on the entire mortar surface, with a Vickers tip and a maximum load of 100mN.

Whereas a bimodal distribution was expected for the mortar, due to the presence of two phases, the bimodality observed for the paste could be considered improper. However, it could be easily explained. The first region of the Weibull distribution in Figure 2.38, characterized by lower mechanical properties if compared to the second one, is related to defects (such as cracks or pores) and impurities (such as non-reacted metakaolin particles) contained into the geopolymer paste and shown in Figure 2.40. In Figure 2.40 a) the presence of cracks, pores, and unreacted metakaolin areas can be clearly observed in the geopolymer paste matrix. The higher magnification of Figure 2.40 b) refers to areas pointed out by dotted white circles of Figure 2.40 a) and confirms the presence of non-reacted metakaolin particles, characterized by a lamellar microstructure [22].

The significant contribution of quartz sand to the improvement of mechanical performances of geopolymers can be also observed in Figure 2.40 a). It is worth noting that the quartz particles are able to arrest the cracks propagation which generate during curing due to the material shrinkage following drying.

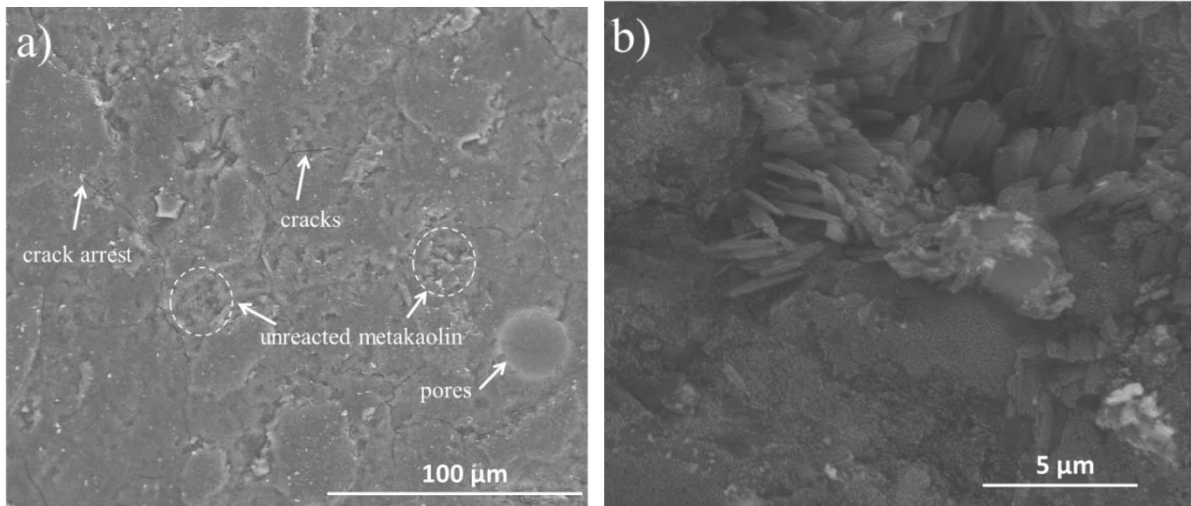


Figure 2.40: SEM image of geopolymer mortar. In figure a) defects such as pores, cracks and unreacted metakaolin areas are shown, while the higher magnification of figure b) shown the unreacted metakaolin with a lamellar structure.

Since the difference between the mechanical properties of paste and quartz sand is quite relevant, such bimodality can't be clearly observed in the first region of Figure 2.39, related to the paste.

The different mechanical behavior between geopolymer paste and quartz sand can be more clearly valued by performing nano indentation tests. Figure 2.41 shows the bimodal Weibull distribution of E_r and H for the geopolymer mortar tested by nano indentation and one can observe that in this case the gap between the first (paste) and the second (quartz sand) region is more prominent.

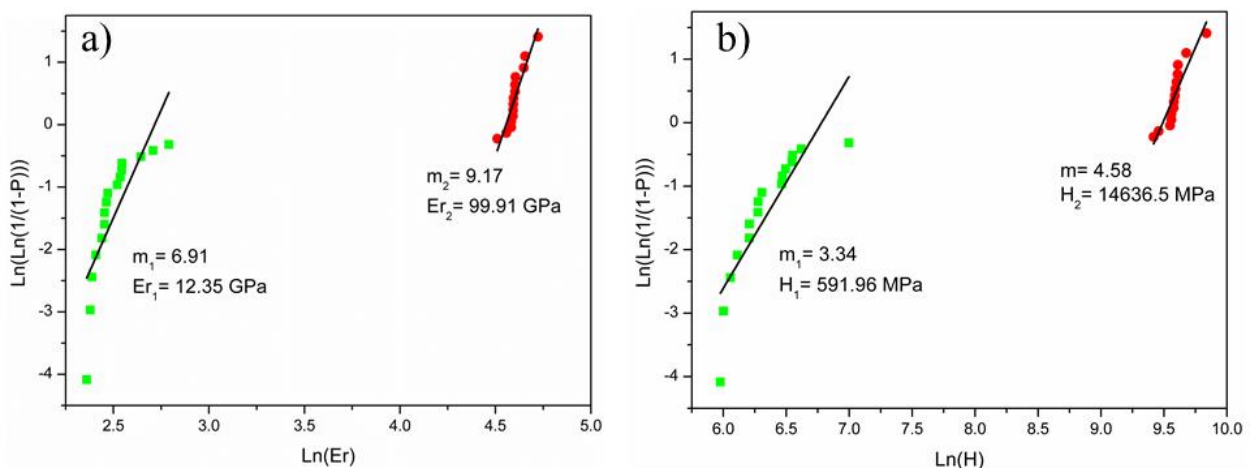


Figure 2.41: Weibull distribution of a) reduced Young modulus E_r and b) hardness H , for nano indentation performed on the entire mortar surface, with a Berkovick tip and a maximum load of 15 mN.

A nano indentation performed with a maximum load of 15 mN is in fact more localized than a micro indentation performed at 100 mN. Since the imprint of the nano indentation is significantly smaller than that produced by micro indentation, the chance to indent only paste or only quartz is higher and the mechanical properties values measured for the two regions are not averaged.

Such difference between the two regions is also highlighted by the nano indentation curves shown in Figure 2.42. It is possible to observe that in the paste phase a higher maximum penetration was noticed (1200 nm versus 200 nm of the quartz phase) as well as a lower slope of the unloading curve. This suggests that the quartz phase is characterized by higher stiffness and hardness, as explained by Equations (1.4-1.16) in Section 1.2.3.

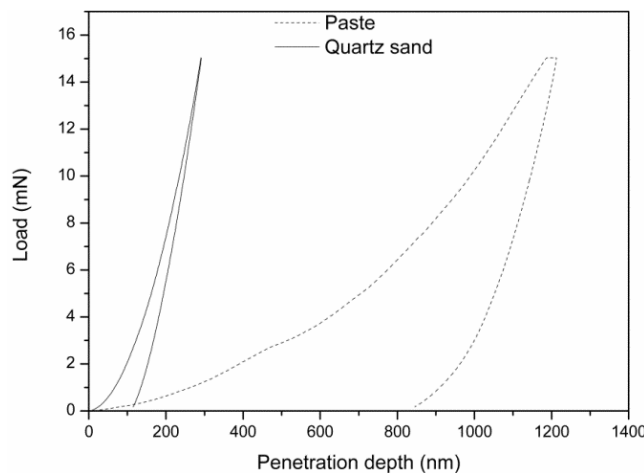


Figure 2.42: Indentation curves for geopolymer paste (dotted line) and quartz sand (continuous line).

Considerations about the relationship between the mechanical properties of geopolymers at different length scale can be carried out by comparing the results obtained by the DIC and Brazilian Disk methodology with those of micro and nano indentation tests.

A Young modulus of 15.21 GPa was measured at the macroscopic scale by using DIC combined with the Brazilian Disk test, whereas a value of 32.16 GPa and 53.74 GPa was obtained with micro and nano indentation, respectively. These last two values were calculated from the indentation

modulus E_r according to Equation 1.2 of Section 1.2.3 by considering the Poisson ratio of 0.192 measured in Section 2.3.1.1 by using DIC and Brazilian Disk test with curve platens (ISRM).

The significant decrease of the Young modulus from the nano to the macro scale can be ascribed to the presence of cracks and macropores which are typical of the material microstructure [22]. Even if the quartz sand prevents the cracks formation, a small amount of micro and macro cracks unavoidably generates during the curing process, due to the volume change of the material (as shown in Figure 2.40). At the nano scale a small volume of material is tested and the influence of defects such as cracks or pores can be considered irrelevant. A larger amount of material is instead considered at the micro scale and the probability of finding defects becomes higher by causing a decrease of the measured mechanical properties. At the macro scale this probability reaches its maximum since all the defects present into the material microstructure and their detrimental effects on the material properties are considered. Such scale effect affects the mechanical properties of almost all materials but it becomes more relevant in ceramic materials, due to their intrinsic porosity and the massive presence of cracks.

2.3.2 Piezoresistive properties

In Figure 2.43 results about piezoresistive characterization of the produced geopolymeric mortar are shown. In particular, in Figure 2.43 (a) one can observe how the electrical resistance signal follows the elastic strain, by revealing the presence of a great piezoresistive effect in geopolymers and, at the same time, the reliability of the dynamic four-probe measurements [130]. Figure 2.43 (b) instead shows the variation of the electrical resistance versus strain for a compression loading/unloading cycle. It is worth noting that the relationship is quite linear, except for a short initial and final region. The same behavior was observed elsewhere [139] and the not linear regions, as like as the small hysteresis, were considered negligible and related to unavoidable experimental errors.

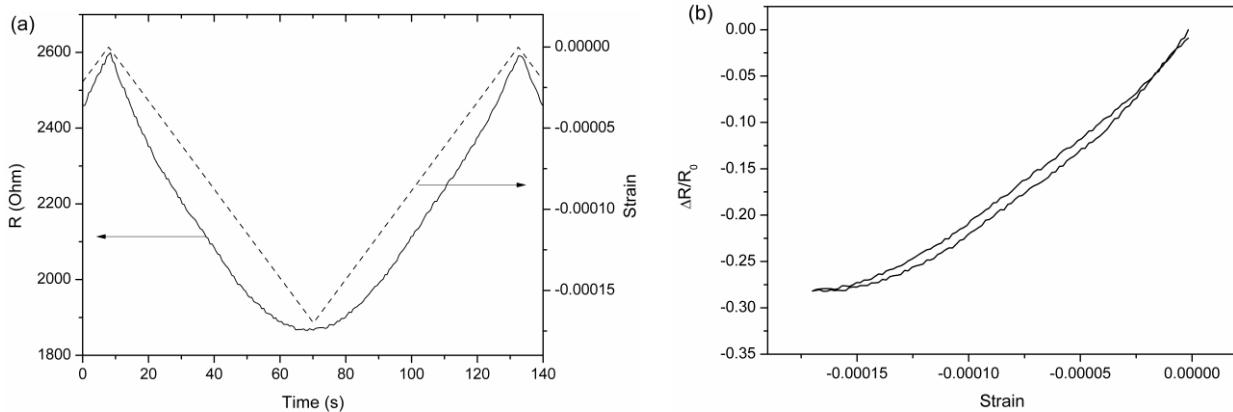


Figure 2.43: (a) electrical resistance and strain signal and (b) variation of the electrical resistance versus strain for a compression loading/unloading cycle.

The value of the frequency of the input AC current was varied in the range 10÷100000Hz in order to find the maximum value of the gauge factor, not influenced by the measurement system. As shown in Figure 2.44, the maximum value of the gauge factor is equal to 1662.43 and it was recorded with a frequency of 15.5 kHz.

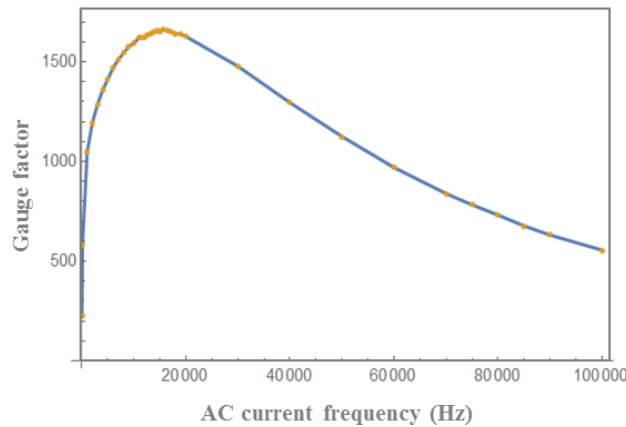


Figure 2.44: gauge factor values recorded for increasing values of the frequency of the input AC current.

One can observe that the measured gauge factor values are significantly high, higher than that of the cement-based materials [139-142]. The recorded values are of the same magnitude of those measured for polymer-derived ceramic systems [143-145]. For these particular systems the significant piezoresistivity was attributed to the tunneling-percolation process [146], related to the

coexistence of a conductive and an insulator phase into the material structure. Considering the chemical structure of geopolymers, the high piezoresistivity of such materials could be attributed to the same physical phenomenon. However, further investigations must be carried out in order to propose a clear physical model.

2.3.3 Piezoelectric properties

Figure 2.45 shows results about the direct piezoelectric characterization along direction 3.

In particular, four batches of five specimens were tested with different load amplitude values. In Figure 2.45 the different curves refer to different batches whereas each point of the curve represents the average value of the five samples of each batch.

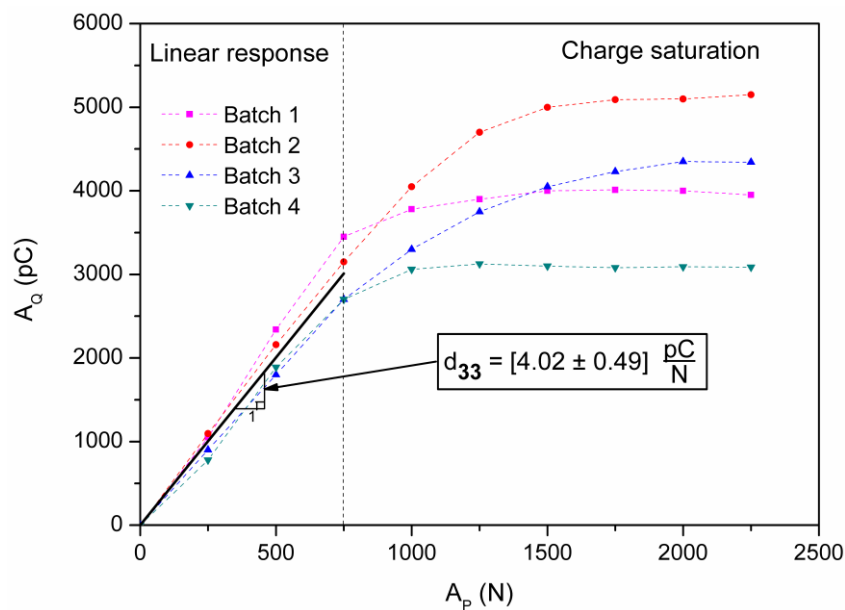


Figure 2.45: Charge amplitude A_Q versus load amplitude A_P for four batches of five samples tested along direction 3, which is that normal to mold's open surface. The continuous black line represents the average curve in the linear region whose slope represents the charge coefficient d_{33} .

It is worth noting that the material exhibits an initial linear behavior followed by a stabilization to a plateau value, associated to charge saturation. The continuous black line in Figure 2.45 represents the average curve in the linear region whose slope represents the charge coefficient d_{33} , equal to

(4.02 ± 0.49) pC/N. Experimental data about the mechanical or electromechanical characterization of ceramic materials are usually quite scattered because of the randomly porous nature of such materials and the standard deviation value of the charge coefficient measured for geopolymers is low enough to highlight the good repeatability of the carried out measurements.

Also d_{11} e d_{22} were determined, but, since the piezoelectric activity along directions 1 and 2 was found to be really weak, their values are negligible because they can be confused with the experimental noise. Such results highlight then the presence of an anisotropic behavior of the piezoelectric effect in geopolymers.

Since piezoelectricity is related to the generation of electrical dipoles within the material microstructure, several analysis were carried out on the produced geopolymer mortar in order to understand the observed phenomena and to propose a chemical-physical model able to explain the piezoelectric mechanism in such a material.

Even if geopolymers are X-ray amorphous, XRD analysis is usually carried out to check the presence of any undesired crystalline phases developed during curing that could affect mechanical properties, such as zeolites, or already present in the parent materials as impurities, like quartz or crystalline kaolinite. In particular, these last, having a non-centrosymmetric structure could contribute to the generation of electrical dipoles during mechanical stress [132]. Figure 2.46 (a) shows the XRD patterns of metakaolin raw powder (lower curve) as well as that of the synthesized geopolymer (upper curve). Metakaolin exhibits a pronounced broad hump centered at approximately $22^\circ 2\theta$ with few peaks, indicating that it contains essentially amorphous silica and alumina and Quartz (PDF n° 01-083-2468) and Muscovite (PDF n° 00-002-0055) impurities as crystalline phases. No diffraction peaks of its parent material, kaolinite, were detected. After reaction with sodium silicate solution, XRD pattern shows a shift of the centre of the original broad hump from $22^\circ 2\theta$ to approximately $28^\circ 2\theta$, that can be considered the typical distinguishing feature of the geopolymeric materials [147]. All sharp peaks from crystalline phase in parent material are

still present in the geopolymer diffraction pattern, thus confirming that they behave as inactive fillers in the geopolymer binder. Quartz could indeed contribute, even if unlikely to occur, since the crystal need to be cut and loaded along its symmetry directions [148], to the generation of electrical dipoles during mechanical stress, thus to piezoelectric activity. The obtained geopolymers show a dense and homogeneous microstructure, as revealed by SEM analysis shown in Figure 2.46 (c), that conventionally is considered as a strong indicator of high strength.

In order understand the structural properties and the formation process of the produced geopolymer and detect a possible generation of electric charge imbalance, solid state ^{29}Si - MAS-NMR, ^{27}Al -MAS-NMR and ^{23}Na - MAS-NMR analyses were carried out.

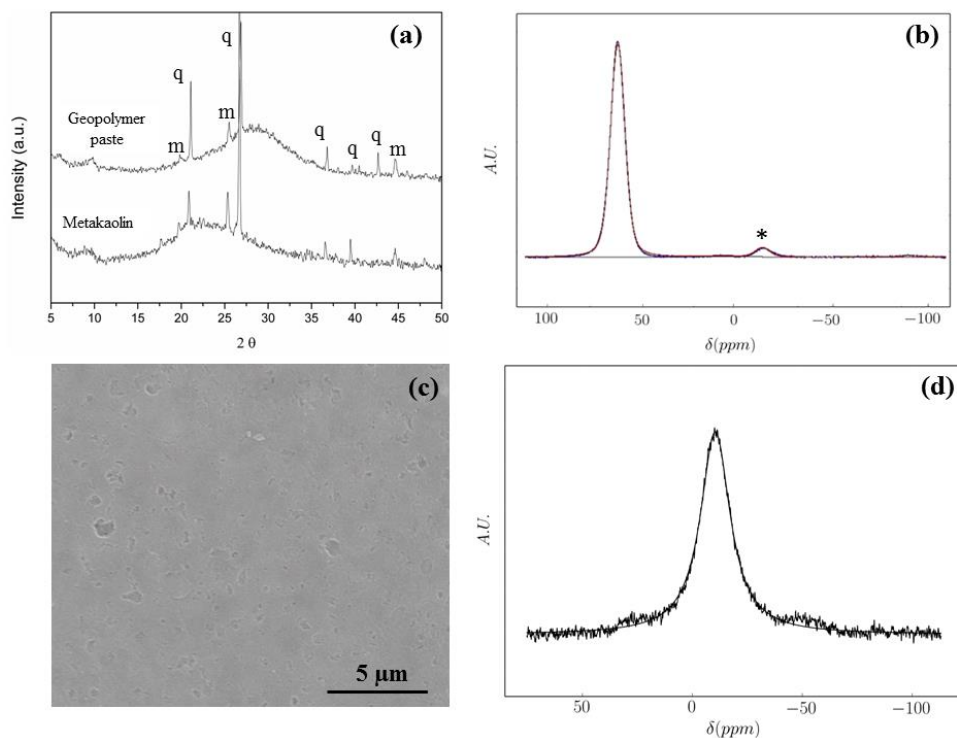


Figure 2.46: a) XRD patterns of metakaolin and geopolymer pastes (q= quartz, m= muscovite); b) ^{27}Al -NMR, c) SEM of geopolymer mortar d) ^{23}Na -NMR of geopolymer paste. The symbol * denotes spinning sidebands.

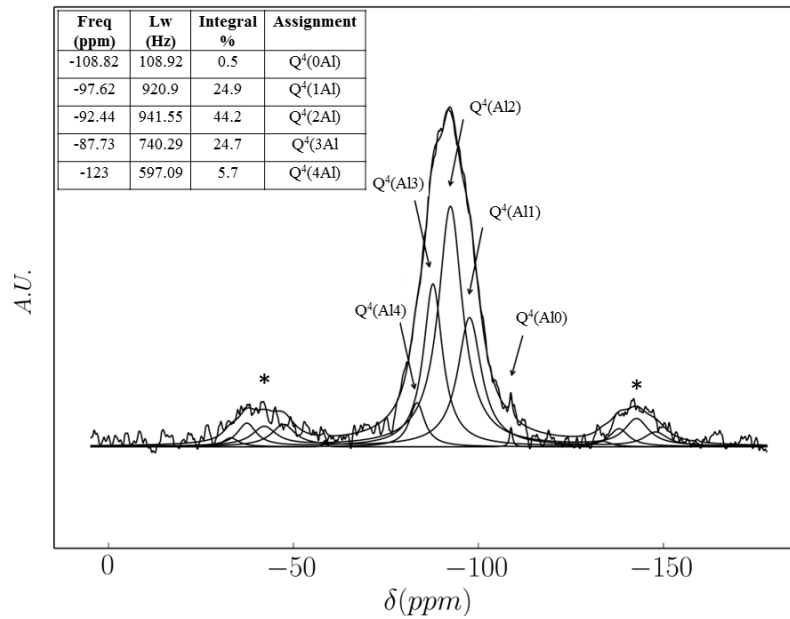


Figure 2.47: ²⁹Si-NMR of geopolymers paste.

Geopolymers can be generally described as a three dimensional amorphous network built from TO₄ (T=Si,Al) tetrahedral, joined at the corners with oxygen. The single negative charge associated with aluminum (III) in tetrahedral co-ordination is usually balanced by extra-framework cations present in framework cavities [149]. Furthermore, recent papers have regarded them as amorphous analogues of zeolites [149,150], because the presence of deformed six-, eight- and ten-membered rings results in the possibility of replacing the extra-framework cations by ion exchange [151].

²⁹Si- MAS-NMR is used to differentiate the connectivity range of SiO₄ tetrahedra and in the determination of substitution of Al for Si tetrahedra. ²⁹Si MAS-NMR decomposed spectrum of geopolymers gel, as reported in Figure 2.47, exhibits a broad spectrum, indicative of short-range ordering, centered at -94 ppm, reflecting the incorporation of Al into the coordination sphere of the Si and comprising all five possible silicon Q⁴(mAl) species. The consistency of the decomposition has been assessed with respect to the nominal composition of geopolymers [152].

²⁷Al- MAS-NMR spectrum of geopolymers, shown in Figure 2.46 (b), provides additional and important structural information, because peaks related to the various coordinations of oxygen

around Al atoms are clearly defined. It exhibits a dominant line at 63 ppm due to tetrahedral aluminum sites, as expected for a true geopolymer [153]. The absence of the resonance line at 28 ppm due to Al(V) clearly shows that almost all Al(V) contained in metakaolin is consumed during the geopolymerization process. The really weak ^{27}Al - MAS-NMR line at about 8 ppm is due to the presence of octahedral Al(VI) aluminum sites and their amount (0.46%) can be attributed to negligible amount of unreacted metakaolin.

The ^{23}Na -NMR spectrum of geopolymer, shown in Figure 2.46 (d), exhibits a signal at -10 ppm, that is associated with the presence of partially hydrated cation Na^+ , coordinated with the aluminium replacing the silicon in a charge balancing arrangement.

The detected presence of the partially hydrated cation Na^+ in charge balancing arrangement is a key factor for the piezoelectric effect explanation in geopolymers. In fact hydration reduces the cation–lattice electrostatic interaction through cation–water interaction, thus resulting in a weaker bonding that promotes the Na^+ migration away from the framework wall during mechanical loading and therefore creates the charge imbalance. Analogue mobility of non-framework cations, by hydrating at ambient conditions or under pressure, in presence of water has been widely studied in zeolite [154-156].

The presence of water inside of the geopolymer structure is therefore another key factor for explaining the observed piezoelectricity and it has been measured through thermogravimetric analysis. The mass loss (TG) and derivative mass loss (DTG) curve are reported in Figure 2.48 (a). The weight loss, of about 8%, has two maximum rates around $50\text{ }^\circ\text{C}$ and $100\text{ }^\circ\text{C}$ and it is completed at $200\text{ }^\circ\text{C}$. It is associated to the dewatering process and it can be attributed to the removal of free water in the pores (up to $\approx 100\text{ }^\circ\text{C}$) or physically adsorbed water, e.g. capillary encapsulated water up to $\approx 200\text{ }^\circ\text{C}$. A residual of 91% remained at $820\text{ }^\circ\text{C}$. The thermogravimetric analysis showed that water is present in geopolymer pores. In order to study the textural properties and the pores morphology of geopolymer paste, N_2 adsorption-desorption isotherms was carried out and

results are reported in Figure 2.48(b). The geopolymer paste shows a type IV isotherm with a H3 hysteresis loop characteristic of slit-shaped mesoporous structure. The specific surface area, with a value equal to $34.2 \text{ m}^2/\text{g}$, was calculated using the Brunauer–Emmet–Teller (BET) method. The total pore volume equal to $0.1888 \text{ cm}^3/\text{g}$ was derived from the amount of vapor adsorbed at a relative pressure close to unity. Mesopore width distributions was determined with the Barret–Joyner–Halenda (BJH) method using the desorption data. The pore size distribution of the specimen, reported in Figure 2.48 (c), is observed to be bimodal. It can be explained as a consequence of the pores interconnectivity and it is expected to favor water mobility under the mechanical loading.

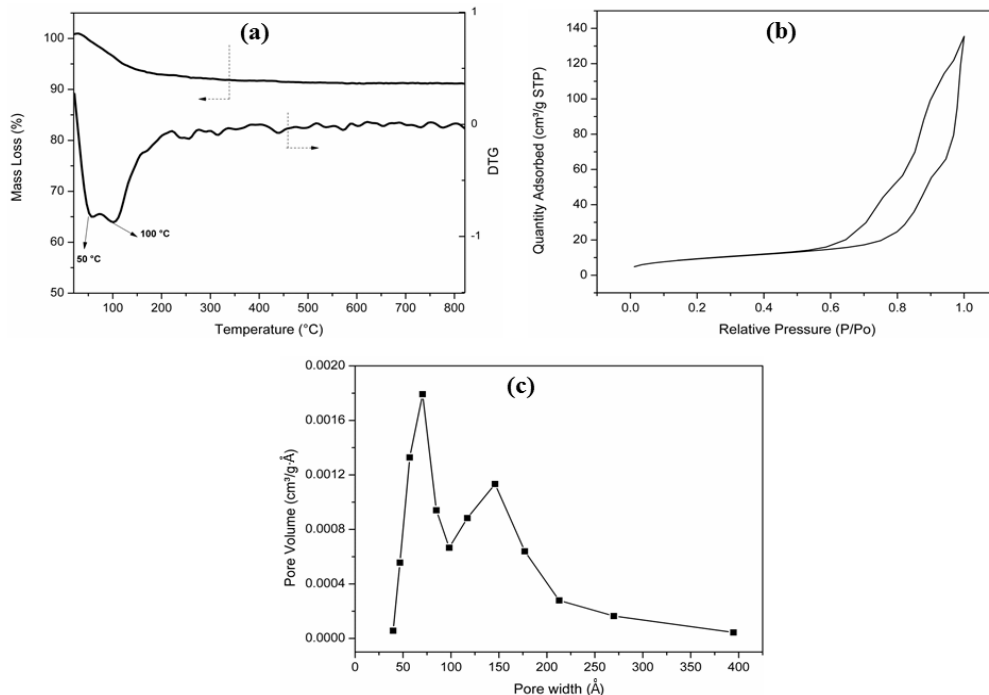


Figure 2.48: a) Thermogravimetric data of geopolymer paste: mass loss and mass loss derivative (DTG) curves; b) N₂ Isotherms of geopolymers paste; c) Pore width distribution (BJH desorption) of geopolymer paste.

On the bases of results of microstructural and chemical characterizations reported above one can propose a plausible model (schematically shown in Figure 2.49) able to explain the detected direct piezoelectric effect in geopolymers. It arises from its dense and homogeneous microstructure with a distributed and interconnected slit-shaped mesoporous porosity which embeds evaporable free or

physically adsorbed water and extraframework, mobile, hydrated alkali Na^+ cations. Piezoelectric effect is thus promoted by the migration of mobile hydrated cations under compressive loading in the pores of the geopolymeric matrix, thus creating a charge imbalance and local dipoles. The mechanism is coherent with the one proposed for explaining the piezoelectric effect in cement pastes [157, 158]. Similarities occur in the elements that determine and control the observed phenomenon, i.e. the presence of porosity, water and the transportation of mobile ions. What differs is the nature and the origin of ions. In Portland cement, the main hydration product is C-S-H. It is in contact with a high pH electrolyte solution, containing $\text{Ca}(\text{OH})_2$ (Portlandite), that promotes the dissociation of its surface silanol group (SiOH) and the successive physical adsorption of mobile calcium ions. The mechanism of surface charge creation (Electric Double Layer) is thus responsible of the charge imbalance and local dipoles under mechanical loading. In the case of geopolymers, instead, as evidenced by all the analysis carried out, it is due to the presence of the non-framework and hydrated Na^+ cations that balance the single negative charge associated with aluminium (III) in tetrahedral co-ordination.

The piezoelectric model proposed in this dissertation is thus mainly based on the ionic mobility phenomenon fostered by the water presence. In order to confirm such model and exclude the presence of other phenomena that could contribute to the electric charge generation during mechanical loading as, for example, the elastic deformation of quartz, some specimens were dried in oven under $50\text{ }^\circ\text{C}$ until no weight decrease was measured. This thermal treatment allows to greatly decrease the water content without altering the geopolymer structure. During dehydration of geopolymer, pores undergo to a shrinkage process, while Na^+ cations and framework generate strong electrostatic interactions as a consequence of the reduced dielectric screening of water, thus inhibiting cations migration [159, 160].

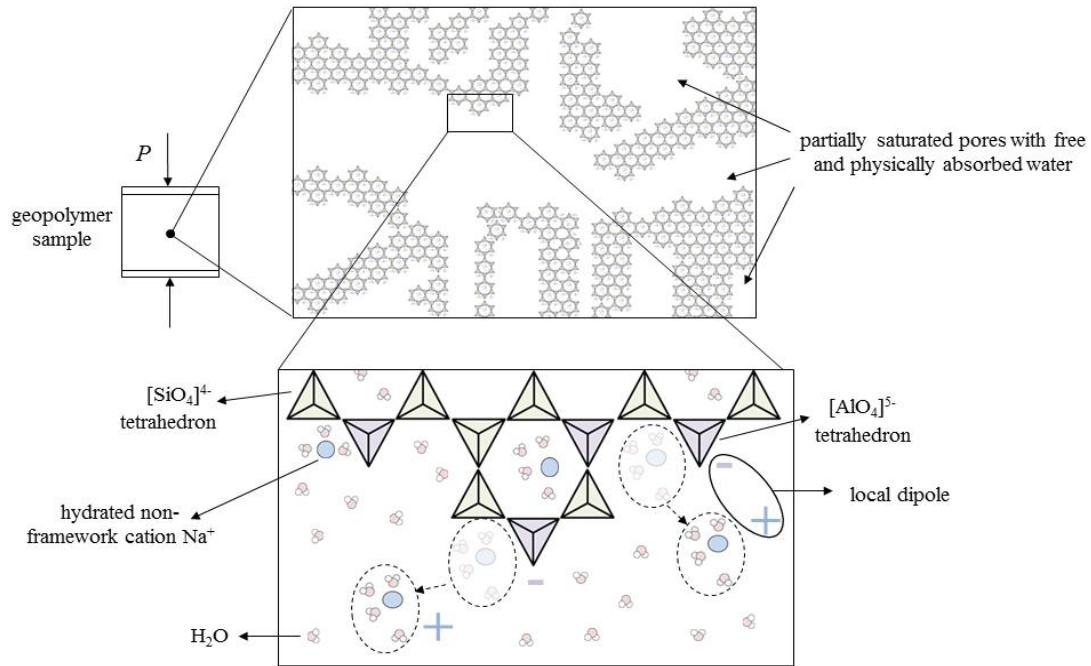


Figure 2.49: Schematic representation of the chemical-physical model proposed for the explanation of the direct piezoelectric effect detected in geopolymers. The lower magnification represents the porous structure of the material, characterized by partially saturated pores, filled with free and physically absorbed water. The higher magnification shows the amorphous network built from SiO_4 and AlO_4^- tetrahedrons, joined at the corners with oxygen. The single negative charge associated with aluminium (III) in tetrahedral co-ordination is balanced by the non-framework and hydrated Na^+ cations. The sample loading causes a distancing between cations and framework (indicated by dashed circles), fostered by hydration that reduces the cation–lattice electrostatic interaction. This distancing causes a charge imbalance and the formation of local dipoles which represent the cause of the piezoelectric effect.

It was observed that a completely dried sample (weight increment of 0 % in Figure 2.50) doesn't exhibit any direct piezoelectric effect, thus excluding any other source of piezoelectricity and confirming the validity of the ionic mobility based model proposed in this dissertation. Subsequently, the samples were stored under controlled humidity environment, thus allowing them to re-absorb water and the charge coefficients were measured for different water contents. From Figure 2.50, it can be observed that the charge coefficient in the predominant piezoelectric direction, d_{33} (black square symbols), increases for increasing values of water content (values more than 40 pC/N were measured in conditions of high hydration, not reported in Figure 2.50).

An converse piezoelectric characterization was also carried out on the geopolymeric samples. They were electrically excited with an external AC voltage signal in a broad frequency spectrum, but any strain was measured by strain gauges glued on samples, thus confirming that any potentially non-centrosymmetric structures, in particular quartz, contribute to the direct piezoelectric effect.

In Figure 2.50 it can also observed that, as previously stated, the direct piezoelectric effect in geopolymers is anisotropic. In particular, the direction perpendicular to the mold's open surface, defined as direction 3 in Figure 2.33, is that along with the higher piezoelectric activity was measured, whereas along directions 1 and 2 the effect is almost negligible and becomes to be influent for high water contents.

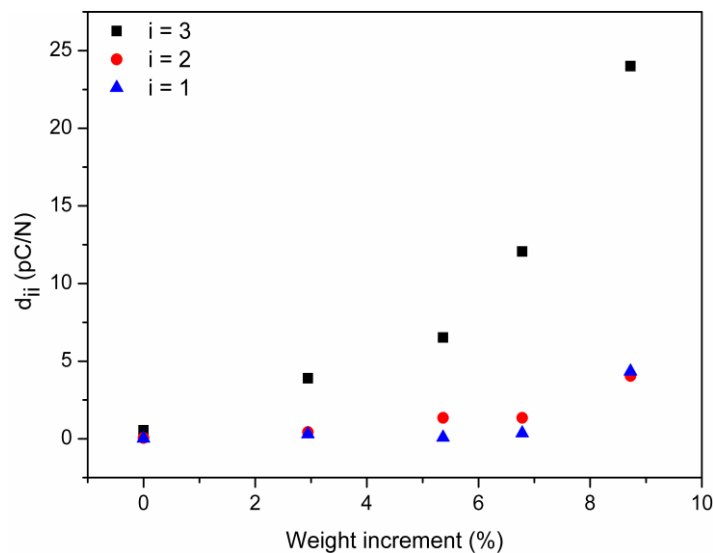


Figure 2.50: Charge coefficients measured for different water contents along three different directions.

The observed anisotropy with respect to the piezoelectric effect in geopolymer mortars could be ascribed to the porous nature of such materials. Anisotropic behaviors are generally found in natural porous argillaceous materials (rocks) [161, 162], and they are attributed to the preferential orientation of clay platelets during sedimentation [163, 164]. Due to such orientation, the fluids present into the material microstructure are forced to move along prefferential directions, by

causing anisotropic performances. Recently, such anisotropic behavior was found also into cementitious mortars and concretes [165-169] and it was attributed to the porosity structure of the material skeleton that influences fluid motion. Since metakaolin (the parent material used to produce geopolymer mortars) presents a microstructure characterized by platelets, as shown in Figure 2.51, and the produced geopolymers are porous materials (as testified by N_2 adsorption-desorption isotherms in Figure 2.48 b), the anisotropy observed for the piezoelectric performances could be due to a particular configuration of the porosity structure which arises from oriented platelets present in the parent material. As described above, the piezoelectric effect of geopolymers is related to ionic mobility and an anisotropic porosity configuration can drive the water present in the microstructure (which carries ions) along a preferential direction. In particular, as shown in Figure 2.50, the direction which presented the highest piezoelectric response in geopolymers was direction 3, i. e. that one perpendicular to the open surface of the molds used for casting (see Figure 2.33). The preferential orientation of the internal porosity then, could be also influenced by the casting and the curing process.

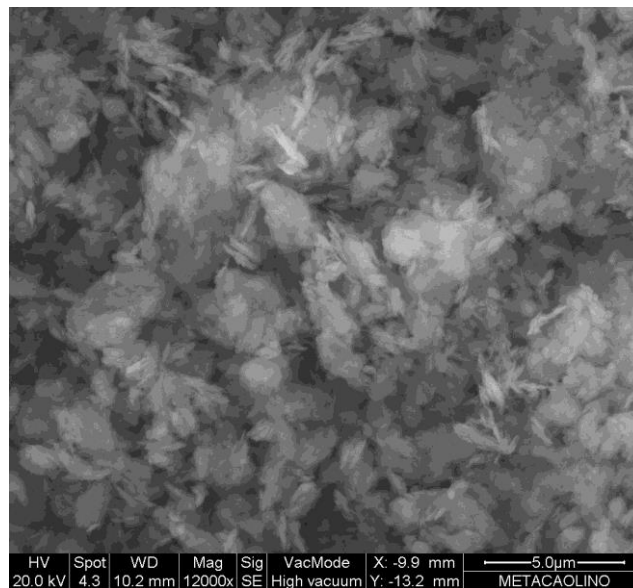


Figure 2.51: SEM analysis of Metakaolin.

In the present dissertation the observed electromechanical coupling was attributed to a direct piezoelectric effect. However, the electromechanical coupling is not only related to piezoelectricity. It could indeed occur through different mechanisms such as electrostriction, flexoelectricity and Maxwell stress.

Concerning electrostriction and Maxwell stress effect, related to the strain produced by the application of an external electric field, because it was verified that the application of an external electrical field doesn't produce any strain in geopolymers, such material can't present these properties.

About flexoelectricity, it occurs in liquid crystals or in solids with a crystal symmetry and it is defined as the polarization produced by a strain gradient. This strain gradient is generally produced by bending stress. In this work geopolymers were tested by means of compression tests that produce a homogeneous strain on the material, therefore the electromechanical coupling can't be related to flexoelectricity because any strain gradient was imposed on the tested samples.

For these reasons the observed electromechanical coupling was attributed to a direct piezoelectric effect.

Since geopolymers don't show any converse piezoelectric effect, they can be only used as sensors. The knowledge of the frequency range which offers the highest response of piezoelectric sensors is fundamental for design and application purposes. Since one of the most common applications of geopolymers is in the civil engineering field, the direct piezoelectric effect can be exploit for the self-monitoring of civil infrastructures. The use of such a material could eliminate or reduce the need for embedded or attached devices, which are expensive, limited in durability and, as in the case of lead zirconate titanate, have negative environmental impact due to the presence of lead. Furthermore, also applications in the energy harvesting field can be really promising (i.e., by producing a geopolymeric road surface the traffic can be monitored, or the mechanical deformation of the road caused by vehicles could be exploit to store electric energy). By considering such

potential applications, the produced geopolymeric mortars were tested in a low range of frequency in order to analyze the effect of the applied load frequency on the piezoelectric coefficient. In particular, the frequency of the applied load lies in the range 0.02 Hz - 20 Hz, whereas the amplitude was set equal to 500 N. Such amplitude value was chosen in order to lie in the linear piezoelectric working range (as shown in Figure 2.45).

Figure 2.52 shows the trend of the charge coefficient d_{33} for increasing values of the applied load frequency. It is worth noting that the maximum piezoelectric response of the material was observed with a frequency of 2 Hz.

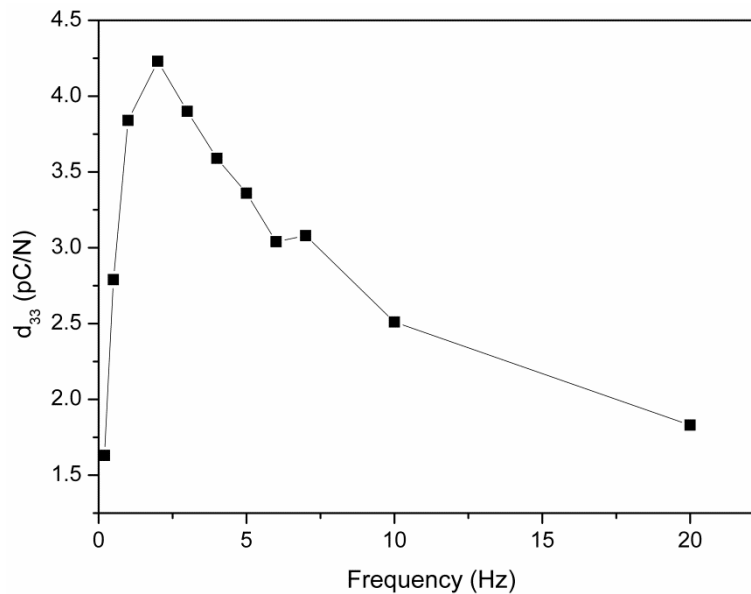


Figure 2.52: influence of applied load frequency on the charge coefficient d_{33} .

Hysteresis is another important phenomenon to be considered for the design and the utilization of piezoelectric sensors. Except in memory applications, which are based on polarization switching and hysteretic polarization-electric field relationships, hysteresis is undesired in high-precision sensor, actuator and capacitor applications. Several approaches were indeed proposed to reduce piezoelectric hysteresis and most of them focus on the microstructural modification of the material [170]. The knowledge of the physical origins of hysteresis is extremely important in order to control

its effects. However, the knowledge, the description and the control of such phenomenon are still open issues. The understanding of hysteresis is particularly hard when it doesn't relate purely electric (e.g. electric polarization-electric field), elastic (strain-stress) or magnetic (magnetization-magnetic field) variables. In particular, the electro-mechanical hysteresis appears between mixed variables such as electric field and mechanical strain (or mechanical pressure and electric charge) and researchers efforts toward the development of models able to represent the nature of such hysteresis are considerable. Among this models, the double layer model [170] is able to describe the piezoelectric hysteresis of ceramic materials characterized by randomly oriented plate-like grains, such as $\text{SrBi}_4\text{Ti}_4\text{O}_{15}$ and $\text{Bi}_4\text{Ti}_3\text{O}_{12}$. In such materials also an anisotropy of the piezoelectric effect was observed.

Figure 2.53 shows the electro-mechanical hysteresis cycles obtained by testing the produced geopolymeric mortar with different frequencies of the applied load. It is worth noting that the area of the cycles increases for increasing values of frequencies from 0.2 Hz to 2 Hz and it subsequently decreases from 2 Hz to 20 Hz, as observed for the piezoelectric coefficient d_{33} in Figure 2.52. There is then an analogous influence of frequency on both piezoelectric coefficient and electro-mechanical hysteresis.

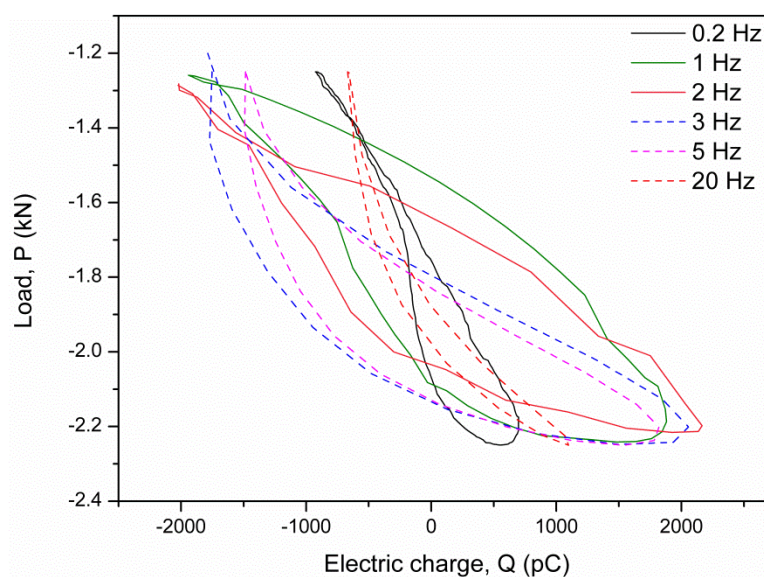


Figure 2.53: electro-mechanical hysteresis cycles obtained for different frequencies of the applied load.

A similar behavior was observed for the ceramic materials mentioned above (e. g., $\text{SrBi}_4\text{Ti}_4\text{O}_{15}$ and $\text{Bi}_4\text{Ti}_3\text{O}_{12}$). Since such materials have characteristic comparable to those of geopolymers (also geopolymers are characterized by a lamellar microstructure and an anisotropic piezoelectric effect, as described above) one can conclude that the double layer model can be considered suitable for the description of the electro-mechanical hysteresis of geopolymers.

2.4 Conclusions

This chapter was focused on the production and characterization of metakaolin-based geopolymer mortars. In particular, both mechanical and electro-mechanical characterization were performed.

Concerning mechanical characterization, it was carried out at different length scales. For the macro scale characterization, an optimized methodology, based on the Brazilian disk test and the application of the Digital Image Correlation technique, was developed. The proposed methodology is really easy to implement because it doesn't need stringent experimental requirements and allows to calculate Young's modulus, Poisson's ratio and the tensile strength of brittle materials by performing a single experiment. For the produced metakaolin-based geopolymer mortars a Young's modulus of 15.21 GPa, a Poisson's ratio of 0.192, and a the tensile strength of 5.47 GPa were obtained.

The micro and nano scale mechanical characterization was instead carried out by means of indentation tests. Results showed that the quartz sand plays a significant role for the improvement of the mechanical properties of the geopolymer paste. The increments recorded by micro indentation for E_r and H were 184 % and 591% respectively. The material microstructure is characterized by two phases: the paste matrix and the quartz sand fillers. The presence of the two different phases is clearly testified by the bimodal Weibull distribution observed for both E_r and H . However, also indentation results for the simple geopolymer paste showed a bimodal distribution, due to the presence of defects (such as cracks or pores) and impurities (such as non-reacted

metakaolin particles). Comparing results of the mechanical characterization at the different length scales, a Young modulus of 15.21 GPa was measured at the macroscopic scale by using DIC combined with the Brazilian Disk test, whereas a value of 32.16 GPa and 53.74 GPa was obtained with micro and nano indentation, respectively. The significant decrease of the Young modulus from the nano to the macro scale can be ascribed to the presence of cracks and macropores which are negligible with a localized nano characterization but became influential at higher scales.

For the electro-mechanical characterization both piezoresistive and piezoelectric characterization were performed.

A very high piezoresistive gauge factor, equal to 1662.43, was recorded by means of dynamic four probes measurements. Such value is significantly higher than that of the cement-based materials and it is of the same magnitude of those measured for polymer-derived ceramic systems. For these particular systems the significant piezoresistivity was attributed to the tunneling-percolation process, related to the coexistence of a conductive and an insulator phase into the material structure. Considering the chemical structure of geopolymers, the high piezoresistivity of such materials could be attributed to the same physical phenomenon. However, further investigations must be carried out in order to verify the high gauge factor values measured and to propose a clear physical model.

Concerning piezoelectricity, the occurrence of a direct piezoelectric effect has been discovered for the first time in metakaolin-based geopolymeric mortars. Unlike any other known piezoelectric material (quartz single-crystal, PZT, PVDF), wherein the formation of local electric dipoles is due to the elastic deformation of the non-centrosymmetric crystalline structures, a new and different piezoelectric mechanism was observed in geopolymers. It is due to a complex interplay that involves not-framework cations, framework and water contained in the material pores. In particular, the proposed model attributes the piezoelectric effect to the charge imbalance and local dipoles generated under compressive stress by the migration, within the network of interconnected pores of geopolymer, of the hydrated Na^+ cations, coordinated in a charge balancing arrangement with the

aluminum tetrahedra. The absence of a charge generation in dehydrated samples and the inexistence of a converse piezoelectric response confirmed that quartz impurities present inside the material don't contribute to the direct piezoelectric effect, thus due only to ionic mobility. Furthermore, an anisotropic behavior of the effect was observed and the measured charge coefficient in the predominant direction was found to lie in the range (4÷40) pC/N, depending on the water content in geopolymers.

The discovery of the piezoelectric activity in geopolymers transforms them into advanced ceramic materials and paves the way for several interesting applications. Due to its promising application in the field of structural components, geopolymer can allow the real time self-monitoring of civil infrastructures. The use of such a material could eliminate or reduce the need for embedded or attached devices, which are expensive, limited in durability and, as in the case of lead zirconate titanate, have negative environmental impact due to the presence of lead. Furthermore, they have low cost production and components of various shapes and dimensions can be easily fabricated. Geopolymers indeed do not need to be cut along particular directions like quartz crystals, neither to be polarized like piezoceramics or piezopolymers materials.

2.5 References:

- [1] Davidovits J.1991. Geopolymers: inorganic polymeric new materials. *J Therm Anal* 37(8):1633–56.
- [2] Davidovits J.1993.Global warming impact on the cement and aggregates industries. *World Resource Rev* (2):263–78.
- [3] D. Hardjito, C. C. Cheak & C. H. L. Ing, 2008 *Modern applied science*, vol. 2(4), pp. 3.
- [4] P. Duxson, A. Fernández-Jiménez, J. L. Provis, G. C. Lukey, A. Palomo & J. S. J. van Deventer, 2007 *Journal of materials and science.*, vol. 42(9), pp. 917-933.
- [5] J. L. Provis, 2006 *Modelling the formation of geopolymers*. (PhD), University of Melbourne.

- [6] Williams, P. Jason, Biernacki, Joseph J., Walker, Larry R., Meyer, Harry M., Rawn, Claudia J., Bai, Jianming, “Microanalysis of Alkali-Activated Fly Ash-CH Pastes”, *Cement and Concrete Research* 32, pp. 963-972, 2002.
- [7] Song, S., Sohn, D., Jennings, H.M., Mason, T.O., “Hydration of Alkali-Activated Ground Granulated Blast Furnace Slag”, *Journal of Materials Science* 35, pp. 249-257, 2000.
- [8] Vijaya Rangan, B., “Fly Ash-Based Geopolymer Concrete”, available at: <http://www.yourbuilding.org/display/yb/Fly+Ash-Based+Geopolymer+Concrete>
- [9] Chen, W., Brouwers, H.J.H., “The Hydration of Slag, Part 1: Reaction Models for Alkali-Activated Slag”, *J Mater Sci* 42, pp. 428-443, 2007.
- [10] Lee, W.K.W., and Van Deventer, J.S.J., “The Interface Between Natural Siliceous Aggregates and Geopolymers”, *Cement and Concrete Research* 34, pp. 195-206, 2004.
- [11] Chareerat, T., Lee-Anansaksiri, A., Chindaprasirt, P., “Synthesis of High Calcium Fly Ash and Calcined Kaoline Geopolymer Mortar”, *International Conference on Pozzolan, Concrete and Geopolymer*, Khhon Kaen, Thailand, May 24-25, 2006.
- [12] Khale, Divya, Chaudhary, Rubina, “Mechanism of Geopolymerization and Factors Influencing Its Development: A Review”, *J Mater Sci* 42, pp.729-746, 2007
- [13] Garcia-Loderio, I., Palomo, A., Fernandez-Jimenez, A., “Alkali-Aggregate Reaction in Activated Fly Ash Systems”, *Cement and Concrete Research* 37, pp. 175-183, 2007.
- [14] McDonald, Mike and LaRosa Thompson, Judy, “Sodium Silicate: A Binder for the 21st Century”, *The PQ Corporation, Industrial Chemicals Division*
- [15] Fernandez-Jimenez, A., Palomo, A., Criado, M., “Microstructure Development of Alkali-Activated Fly Ash Cement: A Descriptive Model”, *Cement and Concrete Research* 35, pp. 1204-1209, 2005.
- [16] M. Kanuchova, L. Kozakova, M. Drabova, M. Sisol, A. Estokova, J. Kanuch & J. Skvarla, *2015 Environmental progress & sustainable energy*, vol. 34(3), pp. 841-849.
- [17] J. Davidovits, 2011 *Geopolymer chemistry and applications*. Saint-Quentin, France.
- [18] F. Škvára, 2007 *International conference alkali activated materials—research, production and utilization*, Česká rozvojová agentura, Praha.
- [19] V. F. Barbosa, K. J. MacKenzie & C. Thaumaturgo, 2000 *International journal of inorganic materials*, vol. 2(4), pp. 309-317.
- [20] Krizan, Darko, Zivanovic, Branislav, “Effects of Dosage and Modulus of Water Glass on Early Hydration of Alkali-Slag Cements”, *Cement and Concrete Research* 32, pp. 1181- 1188, 2002.

- [21] Skvara, Frantisek, Dolezal, Josef, Svoboda, Pavel, Kopecky, Lubomir, Pawlasova, Simona, Lucuk, Martin, Dvoracek, Kamil, Beksa, Martin, Myskova, Lenka, Sulc, Rostislav, “Concrete Based on Fly Ash Geopolymers”, research project CEZ:MSM 6046137302: Preparation and research of functional materials and material technologies using microand nanoscopic methods and Czech Science Foundation Grant 103/05/2314 Mechanical and engineering properties of geopolymer materials based on alkali-activated ashes.
- [22] John L. Provis andJ annie S. J. van Deventer, Geopolymers Structure, processing, properties and industrial applications, First published 2009, Woodhead Publishing Limited and CRC Press LLC.
- [23] Li Chao, Sun Heng, Li Longtu. A review: the comparison between alkaliactivated slag (Si + Ca) and metakaolin (Si + Al) cements. *Cem Concr Res* 2010;40:1341–9.
- [24] Yunsheng Zhang, We Sun, Zuquan Jin, Hongfa Yu, Jia Yantao. In situ observing the hydration process of K-PSS geopolymeric cement with environment scanning electron microscopy. *Mater Lett* 2007;61:1552–7.
- [25] Sum Wei, Zhang Yun-sheng, Lin Wei, Liu Zhi-yong. In situ monitoring of the hydration process of K-PS geopolymer cement with ESEM. *Cem Concr Res* 2004;34:935–40.
- [26] Zhang YS, Sun W, Li ZJ. Hydration process of potassium polysialate (K-PSDS) geopolymer cement. *Adv Cem Res* 2005;17(1):23–8.
- [27] Alonso S, Palomo A. Alkaline activation of metakaolin and calcium hydroxide mixtures: influence of temperature, activator concentration and solids ratio. *Mater Lett* 2001;47:55–62.
- [28] Zhang YS, Sun W, Li JZ. Hydration process of interfacial transition in potassium polysialate 9K-PSDS) geopolymer concrete. *Mag Concr Res* 2005;57:33–8.
- [29] De Silva P, Sagoe-Crenstil K, Sirivivatnanon V. Kinetics of geopolymerization: role of Al₂O₃ and SiO₃. *Cem Concr Res* 2007;37:512–8.
- [30] Rowles M, O’Connor B. Chemical optimization of the compressive strength of aluminosilicate geopolymers synthesized by sodium silicate activation of metakaolinite. *J Mater Chem* 2003;13:1161–5.
- [31] Provis John L, van Deventer SJ. Geopolymerisation kinetics. 1. In situ energy – dispersive X-ray diffractometry. *Chem Eng Sci* 2007;62:2309–17.
- [32] Yunsheng Zhang, Wei Sun, Zongjin Li. Synthesis and microstructural characterization of fully reacted potassium-poly (sialate-siloxo) geopolymeric cement matrix. *ACI Mater J* 2008:156–64. 105-M18.
- [33] Yunsheng Zhang, Wei Sun, Zongjin Li. Composition design and microstructural characterization of calcined kaolin-based geopolymer cement. *Appl Clay Sci* 2010;47:271–5.

- [34] Temuujin Jadambaa, Minjigmaa Amgalan, Rickard William, Lee Melissa, Williams Iestyn, Arie van Riessen. Preparation of metakaolin based geopolymer coatings on metal substrates as thermal barriers. *Appl Clay Sci* 2009;46:265–70.
- [35] Aquino W, Lange DA, Olek J. The influence of metakaolin and silica fume on the chemistry of alkali–silica reaction products. *Cem Concr Compos* 2001;23(6):485–93.
- [36] Mostowicz R, Berak JM. Factors influencing the crystal morphology of ZSM-5 type zeolites. In: Drzaj B et al., editors. *Zeolites*. Amsterdam: Elsevier; 1985. p. 65–72.
- [37] Yao Xiao, Zhang Zuhua, Zhu Huajun, Chen Yue. Geopolymerization process of alkali-metakaolinite characterized by isothermal calorimetry. *Thermochim Acta* 2009;493:49–54.
- [38] Zuhua Z, Xiao Y, Huajun Z, Yue C. Role of water in the synthesis of calcined kaolin-based geopolymer. *Appl Clay Sci* 2009;43:218–23.
- [39] Zhang Zuhua, Yao Xiao, Zhu Huajun. Potential application of geopolymers as protection coatings for marine concrete. I. Basic properties. *Appl Clay Sci* 2010;49:1–6.
- [40] Kong Daniel LY, Sanjayan Jay G, Kwesi Sagoe-Crentsil. Comparative performance of geopolymers made with metakaolin and fly ash after exposure to elevated temperatures. *Cem Concr Res* 2007;37:1583–9.
- [41] Liew YM, Mustafa Al Bakri AM, Bnhussain M, Luqman M, Khairul Nizar I, Ruzaidi CM, et al. Optimization of solids-to-liquid and alkali activator ratios of calcined kaolin geopolymeric powder. *Constr Build Mater* 2012;37:440–51.
- [42] Lin Kae-Long, Shiu Hau-Shing, Shie Je-Lueng, Cheng Ta-Wui, Hwang Chao- Lung. Effect of composition on characteristics of thin film transistor liquid crystal display (TFT-LCD) waste glass-metakaolin-based geopolymers. *Constr Build Mater* 2012;36:501–7.
- [43] Živica Vladimir, Balkovic Svetozar, Drabik Milan. Properties of metakaolin geopolymer hardened paste prepared by high-pressure compaction. *Constr Build Mater* 2011;25:2206–13.
- [44] Ramlochan T, Thomas M, Gruber KA. The effect of metakaolin on alkali–silica reaction in concrete. *Cem Concr Res* 2000;30(3):339–44.
- [45] Perera DS, Uchida O, Vance ER, Finnie KS. Influence of curing schedule on the integrity of geopolymers. *J Mater Sci* 2007;42:3099–106.
- [46] Rovnanik Pavel. Effect of curing temperature on the development of hard structure of metakaolin-based geopolymer. *Constr Build Mater* 2010;24:1176–83.
- [47] Davidovits J. Properties of geopolymer cements. In: Krivenko, editor. 1st International conference on alkaline cements and concretes, Kiev, Ukraine, vol. 1; 1994. p. 131–49.

- [48] Palomo A, Blanco-Varela MT, Granizo ML, Puertas F, Vazquez T, Grutzeck MW. Chemical stability of cementitious materials based on metakaolin. *Cem Concr Res* 1999;29:997–1004.
- [49] Kuenzel C, Grover LM, Vandeperre L, Boccaccini AR, Cheeseman CR. Production of nepheline/quartz ceramics from geopolymer mortars. *J Eur Ceram Soc* 2013;33:251–8.
- [50] Kong Daniel LY, Danjayan Jay G, Kwesi Sagoe-Crentsil. Comparative performance of geopolymers made with metakaolin and fly ash after exposure to elevated temperatures. *Cem Concr Res* 2007;37:1583–9.
- [51] Davidovits J. Synthetic mineral polymer compound of the silicoaluminates family and preparation process. US Patent 4472199; 1984.
- [52] Davidovits J, Davidovits M, Davidovits N. Process for obtaining a geopolymeric aluminosilicate and products thus obtained. US Patent 5342595; 1994.
- [53] Barbosa Valeria FF, MacKenzie KJD. Thermal behavior of inorganic reopolymers and composites derived from sodium polysialate. *Mater Res Bull* 2003;38:319–31.
- [54] Barbosa VFF, MacKenzie KJD. Synthesis and thermal behavior of potassium sialate geopolymers. *Mater Lett* 2003;57:1477–82.
- [55] Kong Daniel LY, Sanjayan Jay G, Kwesi Sagoe-Crentsil. Factors affecting the performance of metakaolin geopolymers exposed to elevated temperatures. *J Mater Sci* 2008;45:824–31.
- [56] Lin TS, Jia DC, He PG, Wang MR. Thermo-mechanical and microstructural characterization of geopolymers with α -Al₂O₃ particle filler. *Int J Thermophys* 2009;30:1568–77.
- [57] Bernal Susan A, Rodriguez Erich D, de Gutierrez Ruby Mejia, Gordillo Marisol, Provis John L. Mechanical and thermal characterisation of geopolymers based on silicate-activated metakaolin/slag blends. *J Mater Sci* 2011. doi:10.1007/s10853-011-5490-z.
- [58] Cheng TW, Chiu JP. Fire-resistant geopolymer produced by granulated blast furnace slag. *Minerals Eng* 2003;16:205–10.
- [59] He Peigang, Jia Dechang, Lin Tiesong, Wang Meirong, Yu Zhou. Effects of high-temperature heat treatment on the mechanical properties of unidirectional carbon reinforced geopolymer composites. *Ceram Int* 2010;36:1447–53.
- [60] He Peigang, Jia Dechang, Wang Meirong, Yu Zhou. Improvement of hightemperature mechanical properties of heat treated Cf/geopolymer composites by Sol–SiO₂ impregnation. *J Eur Ceram Soc* 2010;30:3053–61.
- [61] Bernal Susan A, Julian Bejarano, Cristhian Garzon, de Gutierrez Ruby Mejia, Silvio Delvasto, Rodriguez Erich D. Performance of refractory aluminosilicate particle/fiber-reinforced geopolymer composites. *Composites Part B* 2012;43:1919–28.

- [62] Lin Tiesong, Jia Dechang, He Peigang, Wang Meirong, Liang Defu. Effects of fiber length on mechanical properties and fracture behavior of short carbon fiber reinforced geopolymer matrix composites. *Mater Sci Eng A* 2008;497:181–5.
- [63] Lin Tiesong, Jia Dechang, Wang Meirong, He Peigang, Liang Defu. Effects of fibre content on mechanical properties and fracture behavior of short carbon fibre reinforced geopolymer matrix. *Build Mater Sci* 2009;32(1):77–81.
- [64] Natali A, Manzi S, Bignozzi MC. Novel fiber-reinforced composite materials based on sustainable geopolymer matrix. *Procedia Eng* 2011;21:1124–31.
- [65] Li Zongjin, Yunsheng Zhang, Zhou Xiangming. Short fiber reinforced geopolymer composites manufactured by extrusion. *J Mater Civil Eng, ASCE* 2005:624–31.
- [66] Yunsheng Zhang, Wei Sun, Zongjin Li. Impact behavior and microstructural characteristics of PVA fibers reinforced fly ash-geopolymer boards prepared by extrusion technique. *J Mater Sci* 2006;41:2787–94.
- [67] Zhang Zu-hua, Yao Xiao, Zhu Hua-jun, Hua Su-dong, Chen Yue. Preparation and mechanical properties of polypropylene fiber reinforced calcined kaolin fly ash based geopolymer. *J Cent South Univ Technol* 2009;16:0049–52.
- [68] Yunsheng Zhang, Wei Sun, Li Zongjin, Zhou Xiangming. Impact properties of geopolymer based extrudates incorporated with fly ash and PVA short fiber. *Constr Build Mater* 2008;22:370–83.
- [69] Bankowski P, Zou L, Hodges R. Reduction of metal leaching in brown coal fly ash using geopolymers. *J Hazard Mater* 2004;B114:59–67.
- [70] Phair JW, van Deventer JSJ, Smith JD. Effect of Al source and alkali activation on Pb and Cu immobilization in fly-ash based “geopolymers”. *Appl Geochem* 2004;19:423–34.
- [71] Xu JZ, Zhou YL, Chang Q, Qu HQ. Study on the factors of affecting the immobilization of heavy metals in fly ash-based geopolymers. *Mater Lett* 2006;60:820–2.
- [72] Yunsheng Zhang, Wei Sun, Wei She, Guowei Sun. Synthesis and heavy metal immobilization behaviors of fly ash based geopolymer. *J Wuhan Univ Technol – Mater Sci Ed* 2009;24(5):819–25.
- [73] Arellano Aguilar R, Burciaga Di9az O, Escalante Garc9a JI. Lightweight concretes of activated metakaolin-fly ash binders, with blast furnace slag aggregates. *Constr Build Mater* 2010;24:1166–75.
- [74] Buchwald A, Hilbig H, Kaps Ch. Alkali-activated metakaolin-slag blends performance and structure in dependence of their composition. *J Mater Sci* 2007;42:3024–32.

- [75] Buchwald Anja, Tatarin R, Stephan D. Reaction progress of alkaline-activated metakaolin-ground granulated blast furnace slag blends. *J Mater Sci* 2009;44:5609–17.
- [76] Shen X, Yan S, Wu X, Tang M, Yang L. Immobilization of simulated high level wastes into AASC waste form. *Cem Concr Res* 1994;24(1):133–8.
- [77] Yip Christina K, Provis John L, Lukey Grant C, van Deventer Jannie SJ. Carbonate mineral addition to metakaolin-based geopolymers. *Cem Concr Compos* 2008;30:979–85.
- [78] Burciaga-Diaz Oswaldo, Escalante-Garcia Jose Ivan, Arellano-Aguilar Rafael, Gorokhovskiy Alexander. Statistical analysis of strength development as a function of various parameters on activated metakaolin/slag cements. *J Am Ceram Soc* 2010;93(2):541–7.
- [79] Yunsheng Z, Wei S, Qianli C, Lin C. Synthesis and heavy metal immobilization behaviors of slag based geopolymers. *J Hazard Mater* 2007;143(1–2):206–13.
- [80] Chen Song, Wu Mengqiang, Zhang Shuren. Mineral phases and properties of alkali-activated metakaolin-slag hydroceramics for a disposal of simulated highly-alkaline wastes. *J Nucl Mater* 2010;402:173–8.
- [81] Bernal Susan A, Provis John L, Rose Volker, de Gutierrez Ruby Mejia. Evolution of binder structure in sodium silicate-activated slag-metakaolin blends. *Cem Concr Compos* 2011;33:46–54.
- [82] Bernal Susan A, de Gutierrez Ruby Mejia, Provis John L. Engineering and durability properties of concretes based on alkali-activated granulated blast furnace slag/metakaolin blends. *Constr Build Mater* 2012;33:99–108.
- [83] Wang Jin, Wu Xiu-ling, Wang Jun-xia, Liu Chang-zhen, Lai Yuan-ming, Hong zun-ke. Hydrothermal synthesis and characterization of alkali-activated slagfly ash-metakaolin cementitious materials. *Micropor Mesopor Mater* 2012;155:186–91.
- [84] Yip CK, Lukey GC, Deventer SJs. The coexistence of geopolymeric gel and calcium silicate hydrate gel at the early stage of alkaline activation. *Cem Concr Res* 2005;35(9):1688–97.
- [85] Buchwald A, Dombrowski K, Weil M. The influence of calcium content on the performance of geopolymeric binder especially the resistance against acids. In: Davidovits J, editor. *Proceedings of the world congress geopolymer*, Saint Quentin, France, 28 June–1 July, 2005. p. 35–9.
- [86] Pacheco-Torgal F, Moura D, Yining Ding, Said Jalali. Composition, strength and workability of alkali-activated metakaolin based mortars. *Constr Build Mater* 2011;25:3732–45.
- [87] Yip CK, Deventer SJS. Microanalysis of calcium silicate hydrate gel formed within a geopolymeric binder. *J Mater Sci* 2003;38:3851–60.

- [88] Zhang Yao Jun, Wang Ya Chao, Xu De Long, Li Sheng. Mechanical performance and hydration mechanism of geopolymer composite reinforced by resin. *Mater Sci Eng A* 2010;527:6574–80.
- [89] Komnitsas Kostas, Zaharaki Dimitra, Perdikatsis Vasillios. Effect of synthesis parameters on the compressive strength of low-calcium ferronickel slag inorganic polymers. *J Hazard Mater* 2009;161:760–8.
- [90] Bignozzi MC, Barbieri L, Lancellotti I. New geopolymers based on electric arc furnace slag. *Adv Sci Technol* 2010;69:117–22.
- [91] Bignozzi Maria Chiara, Manzi Stefania, Lancellotti Isabella, Kamseu Elie, Barbieri Luisa, Leonelli Cristina. Mix-design and characterization of alkali activated materials based on metakaolin and ladle slag. *Appl Clay Sci*, in press, corrected proof.
- [92] Bernal Susan A, Rodriguez Erich D, de Gutierrez Ruby Mejia, Provis John L, Delvasto Silvio. Activation of metakaolin/slag blended alkaline solutions based on chemically modified silica fume and rice husk ash. *Waste Biomass Valor* 2011. doi:10.1007/s12649-011-9093-3.
- [93] Yunsheng Zhang, Wei Sun, Li Zongjin. Preparation and microstructure of KPSDS geopolymeric binder. *Colloids Surf A: Physicochem Eng Aspects* 2007;302:473–82.
- [94] Kouamo Tchakoute H, Elimbi A, Ngally Sabouang, Njopwouo D. The effect of adding alumina-oxide to metakaolin and volcanic ash on geopolymer products: a comparative study. *Constr Build Mater* 2012;35:960–9.
- [95] Rajamma Rejini, Labrincha Joao A, Ferreira Victor M. Alkali activation of biomass fly ash-metakaolin blends. *Fuel* 2012;98:265–71.
- [96] Lampris C, Lupo R, Cheeseman CR. Geopolymerisation of silt generated from construction and demolition waste washing plants. *Waste Manage* 2009;29:368–73.
- [97] Chen Ji-Hsien, Huang Jong-Shin, Chang Yi-Wen. Use of reservoir sludge as a partial replacement of metakaolin in the production of geopolymers. *Cem Concr Compos* 2011;33:602–10.
- [98] Wang Hongling, Li Haihong, Yan Fengyuan. Reduction in wear of metakaolinite-based geopolymer composite through filling of PTFE. *Wear* 2005;258:1562–6.
- [99] Wang Hongling, Li Haihong, Yan Fengyuan. Synthesis and tribological behavior of metakaolinite-based geopolymer composites. *Mater Lett* 2005;59:3976–81.
- [100] Xiangke Jiao, Yimin Zhang, Tiejun Chen, Shenxu Bao, Tao Liu, Jing Huang. Geopolymerisation of a silica-rich tailing. *Minerals Eng* 2011;24:1710–2.

- [101] Kouamo Techakoute H, Mbey JA, Elimbi A, Dikko Kenne, Njopwouo D. Synthesis of volcanic ash-based geopolymer mortars by fusion method: effect of adding metakaolin to fused volcanic ash. *Ceram Int* 2013;39:1613–21.
- [102] Kani Ebrahim Najafi, Ali Allahverdi, Provis John L. Efflorescence control in geopolymer binder based on natural pozzolan. *Cem Concr Compos* 2012;34:25–33.
- [103] P. Duxson, S.W. Mallicoat, G.C. Lukey, W.M. Kriven, J.S.J. van Deventer, *Colloids and Surfaces A: Physicochemical and Engineering Aspects*, 2007, 292, 8–20.
- [104] Carneiro FLLB. A new method to determine the tensile strength of concrete. In: Paper presented at the Proceedings of the 5th meeting of the Brazilian Association for Technical Rules, 3d. section 1943.
- [105] Akazawa T. New test method for evaluating internal stress due to compression of concrete: the splitting tension test. *J Japan Soc Civil Eng* 1943; 29:777–787.
- [106] ASTM C496. Standard test method for splitting tensile strength of cylindrical concrete specimens. In *Annual Book of ASTM, Standards*, vol. 0.042. Philadelphia: ASTM 1984; p. 336–41.
- [107] Fairhurst C. On the validity of the ‘Brazilian’ test for brittle materials. *Int J Rock Mech Min Sci Geomech Abstr* 1964; 1(4): 535–546.
- [108] Hooper JA. The failure of glass cylinders in diametral compression. *J Mech Phys Solids* 1971; 19(4):179–200.
- [109] Hudson JA, Brown ET, Rummel F. The controlled failure of rock discs and rings loaded in diametral compression. *Int J Rock Mech Min Sci Geomech Abstr* 1972; 9(2): 241–248.
- [110] Swab JJ, Yu J, Gamble R, Kilczewski S. Analysis of the diametral compression method for determining the tensile strength of transparent magnesium aluminate spinel. *Int J Fract.* 2011; 172:187-192.
- [111] Diyuan Li, Louis Ngai Yuen Wong. The Brazilian Disc Test for Rock Mechanics Application: Review and New Insight. *Rock Mech Rock Eng* 2016; 46: 269-287.
- [112] Wang QZ, Jia XM, Kou SQ, Zhang ZX, Lindqvist PA. The flattened Brazilian disc specimen used for testing elastic modulus, tensile strength and fracture toughness of brittle rocks: analytical and numerical results. *Int J Rock Mech Min Sci* 2004; 41:245–253.
- [113] ISRM. Suggested methods for determining tensile strength of rock materials. *Int J Rock Mech Min Sci* 1978; 15(3):99-103.
- [114] Cardenas-Garcia JF. The Moiré circular disc: two inverse problems. *Mech Res Commun* 2001; 28 (4): 381-387.
- [115] Wang Z, Cardenas-Garcia JF, Han B. Inverse Method to Determine Elastic Constants Using a Circular Disk and Moiré Interferometry. *Exp. Mech.* 2004; 45(1): 27-34.

- [116] Liu C. Elastic Constants Determination and Deformation Observation Using Brazilian Disk Geometry. *Exp Mech* 2010; 50:1025–1039.
- [117] Hild F, Roux S. Digital Image Correlation: from Displacement Measurement to Identification of Elastic Properties – a Review. *Strain* 2006; 42: 69–80.
- [118] Timoshenko S, Goodier J. *Theory of elasticity*, 3rd edition, McGRAW-HILL BOOK COMPANY, INC, New York; 1970.
- [119] Markides ChF, Pazis DN, Kourkoulis SK. Closed full-field solutions for stresses and displacements in the Brazilian disk under distributed radial load. *Int J Rock Mech Min Sci* 2010; 47, pp 227-237.
- [120] Kourkoulis SK, Markides ChF, Chatzistergos PE. The Brazilian disc under parabolically varying load: Theoretical and experimental study of the displacement field. *Int J Solids Struct* 2012; (49): 959-972.
- [121] Muskhelishvili HN. *Some basic problems in mathematic elastic mechanics* (Translated by Zhao Huiyuan). Beijing: Science Press; 1958.
- [122] Yong Yu, Jianmin Yin, Zouwu Zhong. Shape effect in the Brazilian tensile strength test and a 3D FEM correction. *Int J Rock Mech Min Sci* 2006; 43: 623-627.
- [123] ASTM C 1161-02c, Standard Test Method for flexural Strength of Advanced Ceramics at Ambient Temperature, 2003.
- [124] Ajovalasit A. *Analisi Sperimentale delle tensioni con gli estensimetri elettrici a resistenza*, Aracne Editrice S.r.l., Roma, Italy; 2006.
- [125] W.C. Oliver, G.M. Pharr, An improved technique for determining hardness and elastic modulus using load and displacement sensing indentation experiments, *J. Mater. Res.* 7 (1992) 1564-1583.
- [126] W.C. Oliver, G.M. Pharr, Measurement of hardness and elastic modulus by instrumented indentation: Advances in understanding and refinements to methodology, *J. Mater. Res.* 19 (2004) 3-20.
- [127] W. Weibull, A statistical distribution function of wide applicability, *J. Appl. Mech.* 18 (1951) 293-297.
- [128] M. Allen, *Phys. Rev.* 42, 848 (1932).
- [129] HAN Baoguo, QIAO Guofu, JIANG Haifeng, Piezoresistive Response Extraction for Smart Cement-based Composites/Sensors, *Journal of Wuhan University of Technology-Mater. Sci. Ed.*, 2012, Vol.27, No.4.
- [130] Sihai Wen and D. D. L. Chung, Piezoresistivity-Based Strain Sensing in Carbon Fiber-Reinforced Cement, *ACI Materials Journal/March-April* 2007, 171-179.

- [131] L. Coppola, A. Buoso, F. Corazza, The influence of electrode type/set-up and frequency in AC measurements of electrical resistance and piezoresistivity of CNTs reinforced cementitious composites, IX INSTM Conference, 2013.
- [132] Uchino, *Advanced Piezoelectric Materials*, (Woodhead Publishing, 2010).
- [133] P. Dineva et al., *Dynamic Fracture of Piezoelectric Materials*, 7, *Solid Mechanics and Its Applications* 212, Springer International Publishing Switzerland 2014.
- [134] H. Kawai: *Jpn J. Appl. Phys* 8, 975 (1969).
- [135] M. G. Cain, *Characterisation of Ferroelectric Bulk Materials and Thin Films*, Springer Series in Measurement Science and Technology 2, 2014, pages 37-64.
- [136] European standard, EN 50324-2: 2002, Piezoelectric properties of ceramic materials and components, Part 2: Methods of measurement – Low power, CENELEC European Committee for Electrotechnical Standardization, 2002.
- [137] T. L. Jordan, Z. Ounaies, *Piezoelectric Ceramic Characterization*, NASA/CR-2001-211225, ICASE Report No. 2001-28.
- [138] Jaffe, B., Cook, W.R., Jaffe, H.L.: *Piezoelectric ceramics*, ser. In: *Non-metallic Solids*. Academic, Press, New York (1971)
- [139] O. Galao, F.J. Baeza, E. Zornoza, P. Garcés, Strain and damage sensing properties on multifunctional cement composites with CNF admixture, *Cement & Concrete Composites* 46 (2014) 90–98.
- [140] D. D. L. Chung, *Piezoresistive Cement-based Materials for Strain Sensing*, *Journal of Intelligent Material Systems and Structures*, Vol. 00—December 2002, DOI: 10.1106/104538902031861.
- [141] B. Han, J. Ou, Embedded piezoresistive cement-based stress/strain sensor, *Sensors and Actuators A* 138 (2007) 294–298.
- [142] H.K. Kim, I.S. Park, H.K. Lee, Improved piezoresistive sensitivity and stability of CNT/cement mortar composites with low water–binder ratio, *Composite Structures* 116 (2014) 713–719.
- [143] Zhang L, Wang Y, Wei Y, Xu W, Fang D, Zhai L, Lin K, An L (2008) A silicon carbonitride ceramic with anomalously high piezoresistivity. *J Am Ceram Soc* 91:1346–1349. doi:10.1111/j.1551-2916.2008.02275.x
- [144] Terauds K, Sanchez-Jimenez PE, Raj R, Vakifahmetoglu C, Colombo P (2010) Giant piezoresistivity of polymer-derived ceramics at high temperatures. *J Eur Ceram Soc* 30:2203–2207. doi:10.1016/j.jeurceramsoc.2010.02.024

- [145] Wang Y, Zhang L, Fan Y, Jiang D, An L (2009) Stress dependent piezoresistivity in tunneling-percolation systems. *J Mater Sci* 44(11):2814–2819. doi:10.1007/s10853-009-3371-5
- [146] Riedel R, Toma L, Janssen E, Nuffer J, Melz T, Hanselka H (2010) Piezoresistive effect in SiOC ceramics for integrated pressure sensors. *J Am Ceram Soc* 93:920–924. doi:10.1111/j.1551-2916.2009.03496.x
- [147] P. Duxson, A. Fernández Jiménez, J. L. Provis, G. C. Lukey, A. Palomo, J. S. J. van Deventer, *Geopolymer technology: the current state of the art*, *J. Mat Science*, 2007, 42, 2917–2933.
- [148] J.E. Kogel, N.C. Trivedi, J. M. Barker, S.T.Krukowski, *Industrial Minerals & Rocks: Commodities, Markets, and Uses*, 7th EDITION, Society for mining, metallurgy and Exploration Inc. (SME), 2006, pag. 1193-1203, ISBN-13 978-0-87335-233-8.
- [149] O. Bortnovsky, J. Dedeček, Z. Tvarůžková, Z. Sobalík, J. Šubrt, Metal ions as probes for characterization of geopolymer materials, *J. Am. Ceram. Soc.*, 2008, 91 3052–3057.
- [150] W.M. Kriven, J.L. Bell, M. Gordon, Microstructure and microchemistry of fully reacted geopolymer and geopolymer composites, *Ceramic Transactions* 2003, 153, 227-250.
- [151] P. Sazamaa, O. Bortnovsky, J. Dedecek, Z. Tvaruzková, Z. Sobalík, Geopolymer based catalysts—New group of catalytic materials, *Catalysis Today*, 2011, 164, 92–99.
- [152] P. Duxson, John L. Provis, Grant C. Lukey, Frances Separovic, Jannie S. J. van Deventer, ²⁹Si NMR Study of Structural Ordering in Aluminosilicate Geopolymer Gels *Langmuir* 2005, 21, 3028-3036.
- [153] P. Duxson, G. C. Lukey, F. Separovic, J. S. J. van Deventer, Effect of Alkali Cations on Aluminum Incorporation in Geopolymeric Gels *Ind. Eng. Chem. Res.* 2005, 44, 832-839.
- [154] D. W. Breck, *Zeolite Molecular Sieves*, Krieger, Malabar, 1984.
- [155] A. R. Ruiz-Salvador, D. W. Lewis, J. Rubayo-Soneira, G. Rodriguez-Fuentes, L. R. Sierra, C. R. A. Catlow, Aluminum distribution in low Si/Al zeolites: Dehydrated Na-clinoptilolite *J. Phys. Chem. B* 1998, 102 (43), 8417–8425.
- [156] D.Seoung, Y.Lee, C.-C. Kao, T. Vogt, Y. Lee, Super-hydrated zeolites: pressure-induced hydration in natrolites, *Chem. Eur. J.* 2013, 19, 10876 – 10883
- [157] Mingqing Sun, Zhuoqiu Li, Xianhui Song, Piezoelectric effect of hardened cement paste, *Cement and Concrete Composites*, 2004, 26 (6), 717–720
- [158] Y. Elakneswaran, T. Nawa, K. Kurumisawa, Electrokinetic potential of hydrated cement in relation to adsorption of chlorides, *Cement and Concrete Research*, 2009, 39 340–344.
- [159] Y. Lee, J. A. Hriljac, T. Vogt, J. B. Parise, G. Artioli, First Structural Investigation of a Super-Hydrated Zeolite *J. Am. Chem. Soc.* 2001, 123, 12732–12733.

- [160] Y. Lee, T. Vogt, J. A. Hriljac, J. B. Parise, J. C. Hanson, S. J. Kim, Non-framework cation migration and irreversible pressure-induced hydration in a zeolite *Nature* 2002, 420, 485–489.
- [161] Toledo, P. G., H. T. Davis, and L. E. Scriven, Transport properties of anisotropic porous media: Effective medium theory, *Chem. Eng. Sci.* 1992, 47, 391–405.
- [162] S.P. Friedman, S. B. Jones, Measurement and approximate critical path analysis of the pore-scale-induced anisotropy factor of an unsaturated porous medium, *Water Resources Research* 2001, 37-12, 2929–2942.
- [163] L.R. Van Loon, J. Soier, W. Muller, M.H. Bradbury, Anisotropic diffusion in layered argillaceous rocks: a case study with opalinus clay, PSI- Scientific Report 2002 / Volume IV Nuclear Energy and Safety, 97-104, ISSN 1423-7334.
- [164] M. Cieszko, Description of anisotropic pore space structure of permeable materials based on Minkowski metric space, *Arch. Mech.*, 61, 6, pp. 425–444, Warszawa 2009
- [165] F.-J. Ulm, G. Constantinides and F. H. Heukamp, Is concrete a poromechanics materials?—A multiscale investigation of poroelastic properties, *Materials and Structures / Concrete Science and Engineering* 2004, 37, 43-58.
- [166] T. Rougelot F. Skoczylas, N.Burlion, Water desorption and shrinkage in mortars and cement pastes: Experimental study and poromechanical model, *Cement and Concrete Research* 2009, 39, 36–44.
- [167] F. Skoczylas, N.Burlion, I. Yurtdas, About drying effects and pro-mechanical behaviour of mortars, *Cement and Concrete composite* 2007, 29, 383-390.
- [168] J. H.m. Visser, Extensile Hydraulic fracturing of (saturated) porous materials ISBN 90- 407-1699-4/CIP
- [169] J.M. Torrenti, G. Pijaudier-Cabot, J. M. Reynouard Behavior of Concrete, ISBN 978-1-84821-178-0
- [170] Dragan Damjanovic, The Science of Hysteresis, Volume 3; I. Mayergoyz and G.Bertotti (Eds.); Elsevier (2005), Chap. 4 “Hysteresis in Piezoelectric and Ferroelectric Materials”.

Chapter 3

Geopolymers nanocomposites

In the previous chapter of the present dissertation metakaolin-based geopolymer mortars were proposed as advanced materials due to the discovery of excellent electro-mechanical properties such as piezoresistivity and piezoelectricity. The addition of a filler characterized by good mechanical and electrical properties can significantly improve the performances of geopolymers and increase the application fields of such materials. Attractive and innovative applications, such as the self-monitoring of civil infrastructures or the design of piezoelectric devices for energy harvesting purposes, can be developed. Graphene, single-atom thick sheet of sp² hybridized carbon atoms, is the thinnest, stiffest, and strongest material known to date. Known also as “wonder material”, graphene has excellent electrical properties and it is also a perfect filler for the production of nanocomposites due to its high surface/volume ratio. After a brief review of literature studies focused on geopolymer composites and graphene nanocomposites, the production and characterization of metakaolin-based geopolymer/graphene nanocomposites will be proposed in this chapter. In particular, results of the mechanical and electro-mechanical characterization will be described.

With the same goal of improving the mechanical and electro-mechanical response of geopolymers, topological insulators will be proposed as alternative nanofillers in the second part of this chapter. Such materials, also called “graphene like materials”, show a high electron mobility, comparable to that of graphene, and moreover, their surface charge carriers are also spin-polarized. Furthermore, topological insulators are characterized by reliable, large-scale, and low-cost production.

Whereas the mechanical properties of graphene are well known, an experimental mechanical characterization of some topological insulators was never carried out and only theoretical studies can be found in literature. The mechanical characterization of three topological insulators, i. e.

Bi_2Te_3 , Bi_2Se_3 , and SnSe , will be proposed in this chapter. In particular, nanoindentation was used for the characterization and the experimental results were compared with the computational ones, obtained by means of Density Functionl Theory (DFT). Suitable theoretical models were adopted for the experimental-computational comparison. The obtained results are an important starting point for future developments focused on the production and characterization of geopolymers/topological insulators composites.

3.1 Reinforced geopolymer composites: a review

Since the development of geopolymers in 1978, the interest in finding attractive fillers able to improve the chemical and mechanical performances of such materials is increasingly growing. Geopolymers composites can be divided into two different groups: geopolymer-fiber composites and fiber-reinforced geopolymer composites. In the first case the geopolymer binder is a matrix added into a sheet of fibers (or fabric, mat, felt, and unidirectional fiber tape) by means of an impregnation process. In the second category instead, the fibers (short or long) are added to a geopolymer cement or slurry.

Geopolymer-fiber composites are a really valuable solution for applications which require high heat and fire resistance. They in fact can be easily produced at low temperatures (geopolymerization occurs at ambient temperature), are able to counteract very high temperatures (geopolymers can be considered ceramic materials) and show also a suitable mechanical strength (thanks to the presence of fibers). Such properties are impossible to find in most of the organic matrix composites. The first geopolymer-fiber composite was developed in 1997 for the production of fire resistant panels for aircraft cabin interiors and the project was founded by the American Federal Aviation Administration (FAA). In particular, a geopolymer/carbon fiber composite was produced and it was shown that at irradiance levels of 50 kW/m^2 (typical of the heat flux in a well developed fire), such material does not ignite, burn, or release any smoke even after long heat flux exposure, contrary to

the polymeric materials usually used (such as glass- or carbon-reinforced polyester, vinylester, epoxy, bismaleimide, cyanate ester, polyimide, phenolic, and engineering thermoplastic laminates) [1].

However, traditional carbon composites are relatively expensive. E-glass fabrics are approximately one order of magnitude less expensive than similar carbon fabrics and can then represent a valuable alternative. Hammell et al. [2, 3] proposed an interesting solution consisting in a geopolymer-fiber composite characterized by carbon layers alternated with E-glass fabrics. They observed that E-glass bond well with the matrix and provide a good interlaminar plate between carbon layers. Moreover, the addition of E-glass layers increases the deflection at failure of the plate and consequently increases the energy absorption before failure.

Geopolymer was also used in substitution to organic polymers in Portland cement concrete/carbon fiber composites in order to fast the carbon fabrics to concrete and the geopolymer matrix provided better adhesion in comparison with organic polymers [4].

The well known racing cars manufacturer McLaren in 2013 proposed a combination of poly(sialate-multisiloxo) geopolymer matrix and SiC fibers. Such composite provided exceptional heat resistance results at temperature up to 1000°C [5].

Carbon fibers are widely used for geopolymer-fiber composites. However, such fibers are too expensive for low-tech and low-cost applications and are more suitable for high-tech applications, such as aeronautical, automobile and aerospace. Basalt fibers were proposed by several researchers as a valuable and low cost solution [6,7].

Concerning fiber-reinforced geopolymers composites, various type of fibers were proposed as reinforcements for geopolymers in the last decades. Geopolymers possess relatively good mechanical properties and thermal stability, but they usually exhibit a brittle behavior. The addition of fibers can then overcome this limitation, by improving the material strength and toughness. The fiber contents proposed by literature works varies largely, from 0.5 wt.% for short fibers to 20% for

mat or felt, and the application fields cover high-tech/high cost heat resistant technologies down to low-tech /low-cost eco-concrete.

Lin et al [8] showed that the maximum flexural strength of geopolymers of the type poly(sialate-siloxo) increases from 16.8 to 91.3 MPa by adding sheet-like carbon fiber preform, made of short carbon fibers, whereas Yan et al [9] obtained a flexural strength 5.6 times higher than that of the neat geopolymer by adding 2.0 vol% of short SiC fibers with a length of 5mm.

Several papers were dedicated to steel fiber reinforcement of geopolymer cements / concretes [10, 11], but the majority of them do not bring new knowledge since they reported same results and improvements observed for steel fiber Portland cement concrete composites.

Synthetic organic fibers such as poly(vinyl-alcohol) PVA [12], poly(acetal) POM [13] and poly(lactic-acid) PLA [14] provided also good improvements to the ductility and mechanical strength of geopolymers.

Thanks to their high hydrophilicity, bio-fibers are also excellent candidates for geopolymers reinforcement. Alomayri and Low [15] measured significant increments of the compressive strength (from 19.1 to 46.0 MPa) and impact strength (from 1.9 to 4.5 kJ/m²) of fly ash-based geopolymer cement after the addition of 0.5% wt of cotton fibers whereas a flexural strength increment from 8.2 MPa to 31.7 MPa was observed with the addition of 8.3 wt% woven cotton fibers [16]. Alzeer and MacKenzie [17] proposed the use of wool to produce environment-friendly and low-cost composites with improved flexural strength for engineering and construction applications. The same authors proposed also the addition of natural cellulose-based fibers to a poly(sialate-siloxo) geopolymer [18]. Assaedi et al. [19] proposed the fabrication of eco nano-composites using nano-clay and flax fiber as reinforcement of fly ash based geopolymers.

Few studies were finally focused on the production of geopolymers reinforced with graphene nano-sheets. This topic is widely discussed in the next section.

3.2 Geopolymers/graphene nanocomposites

3.2.1 Graphene: properties and applications

Since its rise to prominence in 2004, graphene has attracted the worldwide scientific community, including academia, industry, and government. The great impact of graphene in such a short period of time was probably never experienced by any other known material. Figure 3.1 shows the exponential increase of the number of research papers published on graphene between 2004 and 2013.

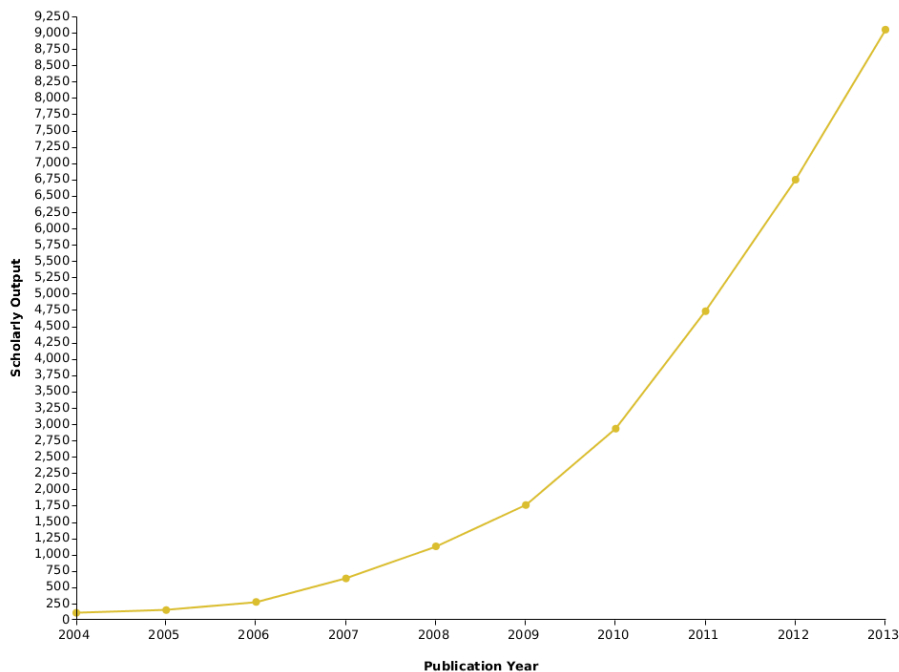


Figure 3.1: Scholarly output (articles only) published in the period 2004-13 from a search for “graphene” in the titles, abstracts or keywords [20].

Graphene is considered the thinnest, stiffest, and strongest material known to date and it is also characterized by excellent thermal and electrical conductivity. Furthermore, it is extremely inert and resistant to oxidation and it can be also an ideal impermeable membrane. The blend of excellent mechanical, electrical, thermal, optical and wetting properties is related to the unique two-dimensional lattice of graphene, characterized by single-carbon-atom-thick hexagonal honeycomb.

Carbon is characterized by an electronic structure which allows him to create different structure, with different configurations and properties. When all the four bonds are equally shared to four neighboring atoms, the four valence electrons of the carbon atom are sp^3 hybridized and the 3D cubic structure of diamond forms. Thanks to its 3D network of carbon-carbon (C-C) bonds, diamond is the hardest material known and it is electrically insulating and thermally conductive at the same time. Graphite instead, is the sp^2 hybridized form of carbon and it contains only three bonds per carbon atom and the fourth valence electron is free to float. The resultant structure is characterized by 2D layers with a hexagonal structure of covalent C-C bonds, bonded with weak Wan der Waals forces along the third direction. Whereas the strong covalent bonds of the 2D layers confer good in-plane mechanical properties, the weak Wan del Waals interactions between layers make graphite much softer than diamond. Similar to diamond, graphite is a good conductor of heat but, unlike diamond, it has also a good in-plane electrical conductivity due to the presence of free electrons. Diamond and graphite are the most known allotropes of carbon. However, various exotic forms of nanocarbon materials have been discovered in the last decades and such discoveries revolutionized carbon science. In 1980s Richard Smalley and Harold Kroto first discovered fullerenes [21]. The most common fullerene, C_{60} , can be obtained by model a single layer of graphite in order to obtain a soccer ball shape. Larger spherical or oblong structures can be produced by adding atoms to the basic structure of a fullerene. Following such concept, in 1991 Sumio Iijima discovered carbon nanotubes (CNT) [22]. A single walled carbon nanotube (SWCNT) can be considered as a single layer of graphite rolled up to form a tube and closed at the end by six pentagonal defects. Multi-walled carbon nanotubes (MWCNT) are instead a defined number of concentric SWCNT around a common axis. The single layer of graphite, i.e., the single-atom thick sheet of sp^2 hybridized carbon atoms packed in a hexagonal honeycomb crystalline structure, is called graphene [23-30]. With a thickness equal to ~ 0.14 nm, which is the atomic diameter of a

carbon atom, it is the thinnest material known to humankind. Because of the high energy of dangling bonds at the edges of the sheet, free-standing (i.e., non-supported) graphene sheets were considered thermodynamically unstable. However, in 2004, by Geim and Novoselov, 2010 Nobel Prize winners in Physics, isolated a single free-standing sheet of graphene for the first time [23]. They used the scotch tape technique to obtain graphene monolayers from the bulk graphite. In Figure 3.2 the allotropes of carbon describe above are shown.

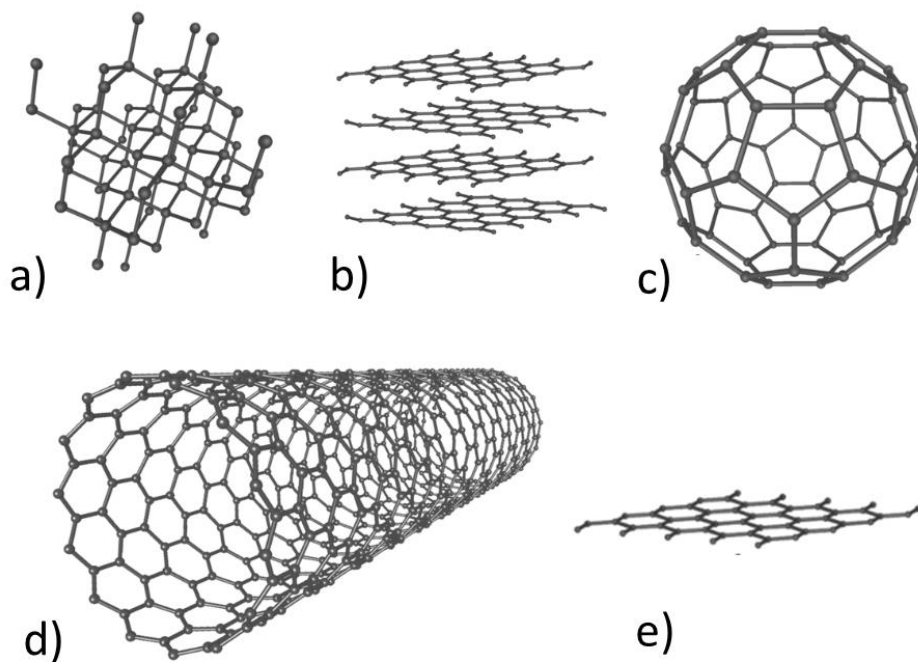


Figure 3.2: allotropes of carbon. a) diamond; b) graphite; c) C_{60} fullerene; d) carbon nanotube (CNT); e) graphene.

The unique atomic structure of graphene offers an extraordinary blend of mechanical, electrical, thermal, and optical properties which pave the way to a variety of possible applications.

Concerning mechanical properties, the elastic modulus of an individual graphene sheet is predicted to be $\sim 1\text{TPa}$ [31]. Such value was measured by means of atomic force microscopy (AFM)-based indentations performed on suspended graphene [32]. Considering the high elastic modulus, and the low density ($\sim 1\text{-}2\text{ g/cm}^3$) of graphene, such material is characterized by a high specific modulus (i.e.,

modulus normalized by density), higher than that of known structural materials such as aluminum, titanium, or steel. Also the fracture strength of ~ 125 GPa [32] is superior to that of the mostly used structural materials.

Concerning electrical properties, graphene shows a very interesting electronic band structure. It is in fact a semi-metal with zero electronic band gap, in which the local density of states at the Fermi level is zero. The conduction hence can be produced only by means of the thermal excitation of electrons [25]. An energy gap can be induced in graphene's band structure using several methods which aim to break the graphene's lattice symmetry. To name but a few, the symmetry can be broken by means of defect generation [33], water adsorption [34], applied bias [35-37], or interaction with gases [38].

Other unique properties of graphene are the exceptionally high in-plane thermal conductivity ($\sim 5,000$ W m⁻¹ K⁻¹), charge carrier mobility (200,000 cm² V⁻¹ s⁻¹) and specific surface area (2,630 m² g⁻¹) [39]. Figure 3.3 shows the mechanical, electrical and thermal properties of graphene compared to those of other well-known materials.

Graphene shows also fascinating phenomena such as the quantum Hall effect, ballistic electron transport, spin resolved quantum interference, and bipolar super-current. However, it is worth noting that such properties are related to the free-standing or suspended graphene and that they significantly degrade when the graphene is supported on a substrate.

The optical transparency is another key property of graphene, particularly important for optoelectronic applications [40-42]. The optical absorption of a single graphene layer is equal to 2.3% over the visible spectrum and such property, combined with its high electrical conductivity [43, 44], allows the production of transparent conductive electrodes [45-48]. Graphene transparent conductive electrodes can be a valuable substitutes of transparent indium tin oxide (ITO)-based electrodes by overcoming their limitations. Despite of ITO which is characterized by a brittle behavior, graphene shows an extreme flexibility and it can be used in flexible electronics. In

addition to optical transparency, graphene possesses also wetting transparency [49] and it has an extraordinary ability to passivate a surface. Graphene is an ideal impermeable membrane since not even a proton can pass through defect-free graphene [50].

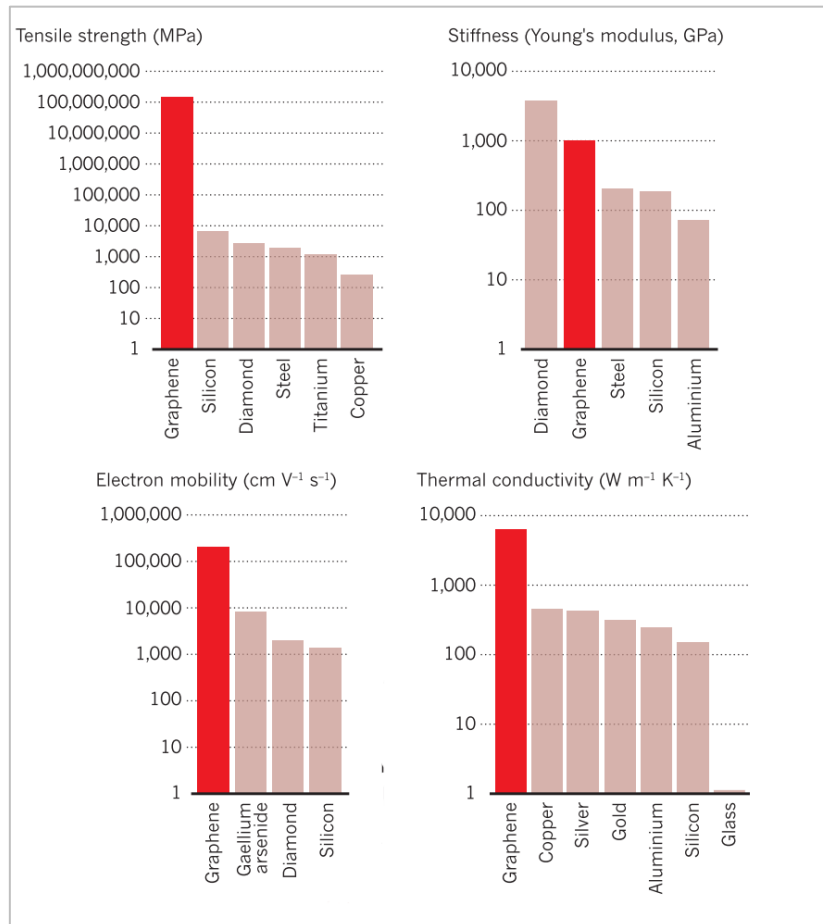


Figure 3.3: mechanical, electrical and thermal properties of graphene compared to those of other well-known materials.

One of the highly promising application of graphene is surely its use as nanofiller in composites materials. A long list of reasons why graphene is a perfect candidate for the improvement of the mechanical, electrical and thermal properties of the host matrix is reported below [51]:

- (1) Graphene has an extraordinary high theoretical surface area of $\sim 2,630 \text{ m}^2 \text{ g}^{-1}$ [39]. In fact both surfaces of a graphene sheet are in contact with the host matrix, contrary to CNTs in which only the outer surface contacts the matrix. The excellent adhesion with the matrix

allows to obtain high improvements with a low content of fillers if compared to other competing nanofillers.

- (2) The rough and wrinkled surface texture of graphene [39] fosters the mechanical interlocking with the matrix and a high load transfer.
- (3) Graphene platelets synthesized from graphite oxide possess high density of surface defects [52] which provide high energy sites for the absorption of polymer chains. Polymers have then a strong propensity to wet graphene sheets.
- (4) Graphene platelets synthesized from graphite oxide are characterized also by residual hydroxyl groups [53] which foster the interaction with the surrounding matrix.
- (5) Thanks to its 2D geometry, graphene carries load equally effectively in-plane and it does not need to be oriented along the loading direction like high aspect ratio fibers.
- (6) The high aspect ratio and the 2D geometry of graphene cause a crack deflection phenomenon, providing significant improvements in the fatigue and fracture behavior of the surrounding matrix.
- (7) The high aspect ratio, the 2D geometry, and the sp² structure allow to form an electrical percolation network at extremely low nanofillers content.
- (8) Thermal conductivity is also fostered by the sp² carbon 2D bonding network if compared to one-dimensional fiber reinforcement.
- (9) Graphene can form highly stable colloidal suspensions with a wide range of organic liquids which pave the way to interesting applications in the nanofluid-based composites field.
- (10) Unlike CNTs which do not exist in nature, graphene sheets are already present in nature and they can be mass produced at low cost by means of top-down methods like exfoliation of graphite oxide.

Figure 3.4 shows the chronological record of publications on graphene reinforced composites, classified according to the different matrix typology.

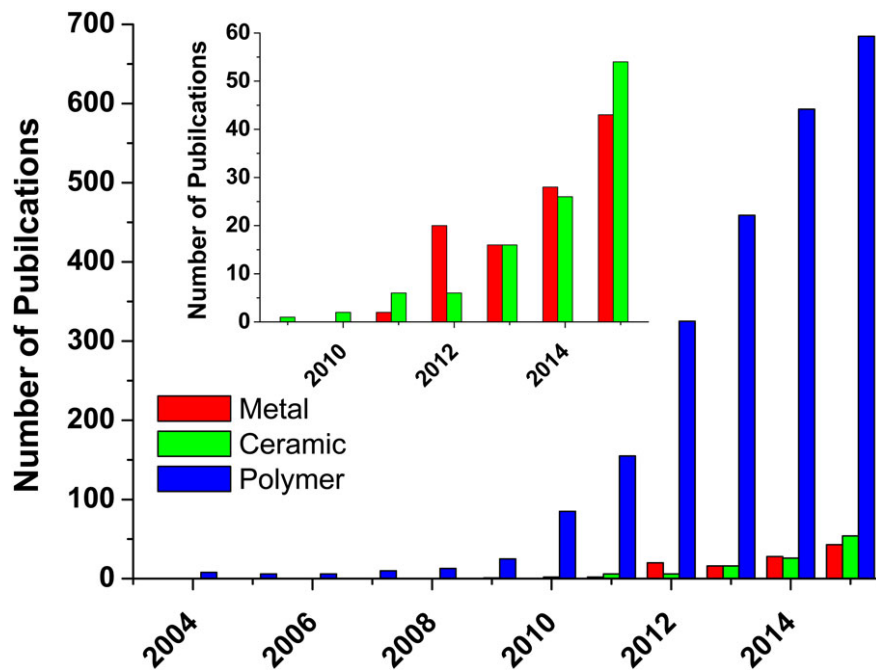


Figure 3.4: Chronological record of publications on graphene reinforced composites. The inset shows the comparative data on publications for only graphene reinforced metal and ceramic-based composites. [54].

It is worth noting that, as observed for CNT reinforced composites, the exploration of polymer matrix composites started before and is more rich than that of metal or ceramic-based composites. This is due to the simple fabrication of polymer-based composites which does not require high temperature or pressure by avoiding the degradation of the filler [55, 56]. A wide range of thermosetting and thermoplastic polymers was used for the production of graphene/polymers composites and different fabrication techniques were proposed [57]. Significant improvements of the electrical, thermal and mechanical properties of polymers were obtained by adding low percentages of graphene nanoplatelets. To name but a few, a 150% improvement of tensile strength and a nearly 10 times increase of Young's modulus were achieved by loading PVA with 1.8 vol% of graphene nanosheets [58], while a 627% increase of thermal conductivity was observed by adding 8%wt of graphene nanoplatelets to epoxy resin [59]. The homogenous dispersion of graphene at the nano scale is essential to significantly improve the polymer properties [60]. A good

and homogenous dispersion in fact, minimizes stress concentrations and foster a uniform load transfer into the matrix [61-63]. However, the achievement of a good graphene dispersion is still challenging because graphene sheets tends to easily bond to each others by means of van der Waals interactions and form macro clusters into the polymer matrix [64, 65, 66]. Graphene dispersion can be studied by means of optical micrographs. Figure 3.5 a) shows an optical micrograph (in the inset) converted into a binary image in order to analyze the average diameter of graphene platelets dispersed into epoxy resin.

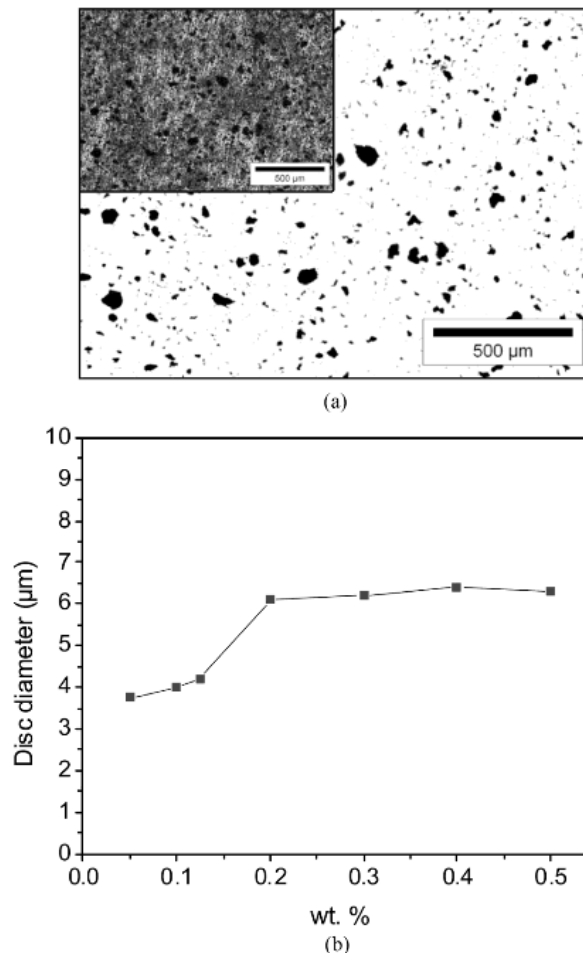


Figure 3.5: a) low magnification binary image of 0.1 %wt of graphene nanoplatelets in epoxy: the inset shows the original optical micrograph. b) graphene platelets diameter as a function of its increasing weight % in epoxy [51].

In Figure 3.5 b) it is worth noting that there is a sharp increase in the graphene sheet dimensions above a loading fraction of $\sim 0.125\%$ wt of graphene nanoplatelets (GNPs) which indicates a significant degradation in dispersion [51].

Concerning metal matrix/graphene composites, it was observed that graphene increases the elastic modulus by up to 131 % [67], flexural strength by 50 % [68], hardness by up to 138 % [69] and decreases ductility by up to 84 % [69]. Significant increments of ultimate tensile strength and yield stress of 68 % [70] and 117 % [71] respectively were also obtained when the formation of carbides is largely avoided.

High increments of fracture toughness (up to 135%) [72] and flexural/fracture strength (up to 103 %) [73] were observed in ceramic matrix/graphene. Such improvements were ascribed to the crack bridging, crack deflection, and graphene nanoplatelets pull-out phenomena, shown in Figure 3.6.

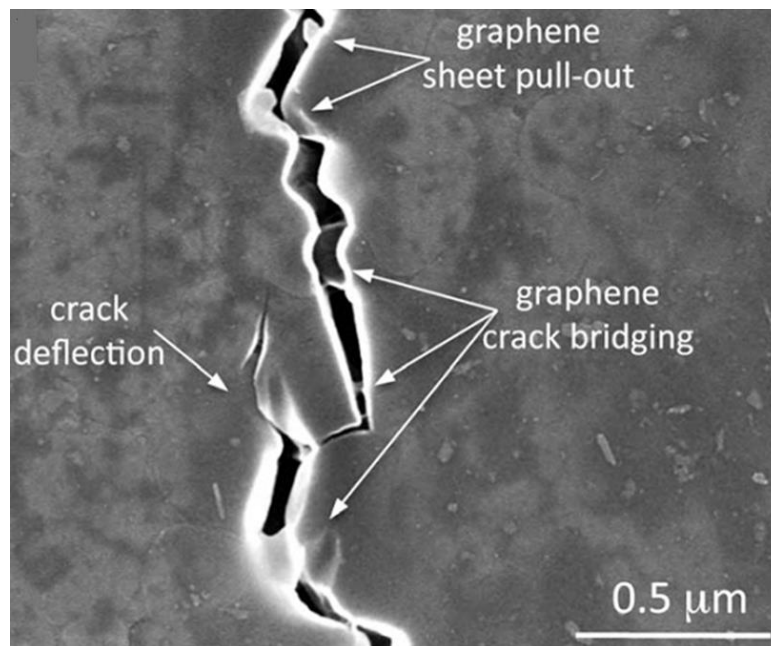


Figure 3.6: Crack deflection, crack bridging, and graphene pull-out phenomena observed in graphene/Si₃N₄ composite [74].

Crack deflection occurs when a graphene platelet changes the direction of a propagating crack, driving it through the path of least resistance. Thanks to their high aspect ratio and high in-plane

strength, GNPs are excellent barrier to the propagation of cracks. Crack bridging instead occurs when a crack propagates through a graphene nanoplatelet and this latter does not fracture because of its high in-plane strength and provides resistance against the further propagation of the crack.

When the crack has a great energy, it can pull the graphene sheet off the bridged grains and in this case GNP pullout occurs. Such phenomenon increases the material resistance because the energy is used for the graphene pullout instead of the crack propagation.

Whereas the increments of fracture toughness and flexural/fracture strength measured in ceramic matrix/graphene composites is significant (due to the phenomena described above), a weak influence of graphene on the Young modulus and the hardness of such materials was observed [75-83]. No variations of stiffness or hardness were usually recorded with a low content of graphene, while decreases were observed with higher percentages of graphene nanoplatelets. High contents of graphene in fact can cause the formation of nanoplatelets clusters, weakly bonded by Van der Waals interactions, which represent a soft phase into the hard and stiff ceramic matrix and can cause the sliding of grains. Studies have also shown that GNPs often generate localized porosity which causes the ceramic grains displacement as the GNPs are deformed [79]. Only few studies [82-84] have reported simultaneous strengthening and toughening in ceramic matrix/graphene composites. Zhang et al. [82] observed improvements in toughness, hardness and elastic modulus of 82, 31 and 44%, respectively, by loading a hydroxyapatite matrix with 1 %wt of GNPs. Such increases are due to the GNPs which in this case are not localized at the grain boundaries (as usual into the ceramic matrix/graphene composites), but are embedded into the grains and act as an anchor between them.

3.2.2 Geopolymers reinforcement with graphene nano-sheets

Really few studies were focused on the production and characterization of geopolymer/graphene composites [85-90]. Saafi et al [85] proposed for the first time the incorporation of in-situ reduced

graphene oxide (rGO) into fly ash-based geopolymers. They observed that the addition of rGO sheets improved the mechanical properties and reduced the porosity of geopolymers. With an rGO concentration of 0.35-wt.% the flexural strength and Young's modulus increased by 134% and 376%, respectively. The moderate increase in toughness (equal to 56%) was ascribed to the formation of hybrid fillers characterized by the combination of stacked rGO sheets and fly ash particles. The same research group analyzed also the influence of rGO sheets on the piezoresistive effect of fly ash-based geopolymers [87]. They measured an increase of ~100% of the gauge factor with an rGO concentration of 0.35-wt.%. The increase in the gauge factors upon adding rGO sheets was attributed to the improved conductivity developed by overlapped graphene sheets [87, 91].

Also Ranjbar et al [86] reported the effect of the addition of graphene nanoplatelets (GNPs) on the microstructure and mechanical properties of a fly ash based geopolymer. They detected overlapping and agglomerate formation of GNPs. However, the results showed that the compressive and flexural strength of the geopolymer improved by 1.44 and 2.16 times, respectively, when adding 1% GNPs.

Yan et al [88-90] produced for the first time graphene/metakaolin-based geopolymers composites through in-situ reduction of graphene oxide in the alkaline solution. They observed an increment of fracture toughness and flexural strength of 17 % and 5% respectively [88].

The review about geopolymers composites (including geopolymer/graphene composites) described above, highlighted that no studies were focused on the electro-mechanical characterization of metakaolin-based geopolymers/graphene nanocomposites. In chapter 2 of the present dissertation, results about the production, the mechanical, and electro-mechanical characterization of metakaolin-based geopolymer mortars were discussed. In particular, high piezoresistive gauge factor values were recorded and the presence of a direct piezoelectric effect was discovered. The addition of graphene, characterized by excellent and unique mechanical and electrical properties [51], could significantly enhance the performances of metakaolin-based geopolymer mortars,

paving the way for a wider range of applications, above all in the self-monitoring and energy harvesting fields.

In the next sections the production process of metakaolin-based geopolymers/GNPs nanocomposites will be described. Results about mechanical characterization at different length scales will be also proposed and results about the electro-mechanical characterization will be shown.

3.2.3 Samples fabrication

Graphene nanoplatelets of Grade C were purchased by COMETOX s.r.l., Milano, Italy. In particular, Grade C is characterized by clusters of particles having an average thickness of a few nanometers, a diameter of less than 2 microns, and an average surface area of $300 \text{ m}^2/\text{g}$ [92].

In order to check the quality of the purchased GNPs, Atomic Force Microscopy (AFM) acquisitions were performed, after depositing a graphene-water solution (stirred for 60 min and sonicated for 90 min) on a silicon substrate. AFM is a powerful tool to obtain the 3D profile of a sample, with a resolution on the order of fractions of a nanometer. During AFM measurements, a probe (i. e., a cantilever beam equipped with a sharp tip) interacts with the sample surface, whose profile can be obtained by measuring the deflection of the cantilever (usually by means of optical techniques).

In particular, an Icon Bruker atomic force microscope (Figure 3.7) was used and tapping mode acquisitions were carried out. A scanning rate of 1Hz was adopted and images were processed by using the software *Nanoscope*.

As shown in Figure 3.8, the GNPs dimensions correspond to those declared by the supplier. The thickness of platelets in fact varies from few nanometers to a maximum of ten nanometers, whereas the in-plane dimensions are in the range of few microns.



Figure 3.7: Icon Bruker Atomic Force Microscope.

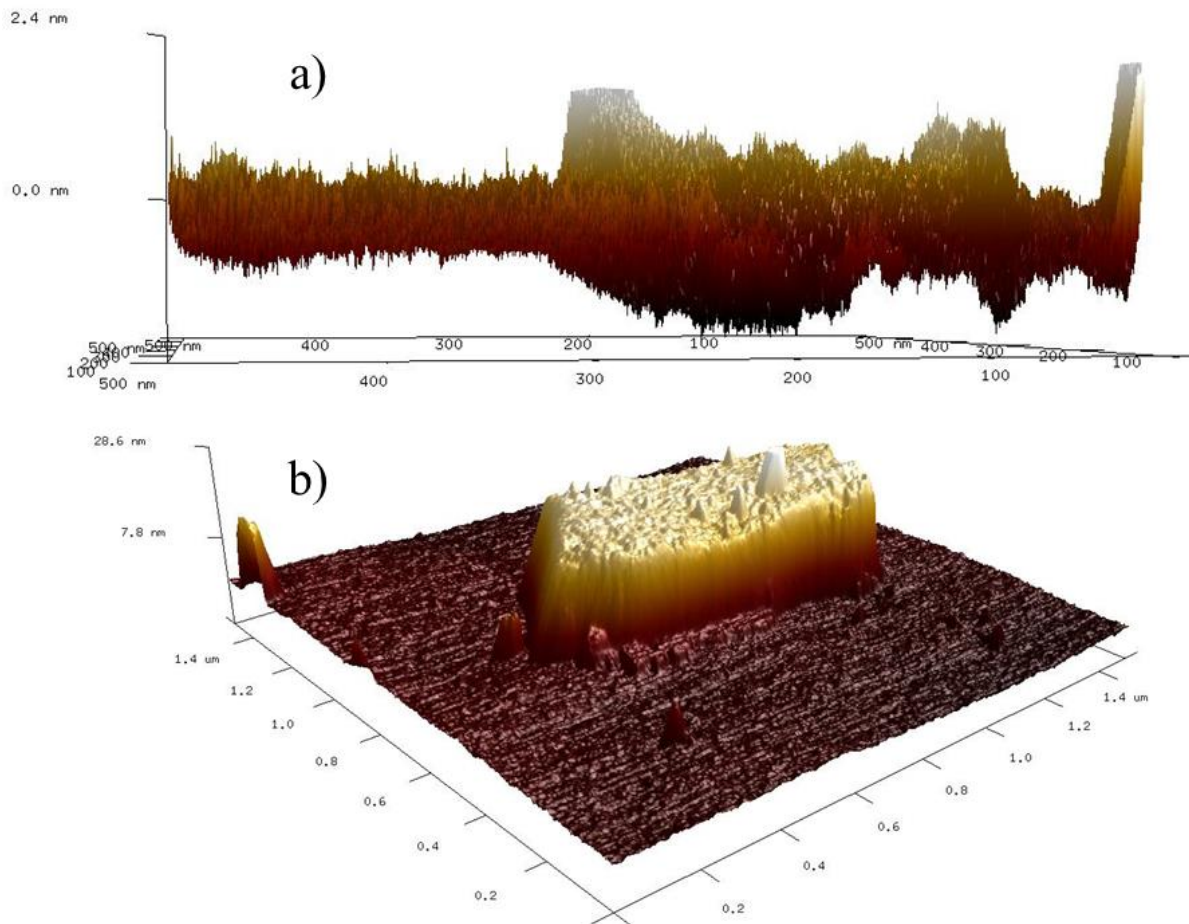


Figure 3.8: AFM acquisitions of graphene-water solution deposited on a silicon substrate. The thickness of platelets varies from a) few nanometers to a maximum of b) ten nanometers whereas the in-plane dimensions are in the range of few microns.

The graphene-water solution deposited on the silicon substrate was also subjected to X-ray photoelectron spectroscopy (XPS) in order to check the graphene purity and the possible oxygen contamination. As shown in Figure 3.9, the values of 531 eV, 285 eV and 15 eV for O1s peak, C1s peak and D parameter respectively, perfectly matched the literature values of pure graphene [51].

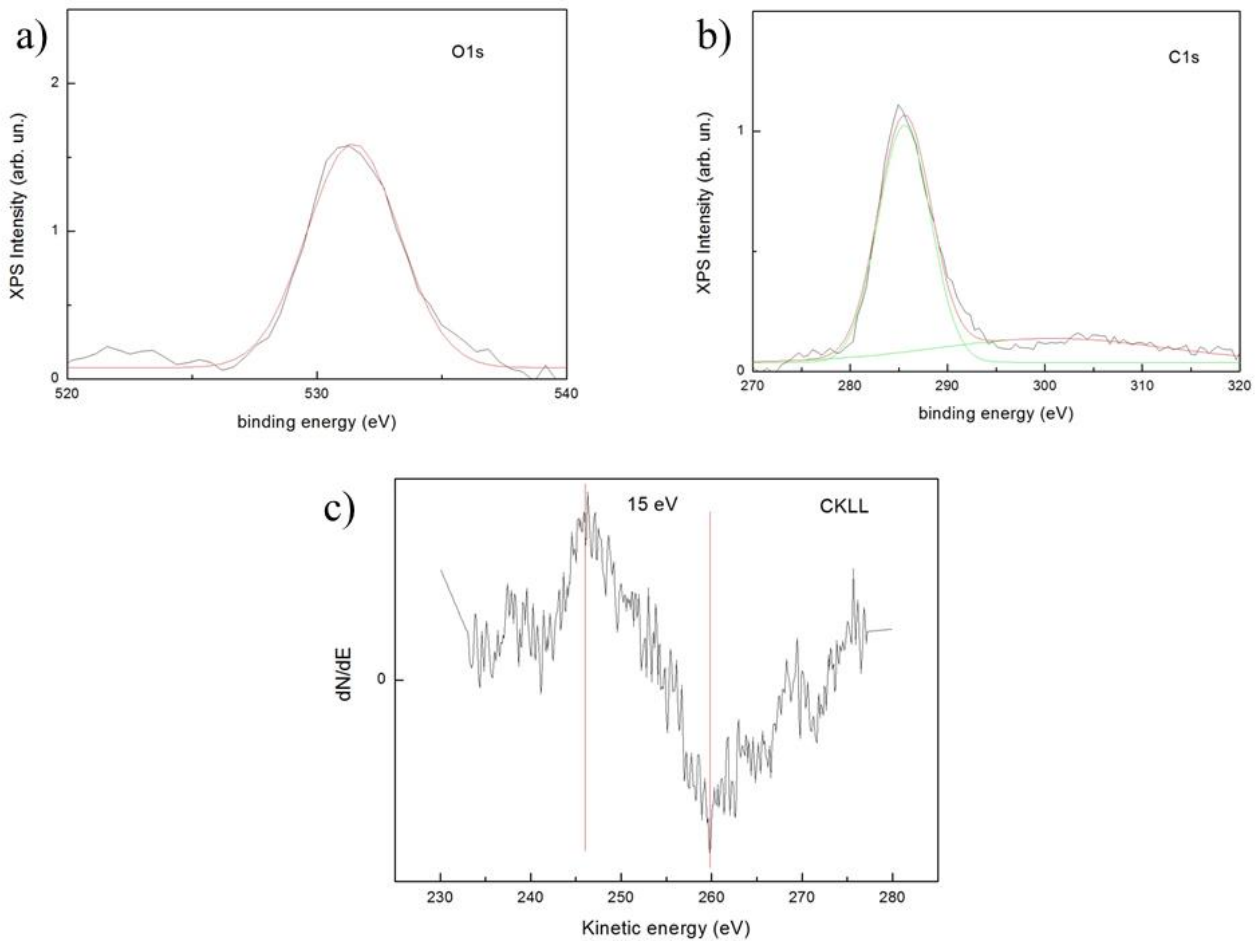


Figure 3.9: results of X-ray photoelectron spectroscopy of graphene platelets, indicating a) O1s peak, b) C1s peak, and c) D parameter value.

After checking the graphene quality, metakaolin-based geopolymer/GNPs nanocomposites were produced according to the procedure schematically shown in Figure 3.10.

Graphene nanoplatelets were dispersed in ultrapure water and mechanically stirred for 60 min. Also NaOH pellets were mixed with water and stirred for 60 min by keeping the beaker sealed to minimize contamination by atmospheric carbonation and prevent water evaporation. Once the

NaOH-water solution became clear and cooled down, it was poured into the graphene-water solution and the final solution was stirred for 40 min and sonicated for 90 min. After the addition of sodium silicate, the compound was stirred for 10 min and sonicated for 120 min. Metakaolin powder and silica sand were finally added, the final slurry was casted into open and dismountable molds and placed on the vibration table to remove entrained air. In order to prevent the moisture loss, the molds were sealed from the atmosphere and cured for 24 h at 50°C. The sealed specimens were then stored at ambient temperature and pressure for four weeks to complete curing. The geopolymer mortar matrix composition is the same described in Section 2.2.1.2.

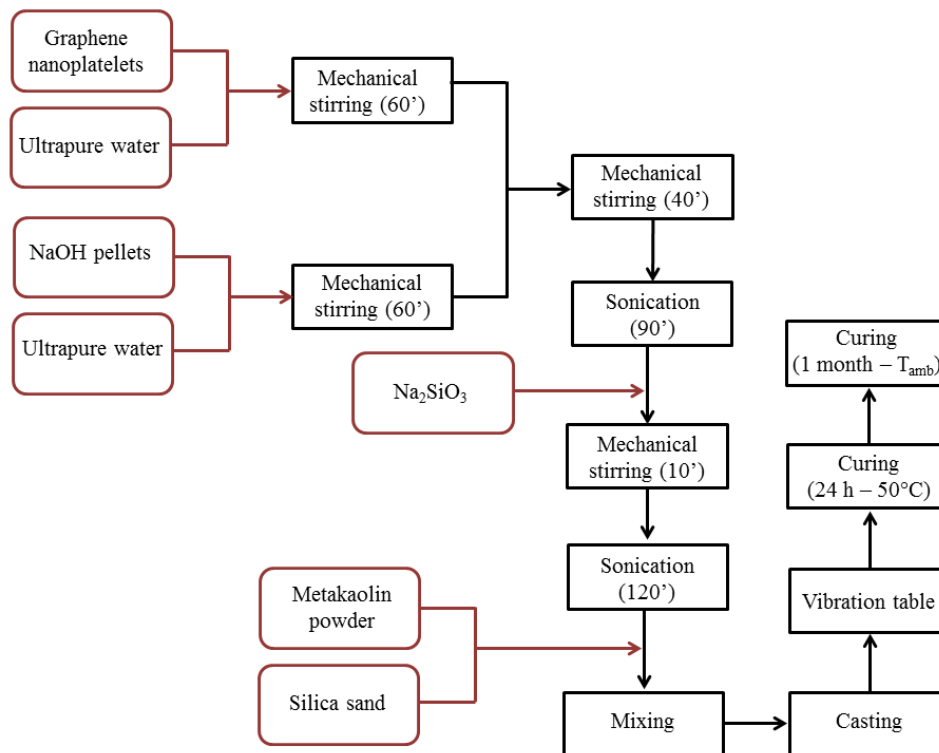


Figure 3.10: schematic representation of the procedure followed for the production of geopolymer/graphene nanocomposites.

In particular, geopolymer mortar/GNPs samples with three different GNPs content (0.1, 0.5 and 1%wt) were produced. A maximum percentage of 1%wt was chosen in order to produce samples

with the same water/binder ratio (i.e. 0.56, as described in Section 2.2.1.2) and a suitable GNPs dispersion. With the fixed amount of water, percentages higher than 1%wt caused sedimentation of GNPs once the water/GNPs solution was removed from the sonication bath. Such sedimentation is due to the incomplete separation of the GNPs bundles into individual flakes and can cause a bad dispersion of graphene into the matrix and the GNPs macro clusters formation (as shown in Figure 3.5) with a detrimental effect on the composite performances. Higher contents of water should be used to disperse GNPs percentages higher than 1%. However, an additional amount of water could lead to an increase of the porosity of the geopolymer composite, by altering the mechanical performances of the material [93].

Indentation tests results performed on the geopolymer mortar, and shown in Section 2.3.1.2, highlighted that quartz sand significantly influence the mechanical properties of the geopolymer paste. Such results suggest that the best choice to analyze the influence of graphene on geopolymers properties is probably the production of geopolymer paste/GNPs samples instead of geopolymer mortar/GNPs, in order to avoid the quartz sand influence. However, the geopolymer paste samples produced (with or without graphene) showed an excessive brittleness which impeded a safe removal from the molds after curing and also the piezoresistive and piezoelectric characterization according to procedures described in Section 2.2.4 and 2.2.5. Moreover, a material with such a brittle behavior is not suitable for those applications which may benefit from the presence of a piezoresistive or piezoelectric effect such as self-monitoring of civil infrastructures or energy harvesting by means of the deformation of a road surface. For such reasons, geopolymer mortar/GNPs composites were produced. In particular, cubic samples of dimension 20 mm and 40 mm and disks of 55 mm diameter and 8.8 mm thickness were fabricated for the mechanical and electro-mechanical characterization. In Figure 3.11 a) the casting of the geopolymer/graphene slurry with 1%wt of graphene is shown whereas Figure 3.11 b) shows cubic samples of dimension 20 mm of geopolymer mortar with 0 %wt, 0.1 %wt, 0.5 %wt, and 1 %wt of graphene. It is worth noting that,

at first glance, the grey color of nanocomposites samples is quite uniform and it becomes darker from sample with the lowest amount of graphene to the sample with the highest content. This could be synonym of a good dispersion of graphene nanoplatelets into the geopolymeric mortar matrix.

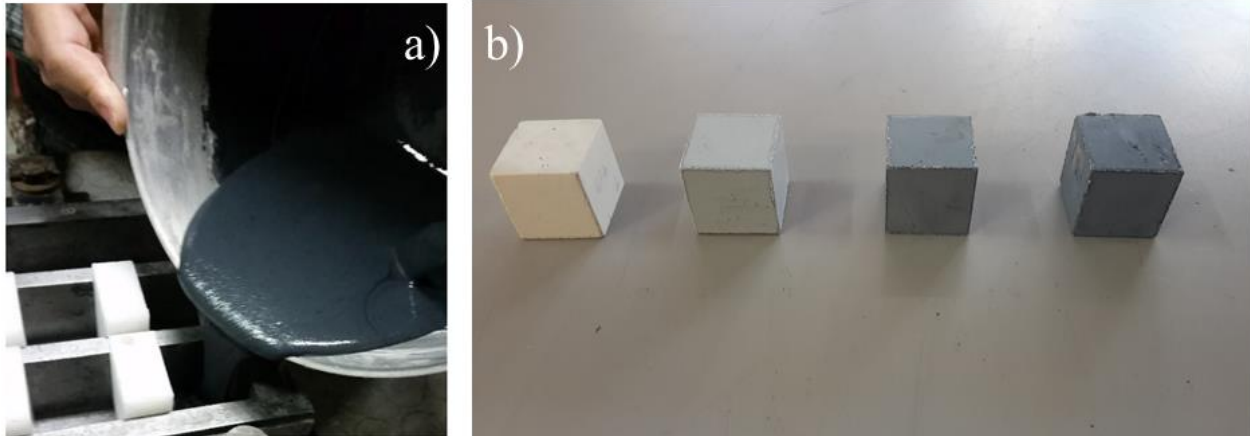


Figure 3.11: a) casting of the geopolymer/graphene slurry with 1%wt of graphene; b) cubic samples of dimension 20 mm of geopolymer mortar with, from left to right, 0 %wt, 0.1 %wt, 0.5 %wt, and 1 %wt of graphene.

3.2.4 Morphology and chemical characterization

In order to investigate the chemical functional group changes and morphological changes of geopolymers containing GNPs at a variety of loadings, XRD, FT-IR, and EDS combined with SEM analysis were performed.

Figure 3.12 shows the XRD patterns of the produced geopolymeric mortars with different graphene contents. All the manufactured geopolymeric mortars show the characteristic broad hump centered at approximately $28^\circ 2\theta$. As elsewhere reported [94], exfoliated graphene nanosheets don't exhibit any diffraction peaks due to the absence of a periodic structure. Aggregation of nano-sized graphene sheets disorderly or parallel oriented can also occur. Their presence results in broad peaks at c.a. 26° , with FWHM of 6° or greater, and $43^\circ 2\theta$ [95]. This occurrence, can't be indeed observed by XRD analysis of the geopolymeric samples, because of the overlapping sharp peaks from

crystalline phases in parent material, identified as quartz and mullite, and minor quantities of graphene used. Thus, it can be only concluded that both the crystalline phases and graphene behave as inactive fillers in the geopolymerization reaction.

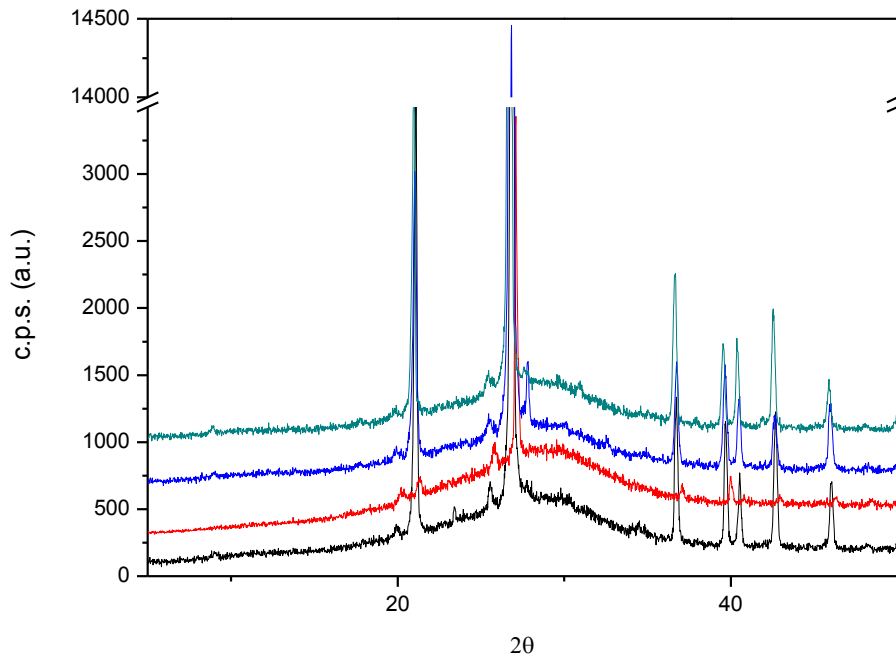


Figure 3.12: XRD patterns of the synthesized geopolymeric mortars with different graphene contents: 0% wt (black line), 0.1% wt (red line), 0.5% wt (blue line), 1.0% wt (green line).

Figure 3.13 shows the FT-IR transmittance spectra of the geopolymeric mortars at different amounts of graphene, cured for 28 days. The strong broad bands at approximately 3450 cm^{-1} and 1650 cm^{-1} can be attributed to stretching and bending vibrations of hydroxyl groups and are due to the presence of adsorbed water. The peak at 696 cm^{-1} is assigned to Si-O symmetric stretching vibration. Moreover, the peak at 794 cm^{-1} is associated with both 4-coordinated Al-O stretching vibration and symmetric stretching of Si-O-Si. The broad band in the region $950\text{--}1200\text{ cm}^{-1}$ is attributed to asymmetric stretching (Si-O-Si and Al-O-Si), while the peak at 1400 cm^{-1} is assigned to O-H bending vibration. The peak at 1460 cm^{-1} is due to the presence of sodium carbonate. Bands at 1522 cm^{-1} , at ca. 2880 cm^{-1} and 2945 cm^{-1} , are respectively associated to skeletal vibration, symmetric stretching of CH_2 , and

asymmetric stretching of methylene groups of graphene sheets [86]. From Figure 3.13 one can observe that these last two peaks are more visible in the sample with the highest content of GNPs (i.e., 1%wt, green curve in Figure 3.13).

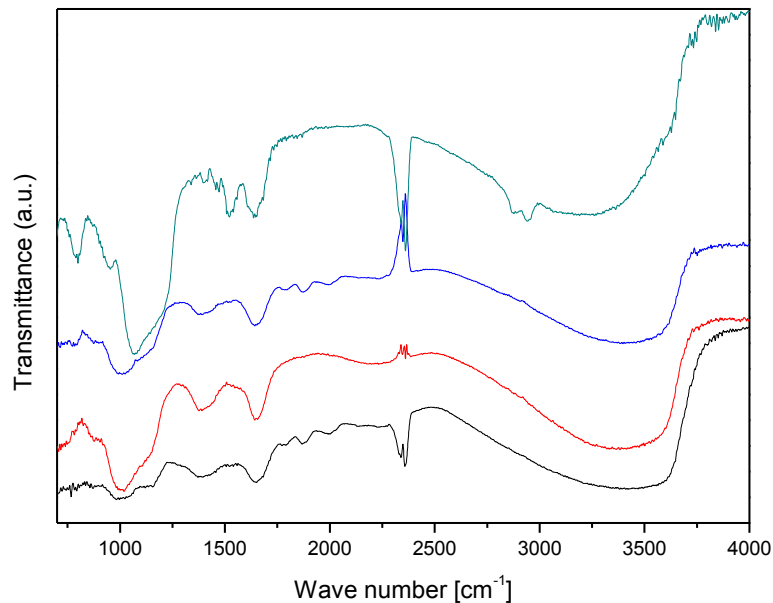


Figure 3.13: FT-IR transmittance spectra of the geopolymer mortars at different amount of graphene: 0% wt (black line), 0.1% wt (red line), 0.5% wt (blue line), 1.0% wt (green line).

The morphology of the geopolymer/GNPs composites was observed by means of SEM analysis and results are shown in Figure 3.14. The presence of GNPs into the geopolymeric matrix can be clearly observed and it is also testified by the EDS results. Besides Si, Al, Na and O, which are the typical elements characterizing geopolymers, a high presence of carbon C, related to the presence of graphene, can be clearly noticed. In particular, GNPs can be found into the matrix in different shapes. The darker spot in the middle of the figure represents a cluster of GNPs, characterized by the typical wrinkled surface and probably composed by several graphene sheets. A very thin graphene nanoplatelet is instead highlighted by the dotted circle on the top left of the SEM picture. The dotted ellipse finally shows one of the rolled up GNPs present in the picture. The GNPs shape

pointed out by the dotted circle is obviously the most suitable one, since it respects the real definition of a graphene nanoplatelet. Further SEM analysis showed that, for all the samples with different GNPs contents, the graphene is equally distributed into the matrix and that the dimensions of GNPs clusters never exceed few tens of microns. Such clusters in fact, characterized by conglomerates of GNPs bonded by weak Van der Waals interactions, if too large can result as defects into the matrix instead of reinforcing fillers.

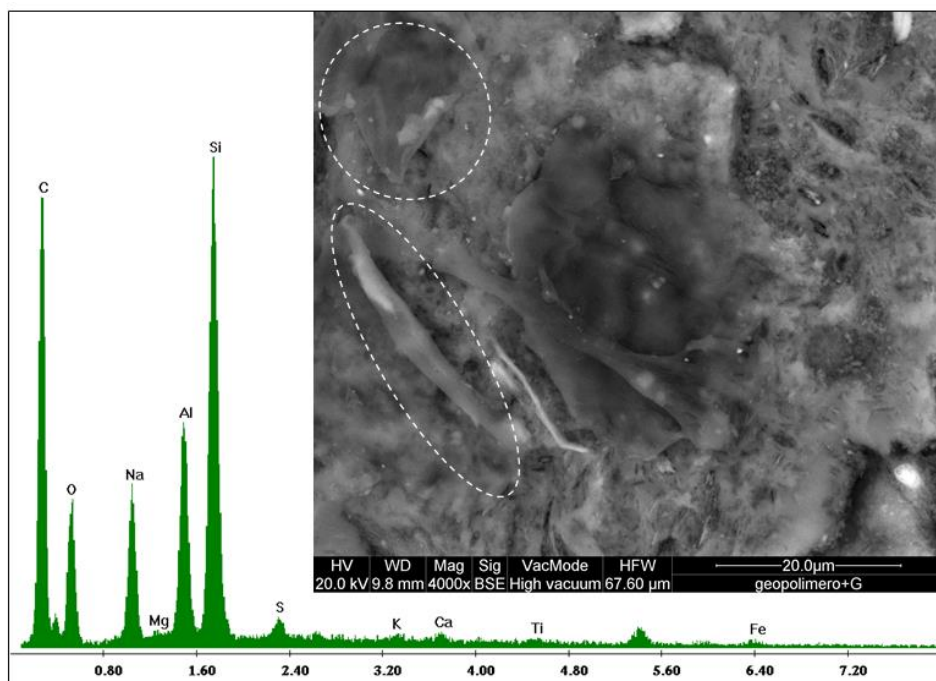


Figure 3.14: Scanning Electron Microscopy (SEM) and Energy Dispersive X-ray Spectrometry (EDS) of the produce geopolymer/GNPs composite.

3.2.5 Mechanical characterization

3.2.5.1 Indentation tests

Nanoindentations tests were firstly performed (by using the equipment described in Section 1.2.3) on the produced samples in order to analyze the influence of the different GNPs contents on the mechanical properties at the nanoscale. Since GNPs were dispersed into the geopolymer paste before the quartz sand addition and since it is obvious that graphene can't be contained into quartz

sand particles, nanoindentations were localized only in the paste area, by avoiding the quartz particles (which have a great influence on the mechanical properties of the geopolymer, as shown in Section 2.3.1.2). In particular, a Berkovich tip, a maximum load of 400mN, a loading and unloading rate of 800 mN/min, and a holding time of 5 sec were used and results are listed in and Table 3.1.

One can observe that the addition of GNPs do not influence the Young modulus and the hardness of the metakaolin-based geopolymer. Very low increments were recorded for E_r and H and such increments can be considered negligible by taking into account the standard deviation values. Data scattering is usually high in ceramic materials characterized by high porosity and defects such as cracks or impurities.

Table 3.1: Results of nanoindentations performed on the geopolymer paste areas with a maximum load of 400mN.

GNPs%wt	Average E_r [GPa]	St. Dev. E_r [GPa]	Incr.% E_r	Average H [MPa]	St. Dev. H [MPa]	Incr.% H
0	11.38	1.27		453.94	31.98	
0.1	11.40	1.67	0.18	445.14	34.84	-1.94
0.5	11.60	1.16	1.92	483.62	47.89	6.54
1	11.77	1.84	3.42	443.65	51.16	-2.27

Also the dimensions of the imprints are in fact similar for all the tested samples, as shown in Figure 3.15. As observed for many other ceramic materials loaded with GNPs and tested by indentation [75-83], the addition of graphene does not improve the stiffness and the hardness of the metakaolin-based geopolymer matrix.

In Figure 3.16 the Weibull distributions of indentation modulus E_r and hardness H for geopolymer mortar samples with a) 0%, b) 0.1%, c) 0.5%, d) 1% wt of GNPs are shown. No bimodality was observed for any of the analyzed samples. In Figure 3.15 b)-d) one can be observed that GNPs (identified by black spots) are uniformly distributed into the geopolymer paste matrix, by creating a quite homogeneous microstructure in which GNPs clusters have stiffness and hardness similar to those of the ceramic matrix. For such reason the resultant Weibull distribution is not bimodal.

Some studies [75-83] reported decreases of Young modulus and hardness with high contents of GNPs, due to the formation of GNPs macro clusters characterized by weak Van der Waals interactions and low mechanical properties. From micrographs of Figure 3.15 an increase of GNPs clusters dimensions can be observed from sample with 0.1% wt (Figure 3.15 b)) to sample with 1% wt (Figure 3.15 d)) of GNPs. However, such dimensions are not such as to cause detrimental effects on the indentation modulus and hardness of the composite material tested by indentation.

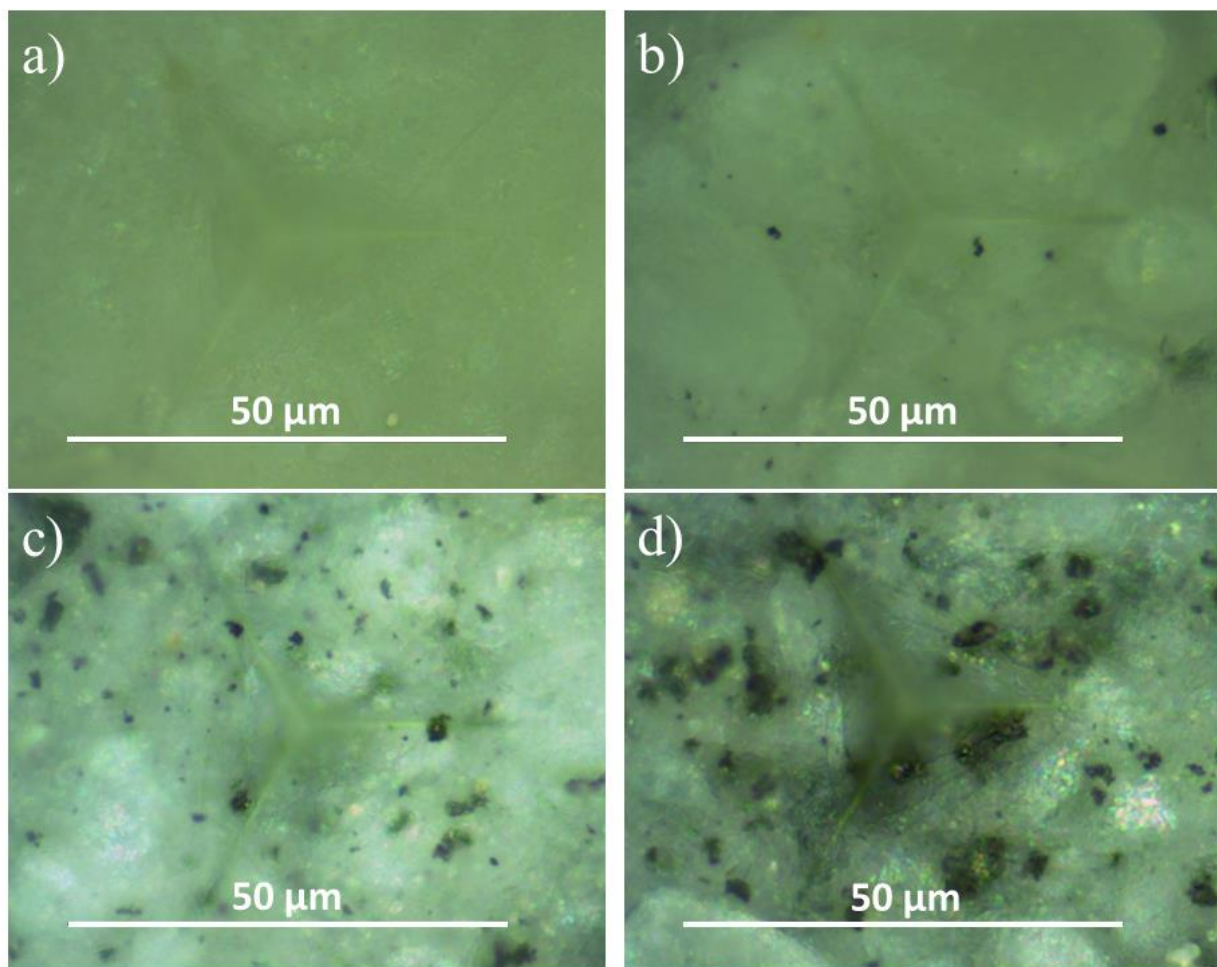


Figure 3.15: Berkovich imprints of indentation performed with a maximum load of 400mN on samples with a) 0% wt, b) 0.1% wt, c) 0.5% wt, d) 1% wt of GNPs.

Concerning the Weibull distribution related to the pure geopolymer paste of Figure 3.16 a), a clarification must be carried out. In Figure 2.38 of Chapter 2 a bimodal Weibull distribution was observed for geopolymer paste samples and the first region with lower mechanical properties was

attributed to the presence of defects and impurities into the material microstructure. Such result may appear to be in contrast with that propose in this section because in this case no bimodality was observed for the same sample. However, such different results are in perfect agreement.

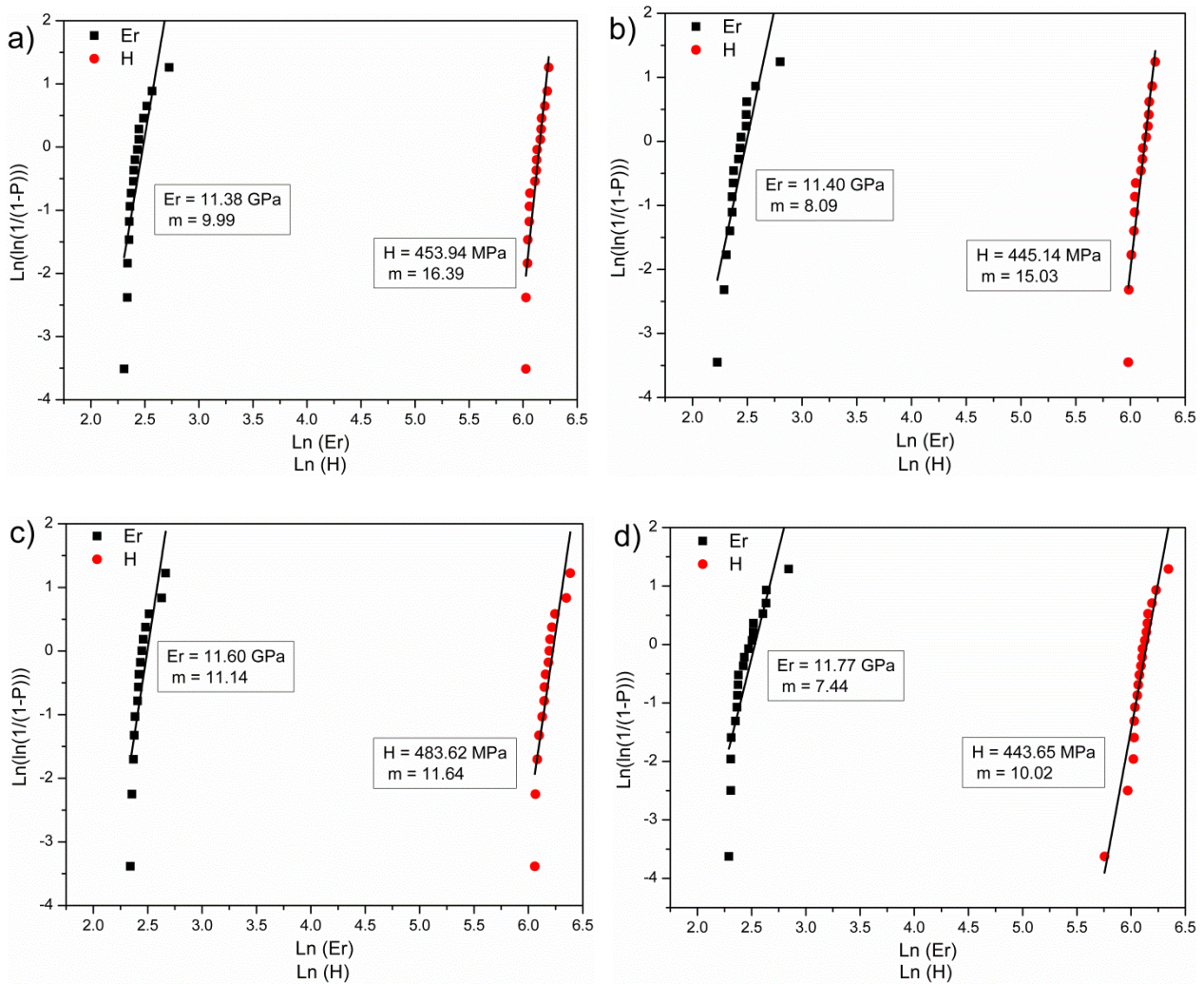


Figure 3.16: Weibull distribution of indentation modulus E_r (square black symbols) and hardness H (circle red symbols) for geopolymer samples with a) 0%, b) 0.1%, c) 0.5%, d) 1% wt of GNPs. Results refer to indentations performed on the geopolymer paste areas with a Berkovick tip and a maximum load of 400 mN.

Results of Chapter 2 in fact refer to indentations performed with a maximum load of 100 mN whereas results of the present Chapter were obtained by using an indentation load of 400 mN. With a higher load the volume of material tested is higher, the analysis is less localized and results are averaged. With a load of 400 mN the bimodality cannot be observed but results are perfectly

averaged. An E_r equal to 11.38 GPa was obtained in this case and such value is the average between the first and the second region values of the bimodal distribution observed with a 100 mN load, equal to 10.39 GPa and 12.04 GPa respectively (see Figure 2.27). Same considerations for the hardness values.

As described above, an indentation load (equal to 400 mN) higher than those used for geopolymers (15 mN and 100 mN, see Section 2.3.1.2) was chosen to analyze the geopolymer/GNPs composites. Such choice is related to the main goal of the indentation tests performed on the produced composite, which is the analysis of the influence of GNPs on the stiffness and hardness values of the geopolymer. The indentation load value of 400 mN was the lowest one able to detect the average influence of GNPs only, in a suitable volume of material, by avoiding the influence of defects and impurities in the geopolymer paste.

3.2.5. 2 DIC and Brazilian Disk tests

A mechanical characterization at the macroscale of the produced GNPs/geopolymer composites was also performed by using the combination between DIC and Brazilian Disk test proposed in Section 2.2.3.1. Such methodology allows to measure the Young modulus E , the Poisson ratio ν , and the ultimate tensile strength σ_T of a material by means of a single test. Table 3.2 shows results obtained for the composites with different GNPs contents.

Table 3.2: Young modulus E , Poisson ratio ν , and ultimate tensile strength σ_T of metakaolin-based geopolymer/GNPs composites measured with the DIC-Brazilian Disk methodology. Five specimens for each GNPs content were tested.

GNPs %wt	E [Gpa]	incr% E	ν	incr% ν	σ_T [GPa]	incr% σ_T
0	15.21 ± 1.47		0.192 ± 0.025		5.47 ± 0.68	
0.1	16.30 ± 0.63	7.2	0.181 ± 0.038	-6.3	5.71 ± 0.34	4.3
0.5	17.44 ± 0.67	14.7	0.171 ± 0.009	-11.6	6.26 ± 0.05	14.4
1	14.09 ± 2.15	-7.4	0.164 ± 0.010	-16.7	5.57 ± 0.39	1.8

In this case higher increments of mechanical properties were obtained if compared to nanoindentation tests results of Table 3.1. Unlike nanoindentation tests, which perform a localized analysis without causing any damage into the material, the macroscopic characterization (like that one carried out by means of a Brazilian Disk test) analyzes the material behavior until failure by inducing several damages (i. e. cracks) into the material microstructure, which propagate until the final collapse. In such context, phenomena related to the GNPs presence, such as crack deflection and bridging described above, play an important role and lead to the improvement of mechanical properties. By analyzing results of Table 3.2, it is worth noting that for both E and σ_T the highest increase was obtained for the samples with a GNPs content of 0.5%wt. In particular, a decrease was measured when the GNPs percentage increases from 0.5 to 1%wt. Such decrease is related to the generation of GNPs macro clusters (shown in Figure 3.15 d)) which are not able to arrest or deflect cracks during the material damaging at the macro scale. Concerning Poisson's ratio, a continuous decrease was recorded for increasing contents of GNPs and this could be due to a sort of hardening caused by the presence of graphene.

However, all the considerations proposed above about the results of Table 3.2 could be considered forced since the increments measured for the mechanical properties are almost nullified by the high standard deviation values.

One can conclude that the GNPs addition to metakaolin-based geopolymer mortars does not represent a smart choice in terms of performances and cost-effectiveness if the main requirement is the high value of mechanical properties. As described in Chapter 2, the quartz sand significantly improves the mechanical properties of the geopolymer paste and its contribution is probably so high that it makes negligible the role of GNPs.

The results obtained from the mechanical characterization of the produced metakaolin-based geopolymer/GNPs composites may appear to be in contrast to those reported by researchers on other geopolymer/GNPs nanocomposites [85-90]. In such studies in fact high improvements of

mechanical performances were obtained as a result of graphene loading. However, these differences can be easily explained. The aluminosilicate precursor used in [85, 86] for the production of geopolymer/GNPs composites was fly ash and, as discussed in Chapter 2, the microstructure of fly ash-based geopolymers is extremely porous and characterized by an high presence of impurities and unreacted particles. The increases of mechanical performances ascribed to GNPs are in fact related to the ability of GNPs of reducing the material porosity. Different results were instead obtained for metakaolin-based/GNPs composites analyzed in [88-90]. Authors reported increments of fracture toughness and flexural strength of 5% and 17% respectively. Such increments are significantly lower than those recorded for fly ash-based geopolymer/GNPs composites (lying in the range of 100-400%). Moreover, by observing the data scattering of results obtained in [88-90] one can conclude that also in this case the increments are completely obscured by the high values of the standard deviation. Concerning Young's modulus, a slight decrease was also reported in [90] with a GNPs content equal to 1%wt. The result proposed in the present dissertation on the mechanical characterization of metakaolin-based geopolymer/GNPs composites are then in agreement with literature data. Whereas GNPs make the microstructure of fly ash-based geopolymer denser and more homogeneous, they have no effect on the microstructure of metakaolin-based geopolymers, characterized by high homogeneity.

Although GNPs do not improve the mechanical properties of metakaolin-based geopolymers, graphene could provide interesting improvements to the electro-mechanical properties, due to its unique electrical properties. For such reason an electro-mechanical characterization was performed and results are discussed in the next section.

3.2.6 Electro-mechanical characterization

A direct piezoelectric characterization along direction 3 (perpendicular to the open surface of the molds, as described in Figure 2.33 of Chapter 2) was carried out on geopolymers/graphene

nanocomposites according to the experimental procedure described in Section 2.2.5.2. In particular, samples with 1%wt GNPs content were tested. Figure 3.17 shows the charge amplitude A_Q versus load amplitude A_P plot obtained for geopolymer mortar/1%wt GNPs composites (circle red symbols), compared to that of geopolymer mortar samples (square black symbols).

If compared to results obtained from the direct piezoelectric characterization of geopolymer mortar samples, results of geopolymer mortar/1%wt GNPs nanocomposites are significantly striking. For geopolymer mortars in fact a linear behavior was obtained only for load values lying in the range $0 \text{ N} \div 750 \text{ N}$ and for loads higher than 750 N a plateau in the $A_Q - A_P$ plot was observed. Such plateau was attributed to a charge saturation due to the limited amount of mobile cations Na^+ contained into the material microstructure. Instead, a linear behavior can be clearly observed from 0 N to 2500 N for nanocomposites samples. Moreover, a value of the charge coefficient d_{33} equal to 11.99 pC/N was measured for nanocomposites and this value is 198% higher than that measured for simple mortars, equal to 4.02 pC/N .

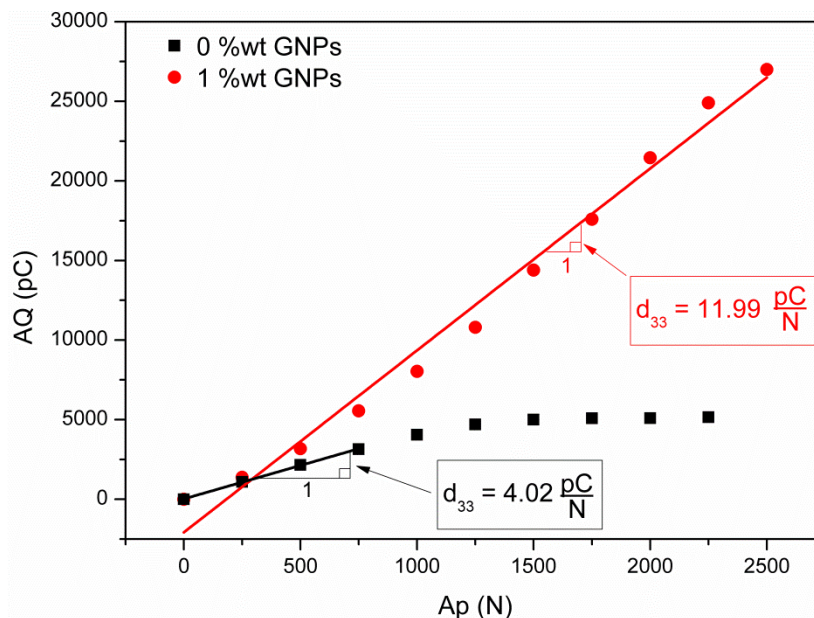


Figure 3.17: Charge amplitude A_Q versus load amplitude A_P for geopolymer mortar (square black symbols) and geopolymer mortar/1%wt GNPs (circle red symbols) samples, tested along direction 3, which is that normal to mold's open surface. The slope of the linear fitting lines represents the charge coefficient d_{33} .

The improvements provided by the addition of GNPs to the piezoelectric properties of geopolymeric mortars are then strongly valuable. A higher charge coefficient allows to exploit the piezoelectric effect in a wider range of applications, paving the way to several applications in the energy harvesting field in which high piezoelectric coefficients are required. It is worth noting that the d_{33} value of 11.99 pC/N of geopolymer mortar/1%wt GNPs nanocomposites was measured after the curing of such materials by disregarding considerations about the water content. As shown in Section 2.3.3, a higher content of water into the geopolymers microstructure fosters the ionic mobility by providing increments of the charge coefficient. The d_{33} value of 11.99 pC/N can then be further increased by acting on the percentage of water contained in the geopolymer/graphene nanocomposites. However, the GNPs/water interaction must be considered and studied in this case. The load range in which a material shows a linear piezoelectric behavior is also another key issue to be considered for the design of piezoelectric devices since linearity implies an easier modeling of the device behavior. As shown in Figure 3.17, the GNPs addition increases such linearity load range by contributing to a greater development of geopolymers as piezoelectric materials.

The enhancements produced by graphene on the piezoelectric performances of geopolymers can be ascribed to the high electrical conductivity of GNPs which promotes the mobility of the Na^+ cations contained into the material, responsible of the observed piezoelectric effect.

Concerning piezoresistivity, a gauge factor increase of around 20% was also measured as a result of the addition of 1%wt of GNPs into the metakaolin-based geopolymer mortar matrix. In this case the improvement of the piezoresistive activity can be related to the high conductivity developed by overlapped graphene sheets, as observed elsewhere [87, 91].

3.3 New potential nanofillers: “graphene like” materials

3.3.1 Topological insulators: properties and applications

Topological insulators (TIs) represent a novel quantum phase of matter [96]. TIs are semiconductors in the bulk, but they show metallic conduction at the surface [97, 98]. The nature of these surface states is related to the nontrivial topology of the electronic bands of the bulk [99, 100]. Charge carriers from topologically protected surface states show a high mobility [99] comparable to that of graphene [102, 103]. Moreover, surface charge carriers are also spin-polarized [100] and protected from back-scattering by time-reversal symmetry [104]. While in ordinary materials electrons are back scattered (i.e., take a U turn) when they collide with crystal defects, on the surface of TIs the back-scattering is absent and the charge transport is dissipationless. Figure 3.18 helps to clarify the understanding of such properties. On the top of the figure, the electronic state of an insulator material is depicted. Electrons (blue particles on the left of Figure 3.18) in an insulator are bound in localized orbitals and have an energy gap separating filled and empty bands (i.e. the valence and the conduction band, respectively) of electronic states. Since a certain energy is required to dislodge an electron, such material is electrically inert. In the middle of Figure 3.18 the quantum Hall state is shown and it can be considered the predecessor of TIs properties. In a quantum Hall system, an intense magnetic field (letter B in the picture) is applied along the direction perpendicular to the 2D plane where electrons are confined and drives them to circulate in quantized orbitals. The result is that the system is an insulator in the bulk but not along the sample edge, where electrons can flow. The dissipationless electric conductivity is obtained because in such state the electronic charge can propagate only in one direction and it cannot be reflected back, neither scattered. The potential applications of the quantum Hall effect is however limited by the need of an intense external magnetic field. In TIs instead (bottom of Figure 3.18), such magnetic field is not required because electrons are moved by a spin-dependent force [105]. This state exhibits a quantum spin Hall effect because electrons with spin-up and those with spin-down

propagate in opposite directions. Since in graphene the carbon's spinorbit interaction is weak and the energy gap is hence small and susceptible to thermal fluctuations, the quantum spin Hall effect is hard to be observed [106].

Due to properties described above, topological insulators offer promising prospects for applications in micro and nanoelectronics [107-114], optoelectronics [115-118] and as mechanical metamaterials [119]. These features explain their groundbreaking impact in research fields associated to physics and materials science [120].

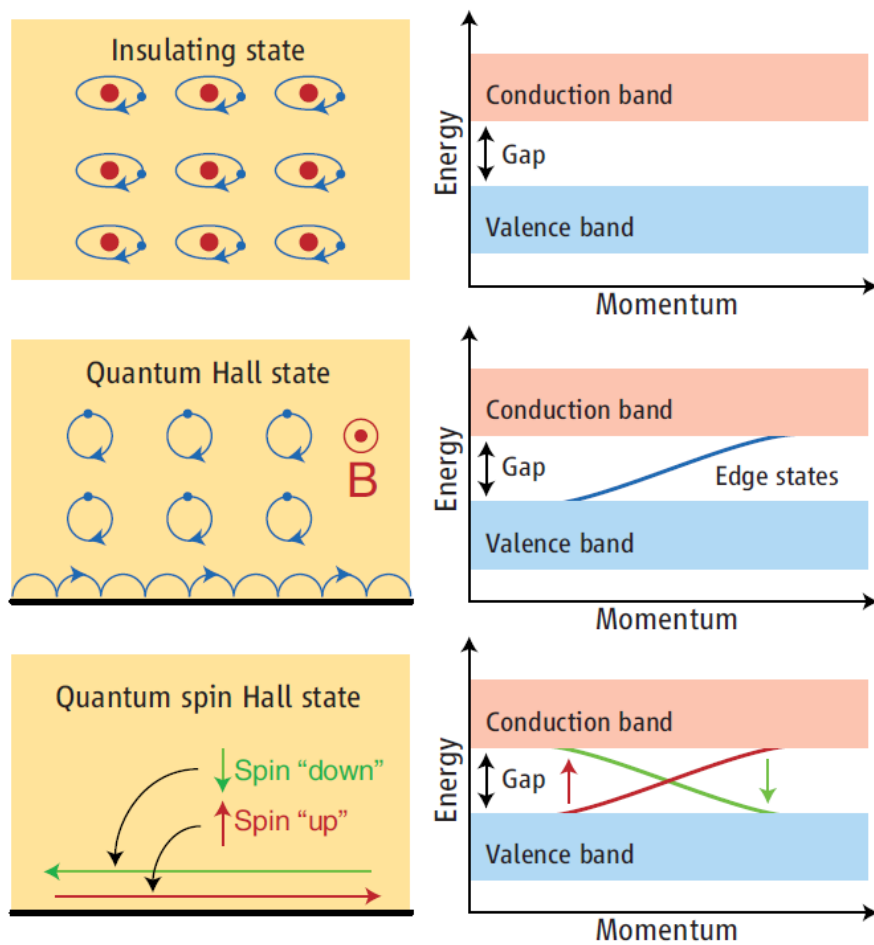


Figure 3.18: (Top) Insulating state; (Middle) A two-dimensional quantum Hall state; (Bottom) A quantum spin Hall state [106].

A crucial aspect for future applications based on TIs involves their reliable, large-scale, and low-cost production. Samples of topological insulators are commonly grown as thin films using sputtering, electrochemical deposition, molecular beam epitaxy, and pulsed laser deposition [121-

125]. However, the occurrence of vacancies shifts the Fermi level from the bulk band gap and induces the formation of Bi–O bonds [126], while surface oxidation implies the degradation of the peculiar electronic properties of TIs [127]. Moreover, crystal defects, whose amount is relatively large in some of the above-mentioned growth processes, could also have a detrimental effect on the mechanical properties [128, 129]. Therefore, TIs displaying high amount of crystal defects cannot be successfully employed in technological applications. The growth of single-crystal TIs through an optimal use of the Bridgman–Stockbarger method can strongly reduce the formation and amount of defects, thereby favoring the attainment of chemical inertness toward surface oxidation and the enhancement of mechanical properties [130–132] with potential implications for TI-based technological applications. Moreover, the notable control of crystal growth allows to tune the position of the Fermi level [133], or even the position of the Dirac point [134], and to tailor the band structure of TI heterostructures [135]. Figure 3.19 shown the working principle of the vertical Bridgman–Stockbarger method.

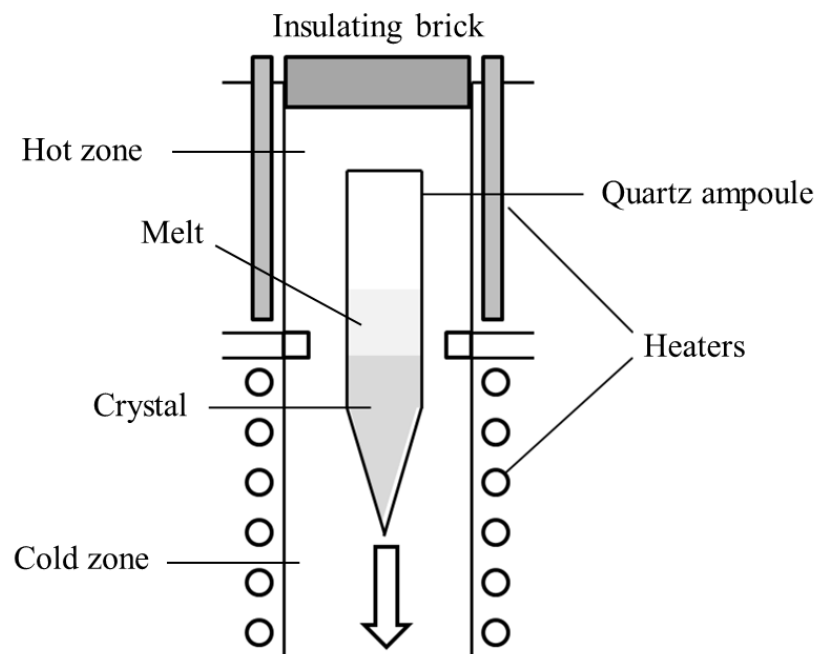


Figure 3.19: vertical Bridgman–Stockbarger method for crystals growth.

A polycrystalline material is heated in a sealed ampoule, characterized by a cylindrical shape and a conical lower end. Special heaters maintain the molten state. The crystal starts growing in the conical tip while the ampoule is slowly lowered from a hot zone to a cold zone. The rate used to move the ampoule depends on the material and it has to be chosen in order to maintain always the same temperature at the melt/crystal interface.

Among the most interesting and studied topological insulators we can find Bi_2Te_3 [136-140], Bi_2Se_3 [141-146], and SnSe [147-153]. They are layered and anisotropic material, whose crystal structure is shown in Figure 3.20 and 3.21. Both Bi_2Te_3 and Bi_2Se_3 are characterized by quintuple layers bonded by Van der Waals interactions, as shown in Figure 3.20, and (0001) represents the cleavage plane. SnSe is instead characterized by a layered orthorhombic crystal structure at room temperature [154].

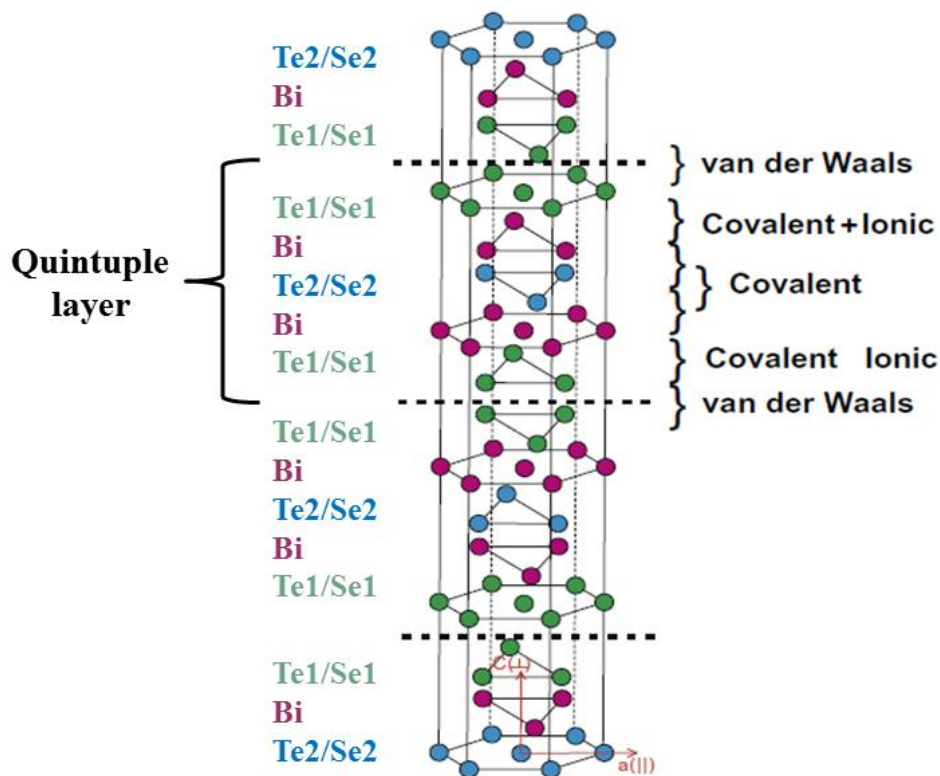


Figure 3.20: crystal structure of Bi_2Te_3 and Bi_2Se_3 .

Figures 3.21 a–d show the SnSe crystal structure along the a, b and c axial directions. One can observe the presence of two-atom-thick SnSe slabs along the b-c plane. While there are strong Sn–Se bonds along the b-c plane, Sn and Se atoms are bonded by weak interactions along direction a. In particular, the SnSe slabs create a zig-zag and accordionlike projection along the b axis. An easy cleavage in this material can be obtained along the (100) planes.

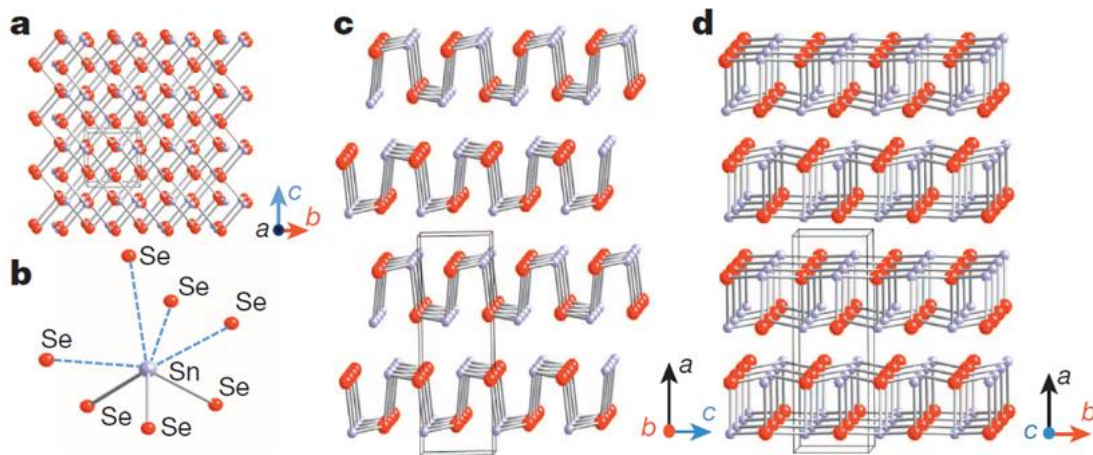


Figure 3.21: a) crystal structure of SnSe along the b-c plane (Sn atoms in grey, Se atoms in red); b) highly distorted SnSe₇ coordination polyhedron with three short and four long Sn–Se bonds; c) crystal structure along the b axis; d) structure along the c axis [154].

Such materials are suitable for thermoelectric solar cells [155], waste heat recovery units [156, 157], power generation [156, 158], flexible nanoelectronics [159], and nanoelectromechanical resonators [160]. Bi₂Te₃ and Bi₂Se₃ nanoplatelets were also used as fillers into nanocomposites for biomedical applications [161], or to enhance thermoelectricity [162-164]. However, such materials were never proposed as nanofillers for ceramic matrix composites for the improvement of electro-mechanical properties. Due to their unique electrical properties, described above, they could be promising nanofillers for the enhancement of the electro-mechanical performances of geopolymer. To this purpose, the knowledge of the mechanical properties of these nanofillers is fundamental for the design, the production, and the characterization of the proposed geopolymeric nanocomposites.

Previous related works on Bi_2Te_3 , Bi_2Se_3 , and SnSe TIs were mostly focused on the optoelectronic and thermoelectric properties [165, 166, 141, 167, 150], while there is a relative lack of research efforts devoted to the mechanical characterization. Several computational studies, employing both classical interatomic potential models and ab-initio calculations, were carried out in order to predict the mechanical properties of such materials along different directions [168-170] but very few experimental investigations were carried out [128, 129, 171]. Moreover, all the proposed experimental characterizations disregarded the anisotropy which characterized the mechanical properties of these materials. In the following section a joint experimental and theoretical investigation of the mechanical properties of Bi_2Te_3 , Bi_2Se_3 , and SnSe is proposed, by taking into account the material anisotropy. The obtained results represent an important starting point for all ambitious future works devoted to the development and characterization of TIs/geopolymers nanocomposites.

3.3.2 Mechanical characterization of topological insulators by nanoindentation and DFT computations

3.3.2.1 Bi_2Te_3

Sample growth

Bi_2Te_3 samples were produced at the Institute of Catalysis and Inorganic Chemistry, ANAS, AZ1143 Baku, Azerbaijan. Single crystalline Bi_2Te_3 ingots were grown from melted polycrystalline material by the vertical Bridgman–Stockbarger method featuring a conical-bottom quartz ampoule sealed under vacuum. In the growth process, the ampoule moves from the “hot” zone (80 K higher than melting point) to the “cold” zone with the required rate of 1.2 mm/h. The temperature of the “cold” zone was about 100 K lower than the melting point. The grown ingot consisted of one or several large single-crystalline blocks, exhibiting chemical inertness toward surface oxidation after exposition up to one month in air, as already shown elsewhere [131]. Figure 3.22 shows the grown ingot sectioned along the direction parallel to the (0001)-oriented surfaces.

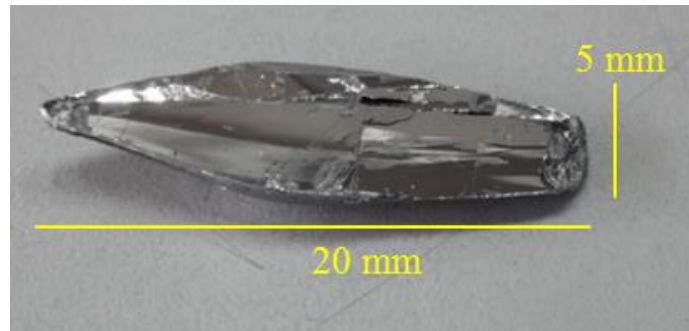


Figure 3.22: Bi_2Te_3 ingot sectioned along the direction parallel to the (0001) plane.

Surface characterization

Sample crystallinity was assessed through XRD experiments carried out using a Bruker D8 ADVANCE diffractometer with Cu-K_α radiation. The c parameter was evaluated by using EVA and TOPAS V3.0 software. The analysis of core levels by XPS was carried out using synchrotron radiation light source at the BACH beamline at Elettra Sincrotrone Trieste S.C.p.A. A Scienta R3000 hemispherical analyzer was employed with an energy resolution ranging from 0.1 to 0.2 eV. The photon energy was set equal to 640 eV, while the XPS spectra were acquired in normal incidence.

The obtained XRD pattern (Figure 3.23) confirmed the formation of single-phase Bi_2Te_3 crystal, which has a rhombohedral lattice of the space group $R\bar{3}m$ [172].

Structural parameters, calculated from the XRD pattern, well agree with previous reports [173]. The clear presence of diffraction peaks of (003), (006), (0015), (0018) and (0021) indicates that Bi_2Te_3 samples are highly c -axis-oriented textured.

The possible presence of oxide phases at the surface of topological insulators could modify the surface properties probed by nanoindentation. In particular, surface mechanical properties could be influenced by the presence of BiO_x and TeO_x oxides arising from the chemical reactivity of vacancy defects toward oxygen. Hence, the analysis of core levels by XPS can provide detailed information

about surface chemical bonds. The eventual presence of oxide phases could be put in evidence by XPS since the occurrence of BiO_x and/or TeO_x would imply core-level shifts compared to core levels of metallic Bi and Te. Figure 3.24 shows a survey XPS spectrum acquired with synchrotron radiation.

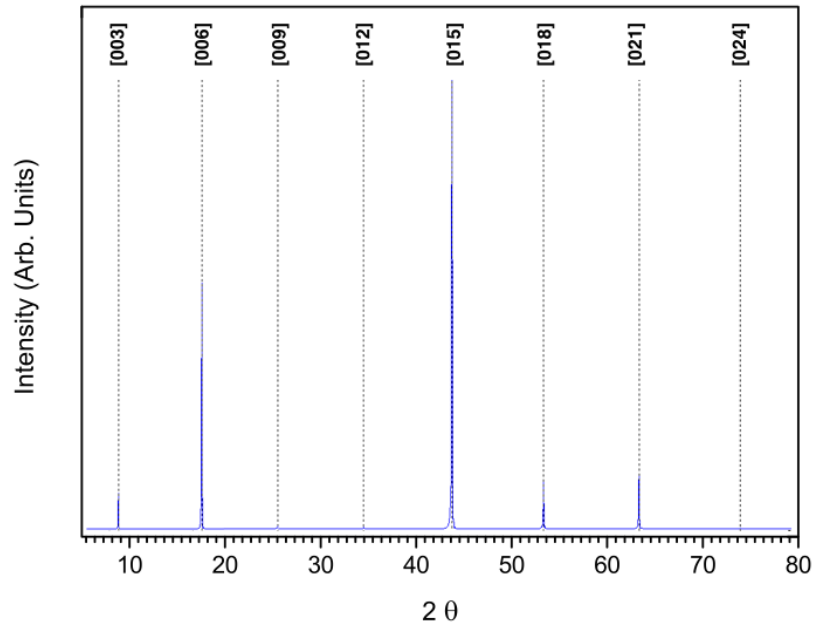


Figure 3.23: XRD pattern of single-crystal Bi_2Te_3 .

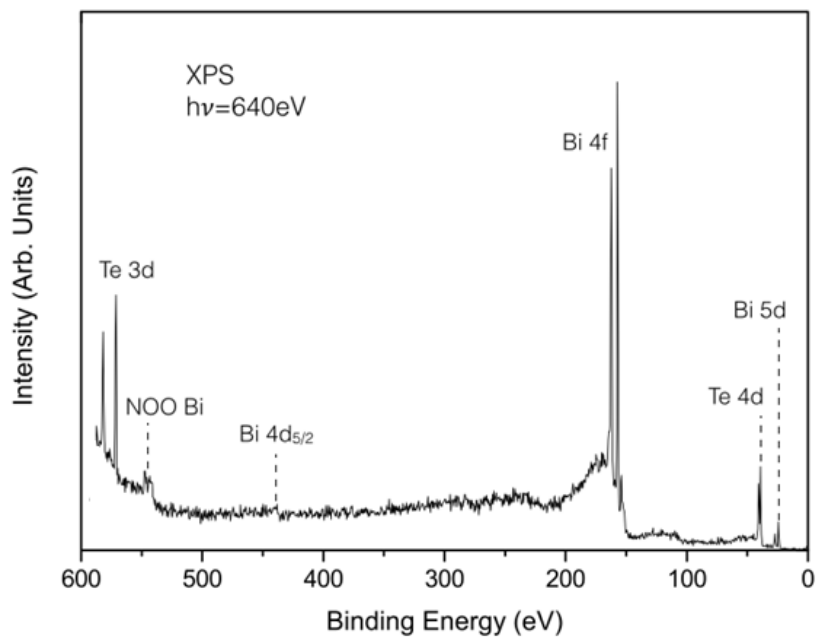


Figure 3.24: XPS spectrum of single crystal of Bi_2Te_3 acquired with a photon energy of 640 eV.

Only core-level or Auger peaks of Bi and Te have been measured. The absence of peaks from O1s and C1s in the XPS spectrum indicates the lack of any contaminant or surface-oxide phase in the outermost surface layers, as also shown by a closer inspection of the line-shape of Bi and Te core levels.

The quality of samples, including the sample crystallinity and absence of contamination, were checked with XRD and XPS. However, sample surface may exhibit different domains and domain boundary on the cleavage plane. AFM acquisitions were then performed on the cleavage plane in order to verify the quality of samples. Figure 3.25 shows the high quality of the sample surface, characterized by superb flatness and large-scale domains whose extension exceeds 20 micron.

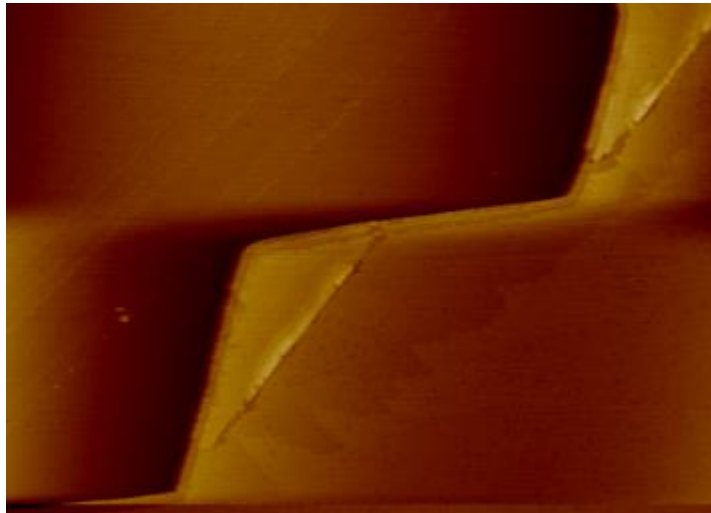


Figure 3.25: Atomic Force Microscopy of the Bi_2Te_3 surface on the cleavage plane.

Figure 3.26 shows the low-energy electron diffraction (LEED) pattern of the Bi_2Te_3 surface. The diffraction of either photons or electrons is a powerful technique for determining surface structure. The diffraction pattern allows to visualize the real-space arrangement of the atoms in a solid or on a surface. In particular, the use of impinging electrons with a low kinetic energy (74 eV) enable the visualization of the reciprocal space of the surface. The hexagonal pattern observed in the reciprocal space is related to the hexagonal symmetry of the atomic arrangement of the surface.

The presence of sharp spots with a reduced background indicates the outstanding crystalline quality of the single-crystal samples, which also reflects into large-scale terraces.

The presence of large-scale domains is also unambiguously supported by the presence of a well-defined Dirac cone in the band structure probed by angle-resolved photoemission spectroscopy.

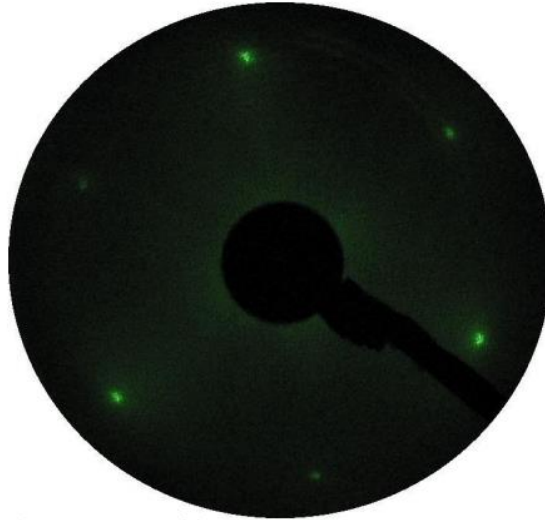


Figure 3.26: low-energy electron diffraction pattern of the Bi₂Te₃ surface, acquired at a primary electron beam energy of 74 eV and at room temperature.

Nanoindentation tests and DFT computations

A. Preliminary nanoindentation tests

Nanoindentation tests were carried out with the equipment described in Section 1.2.3.

A first set of indentation tests were performed in the direction perpendicular to the (0001) basal plane. The single crystals were cut with a scalpel and cleaved, by using a special tweezers, along the basal plane to obtain (0001)-oriented surfaces to be indented. The sample used for nanoindentation experiments had thickness approximately equal to 500 μm . A scotch tape procedure is usually used to obtain fresh (0001)-oriented surfaces of Bi₂Te₃ to be tested, however such procedure is not suitable for the mechanical characterization by means of indentation tests since it creates a non-homogenous cleavage and a rough surface, as shown in Figure 3.27 (b). In order to perform

indentation tests indeed the surface of the sample must be perfectly flat. The surface was then tested immediately after the cleavage process and a perfect flatness was observed, as shown in Figure 3.27

a).

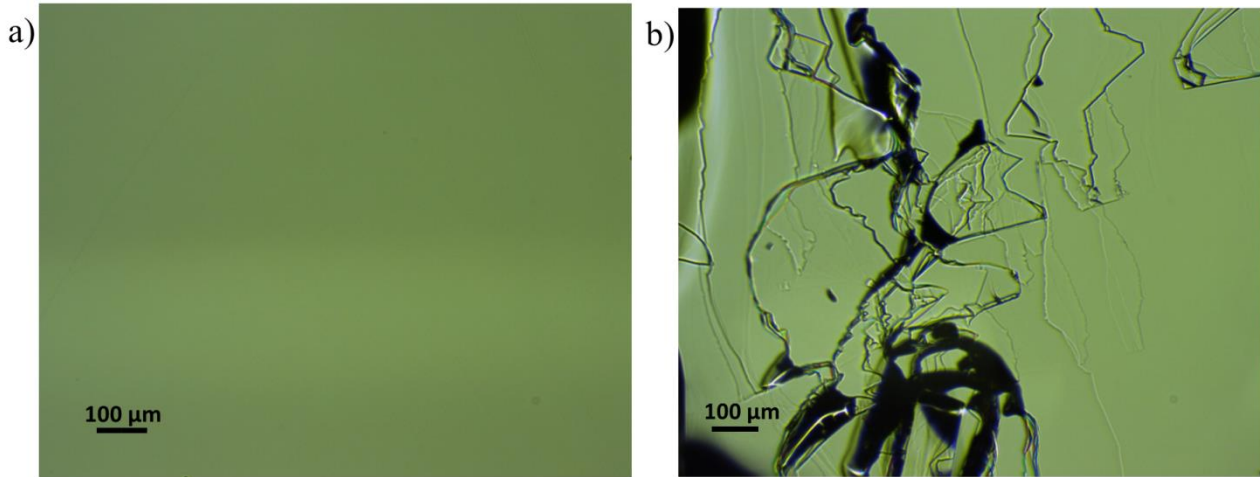


Figure 3.27: Optical micrograph of Bi_2Te_3 (0001)-oriented surface a) after cleavage and b) after cleavage and scotch tape procedure. Whereas with a simple cleavage by means of a special tweezers the surface of the sample is perfectly flat, the addition of a scotch tape process causes an non-homogenous cleavage. In Figure A b) in fact areas with different number of layers can be clearly observed.

Nanoindentations were initially performed using a linear force signal with the Berkovich tip perpendicular to the (0001) basal plane. In particular, a maximum load varying between 10 mN and 30 mN was used in order to identify the load value able to measure the mechanical properties of the material without causing any damage on its surface. Notice that the maximum penetration depth (h) never exceeded 10% of the sample thickness. Therefore, the substrate effect on the outcome of the tests was prevented [174]. However, the results turned out to be unsuitable for the determination of mechanical properties, because of the occurrence of significant cracks and subsurface delamination, as highlighted in the inset reported in Figure. 3.28 (which refers to an indentation performed with a maximum load of 30 mN). The latter, which is likely due to the shear stresses generated at the Berkovich tip edges, induced an asymmetric surface bulging around the indentation area.

The features of the load-depth (P - h) curve, shown in Figure 3.28, can be associated to such damage phenomena and, in turn, testify the brittle behavior of the material. It is worth noting that the P - h

response exhibits several pop-in events, such as those indicated by the arrows, consisting in sudden displacement jumps at a given load level, which are usually related to the nucleation of dislocations and plastic deformations [175], as well as to the formation of cracks [176].

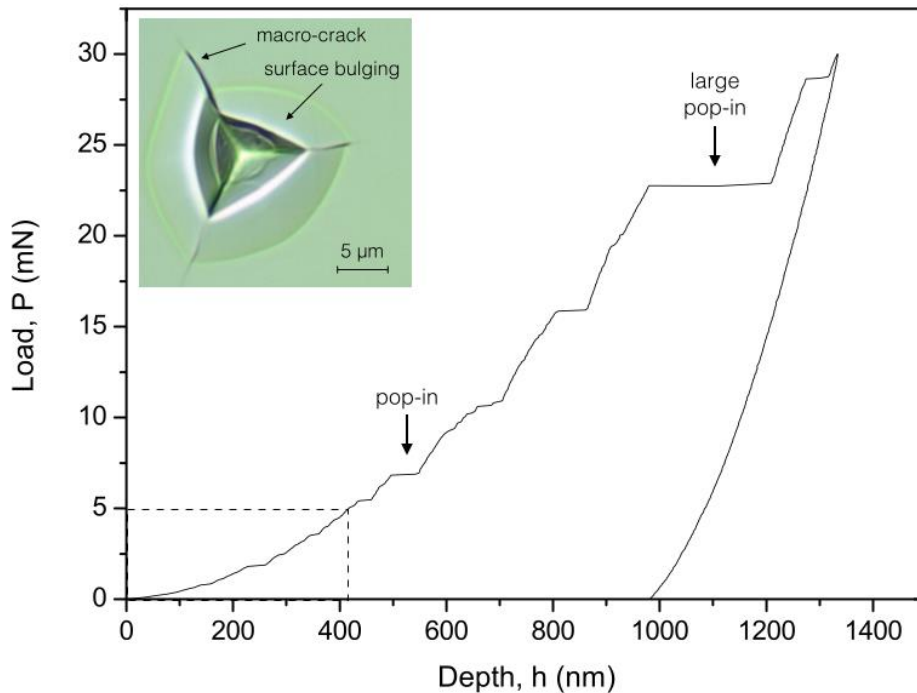


Figure 3.28: Load-depth curve corresponding to the nanoindentation performed at a maximum load of 30 mN. The insert shows the indentation imprint featuring large cracks and surface bulging.

To prevent the detrimental effect associated to the occurrence of cracks and damage, the Continuous Stiffness Measurement (CSM) technique was deployed [177]. The latter is accomplished by superimposing a small sinusoidal varying force (frequency, f , 20 Hz, amplitude, A , 0.5 mN) on the main linear signal, as shown in Figure 3.29. The main linear force (P) signal had a rate of 5 mN/min, a maximum load of 5 mN and an holding time at maximum load of 10 s. The unloading rate was set equal to 20 mN/min. A maximum load of 5 mN was chosen since, as shown in the dashed box in Figure 3.28, no large pop-in phenomena were observed in such range.

A dynamic calibration of the nanoindenter was carried out before testing. In this case, since the indentation depths achieved during the test are much smaller, the extent of the induced damage can

be reduced. The CSM technique allows obtaining the mechanical properties as a function of the indentation depth and, therefore, it can be successfully used to analyze multilayered materials, such as single-crystal Bi_2Te_3 . In particular, indentations were performed setting the maximum load equal to 5 mN, because, as highlighted in the dashed area in Figure 3.28, indentation loads below this value did not induce significant damage or large pop-in events.

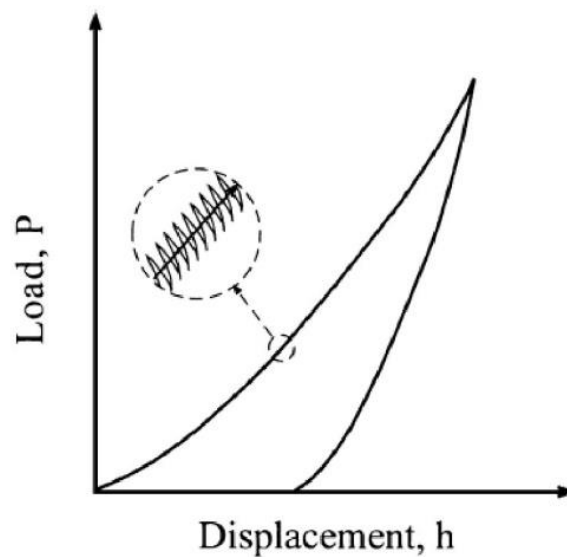


Figure 3.29: Continuous Stiffness Measurement (CSM) indentation technique [177].

The distribution of mechanical properties in the depth direction (perpendicular to the basal plane) was resolved. The obtained values of Young's modulus, E_r , and material hardness, H , are reported in Figure 3.30.

They displayed an initial increase with penetration depth, followed by a decrease toward nearly constant values. Similar behavior was already observed in polycrystalline Bi_2Te_3 thin films [146]. The initial increase was ascribed to the transition from elastic to elasto-plastic contact conditions, whereas the subsequent decrease was related to the establishment of fully plastic contact [146]. It is worth noting that only in the latter case the mean contact pressure can be fairly well represented, thereby providing consistent values of material properties. The results of five consecutive tests were averaged after the establishment of fully plastic contact conditions ($h \approx 100$ nm) and the reduced

Young's modulus and the hardness were found to lie in the range $E_r=(32.4\pm 2.9)$ GPa and $H=(1.6\pm 0.2)$ GPa, respectively. These values can be reasonably assumed to be intrinsic material properties of the single crystal within the depth range $\approx(100\div 400)$ nm. The data scatter is related to the occurrence of pop-in events, whose signature is also highlighted by the arrows reported in the inset of Figure 3.30, which caused a few drops in the values of the mechanical properties. Although a few pop-in events still occurred in the above range, it is emphasized that the analysis of indentation imprints indicated that significant cracks and/or damage phenomena, such as those reported in Figure 3.28, were absent.

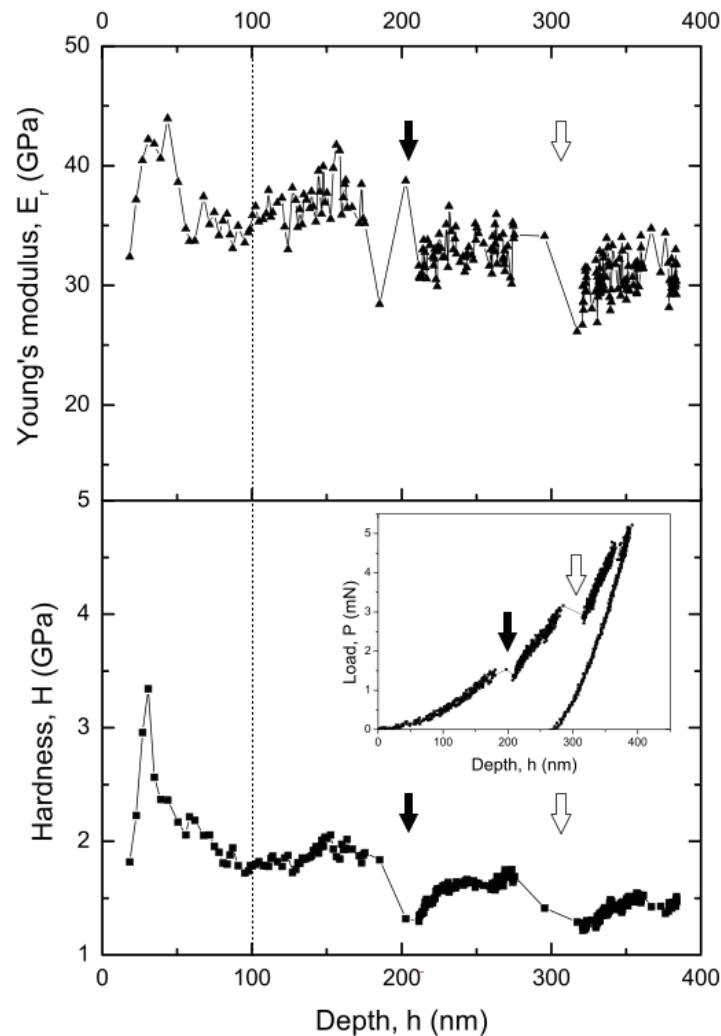


Figure 3.30: Distribution of reduced Young's modulus and material hardness as a function of the penetration depth obtained using the CSM technique with a maximum load equal to 5 mN. The insert shows the corresponding load-depth response.

It should be noted that pop-ins were also reported during CSM nanoindentations carried out on Bi₂Te₃ polycrystalline thin films and were ascribed to the nucleation of dislocations [178]. However, the ones observed here, which occurred at significantly higher penetration depth, might be rather associated to shear induced delamination and micro-cracking within the damage volume of material beneath the indenter tip.

It is now interesting to compare the obtained values of mechanical properties with those reported in recent literature works. Tasi et al. [179] analyzed Bi₂Te₃ polycrystalline thin films grown by laser ablation by using the nanoindentation technique. They found $E_r=(121.5\pm 9.2)$ GPa and $H=(4.02\pm 0.14)$ GPa. The difference with respect to the values herein obtained can be associated to the effect of grain boundaries, which inhibit dislocations mobility in polycrystalline films [179]. Conversely, Guo et al [128] analyzed the elastic properties of Bi₂Te₃ 2D nanosheets, grown by van der Waals epitaxy, by means of atomic force microscopy-based indentation. They analyzed samples with thicknesses ranging from 5 to 14 quintuple-layers (1QLs \approx 1nm) and they found that the reduced Young's modulus was independent on sample thickness and was lying in the range (19.5 \pm 7.0) GPa. This value is lower than that found herein and the difference is related to the presence of crystal defects, such as antisites and/or vacancies, which are associated to the employed growth process in Ref. [128].

B. Fracture toughness evaluation

B.1 Selection of the model for the indentation fracture toughness evaluation of bulk Bi₂Te₃

The estimation of fracture toughness of brittle materials by indentation with a Vickers tip was firstly performed by Palmqvist [180], who studied the radial crack propagation and noted that the crack length l (measured from the corner of each imprint, as shown in Figure 3.31) varied as a linear function of the indentation load, P . Subsequently, half-penny cracks were also addressed in Ref. [181] and therein it was observed that the ratio $P/c^{3/2}$ (with c measured from the center of contact to

the end of the crack corner) is constant and depends on the material properties. The fracture toughness was then estimated through the following equation [181]:

$$K_c = k \left(\frac{E}{H} \right)^n \frac{P}{c^{3/2}} \quad (3.1)$$

where E is the elastic modulus, H the hardness, and k and n are empirical calibration constants that have been set equal to 0.016 and 0.5, respectively.

Additional studies proposed refined estimations of these empirical calibration constants through fitting the results obtained in conventional tests [182]. The different behavior observed between radial and half-penny cracks allows allocating them into two main groups.

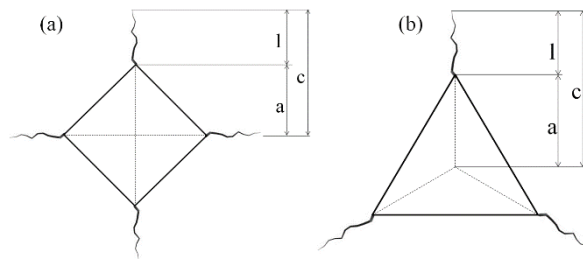


Figure 3.31: Indentation induced crack geometries for (a) Vickers and (b) Berkovich tip.

Laugier [183] reviewed existing experiments and determined that the relationship for the half-penny cracks can also be applied to materials exhibiting radial cracking whenever $c/a > 2.5$ (where a is measured from the center of the contact to the corner of the imprint). This suggests that local conditions near the intersection of the crack front and the material surface remain relatively unchanged for both crack typologies. The fracture toughness equation for radial crack extension, proposed by Laugier, may be written as [181]:

$$K_c = x_v \left(\frac{a}{l}\right)^{1/2} \left(\frac{E}{H}\right)^{2/3} \frac{P}{c^{3/2}} \quad (3.2)$$

with $x_v = 0.015$. By comparing Equation (3.2) with Equation (3.1) one can observe that Laugier [183] introduced the $(a/l)^{1/2}$ term. This term experimentally exhibits only slight variation between glasses (half-penny cracks) and ceramics (radial cracks) and a mean value of 0.68 was measured for different materials.

The vast majority of the models employed for determining the fracture toughness through instrumented indentation is performed with a Vickers diamond pyramid indenter; however, it is not suitable for nanoscale characterization, for which the Berkovich indenter is the most common choice. While the symmetrical geometry of the Vickers tip can induce both halfpenny and radial cracks, the asymmetric shape of the Berkovich tip does not allow the cracks to conform the halfpenny configuration, i.e. the cracks do not join two corners of the imprint and to pass through the center of the indentation. Therefore, the formation of radial cracks is more likely to occur.

Dukino and Swain [184] modified Laugier's model [183] with a correction factor, originally proposed in Ref. [185], in order to accommodate the treatment of crack geometry induced in Berkovich tip geometry:

$$K_c = 1.073 x_v \left(\frac{a}{l}\right)^{1/2} \left(\frac{E}{H}\right)^{2/3} \frac{P}{c^{3/2}} \quad (3.3)$$

They studied the different effect associated to the use of Vickers and Berkovich indenters on the determination of fracture toughness in brittle materials. They found that at low indentations loads (lower than 1 N) a Vickers indenter induces c/a ratios less than 2.5 and, as observed by Laugier [183], whenever $c/a < 2.5$, K_c is no longer proportional to $P/c^{3/2}$ and Equation (3.2) cannot be used for toughness evaluation. Conversely, when a Berkovich indenter was used, the measured c/a ratio

was usually equal to or greater than 2.5, also for very low indentation loads. It is then apparent that the Berkovich tip is more suitable for the determination of fracture toughness using Laugier's model [183].

The model proposed by Dukino and Swain [184], which can be considered an extension of Laugier's model [183] to a Berkovich tip, is deemed suitable for the analysis of Bi_2Te_3 bulk single crystal, as described in Section B.2.

B.2 Results and Discussion

Preliminary tests were carried out at different load levels in order to identify the most suitable model for the determination of fracture toughness. Cracks were already observed at very low applied load (≤ 10 mN), and the c/a ratio was usually equal to or greater than 2.5. The measured c/a ratio indicated that the use of Laugier's model is therefore appropriate [183]. This choice obviated the issues related to the identification of the actual crack geometry (half-penny or radial). Moreover, the occurrence of cracks at very low loads suggested the use of the Berkovich tip since, as highlighted in Section B.1, Dukino and Swain [184] showed that the Vickers tip is unsuitable for the determination of the fracture toughness at loads lower than 1 N. Their model [184], that adapts the Laugier's model [183] to the Berkovich tip geometry, is thus the most suitable for the estimation of the fracture toughness of the analyzed material.

A set of 30 nanoindentations with increasing load was performed in order to calculate the fracture toughness of the bulk Bi_2Te_3 , according to Equation (3.3). In particular, the maximum load varied from 1 to 30 mN, with increments of 1 mN, whereas the loading rate and the holding period at the maximum load were kept constant at 5 mN/min and 10 s, respectively. The indentations were placed at a distance of at least three times the largest dimension of the imprint in order to avoid the mutual influence of close indentations [186]. Figure 3.32 (a) shows the SEM picture of the imprint

for the nanoindentation performed with a maximum load of 12 mN, whereas Figure 3.32 (b) shows the corresponding load-penetration depth curve.

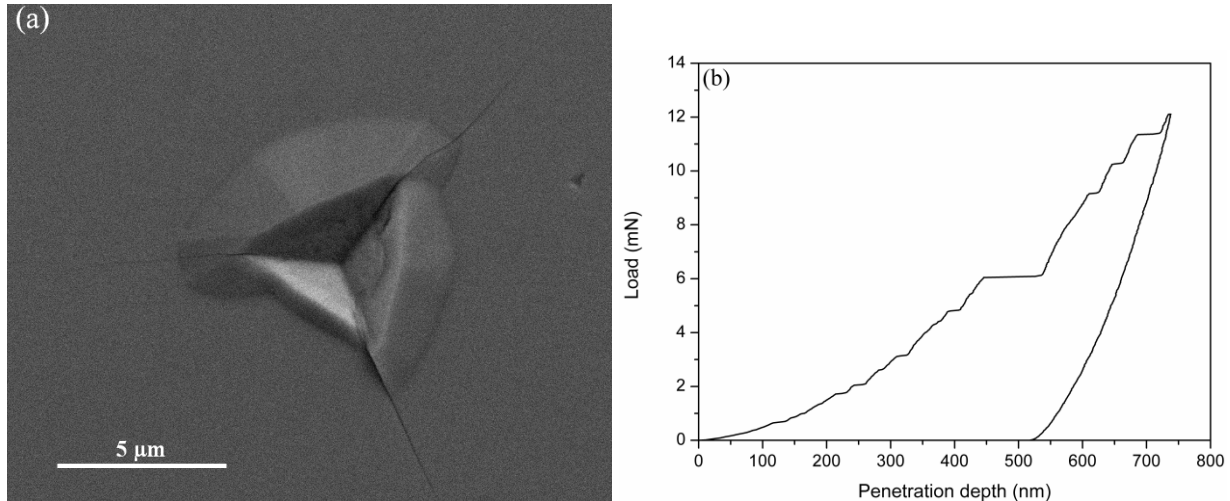


Figure 3.32: (a) Berkovich imprint and (b) load-penetration depth curve for the nanoindentation with a maximum load of 12 mN.

Figure 3.32 (a) displays significant cracks arising from the corners of the imprint, whose length can be determined from SEM analysis and used in Equation (3.3). The occurrence of cracks is also testified by the load-penetration response which features several pop-in phenomena, consisting in sudden displacement increases at a certain load level. As already observed in previous related works, these displacement jumps are related to the occurrence of cracks [187] or the nucleation of dislocations [188].

The values of reduced Young modulus and hardness obtained in Section A ($E_r=(32.4\pm 2.9)$ GPa and $H=(1.6\pm 0.2)$ GPa) was used for the calculation of K_c . A Poisson's ratio of 0.25 was assumed [129]). It is worth noting that the measured value of the hardness is much higher than the previously reported value for Bi_2Te_3 bulk samples [139, 140]. Such a difference is due to the dissimilar microstructure of tested materials. In details, samples analyzed in Ref. [140] are sintered polycrystals, whereas in the present study high-quality single crystals, grown with the Bridgman-Stockbarger method are investigated. However, apart from differences in the crystalline structure,

any comparison is inappropriate, since different characterization scale were used. Indeed, the hardness values proposed above refer to instrumented nanoindentation tests performed with a Berkovich tip and an indentation load of 5mN, whereas in Ref. [140] a Vickers hardness tester and a load of 4.9 N were used. Moving from the nano- to the macro-scale, a change of measured mechanical properties, due to the presence of defects in the larger amount of analyzed material volume, is often observed during mechanical characterization by means of indentation tests [189].

For each imprint characterized by cracks, the values of a and l (Figure 3.31) were obtained as the average of three measurements. The parameter c was calculated as the sum of a and l . Figure 3.33 shows the plot of $c^{3/2}$ versus the applied indentation load. One can observe that the relationship is approximately linear, as expected from the Equation (3.3). Figure 3.34 demonstrates that the model proposed by Dukino and Swain [184] represents the most suitable one for the tested material. Indeed, it can be observed that when $c/a \geq 2.5$ (dashed line) the term $(a/l)^{1/2}$ tends to 0.68, that is the very same value already found for glasses (half-penny cracks) and ceramics (radial cracks), on which the Laugier model [183] was applied, as discussed in Section B.1. This result allows us to use the Laugier's model [183] by neglecting the crack geometry identification. In addition, the stabilization of K_c for $a/c > 2.5$ further confirms the consistency of the chosen model for the determination of fracture toughness.

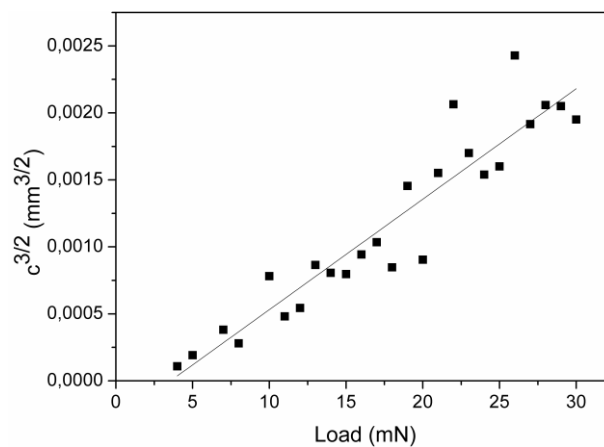


Figure 3.33: Plots of $c^{3/2}$ versus load for the performed nanoindentations.

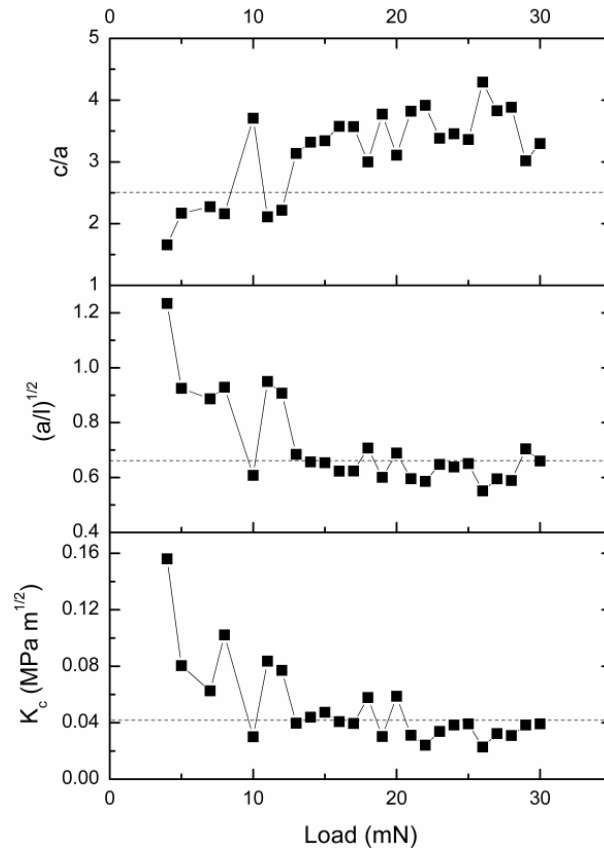


Figure 3.34: c/a , $(a/l)^{(1/2)}$ and K_c of Bi_2Te_3 (estimated by the model in Ref. [56]) for different indentation loads.

By inspecting Figure 3.34, one can notice that for low loads (up to 13 mN) the aforementioned conditions are unsatisfied. As a matter of fact, for these indentations undesired crack configurations were observed, as shown in Figure 3.32 (a) and 3.35 (a). The high shear stresses induced by the indenter edges caused subsurface delamination cracks, symmetric (Figure 3.35 (a)) or asymmetric (Figure 3.32 (a)), which induced surface bulging around the indentation area. In these cases, crack nucleation and propagation is not conforming to any of the indentation fracture toughness models, thereby leading to potential inaccurate estimates of fracture toughness [190]

On the other hand, for maximum applied loads ranging from 13 to 30 mN, the theoretical crack configuration was achieved, like that shown in Figure 3.35 (b), and, as shown in Figure 3.34, a stable value for K_c was obtained. The fracture toughness of Bi_2Te_3 bulk single crystal was then

estimated to be equal to $0.042 \pm 0.016 \text{ MPa } \sqrt{\text{m}}$. As a comparison, graphite shows values 12-25 times higher [191, 192].

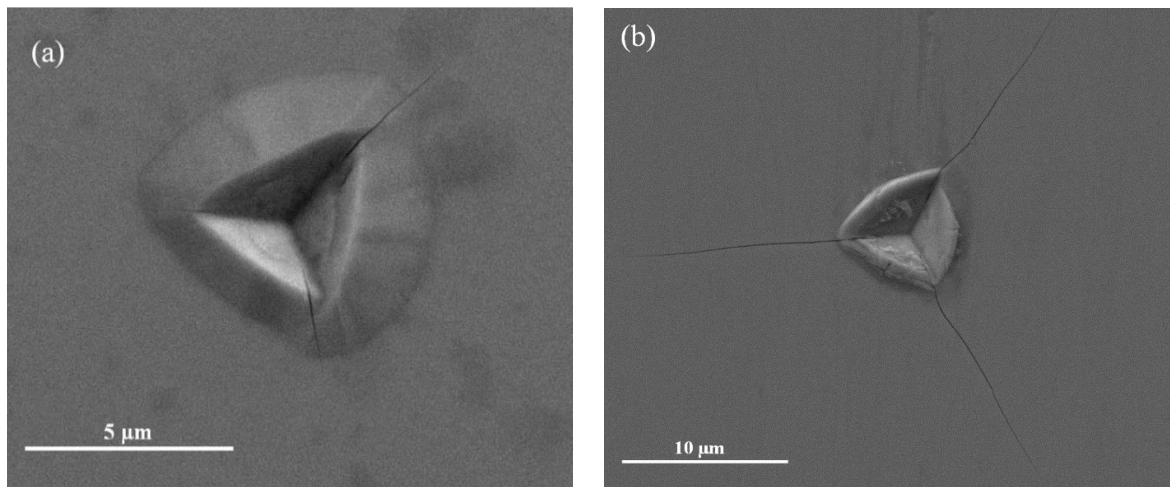


Figure 3.35: Berkovich imprints for the nanoindentation with a maximum load: (a) 7 mN and (b) 26 mN.

A comparison with sintered polycrystals [140] would not be straightforward for the same reasons mentioned concerning differences in the values of the hardness. Moreover, sintered polycrystals of Bi_2Te_3 are not topological insulators, since they do not show massless Dirac fermions and high charge mobility, which are at the basis of the huge technological potential of topological insulators. Samples with thickness lower than $1 \mu\text{m}$ in principle could be probed by indentation with atomic force microscopy. However, it should be recognized that the main characteristic of topological insulators, i.e. the occurrence of topological surface states, is absent in the limit of the single quintuple-layer (QL) Bi_2Te_3 unit [193], which does not behave as a topological insulator. As a matter of fact, in 1 QL regime, bismuth chalcogenides exhibit energy gap opening [194] and topologically trivial behavior [195]. By increasing the thickness, a well-defined Dirac cone appears in correspondence of 6 QLs [194], showing negligible variation with the number of layers [196]. It should be noted that the maximum penetration depth reached in the present indentation tests was approximately equal to $1 \mu\text{m}$. In the vast majority of the application fields of Bi_2Te_3 bulk single crystal, the thickness rarely goes above such value [197]. Hence, the nanoindentation test, in the

selected load range, can represent a convenient methodology for the evaluation of the fracture toughness of such materials.

C. Theoretical and experimental investigation by taking into account the material anisotropy

The indentation investigations presented in the previous sections disregarded the anisotropic behavior of bismuth chalcogenides since the tests were carried out only in the direction perpendicular to the (0001) basal plane. Furthermore, it is important to notice that the mechanical properties of Bi_2Te_3 have been evaluated within the framework of the model by Oliver and Pharr [198, 199], which has been developed for isotropic materials. A more careful treatment of nanoindentation data is then required in order to properly describe the anisotropic mechanical properties of Bi_2Te_3 . To this purpose a joint experimental and theoretical investigation of mechanical properties of bulk single crystals of Bi_2Te_3 was carried out by taking into account the material anisotropy. In particular, depth sensing nanoindentation tests were performed along two different directions, parallel and perpendicular to the basal plane (as shown in Figure 3.36), in order to measure the indentation Young's modulus. Density functional theory (DFT) calculations, with different exchange-correlation functional approximations, were performed in order to obtain the stiffness matrix of Bi_2Te_3 and, subsequently, a theoretical estimate of the indentation modulus by using the model developed in Ref. [200].

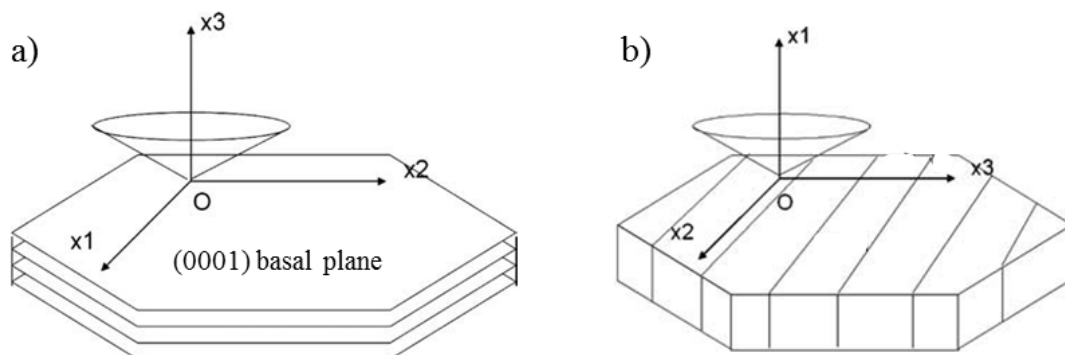


Figure 3.36: Schematic representation of two different indentation directions: a) perpendicular and b) parallel to the (0001) basal plane.

C.1 Computational details

Bi_2Te_3 has a rhombohedral crystal structure with five atoms per unit cell. It belongs to the D_{3d}^5 (R-3m) space group. The structure consists of covalently bonded quintuple layers [Se(1)-Bi-Se(2)-Bi-Se(1)] separated by weak Van der Waals bonds (Figure 3.37).

The structural and elastic properties of Bi_2Te_3 were calculated using DFT, as implemented in the QUANTUM-ESPRESSO package [201], using a norm conserving scalar relativistic pseudopotentials with only the outermost s and p states in valence band. Both the local density approximation (LDA) [202] and the generalized gradient Perdew-Burke-Ernzerhof (PBE) [203] approximation for the exchange-correlation energy functional were used. A semiempirical Van der Waals correction, as described in Ref. [204], was added in the case of PBE approximation. The electronic wave functions were expanded in plane waves up to a 90 Ry energy cut-off. The bulk geometry was optimized using the non-elemental hexagonal cell and by integrating the Brillouin zone over a $8 \times 8 \times 2$ Monkhorst-Pack mesh [205]. Atomic positions were relaxed until the forces were below a $5 \cdot 10^{-5}$ a.u. threshold. The lattice parameters for the optimized geometries are reported in Table 3.3 compared with the experimental values.

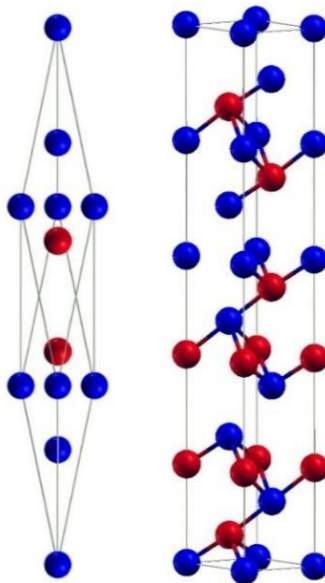


Figure 3.37: Unit cell (rhombohedral) and conventional cell (hexagonal) of Bi_2Te_3 . Bismuth atoms are represented in red, tellurium atoms in blue.

Table 3.3: equilibrium lattice parameters

	Experimental values	LDA	PBE+VDW
Lattice parameters [Å]	a=4.38 c=30.50	a=4.33 c=29.82	a=4.31 c=30.94

The obtained values of equilibrium lattice parameters for both LDA and PBE+VDW are in good agreement with experimental values [206] within an error of 1.1% and 1.5% in the two cases, respectively, and, moreover, with previous ab-initio calculations [207].

The elastic constants were evaluated from the stress-strain relation, following the procedure described in Refs. [208, 209] and applying deformations from 0.2% to 2%.

C.2 Model for the estimation of the indentation modulus for anisotropic materials

Oliver and Pharr theory (described in section 1.2.3) allows the calculation of hardness and Young's modulus of materials by indentation. However, this theory is related to homogeneous and isotropic materials and it has to be modified when an anisotropic material is analyzed by means of indentation tests.

Vlassak and Nix [210] studied the contact problem of a flat circular punch and a paraboloid on an elastically anisotropic half space and they showed that Equations (1.14) and (1.15) can be used for anisotropic materials as long as the half space has three or fourfold rotational symmetry. In the case of lower symmetry, the indentation modulus depends on the shape of the indenter. Subsequently, they proposed [211] a relation in order to estimate the indentation modulus E_r from the stiffness matrix of an arbitrary anisotropic solid (alternative to Equation (1.3)). However, such a relation is a really complex and it can be analytically solved only in particular cases, such as for transversely

isotropic materials [212]. Recently, Vlassak et al [200] simplified relation of Ref. [211] and suggested a simple equation for the estimation of the indentation modulus:

$$M = \frac{1}{\pi h_0} \quad (3.4)$$

where h_0 is the first term of the Fourier series expansion of surface Green's function and it can be obtained from the elastic constants C_{ij} of the anisotropic material. Model in Ref. [198] was generalized for indenters of arbitrary shapes and verified on different anisotropic materials, also on solids with a R-3m symmetry, like Bi_2Te_3 single crystal analyzed in this work. For these reasons, this model was chosen in order to estimate the theoretical indentation modulus of bulk Bi_2Te_3 by using C_{ij} constants calculated by DFT. The estimated modulus was then compared with the experimental one, obtained by means of nanoindentation tests .

The constant h_0 is also related to the angle between the tip's axis and the material basal plane. Indentations were performed only along the directions parallel and perpendicular to the Bi_2Te_3 basal plane because in these directions samples are easier to cut and prepare for the indentation test.

C.3 Indentation tests

Nanoindentation tests were performed with the equipment described in section 1.2.3 provided with a spherical tip ($R = 20\mu\text{m}$, $\alpha = 90^\circ$) and the mechanical properties, i.e. hardness (H) and the reduced Young's modulus (E_r), were determined in the directions perpendicular and parallel to the (0001) basal plane.

In particular, the Continuous Stiffness Measurements (CSM) technique [177] was deployed.

For the direction parallel to the basal plane the following indentation parameters were set: amplitude of the sinusoidal varying force 0.5 mN, frequency 20 Hz, maximum load 5 mN, loading rate 5 mN/min, unloading rate 20 mN/min, holding time at maximum load 10 s.

For the direction perpendicular to the basal plane the following parameters were used: amplitude of the sinusoidal varying force 1 mN, frequency 20 Hz, maximum load 10 mN, loading rate 10 mN/min, unloading rate 40 mN/min, holding time at maximum load 10 s.

A dynamic calibration of the nanoindenter was carried out before testing, whereas the distance between each indents was kept at least three times the maximum diagonal of the imprint in order to avoid the mutual influence of adjacent indentations.

The mechanical properties were obtained according to the Oliver and Pharr theory [198, 199]. In particular, the experimental indentation modulus was obtained according to Equation (1.14).

C.4 Results and discussion

Bulk Bi_2Te_3 is a layered anisotropic material and, thus, it is characterized by different mechanical properties along different directions.

DFT calculations, with the parameters described in section C.1, were carried out in order to put in evidence the anisotropic behavior of mechanical properties. In Table 3.4, the six independent coefficients of the stiffness matrix of Bi_2Te_3 , obtained with both the LDA approximation and the PBE approximation with the semiempirical Van der Waals correction (PBE+VDW), are reported and compared with data available in literature.

The analysis of data in Table 3.4 indicates that LDA well reproduces the experimental values of C_{12} and C_{13} , while PBE-VDW better reproduces C_{11} . On the other hand, the theoretical model in Ref. [214] is appropriate for reproducing C_{14} , C_{44} and C_{66} and it also fails for C_{11} , C_{12} , and C_{13} .

The corresponding indentation moduli, along directions parallel and perpendicular to the c axis of the hexagonal cell, calculated according to Equation (3.4) by using C_{ij} constants in Table 3.4, are reported in Table 3.5.

Table 3.4: Comparison of calculated and experimental elastic modulus C_{ij}

	C_{11}	C_{12}	C_{13}	C_{14}	C_{33}	C_{44}
LDA (our work)	81.5	22.2	31.2	19.4	56.4	42.7
PBE-VDW (our work)	78.3	13.8	23.2	20.7	35.7	35.5
Experiment Ref. [213]	74.4	21.7	27.0	13.3	47.7	27.4
DFT, Ref. [214]	65.4	14.0	19.0	10.9	50.7	26.5

Table 3.5: Comparison of calculated indentation moduli

	Perpendicular to the lamellae (GPa)	Parallel to the lamellae (GPa)
LDA (our work)	60.21	69.45
PBE-VDW (our work)	42.46	62.40
Experiment Ref. [213]	47.71	59.74
DFT, Ref. [214]	51.26	57.67

To experimentally validate computational results, nanoindentation test were carried out (according to methodologies listed in Section 2.4).

In Figure 3.38 the trend of the reduced Young's modulus E_r as a function of the penetration depth is shown for both the indentation directions, perpendicular (top panel) and parallel (bottom panel) to the cleavage plane. One can observe that for the direction perpendicular to the cleavage plane, when E_r stabilizes, it reaches exactly the value of the indentation modulus calculated using the PBE+VDW approximation. The value of the indentation modulus estimated with the LDA approximation is instead considerably higher than the experimental one. This can be ascribed to the

problem of over-binding usually shown by the LDA approximation that lead to higher binding energies and shorter bond lengths with respect to the experimental ones and that becomes particularly relevant in presence of weak Van der Waals bonds.

As shown in Figure 3.38, the indentation moduli estimated by using data reported in literature lie in the middle of the range defined by our LDA and PBE+VDW calculations.

Along the direction parallel to cleavage plane (bottom panel) all calculated values of E_r are rather higher than the experimental value after data stabilization.

In order to explain these differences along the two directions of indentation, considerations about the effect of the indentation process on layered materials have to be carried out.

Different studies about the indentation of layered material were proposed [215-217]. In particular, it was observed that along the direction perpendicular to the cleavage plane the formation of kink bands can occur [216]. Kink bands are walls of dislocations of opposed polarity which develop on the indented material after the contact with the tip and they cause the delamination of material's layers. Such delamination can be observed on the indented sample as a surface bulging around the indentation area and it mainly occurs with sharp tips and high indentation loads, as observed in [218]. This damage can be also observed in the load-penetration depth curve, characterized by pop-in phenomena [218].

For this work, as described in Section C.3, indentation tests were performed with a spherical tip at very low loads by using the CSM technique in order to avoid the material damage during the indentation process which could lead to a wrong estimation of mechanical properties. Any damage was indeed observed on the indented samples, as well as any pop-in phenomena was recorded in the load-penetration depth curves. Indentation experimental results can thus be compared to the computational one.

Along the direction parallel to the cleavage plane instead, some studies carried out on pyrolytic carbon [215, 217] showed the occurrence of elastic nanobuckling of the material layers also for low

indentation loads. The discrepancies observed in the bottom panel of Figure 3.38 between theoretical and experimental results can thus be related to the nanobuckling induced during the indentation process that leads to an underestimation of mechanical properties.

Also the measured value of hardness is lower in the direction parallel to the cleavage plane (Figure 3.39). For the perpendicular direction (top panel), the hardness stabilizes around 1.7 GPa whereas its saturation value is about 0.9 GPa in the parallel direction (bottom panel). As observed for the Bi_2Te_3 thin films [219], the hardness has an initial increase at small penetration depth, attributed to the transition between purely elastic to elastic/plastic contact, and a following decrease until a stabilized value, related to the transition between elastic/plastic and fully plastic contacts.

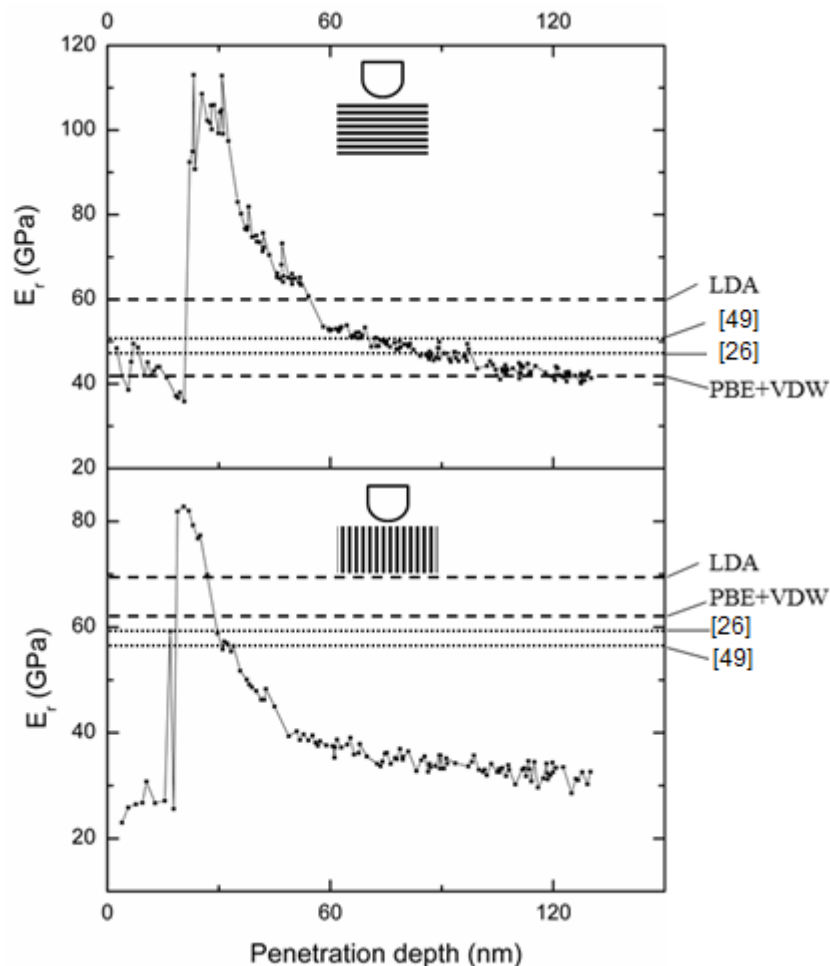


Figure 3.38: E_r profile with increasing values of penetration depth for a CSM nanoindentation carried out along the direction perpendicular (top panel) and parallel (bottom panel) to the cleavage plane. The dashed lines represent the indentation modulus calculated according to Equation (3.4) using constants C_{ij} calculated with the LDA and PBE+VDW approximations, whereas the dotted lines refer to constants C_{ij} reported in literature.

Until the fully plastic contact is not reached, the measured hardness is actually reflecting the mean contact pressure and it does not represent the intrinsic hardness of the material.

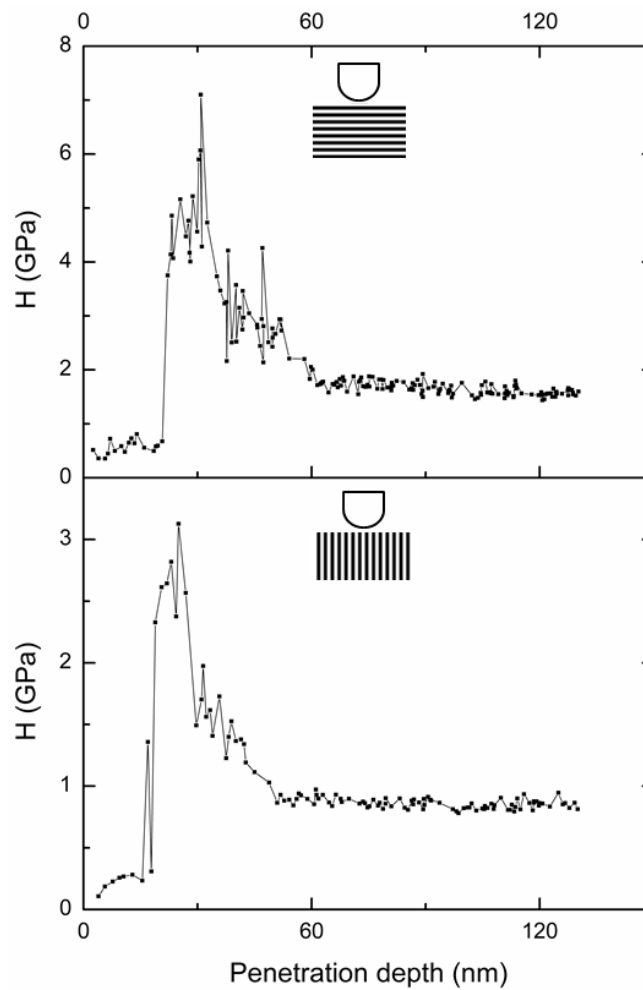


Figure 3.39: H profile with increasing values of penetration depth for a CSM nanoindentation carried out along the direction perpendicular (top panel) and parallel (bottom panel) to the cleavage plane.

3.3.2.2 Bi_2Se_3

Surface characterization

Single crystalline samples of Bi_2Se_3 , grown with the Bridgman-Stockbarger method, have been purchased from a commercial supplier. The crystalline quality has been checked by means of low-energy electron diffraction (LEED). Angle-resolved photoemission spectroscopy (ARPES) has been

used to ensure about the presence of the spectroscopic fingerprint of the TI phase, i.e. the Dirac cone, in the samples.

X-ray photoemission spectroscopy (XPS) has been used to check the presence of contaminants or surface oxides and results are shown in Figure 3.40. The absence of signal from O 1s and C 1s in the XPS spectrum of Bi_2Se_3 excludes the presence of any contaminant in the topmost layers of the surface, also confirmed by the inspection of the line-shape of Bi and Se core levels.

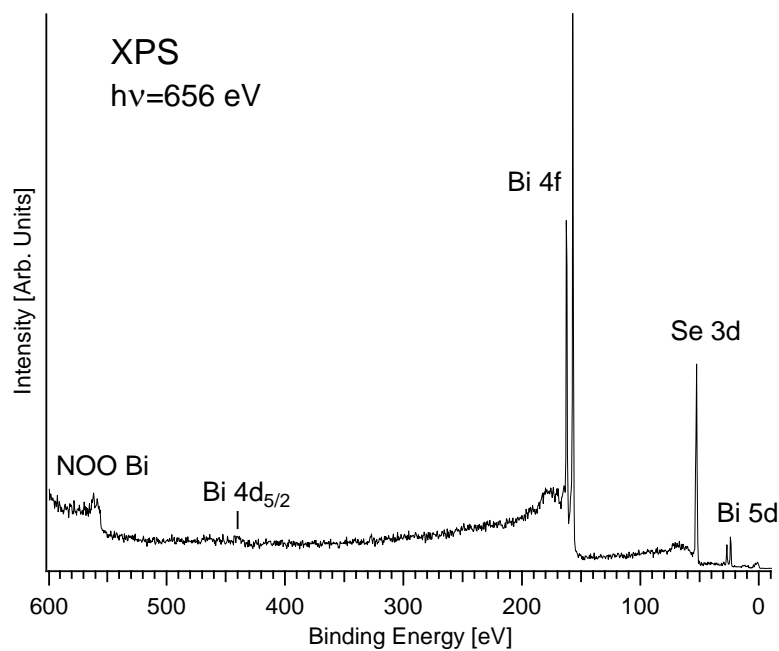


Figure 3.40: XPS spectrum of Bi_2Se_3 .

Nanoindentation tests and DFT computations

The single crystals were cut and cleaved along the basal plane to obtain (0001)-oriented surfaces to be indented, as described in Section 3.2.1.3 A for Bi_2Te_3 . The same procedure describe in Section 3.2.1.3 C was adopted for the evaluation of the mechanical properties of Bi_2Se_3 by means of DFT computations and indentation tests. However, only the direction perpendicular to the (0001) basal plane was indented. Figure 3.41 shows experimental results obtained by means of a CSM nanoindentation test performed according to the following parameters: amplitude of the sinusoidal

varying force 1 mN, frequency 20 Hz, maximum load 10 mN, loading rate 10 mN/min, unloading rate 40 mN/min, holding time at maximum load 10 s. One can observe that the reduced Young modulus stabilizes to a value of approximately 6 GPa whereas the hardness is equal to 0.48 GPa. In this case no damage was observed on the surface of the sample, as testified in Figure 3.42. In Figure 3.42 a) it is worth noting that no pop-in events occurred in the load-penetration depth curve, whereas Figure 3.42 b) shows that no cracks or surface bulging was observed around the indentation imprint.

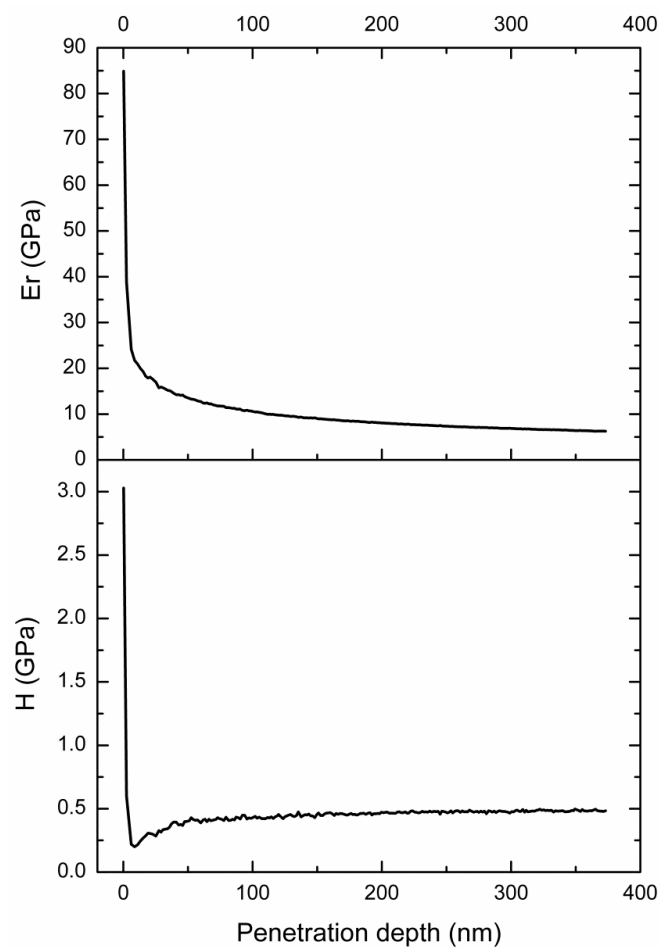


Figure 3.41: E_r (top panel) and H (lower panel) profile with increasing values of penetration depth for a CSM nanoindentation carried out along the direction perpendicular to the cleavage plane.

However, concerning indentation modulus, the measured value is quite far from theoretical predictions. A value of 57.7 GPa was obtained from Equation 3.4 by computing the C_{ij} constant with DFT simulation, using the PBE-VDW approximation (and the same computational details

described in Section 3.3.2.1 C1 for Bi_2Te_3). On the other hand, nanoindentation experiments [171] on bulk samples of Bi_2Se_3 grown by the vertical Bridgman high-temperature melt technique provided a value of the Young's modulus of 6.361 GPa and hardness of 0.85 GPa for the (001) plane. Such experimental results are then very close to those shown in Figure 3.41.

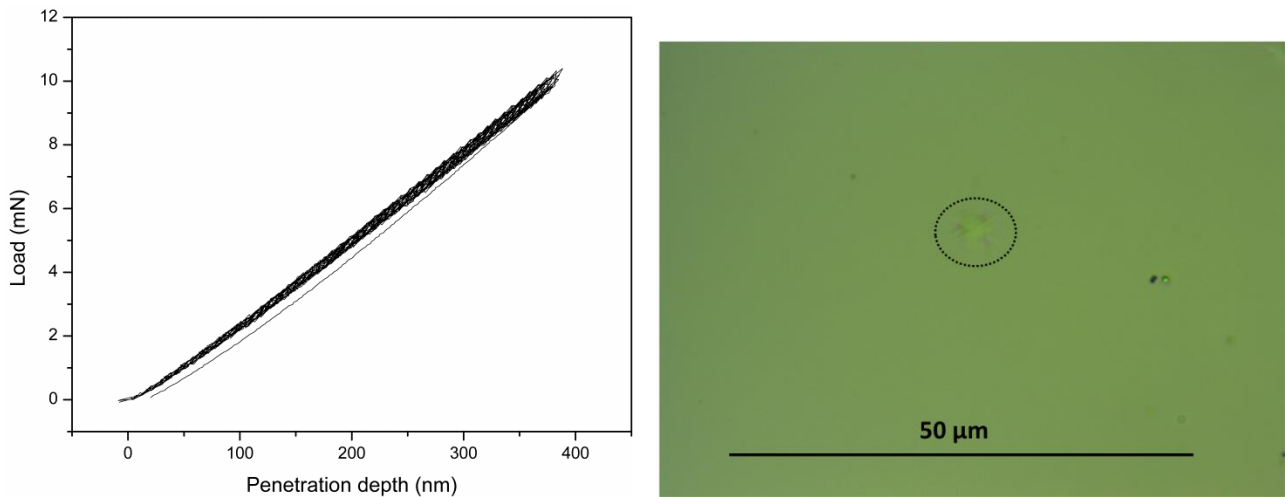


Figure 3.42: a) indentation curve and b) imprint for a CSM nanoindentation performed with a maximum load of 10 mN.

3.3.2.3 SnSe

Growth and surface characterization

Single crystals of SnSe have been grown by means of the chemical (iodine) vapor transport. A mixture of elements 99.99% pure Sn and Se was put in a quartz ampoule with an iodine capillary. The ampoule was slowly cooled, evacuated to around 10^{-3} torr and sealed off. The ampoule was placed in the dual zone horizontal furnace. A reverse temperature profile was developed across the ampoule over several hours to get cleaning effect on the quartz walls of growth zone. The duration for cleaning effect was 27 hours. After this, the temperature of source zone and growth zone were maintained at 1073 and 1033 K, respectively. The duration of growth was 48 hours, and then the furnace was slowly cooled at the rate of 10 K/h up to 323K.

The obtained chemical composition of the as-grown single crystals using EDAX show that the crystals possessed near stoichiometry without any impurities. X-ray diffraction (XRD) pattern for SnSe has been measured with Philips X'PERT MPD X-ray diffractometer employing Cu K_{α} radiation and results are shown in Figure 3.43.

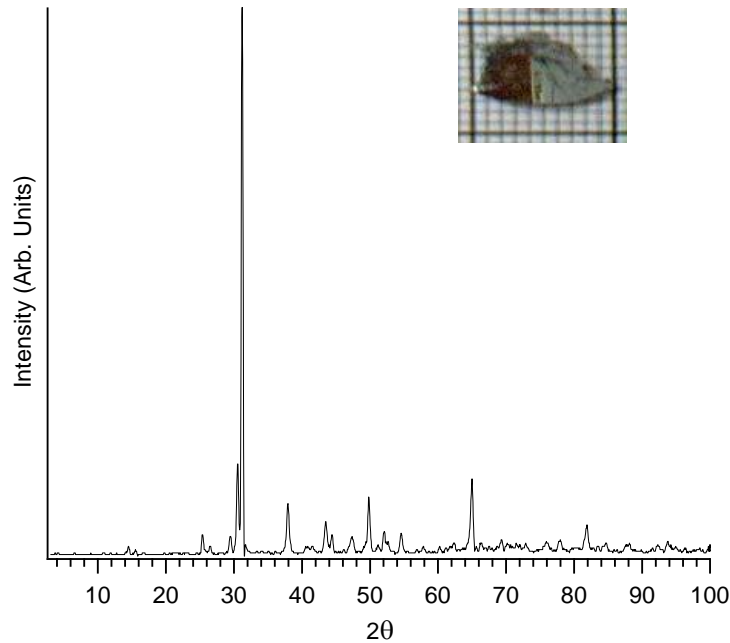


Figure 3.43: XRD of SnSe single crystals, whose photograph is reported in the inset

The XRD analysis provides $a = 4.45 \text{ \AA}$, $b = 4.16 \text{ \AA}$, $c = 11.45 \text{ \AA}$ and $\alpha=\beta=\gamma=90^\circ$, in good agreement with the previously reported values [220].

DFT computations

The structural and elastic properties of SnSe were calculated using DFT, as implemented in the QUANTUM-ESPRESSO package [201]. Bulk SnSe is a layered semiconductor with a distorted rocksalt structure belonging to the Pnma space group. Each two-atoms-thick buckled layer is connected with the others via weak van der Waals (vdW) bonding. The description of weakly bonded materials within the DFT framework is notoriously challenging, and even though in recent years several efforts have been made to improve and validate the description of the vdW interaction

within DFT [221, 222], the accurate calculation of properties such as elastic constants remain a delicate problem. For this reason several exchange-correlation functionals and methods to deal with vdW interactions, as listed in Table 3.6, were used and compared. In particular, a PBE functional [223], with the semi-empirical dispersion correction developed by Grimme [224] (PBE-D2) and with the charge density dependent Tkatchenko-Scheffler correction [225] (PBE-TS), was used.

Table 3.6: equilibrium lattice parameters obtained with different functionals and compared with experimental values

	a(Å)	b(Å)	c(Å)
LDA	4.31	4.11	11.30
PBE	4.555	4.205	11.76
PBEsol	4.36	4.15	11.43
PBE-D2	4.40	4.18	11.62
PBE-TS	4.46	4.22	11.71
vdW-DF-02-C09	4.44	4.19	11.52
vdW-DF-C09	4.35	4.16	11.45
vdW-DF-CX	4.37	4.17	11.48
vdW-DF-02-B86R	4.35	4.20	11.65
vdW-DF-OB86	4.43	4.19	11.60
vdW-DF-rvv10	4.55	4.35	11.83
Exp.	4.45	4.16	11.45

Moreover it was used the non local van der Waals density functional (vdW-DF) method developed by Dion et al. [226] and its revised version with a modified interaction kernel by Lee et al. [227] (vdW-DF2) both paired with different exchange functionals, namely the C09 by Cooper [228], the consistent-exchange (CX) functional [229] and variations of the PW86 functional [230] such as the

B86R [231] and OB86R [232]. The RVV10 method as implemented by Sabatini et al. [233] was also employed. Finally, as a matter of comparison, standard non vdW corrected functionals LDA [234], PBE [223] and PBEsol [235] were used. Norm conserving scalar relativistic pseudopotentials were used for the LDA calculation while ultrasoft pseudopotentials [236] were employed for the other methods. In both cases only the outermost *s* and *p* states were explicitly considered in valence. The electronic wave functions were expanded in plane waves up to a 90 Ry energy cut-off with the norm conserving pseudopotentials while a cut-off of 35 Ry on the plane waves and 320 Ry on the charge density was used for the ultrasofts. The integration over the Brillouin zone was carried out using a 8x8x4 Monkhorst-Pack mesh [205]. Atomic positions were relaxed until the forces were below a $5 \cdot 10^{-5}$ a.u. threshold.

The lattice parameters for the theoretical equilibrium geometries for the different functionals are reported in Table 3.6 compared with the experimental values. The obtained values of equilibrium lattice parameters estimated by DFT calculations well reproduce the experimental values. In particular, the values obtained vdW-DF functional shows only 0.7% deviation compared to XRD data. Conversely, as one could expect, standard DFT functionals perform significantly worse with LDA showing a maximum deviation of 3.1%

The elastic constants C_{ij} of SnSe were also evaluated from the stress-strain relation, following the procedure described in Refs. [208, 209] and applying deformations from 0.2% to 2%. Results for different exchange-correlation energy functional are shown in Table 3.7.

In the last column of Table 3.7 are also listed values of the estimated indentation modulus calculated according to Equation (3.4) for the direction perpendicular to the cleavage plane.

Table 3.7: elastic constants C_{ij} obtained with different functionals. The last column shows values of the estimated indentation modulus calculated according to Equation (3.4) for the direction perpendicular to the cleavage plane.

	C_{11}	C_{12}	C_{13}	C_{22}	C_{23}	C_{33}	C_{44}	C_{55}	C_{66}	M
LDA	84.8	19.0	22.1	89.3	40.3	53.4	50.8	22.6	18.4	56.2
PBE	43.5	8.3	11.2	65.6	26.1	30.4	29.4	15.4	11.6	33.1
PBEsol	74.5	16.1	19.0	81.3	36.5	46.5	44.7	20.9	17.2	49.5
PBE-D2	92.8	18.7	14.4	70.3	29.1	24.8	36.7	19.4	20.7	31.2
PBE-TS	44.9	5.8	14.9	65.5	28.4	30.9	33.2	13.4	10.9	31.9
vdW-DF-02-C09	66.2	12.1	16.7	72.7	34.1	38.3	38.7	18.9	15.2	40.7
vdW-DF-C09	78.7	15.0	18.5	81.5	39.8	49.3	48.0	20.8	17.6	51.2
vdW-DF-CX	75.2	14.4	16.8	79.8	37.5	47.9	45.8	20.2	16.9	50.2
vdW-DF-02-B86R	67.5	11.9	14.8	79.7	38.2	52.3	46.8	17.7	13.8	51.9
vdW-DF-OB86	64.7	11.5	15.6	74.3	34.9	41.4	39.7	18.3	14.5	43.1
vdW-DF-rvv10	55.8	11.7	16.4	67.8	33.1	37.1	32.1	14.5	10.3	36.1

Nanoindentation tests

As described in Section 3.2.2.2 for Bi_2Se_3 , the SnSe single crystals were cut and cleaved along the cleavage plane in order to obtain surfaces to be indented. The same procedure described in Section 3.2.1.3 C was adopted for the evaluation of the mechanical properties of SnSe by means of DFT computations and indentation tests. Also in this case only the direction perpendicular to the cleavage plane was indented.

A first set of CSM nanoindentation tests was performed by using a maximum load of 10 mN, an amplitude of the sinusoidal varying force of 1 mN, a frequency of 20 Hz, a loading rate of 10 mN/min, unloading rate of 40 mN/min and an holding time at maximum load of 10 s. The absence of pop-in events in the indentation curve shown in Figure 3.45 a) testifies that the material was not damaged during indentation. However, as shown in Figure 3.44 a), whereas the E_r value stabilizes

at 25 GPa at the maximum penetration depth reached, the H value does not stabilize and an evaluation of the material hardness cannot be pursued.

A second set of CSM nanoindentation was then performed with a higher load in order to obtain stable values of both Young's modulus and hardness. In particular, the following parameters were used: maximum load 100 mN, amplitude of the sinusoidal varying force 10 mN, frequency 20 Hz, loading rate 50 mN/min, unloading rate 400 mN/min and holding time at maximum load 10 s. Results in Figure 3.44 b) show that H stabilizes at a value of 0.8 GPa and E_r at a value around 25 GPa (the same value observed with a lower indentation load) before decreasing for increasing values of the penetration depth. Such decrease is caused by the material damage during the indentation process, as testified by the pop-in events observed in the load-penetration depth curve of Figure 3.45 b), as discussed in Section 3.2.1.3 for Bi_2Te_3 .

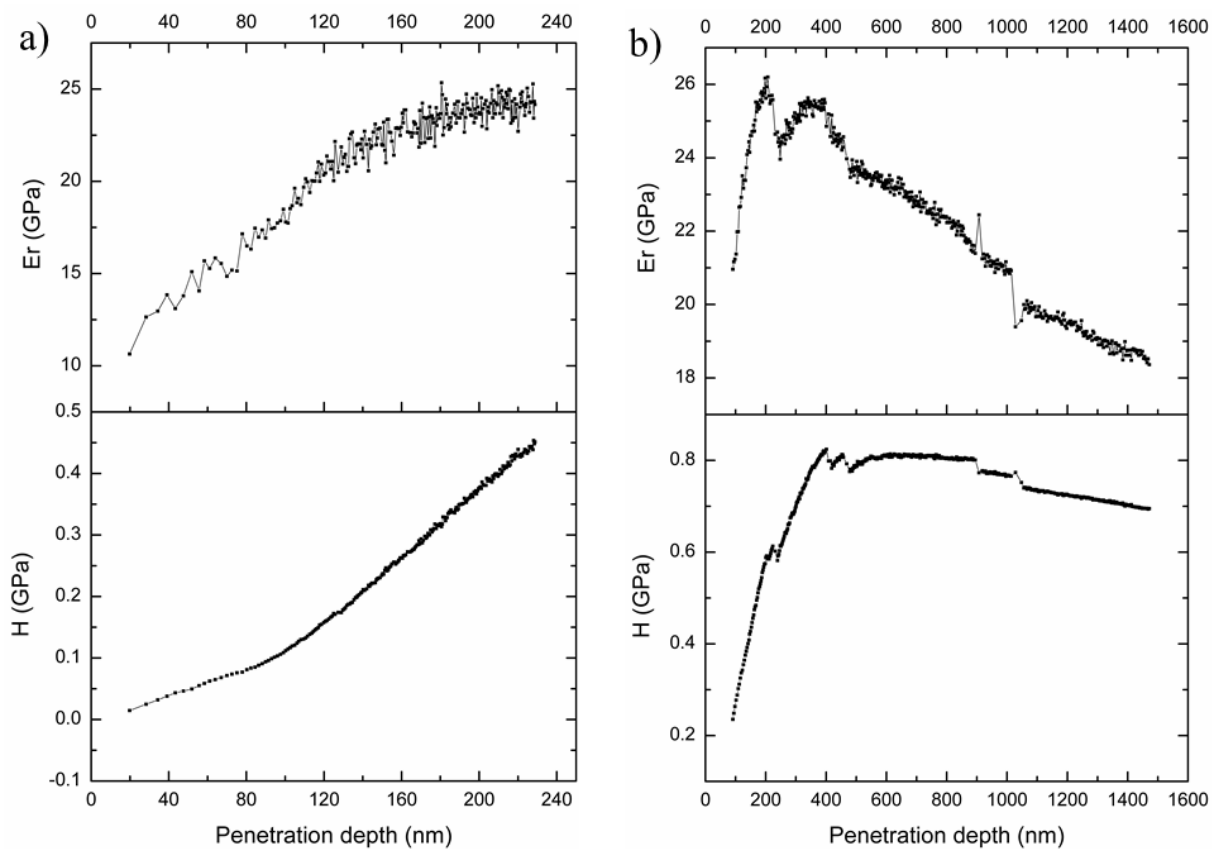


Figure 3.44: E_r (top panel) and H (lower panel) profile with increasing values of penetration depth for a CSM nanoindentation carried out along the direction perpendicular to the cleavage plane by using a maximum load of a) 10 mN and b) 100 mN.

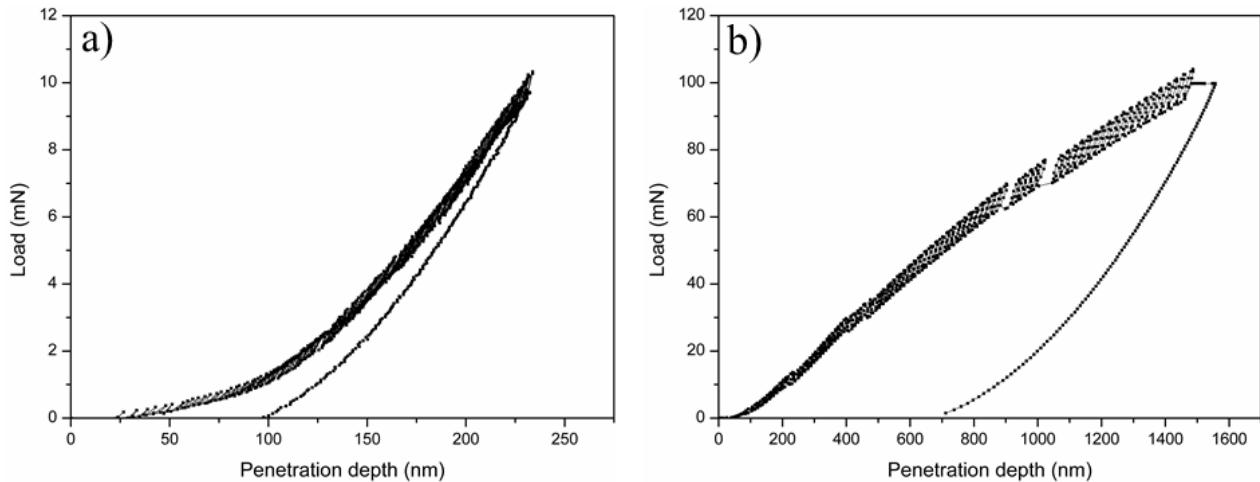


Figure 3.45: Load-penetration depth curve for CSM indentation performed with a maximum load of a) 10 mN and b) 100mN.

In correspondence of 200 nm a small decrease of both hardness and Young's modulus can be observed in Figure 3.44 b) and this can be caused by a slight damage of the material. However, this damage can be neglected since both H and E_r values increase again after this jump which could also be due to experimental noise. Also the pop-in observed in Figure 3.45 b) at 200 nm is really small if compared with the larger pop-in events observed for higher penetration depths. The measured values of 0.8 GPa and 25 GPa for H and E_r respectively can be then considered reliable. Such values were also verified by additional CSM indentation tests performed at different loads. As an example, Figure 3.46 shows the results obtained with a maximum indentation load of 30 mN. Also in this case, the Young modulus stabilizes at a value of 25 GPa. However, as for the indentation performed with a maximum load of 10 mN, the hardness value does not stabilize and continues to increase. The indentation load of 30 mN then is not enough to establish a fully plastic contact which allows to evaluate a load-independent value for the hardness (as that shown in Figure 3.44 b) for the indentation load at 100 mN).

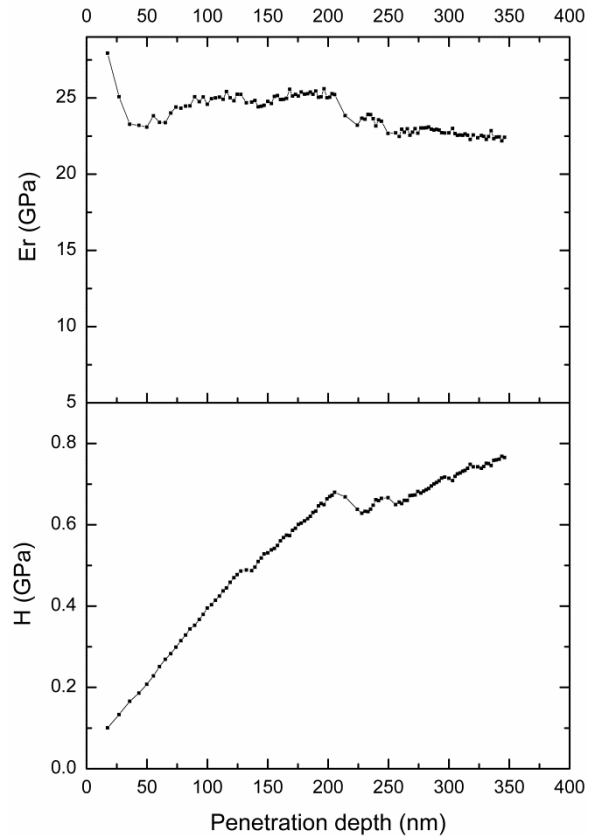


Figure 3.46: E_r (top panel) and H (lower panel) profile with increasing values of penetration depth for a CSM nanoindentation carried out along the direction perpendicular to the cleavage plane by using a maximum load of 30 mN.

However, the experimental value of the indentation modulus of 25 GPa is lower than computational estimates shown in the last column of Table 3.7 for all the different exchange-correlation energy functional used. This is a slight discrepancy if compared with that one observed for Bi_2Se_3 between computational and experimental results.

In conclusion, considering the direction perpendicular to the cleavage plane, whereas for Bi_2Te_3 a good agreement is observed between DFT and indentation results, such agreement is weaker for SnSe and completely absent for Bi_2Se_3 . This could be due to different deformation mechanisms which characterize the materials during the indentation process.

3.4 Conclusions

Results about the production and characterization of metakaolin-based geopolymers/graphene nanoplatelets (GNPs) nanocomposites were proposed in the first part of this chapter. Concerning mechanical characterization, a multiscale characterization was performed by means of nanoindentation tests and the combination of DIC and Brazilian disk test proposed in Chapter 2. No increments of indentation modulus and hardness were recorded from indentation tests after the addition of GNPs into the geopolymer paste for all the different GNPs contents analyzed (e. g., 0.1, 0.5, and 1%wt). Slight variations of Young modulus E , Poissons's ratio ν , and ultimate tensile strength σ_T , were observed with the macro scale characterization carried out by DIC and Brazilian disk tests. In particular, an increase of $\sim 14\%$ was measured for E and σ_T with a GNPs content of 0.5%wt. However, the increments measured for the mechanical properties are almost nullified by the high standard deviation values. One can conclude that the GNPs addition has not a real influence on the mechanical performances of the produced metakaolin-based geopolymers. Such result are in good agreement with previous literature results focused on the mechanical characterization of ceramic matrix/graphene composites. Graphene fillers, consisting of several platelets bonded by weak Van der Waals interactions, can be in fact considered as a soft phase into the stiff and hard ceramic matrix. Improvements of mechanical properties were obtained by researchers by adding GNPs into a fly ash-based geopolymer matrix, due to the porosity decrease provided by graphene. Such enhancements were not obtained for the produced metakaolin-based geopolymers/GNPs composites since they present a more dense and homogenous microstructure which is not modified by the GNPs addition. However, promising results were obtained from electro-mechanical characterization. Increases of 198% and 20% were recorded for the piezoelectric charge coefficient d_{33} and the piezoresistive gauge factor, respectively, with the addition of 1% of GNPs. Further investigations must be carried out in order to propose a detailed model, able to

explain the role of graphene in the enhancement of the electro-mechanical response of metakaolin-based geopolymers.

In the second part of this chapter, topological insulators (TIs) were proposed as alternative nanofillers for geopolymers. Such materials are characterized by a high surface charge carriers mobility, comparable to that of graphene. Moreover, they present also a dissipationless electric conductivity. Such properties are extremely attractive for the improvement of the electro-mechanical performances of geopolymers. However, the production and characterization of TIs/geopolymer composites cannot be pursued without knowing the mechanical properties of nanofillers. To this purpose, the mechanical characterization of three TIs, namely Bi_2Te_3 , Bi_2Se_3 , and SnSe , was carried out by means of nanoindentation tests and DFT simulations, by taking into account the anisotropy of such layered materials. Concerning Bi_2Te_3 , the indentation modulus and the hardness were measured in both the direction perpendicular and parallel to the cleavage plane. Values of 42 GPa for E_r and 1.8 GPa for H were obtained along the direction perpendicular to the cleavage plane, whereas values of 46 GPa for E_r and 0.8 GPa for H were measured along the direction parallel to the cleavage plane. While there is a good agreement between experimental and computational results in the direction perpendicular to the cleavage plane, tip-induced nanoscale buckling affects the experimental measurement of the indentation Young's modulus along the cleavage plane and discrepancies between experimental values and computational-theoretical predictions were observed. After choosing the suitable model able to evaluate the fracture toughness of Bi_2Te_3 by indentation tests, a value of $0.042 \pm 0.016 \text{ MPa} \sqrt{\text{m}}$ was measured and herein proposed for the first time. Based on such results, it is concluded that the low values of fracture toughness of Bi_2Te_3 bulk single crystals, grown with the Brigman-Stockbarger method, could limit the use of this topological insulator in flexible microelectronics and/or nanoelectromechanical devices, in contrast with the results obtained with black phosphorus [237], graphene [238], and MoS_2 [239]. Such low value of fracture toughness could also represent a limit for the mechanical performances of

Bi_2Te_3 /geopolymer composites, by preventing beneficial phenomena such as crack bridging and crack deflection that nanofillers (including graphene) usually show.

Bi_2Se_3 and SnSe were tested by nanoindentation only in the direction perpendicular to the cleavage plane. A value of 6 GPa for Er and 0.48 GPa for H were obtained for Bi_2Se_3 whereas values of 25 GPa for Er and 0.8 GPa for H were measured for SnSe. Whereas for Bi_2Te_3 a good agreement is observed between DFT and indentation results, such agreement is weaker for SnSe and completely absent for Bi_2Se_3 (in this latter case in fact the Er values estimated by DFT combined with the chosen theoretical model is equal to 57.7 GPa). Such discrepancy between experimental results and theoretical predictions can be considered a kind of Gordian knot and the results proposed in the present dissertation represent an interesting starting point for future research activities in the scientific community, in both physics and mechanical engineering fields.

3.5 References:

- [1] Lyon R.E, Foden A.J., Balaguru P.N., Davidovits J. and Davidovics M., (1997), Properties of Geopolymer Matrix-Carbon Fiber Composites, *Fire and Materials*, 21, 67–73.
- [2] Hammell, J.A., Balaguru, P.N., and Lyon, R.E., (1998), Influence of Reinforcement Types on the Flexural Properties of Geopolymer Composites, *SAMPE International Symposium*, 43, 1998.
- [3] Hammell J.A, Balaguru P.N, Lyon R.E, (2000), Strength retention of fire resistant aluminosilicate–carbon composites under wet–dry conditions, *Composites: Part B* 31, 107–111.
- [4] P. Balaguru, Stephen Kurtz, and Jon Rudolph, Geopolymer-Carbon Composite for Repair and Rehabilitation of Reinforced Concrete Beams, Geopolymer Institute Library Technical paper #2 Reinforced Concrete Beams, 1997.
- [5] Mills-Brown J., Potter K., Foster S., Batho T., (2013) The development of a high temperature tensile testing rig for composite laminates, *Composites: Part A* 52, 99–105.
- [6] Ribero D. and Kriven W. M., (2016), Properties of Geopolymer Composites Reinforced with Basalt Chopped Strand Mat or Woven Fabric, *J. Am. Ceram. Soc.*, 99 [4] 1192–1199

- [7] M. Welter, M. Schmücker, K.J.D. MacKenzie, (2015), Evolution of the Fibre-Matrix Interactions in Basalt-Fibre-Reinforced Geopolymer-Matrix Composites after Heating, *J. Ceram. Sci. Tech.*, 06 [01] 17-24.
- [8] Lin T., Jia D., He P., Wang M., Liang D., Effects of fiber length on mechanical properties and fracture behavior of short carbon fiber reinforced geopolymer matrix composites, *Materials Science and Engineering A* 497 (2008) 181–185.
- [9] Yuan J., He P., Jia D., Yan S., Cai D., Xu L., Yang Z., Duan X., Wang S., Zhou Y., (2016), SiC fiber reinforced geopolymer composites, part 1: Short SiC fiber, *Ceramics International* 42, 5345–5352.
- [10] Susan Bernal, Ruby De Gutierrez, Silvio Delvasto, Erich Rodriguez, Performance of an alkali-activated slag concrete reinforced with steel fibers, *Construction and Building Materials*, Volume 24, Issue 2, February 2010, Pages 208–214.
- [11] N. Ganesan, P.V. Indira and Anjana Santhakumar, Engineering properties of steel fibre reinforced geopolymer concrete, *Advances in Concrete Construction*, Vol. 1, No. 4 (2013) 305-318.
- [12] Zhang Y., Sun W., Li Z., Zhou X., Eddie, Chau C., (2008), Impact properties of geopolymer based extrudates incorporated with fly ash and PVA short fiber, *Construction and Building Materials* 22, 370–383.
- [13] Zhao W., Wang Y., Wang X., Wu D., (2016), Fabrication, mechanical performance and tribological behaviors of polyacetal-fiber-reinforced metakaolin-based geopolymeric composites, *Ceramics International* 42, 6329–6341.
- [14] Okada K., Imase A., Isobe T., Nakajima A., (2011), Capillary rise properties of porous geopolymers prepared by an extrusion method using polylactic acid (PLA) fibers as the pore formers, *Journal of the European Ceramic Society* 31, 461–467.
- [15] Alomayri T., Low I.M., (2013), Synthesis and characterization of mechanical properties in cotton fiber-reinforced geopolymer composites, *Journal of Asian Ceramic Societies* 1, 30–34.
- [16] Alomayri T., Shaikh F.U.A., Low I.M., (2014), Synthesis and mechanical properties of cotton fabric reinforced geopolymer composites, *Composites: Part B* 60, 36–42.
- [17] Alzeer M. and MacKenzie K. J. D., (2012), Synthesis and mechanical properties of new fiber-reinforced composites of inorganic polymers with natural wool fibers, *J. Mater. Sci.* 47, 6958-6965.
- [18] Alzeer M. and MacKenzie K. J. D., (2013), Synthesis and mechanical properties of novel composites of inorganic polymers (geopolymers) with unidirectional natural flax fibers (phormium tenax), *Applied Clay Science* 75–76 ,148–152.

- [19] Assaedi H., Shaikh F.U.A., Low I.M., (2016), Characterizations of flax fabric reinforced nano-clay-geopolymer composites, *Composites Part B* 95, 412-422.
- [20] <https://www.researchtrends.com/issue-38-september-2014/graphene-ten-years-of-the-gold-rush/>
- [21] Kroto H. W., Heath J. R., O' Brien S. C., Curl R. F., Smalley R. E., C60: Buckminsterfullerene, *Nature* 1985, 318, 162.
- [22] Iijima S., Helical microtubules of graphitic carbon, *Nature* 1991, 354, 56.
- [23] Novoselov K. S et al, Electric field effect in atomically thin carbon carbon films, *Science* 2004, 306, 666-669.
- [24] Novoselov K. S et al, Two-dimensional gas of massless Dirac fermions in graphene, *Nature* 2005, 438, 197-200.
- [25] Zhang Y, Tan Y. W., Stormer H. L., Kim P., Experimental observation of the quantum Hall effects and Barry's phase in graphene, *Nature* 2005, 438, 201-204.
- [26] Li, D., Kaner R. B., Graphene-based materials, *Science* 2008, 320, 1170.
- [27] Geim A. K., Novoselov K. S., The rise of graphene, *Nat. Mater.* 2007, 6, 183.
- [28] Schedin F., Geim A. K., Morozov S. V., Hill E. W., Blake P., Katsnelson M. I., Novoselov K. S., Detection of individual gas molecules adsorbed on graphene, *Nat. Mater.* 2007, 6, 652.
- [29] Elias D. C., Nair R. R., Mohiuddin T. H. G., Morozov S. V., Blake P., Halsall M. P., Ferrari A. C., Boukhvalov D. W., Katnelson M. I., Geim A. K., Novoselov K. S., Control of graphene's properties by reversible hydrogenation: evidence for graphene, *Science* 2009, 323, 610.
- [30] Zhou S. Y., Gweon G. H., Fedorov A. V., First P. N., De Heer W. A., Lee D. H., Guinea F., Castro Neto A. H., Lanzara A., Substrate-induced bandgap opening in epitaxial graphene, *Nat. Mater.* 2007, 6, 770.
- [31] Kudin K. N., Scuseria G. E., Yakobson B. I., C2F, BN, and C nanoshell elasticity from ab initio computations, *Phys. Rev. B* 2001, 64, 235406.
- [32] Lee C., Wei X., Kysar J. W., Hone J., Measurement of the elastic properties and intrinsic strength of monolayer graphene, *Science* 2008, 321, 385.
- [33] Dong X., Shi Y., Zhao Y., Chen D., Ye J., Yao Y., Gao F., Ni Z., Yu T., Shen Z., Huang Y., Chen P., Li L., Symmetry breaking of graphene monolayers by molecular decoration, *Phys. Rev. Lett.* 2009, 102, 135501.

- [34] Yavari F., Kritzinger C., Gaire C., Song L., Gulapalli H., Borca-Tasciuc T., Ajayan P. M., Koratkar N., Tunable bandgap in graphene by the controlled absorption of water molecule, *Small* 2010, 6, 2535-2538.
- [35] Rudberg E., Salek P., Luo Y., Nonlocal exchange interaction removes half-metallicity in graphene nanoribbons, *Nano Lett.* 2007, 7, 2211-2213.
- [36] Son Y. W., Cohen M. L., Louie S. G., Half-metallic graphene nanoribbons, *Nature* 2006, 444, 347.
- [37] Zhang Y., Tang T., Girit C., Hao Z., Martin M. C., Zettl A., Crommie M. F., Shen Y. R., Wang F., Direct observation of a widely tunable bandgap in bilayer, *Nature* 2009, 459, 820.
- [38] Zou S. Y., Siegel D. A., Fedorov A. V., Lanzara A., Metal to insulator transition in epitaxial graphene induced by molecular doping, *Phys. Rev. Lett.* 2008, 101, 086402.
- [39] Park S., Ruoff R. S., Chemical method for the production of graphene, *Nat. Nanotech.* 2009, 4, 217-224.
- [40] Nair R. R. et al., Fine structure constant defines visual transparency of graphene, *Science* 2008, 320, 1308.
- [41] Bonaccorso F., Sun Z., Hasan T., Ferrari A. C., Graphene photonics and optoelectronics, *Nat. Photonics* 2010, 4, 611-620.
- [42] Roddaro S. et al., The optical visibility of graphene: interference colors of ultrathin graphite on SiO₂, *Nano Lett.* 2007, 7, 2707-2710.
- [43] Chen Z., Ren W., Gao L., Liu B., Pei S., Chen H., Three-dimensional flexible and conductive interconnected graphene networks grown by chemical vapor deposition, *Nat. Mat.* 2011, 10, 424-428.
- [44] Li X., Zhang G., Bai X., Sun X., Wang X., Wang E., Dai H., Highly conducting graphene sheets and Langmuir Blodgett films, *Nat. Nanotech.* 2008, 3, 538-542.
- [45] Li X., Cai W., An J., Kim S., Nah J., Yang D., Piner R., Velamakanni A., Jung I., Tutuc E., Banerjee S. K., Colombo L., Ruoff R. S., Large-area synthesis of high quality and uniform graphene films on Cu foils, *Science* 2009, 324, 1312-1314.
- [46] Li X. Zhu Y., Cai W., Borysiak M., Chen D., Piner R. D., Colombo L., Ruoff R. S., Transfer of large area graphene films for high performance transparent conductive electrodes, *Nano Lett* 2009, 9, 4359-4363.
- [47] Bae S. et al., Roll-to-roll production of 30-inch graphene films for transparent electrodes, *Nat. Nanotech.* 2010, 5, 574-578.

- [48] Eda G., Fanchini G., Chowalla M., Large-area ultrathin films reduce graphene oxide as a transparent and flexible electronic material, *Nat. Nanotech* 2008, 270-274.
- [49] Rafiee J et al., Wetting transparency of graphene, *Nat. Mater.* 2012, 11, 217-222.
- [50] Chen S. et al., Oxidation resistance of graphene-coated Cu and Cu/Ni alloy, *ACS Nano* 2011, 5, 1321-1327.
- [51] Nihil A. Koratkar, *Graphene in Composite Materials: Synthesis, Characterization and Applications*, DEStech Publications, Inc., Lancaster, Pennsylvania 17602, USA.
- [52] Soldano C., Mahmood A., Dujardin E., Production, properties and potential of graphene, *Carbon* 2010, 48, 2127-2150.
- [53] Inagaki M., Kim J. A., Endo M., Graphene: preparation and structural perfection, *J. Mater. Chem* 2010, DOI: 10.1039/c0jm02991b.
- [54] Andy Nieto, Ankita Bisht, Debrupa Lahiri, Cheng Zhang & Arvind Agarwal, Graphene reinforced metal and ceramic matrix composites: a review, *International Materials Reviews* 2016, DOI: 10.1080/09506608.2016.1219481.
- [55] Spitalsky Z, Tasis D, Papagelis K, et al. Carbon nanotube–polymer composites: Chemistry, processing, mechanical and electrical properties. *Prog Polym Sci.* 2010;35:357–401.
- [56] Agrawal R, Nieto A, Chen H, et al. Nanoscale damping characteristics of boron nitride nanotubes and carbon nanotubes reinforced polymer composites. *ACS Appl Mater Interfaces.* 2013;5:12052–12057.
- [57] Josphat Phiri, Patrick Gane, Thad C. Maloney, General overview of graphene: Production, properties and application in polymer composites, *Materials Science and Engineering B* 215 (2017) 9–28.
- [58] X. Zhao, Q. Zhang, D. Chen, P. Lu, Enhanced mechanical properties of graphene-based poly(vinyl alcohol) composites, *Macromolecules* 43 (2010) 2357–2363.
- [59] Yi Wang, Jinhong Yu, Wen Dai, Yingze Song, Dong Wang, Liming Zeng, Nan Jiang, Enhanced Thermal and Electrical Properties of Epoxy Composites Reinforced With Graphene Nanoplatelets, *POLYMER COMPOSITES—2014*, DOI 10.1002/pc.
- [60] V. Mittal, Functional polymer nanocomposites with graphene: a review, *Macromol. Mater. Eng.* 299 (2014) 906–931.
- [61] Y. Wan, L. Tang, D. Yan, L. Zhao, Y. Li, L. Wu, J. Jiang, G. Lai, Improved dispersion and interface in the graphene/epoxy composites via a facile surfactant-assisted process, *Compos. Sci. Technol.* 82 (2013) 60–68.
- [62] X. Liu, L. Wang, L. Zhao, H. He, X. Shao, G. Fang, Z. Wan, R. Zeng, Research progress of graphene-based rubber nanocomposites, *Polym. Compos.* (2016).

- [63] P.M. Ajayan, J.M. Tour, Materials science: nanotube composites, *Nature* 447 (2007) 1066–1068.
- [64] J. Du, H. Cheng, The fabrication, properties, and uses of graphene/polymer composites, macromolecular chemistry and physics., *Macromol. Chem. Phys.* 213 (2012) 1060–1077.
- [65] H. Pathangi, P.M. Vereecken, A. Klekachev, G. Groeseneken, A. Witvrouw, Quantifying the aggregation factor in carbon nanotube dispersions by absorption spectroscopy, *J. Nanosci.* 2014 (2014) 13.
- [66] F. Inam, T. Peijs, Re-aggregation of carbon nanotubes in two-component epoxy system, *J. Nanostruct. Polym. Nanocompos.* 2 (2006) 86–94.
- [67] Rashad M, Pan F, Hua H, et al. Enhanced tensile properties of magnesium composites reinforced with graphene nanoplatelets. *Mater Sci Eng A.* 2015;630:36–44.
- [68] Bastwros M, Kim G-Y, Zhu C, et al. Effect of ball milling on graphene reinforced Al6061 composite fabricated by semi-solid sintering. *Compos B.* 2014;60:111–118.
- [69] Bustamante RP, Morales DB, Martínez JB, et al. Microstructural and hardness behavior of graphenenanoplatelets/ aluminum composites synthesized by mechanical alloying. *J Alloys Compd.* 2014;615: S578–S582.
- [70] Li JL, Xiong YC, Wang XD, et al. Microstructure and tensile properties of bulk nanostructured aluminum/ graphene composites prepared via cryomilling. *Mater Sci Eng A.* 2015;626:400–405.
- [71] Rashad M, Pan F, Asif M, et al. Improved mechanical properties of magnesium–graphene composites with copper–graphene hybrids. *Mater Sci Technol.* 2015;31:1452–1461.
- [72] Walker LS, Marotto VR, Rafiee MA, et al. Toughening in graphene ceramic composites. *ACS Nano.* 2011;5:3182–3190.
- [73] Liu J, Li Z, Yan H, et al. Spark plasma sintering of alumina composites with graphene platelets and silicon carbide nanoparticles. *Adv Eng Mater.* 2014;16:1111–1118.
- [74] Walker L. S., Marotto V. R., Rafiee M. A., Koratkar N., Corral E. L., Toughening in graphene ceramic composites, *ACS Nano* 2011, 5, 3182-3190.
- [75] Porwal H, Tatarko P, Grasso S, et al. Graphene reinforced alumina nano-composites. *Carbon.* 2013;64:359–369.
- [76] Nieto A, Lahiri D, Agarwal A. Graphene NanoPlatelets reinforced tantalum carbide consolidated by spark plasma sintering. *Mater Sci Eng A.* 2013;582:338–346.
- [77] Kun P, Tapaszto O, Weber F, et al. Determination of structural and mechanical properties of multilayer graphene added silicon nitride-based composites. *Ceram Int.* 2012;38:211–216.
- [78] Asl MS, Kakroudi MG. Characterization of hotpressed graphene reinforced ZrB₂–SiC composite. *Mater Sci Eng A.* 2015;625:385–392.

- [79] Fan Y, Estili M, Igarashi G, et al. The effect of homogeneously dispersed few-layer graphene on microstructure and mechanical properties of Al₂O₃ nanocomposites. *J Eur Ceram Soc.* 2014;34:443–451.
- [80] Tapaszto O, Tapaszto L, Marko M, et al. Dispersion patterns of graphene and carbon nanotubes in ceramic matrix composites. *Chem Phys Lett.* 2011;511:340–343.
- [81] Ramirez C, Miranzo P, Belmonte M, et al. Extraordinary toughening enhancement and flexural strength in Si₃N₄ composites using graphene sheets. *J Eur Ceram Soc.* 2014;34:161–169.
- [82] Zhang L, Liu W, Yue C, et al. A tough graphene nanosheet/hydroxyapatite composite with improved in vitro biocompatibility. *Carbon.* 2013;61:105–115.
- [83] Baradaran S, Moghaddam E, Nasiri-Tabrizi B, et al. Characterization of nickel-doped biphasic calcium phosphate/graphene nanoplatelet composites for biomedical application. *Mater Sci Eng C.* 2015;49:656–668.
- [84] Lee B, Koo MY, Jin SH, et al. Simultaneous strengthening and toughening of reduced graphene oxide/ alumina composites fabricated by molecular-level mixing process. *Carbon* 2014;78:212–219.
- [85] Mohamed Saafi, Leung Tang, Jason Fung, Mahbubur Rahman, John Liggat, Enhanced properties of graphene/fly ash geopolymeric composite cement, *Cement and Concrete Research* 67 (2015) 292–299.
- [86] Navid Ranjbar, Mehdi Mehrali, Mohammad Mehrali, U. Johnson Alengaram, Mohd Zamin Jumaat, Graphene nanoplatelet-fly ash based geopolymer composites, *Cement and Concrete Research* 76 (2015) 222–231.
- [87] Mohamed Saafi, Leung Tang, Jason Fung, Mahbubur Rahman, Fiona Sillars, John Liggat and Xiangming Zhou, Graphene/fly ash geopolymeric composites as self-sensing structural materials, *Smart Mater. Struct.* 23 (2014) 065006 (10pp) doi:10.1088.
- [88] Shu Yan, Peigang He, Dechang Jia, Zhihua Yang, Xiaoming Duan, Shengjin Wang, Yu Zhou, In situ fabrication and characterization of graphene/geopolymer composites, *Ceramics International* 41 (2015) 11242–11250.
- [89] Shu Yan, Peigang He, Dechang Jia, Xiaoming Duan, Zhihua Yang, Shengjin Wang, Yu Zhou, Crystallization kinetics and microstructure evolution of reduced graphene oxide/geopolymer composites, *Journal of the European Ceramic Society* 36 (2016) 2601–2609.
- [90] Shu Yan, Peigang He, Dechang Jia, Xiaoming Duan, Zhihua Yang, Shengjin Wang, and Yu Zhou, In Situ Processing of Graphene/Leucite Nanocomposite Through Graphene Oxide/Geopolymer, *J. Am. Ceram. Soc.*, 99 [4] 1164–1173 (2016).
- [91] Zhao J, Zhang G-Y and Shi D-X 2013 Review of graphene based strain sensors *Chin. Phys. B* 22 057701.
- [92] <http://www.grafene.it/>

- [93] D. Hardjito, S.E. Wallah, D.M. Sumajouw, B.V. Rangan, On the development of fly ash-based geopolymer concrete, *ACI Mater. J.* 101 (2004).
- [94] Peichao Lian, Xuefeng Zhu, Shuzhao Liang, Zhong Li, Weishen Yang, Haihui Wang, Large reversible capacity of high quality graphene sheets as an anode material for lithium-ion batteries, *Electrochimica Acta*, Volume 55, Issue 12, 30 April 2010, Pages 3909–3914.
- [95] Hao-Bin Zhang, Wen-Ge Zheng, Qing Yan, Yong Yang, Ji-Wen Wang, Zhao-Hui Lu, Guo-Ying Ji, Zhong-Zhen Yu, Electrically conductive polyethylene terephthalate/graphene nanocomposites prepared by melt compounding, *Polymer*, Volume 51, Issue 5, 2 March 2010, Pages 1191–1196
- [96] M. Z. Hasan and C. L. Kane, *Rev. Mod. Phys.* 82, 3045 (2010).
- [97] Wang, Z. H.; Qiu, R. L. J.; Lee, C. H.; Zhang, Z. D.; Gao, X. P. A. Ambipolar surface conduction in ternary topological insulator $\text{Bi}_2(\text{Te}_{1-x}\text{Se}_x)_3$ nanoribbons. *ACS Nano* 2013, 7, 2126–2131.
- [98] Kim, D.; Cho, S.; Butch, N. P.; Syers, P.; Kirshenbaum, K.; Adam, S.; Paglione, J.; Fuhrer, M. S. Surface conduction of topological Dirac electrons in bulk insulating Bi_2Se_3 . *Nat. Phys.* 2012, 8, 459–463.
- [99] Wang, Z.; Qi, X. L.; Zhang, S. C. Topological order parameters for interacting topological insulators. *Phys. Rev. Lett.* 2010, 105, 256803.
- [100] Henk, J.; Ernst, A.; Ereameev, S. V.; Chulkov, E. V.; Maznichenko, I. V.; Mertig, I. Complex spin texture in the pure and Mn-doped topological insulator Bi_2Te_3 . *Phys. Rev. Lett.* 2012, 108, 206801.
- [101] Hancock, J. N.; Van Mechelen, J. L. M.; Kuzmenko, A. B.; Van Der Marel, D.; Brüne, C.; Novik, E. G.; Astakhov, G. V.; Buhmann, H.; Molenkamp, L. W. Surface state charge dynamics of a high-mobility three-dimensional topological insulator. *Phys. Rev. Lett.* 2011, 107, 136803.
- [102] Orlita, M.; Faugeras, C.; Plochocka, P.; Neugebauer, P.; Martinez, G.; Maude, D. K.; Barra, A. L.; Sprinkle, M.; Berger, C.; de Heer, W. A. et al. Approaching the dirac point in high-mobility multilayer epitaxial graphene. *Phys. Rev. Lett.* 2008, 101, 267601.
- [103] Morozov, S. V.; Novoselov, K. S.; Katsnelson, M. I.; Schedin, F.; Elias, D. C.; Jaszczak, J. A.; Geim, A. K. Giant intrinsic carrier mobilities in graphene and its bilayer. *Phys. Rev. Lett.* 2008, 100, 016602.
- [104] T. Zhang, P. Cheng, X. Chen, J. F. Jia, X. Ma, K. He, L. Wang, H. Zhang, X. Dai, Z. Fang, X. Xie, and Q. K. Xue, *Phys. Rev. Lett.* 103, 266803 (2009).
- [105] Desheng Kong and Yi Cui, Opportunities in chemistry and materials science for topological insulators and their nanostructures, *Nature Chemistry* 2011, 3, 845-849.
- [106] Charles L. Kane and Eugene J. Mele, A New Spin on the Insulating State, *Science* 2006, 314, 1692-1693.

- [107] Peng, H. L.; Dang, W. H.; Cao, J.; Chen, Y. L.; Wu, D.; Zheng, W. S.; Li, H.; Shen, Z. X.; Liu, Z. F. Topological insulator nanostructures for near-infrared transparent flexible electrodes. *Nat. Chem.* 2012, 4, 281–286.
- [108] Sulaev, A.; Zeng, M. G.; Shen, S.-Q.; Cho, S. K.; Zhu, W. G.; Feng, Y. P.; Eremeev, S. V.; Kawazoe, Y.; Shen, L.; Wang, L. Electrically tunable in-plane anisotropic magnetoresistance in topological insulator BiSbTeSe₂ nanodevices. *Nano Lett.* 2015, 15, 2061–2066.
- [109] Lu, Y.; Guo, J. Quantum simulation of topological insulator based spin transfer torque device. *Appl. Phys. Lett.* 2013, 102, 073106.
- [110] Williams, J. R.; Bestwick, A. J.; Gallagher, P.; Hong, S. S.; Cui, Y.; Bleich, A. S.; Analytis, J. G.; Fisher, I. R.; Goldhaber-Gordon, D. Unconventional Josephson effect in hybrid superconductor-topological insulator devices. *Phys. Rev. Lett.* 2012, 109, 056803.
- [111] Steinberg, H.; Gardner, D. R.; Lee, Y. S.; Jarillo-Herrero, P. Surface state transport and ambipolar electric field effect in Bi₂Se₃ nanodevices. *Nano Lett.* 2010, 10, 5032–5036.
- [112] Ou, J.-Y.; So, J.-K.; Adamo, G.; Sulaev, A.; Wang, L.; Zheludev, N. I. Ultraviolet and visible range plasmonics in the topological insulator Bi_{1.5}Sb_{0.5}Te_{1.8}Se_{1.2}. *Nat. Commun.* 2014, 5, 5139.
- [113] Qiao, H.; Yuan, J.; Xu, Z. Q.; Chen, C. Y.; Lin, S. H.; Wang, Y. S.; Song, J. C.; Liu, Y.; Khan, Q.; Hoh, H. Y. et al. Broadband photodetectors based on graphene–Bi₂Te₃ heterostructure. *ACS Nano* 2015, 9, 1886–1894.
- [114] Zhang, X.; Wang, J.; Zhang, S. C. Topological insulators for high-performance terahertz to infrared applications. *Phys. Rev. B* 2010, 82, 245107.
- [115] Luo, Z.-C.; Liu, M.; Liu, H.; Zheng, X.-W.; Luo, A.-P.; Zhao, C.-J.; Zhang, H.; Wen, S.-C.; Xu, W.-C. 2 GHz passively harmonic mode-locked fiber laser by a microfiberbased topological insulator saturable absorber. *Opt. Lett.* 2013, 38, 5212–5215.
- [116] Zhao, C. J.; Zhang, H.; Qi, X.; Chen, Y.; Wang, Z. T.; Wen, S. C.; Tang, D. Y. Ultra-short pulse generation by a topological insulator based saturable absorber. *Appl. Phys. Lett.* 2012, 101, 211106.
- [117] Lin, Y. H.; Yang, C. Y.; Lin, S. F.; Tseng, W. H.; Bao, Q. L.; Wu, C. I.; Lin, G. R. Soliton compression of the erbiumdoped fiber laser weakly started mode-locking by nanoscale p-type Bi₂Te₃ topological insulator particles. *Laser Phys. Lett.* 2014, 11, 055107.
- [118] Viti, L.; Coquillat, D.; Politano, A.; Kokh, K. A.; Aliev, Z. S.; Babanly, M. B.; Tereshchenko, O. E.; Knap, W.; Chulkov, E. V.; Vitiello, M. S. Plasma-wave terahertz detection mediated by topological insulators surface states. *Nano Lett.* 2016, 16, 80.
- [119] Süsstrunk, R.; Huber, S. D. Observation of phononic helical edge states in a mechanical topological insulator. *Science* 2015, 349, 47–50.
- [120] Hasan, M. Z.; Kane, C. L. Colloquium: Topological insulators. *Rev. Mod. Phys.* 2010, 82, 3045–3067.
- [121] M. Zhang, L. Lv, Z. Wei, C. Guo, X. Yang, and Y. Zhao, *Mater. Lett.* 123, 87–89 (2014).

- [122] S. W. Han, M. A. Hasan, K. H. Cho, and H. J. Lee, *Int. J. Mod. Phys. B* 20, 4063 (2006).
- [123] R. Rostek, V. Sklyarenko, and P. Woias, *J. Mater. Res.* 26, 1785 (2011).
- [124] S. E. Harrison, L. J. Collins-McIntyre, S. Li, A. A. Baker, L. R. Shelford, Y. Huo, A. Pushp, S. S. P. Parkin, J. S. Harris, E. Arenholz, G. van der Laan, and T. Hesjedal, *J. Appl. Phys.* 115, 023904 (2014).
- [125] F. Bailini, M. Donati, V. Zamboni, M. Russo, C. S. Passoni, A. L. Casari, C. E. Bassi, and C. E. Bottani, *Appl. Surf. Sci.* 254, 1249 (2007).
- [126] V. A. Golyashov, K. A. Kokh, S. V. Makarenko, K. N. Romanyuk, I. P. Prosvirin, A. V. Kalinkin, O. E. Tereshchenko, A. S. Kozhukhov, D. V. Sheglov, S. V. Ereemeev, S. D. Borisova, and E. V. Chulkov, *J. Appl. Phys.* 112, 113702 (2012).
- [127] D. Kong, J. J. Cha, K. Lai, H. Peng, J. G. Analytis, S. Meister, Y. Chen, H. J. Zhang, I. R. Fisher, Z. X. Shen, and Y. Cui, *ACS Nano* 5, 4698–4703 (2011).
- [128] I. Guo, H. Yan, Q. Moore, M. Buettner, J. Song, L. Li, P. T. Araujo, and H. T. Wang, *Nanoscale* 7, 11915–11921 (2015).
- [129] C.-H. Tasi, Y.-C. Tseng, S.-R. Jian, Y.-Y. Liao, C.-M. Lin, P.-F. Yang, D.-L. Chen, H.-J. Chen, C.-W. Luo, and J.-Y. Juang, *J. Alloys Compd.* 619, 834–838 (2015).
- [130] V. V. Atuchin, V. A. Golyashov, K. Kokh, I. V. Korolkov, A. A. Kozhukhov, V. N. Kruchinin, S. V. Makarenko, L. D. Pokrovsky, I. P. Prosvirin, K. N. Romanyuk, and O. E. Tereshchenko, *Cryst. Growth Des.* 11, 5507–5514 (2011).
- [131] A. Politano, M. Caputo, S. Nappini, F. Bondino, E. Magnano, Z. S. Aliev, M. B. Babanly, A. Goldoni, G. Chiarello, and E. V. Chulkov, *J. Phys. Chem. C* 118, 21517–21522 (2014).
- [132] I. V. Yashina, J. Sanchez-Barriga, M. R. Scholz, A. A. Volykhov, A. P. Sirotina, V. S. Neudachina, M. E. Tamm, A. Varykhalov, D. Marchenko, G. Springholz, G. Bauer, A. Knop-Gericke, and O. Rader, *ACS Nano* 7, 5181–5191 (2013).
- [133] P. Wei, Z. Wang, X. Liu, and V. Aji, *J. Shi, Phys. Rev. B* 85, 201402 (2012).
- [134] S. Roy, H. L. Meyerheim, A. Ernst, K. Mohseni, C. Tusche, M. G. Vergniory, T. V. Menshchikova, M. M. Otrokov, A. G. Ryabishchenkova, Z. S. Aliev, M. B. Babanly, K. A. Kokh, O. E. Tereshchenko, E. V. Chulkov, J. Schneider, and J. Kirschner, *Phys. Rev. Lett.* 113, 116802 (2014).
- [135] T. V. Menshchikova, M. M. Otrokov, S. S. Tsirkin, D. A. Samorokov, V. V. Bebneva, A. Ernst, V. M. Kuznetsov, and E. V. Chulkov, *Nano Lett.* 13, 6064–6069 (2013).
- [136] Poudel, B.; Hao, Q.; Ma, Y.; Lan, Y.; Minnich, A.; Yu, B.; Yan, X.; Wang, D.; Muto, A.; Vashaee, D. et al. Highthermoelectric performance of nanostructured bismuth antimony telluride bulk alloys. *Science* 2008, 320, 634–638.
- [137] Hamdou, B.; Kimling, J.; Dorn, A.; Pippel, E.; Rostek, R.; Woias, P.; Nielsch, K. Thermoelectric characterization of bismuth telluride nanowires, synthesized via catalytic growth and post-annealing. *Adv. Mater.* 2013, 25, 239–244.

- [138] Purkayastha, A.; Kim, S.; Gandhi, D. D.; Ganesan, P. G.; Borca-Tasciuc, T.; Ramanath, G. Molecularly protected bismuth telluride nanoparticles: Microemulsion synthesis and thermoelectric transport properties. *Adv. Mater.* 2006, 18, 2958–2963.
- [139] Zhao, L. L.; Wang, X. L.; Fei, F. Y.; Wang, J. Y.; Cheng, Z. X.; Dou, S. X.; Wang, J.; Snyder, G. J. High thermoelectric and mechanical performance in highly dense Cu_{2-x}S bulks prepared by a melt-solidification technique. *J. Mater. Chem. A* 2015, 3, 9432–9437.
- [140] Zhao, L.-D.; Zhang, B.-P.; Li, J.-F.; Zhou, M.; Liu, W.-S.; Liu, J. Thermoelectric and mechanical properties of nano- SiC-dispersed Bi_2Te_3 fabricated by mechanical alloying and spark plasma sintering. *J. Alloys Compd.* 2008, 455, 259–264.
- [141] S.-C. Liufu, L.-D. Chen, Q. Yao and C.-F. Wang, Assembly of one-dimensional nanorods into Bi_2S_3 films with enhanced thermoelectric transport properties, *Appl. Phys. Lett.* 90 (2007) 112106.
- [142] T. Kondo, Y. Nakashima, Y. Ota, Y. Ishida, W. Malaeb, K. Okazaki, S. Shin, M. Kriener, S. Sasaki, K. Segawa and Y. Ando, Anomalous Dressing of Dirac Fermions in the Topological Surface State of Bi_2Se_3 , Bi_2Te_3 , and Cu-Doped Bi_2Se_3 , *Phys. Rev. Lett.* 110 (2013) 217601.
- [143] M. Z. Hasan and C. L. Kane, Colloquium: Topological insulators, *Rev. Mod. Phys.* 82 (2010) 3045.
- [144] P. Roushan, J. Seo, C. V. Parker, Y. S. Hor, D. Hsieh, D. Qian, A. Richardella, M. Z. Hasan, R. J. Cava and A. Yazdani, Topological surface states protected from backscattering by chiral spin texture, *Nature* 460 (2009) 1106.
- [145] H. Zhang, C. X. Liu, X. L. Qi, X. Dai, Z. Fang and S. C. Zhang, Topological insulators in Bi_2Se_3 , Bi_2Te_3 and Sb_2Te_3 with a single Dirac cone on the surface, *Nat. Phys.* 5 (2009) 438.
- [146] V. V. Atuchin, V. A. Golyashov, K. A. Kokh, I. V. Korolkov, A. S. Kozhukhov, V. N. Kruchinin, S. V. Makarenko, L. D. Pokrovsky, I. P. Prosvirin, K. N. Romanyuk and O. E. Tereshchenko, Formation of Inert $\text{Bi}_2\text{Se}_3(0001)$ Cleaved Surface, *Cryst. Growth Des.* 11 (2011) 5507.
- [147] Zhao, S.; Wang, H.; Zhou, Y.; Liao, L.; Jiang, Y.; Yang, X.; Chen, G.; Lin, M.; Wang, Y.; Peng, H.; Liu, Z. Controlled synthesis of single-crystal SnSe nanoplates. *Nano Res.* 2015, 8, 288-295.
- [148] Zhao, L.-D.; Tan, G.; Hao, S.; He, J.; Pei, Y.; Chi, H.; Wang, H.; Gong, S.; Xu, H.; Dravid, V. P.; Uher, C.; Snyder, G. J.; Wolverton, C.; Kanatzidis, M. G. Ultrahigh power factor and thermoelectric performance in hole-doped single-crystal SnSe. *Science* 2016, 351, 141-144.
- [149] Shi, G.; Kioupakis, E. Anisotropic Spin Transport and Strong Visible-Light Absorbance in Few-Layer SnSe and GeSe. *Nano Lett.* 2015, 15, 6926-6931.
- [150] Zhao, L.-D.; Lo, S.-H.; Zhang, Y.; Sun, H.; Tan, G.; Uher, C.; Wolverton, C.; Dravid, V. P.; Kanatzidis, M. G. Ultralow thermal conductivity and high thermoelectric figure of merit in SnSe crystals. *Nature* 2014, 508, 373-377.

- [151] Zhang, L.-C.; Qin, G.; Fang, W.-Z.; Cui, H.-J.; Zheng, Q.-R.; Yan, Q.-B.; Su, G. Tinselenidene: a Two-dimensional Auxetic Material with Ultralow Lattice Thermal Conductivity and Ultrahigh Hole Mobility. *Sci. Rep.* 2016, 6, 19830.
- [152] Li, C. W.; Hong, J.; May, A. F.; Bansal, D.; Chi, S.; Hong, T.; Ehlers, G.; Delaire, O. Orbitally driven giant phonon anharmonicity in SnSe. *Nat. Phys.* 2015, 11, 1063-1069.
- [153] Zhang, C.; Yin, H.; Han, M.; Dai, Z.; Pang, H.; Zheng, Y.; Lan, Y. Q.; Bao, J.; Zhu, J. Two-dimensional tin selenide nanostructures for flexible all-solid-state supercapacitors. *ACS Nano* 2014, 8, 3761-3770.
- [154] Li-Dong Zhao, Shih-Han Lo, Yongsheng Zhang, Hui Sun, Gangjian Tan, Ctirad Uher, C. Wolverton, Vinayak P. Dravid & Mercouri G. Kanatzidis, Ultralow thermal conductivity and high thermoelectric figure of merit in SnSe crystals, *Nature* 2014, 508, 373-378.
- [155] Kraemer, D.; Poudel, B.; Feng, H.-P.; Caylor, J. C.; Yu, B.; Yan, X.; Ma, Y.; Wang, X. W.; Wang, D. Z.; Muto, A. et al. High-performance flat-panel solar thermoelectric generators with high thermal concentration. *Nat. Mater.* 2011, 10, 532–538.
- [156] Bell, L. E. Cooling, heating, generating power, and recovering waste heat with thermoelectric systems. *Science* 2008, 321, 1457–1461.
- [157] Parker, D.; Singh, D. J. Potential thermoelectric performance from optimization of hole-doped Bi₂Se₃. *Phys. Rev. X* 2011, 1, 021005.
- [158] Menke, E. J.; Brown, M. A.; Li, Q.; Hemminger, J. C.; Penner, R. M. Bismuth telluride (Bi₂Te₃) nanowires: Synthesis by cyclic electrodeposition/stripping, thinning by electrooxidation, and electrical power generation. *Langmuir* 2006, 22, 10564–10574.
- [159] D. Akinwande, N. Petrone and J. Hone, Two-dimensional flexible nanoelectronics, *Nat. Commun.* 5 (2014) 5678.
- [160] X. Li, T. Ono, Y. Wang and M. Esashi, Ultrathin single-crystalline-silicon cantilever resonators: Fabrication technology and significant specimen size effect on Young's modulus, *Appl. Phys. Lett.* 83 (2003) 3081.
- [161] Zhenglin Li, Ying Hu, Kenneth A. Howard, Tingting Jiang, Xuelei Fan, Zhaohua Miao, Ye Sun, Flemming Besenbacher, and Miao Yu, Multifunctional Bismuth Selenide Nanocomposites for Antitumor Thermo- Chemotherapy and Imaging, *ACS Nano* 2016, 10, 984–997.
- [162] Chaochao Dun, Corey A. Hewitt, Huihui Huang, Junwei Xu, David S. Montgomery, Wanyi Nie, Qike Jiang, and David L. Carroll, Layered Bi₂Se₃ Nanoplate/Polyvinylidene Fluoride Composite Based n-type Thermoelectric Fabrics, *ACS Appl. Mater. Interfaces* 2015, 7, 7054–7059.
- [163] Yong Du, K. F. Cai, Song Chen, Pavel Cizek, and Tong Lin, Facile Preparation and Thermoelectric Properties of Bi₂Te₃ Based Alloy Nanosheet/PEDOT:PSS Composite Films, *ACS Appl. Mater. Interfaces* 2014, 6, 5735–5743.
- [164] Yuho Min, Jong Wook Roh, Heeseung Yang, Minwoo Park, Sang Il Kim, Sungwoo Hwang, Sang Mock Lee, Kyu Hyoung Lee, and Unyong Jeong, Surfactant-Free Scalable Synthesis of

- Bi₂Te₃ and Bi₂Se₃ Nanoflakes and Enhanced Thermoelectric Properties of Their Nanocomposites, *Adv. Mater.* 2013, 25, 1425–1429.
- [165] C. W. Luo, H. J. Wang, S. A. Ku, H. J. Chen, T. T. Yeh, J. Y. Lin, K. H. Wu, J. Y. Juang, B. L. Young, T. Kobayashi, C. M. Cheng, C. H. Chen, K. D. Tsuei, R. Sankar, F. C. Chou, K. A. Kokh, O. E. Tereshchenko, E. V. Chulkov, Y. M. Andreev, and G. D. Gu, *Nano Lett.* 13, 5797 (2013).
- [166] W. Liu, H. S. Kim, Q. Jie, and Z. Ren, *Scr. Mater.* 111, 3–9 (2016).
- [167] A. Politano, M. Caputo, S. Nappini, F. Bondino, E. Magnano, Z. S. Aliev, M. B. Babanly, A. Goldoni, G. Chiarello and E. V. Chulkov, Exploring the Surface Chemical Reactivity of Single Crystals of Binary and Ternary Bismuth Chalcogenides, *J. Phys. Chem. C* 118 (2014) 21517.
- [168] S. Feng, S. Li, H. Fu, *Comput. Mater. Sci.* 82 (2014) 45–49.
- [169] Y. Tong, F. Yi, L. Liu, P. Zhai, Q. Zhang, *Comput. Mater. Sci.* 48 (2010) 343–348.
- [170] Z. Xiong, X. An, Z. Li, T. Xiao, X. Chen, *J. Alloys Compd.* 586 (2014) 392–398.
- [171] S. Gupta, N. Vijayan, A. Krishna, K. Thukral, K. K. Maurya, S. Muthiah, A. Dhar, B. Singh and G. Bhagavannarayana, Enhancement of thermoelectric figure of merit in Bi₂Se₃ crystals through a necking process, *J. Appl. Crystallogr.* 48 (2015) 533.
- [172] Manjón, F. J.; Vilaplana, R.; Gomis, O.; Pérez-González, E.; Santamaría-Pérez, D.; Marín-Borrás, V.; Segura, A.; González, J.; Rodríguez-Hernández, P.; Muñoz, A. et al. High-pressure studies of topological insulators Bi₂Se₃, Bi₂Te₃, and Sb₂Te₃. *Phys. Status Solidi B* 2013, 250, 669–676.
- [173] Koukharenko, E.; Fréty, N.; Nabias, G.; Shepelevich, V. G.; Tedenac, J. C. Microstructural study of Bi₂Te₃ material obtained by ultrarapid quenching process route. *J. Cryst. Growth* 2000, 209, 773–778.
- [174] D. Kong, J. J. Cha, K. Lai, H. Peng, J. G. Analytis, S. Meister, Y. Chen, H. J. Zhang, I. R. Fisher, Z. X. Shen, and Y. Cui, *ACS Nano* 5, 4698–4703 (2011).
- [175] S. R. Jian, G. J. Chen, and T. C. Lin, *Nanoscale Res. Lett.* 5, 935–940 (2010).
- [176] S. J. Bull, *J. Phys. D: Appl. Phys.* 38, R393–R413 (2005).
- [177] X. Li and B. Bhushan, *Mater. Charact.* 48, 11–36 (2002).
- [178] I. L. Johnson, *Contact Mechanics* (Cambridge University Press, Cambridge, 1987).
- [179] C.-H. Tasi, S.-Y. Huang, and C.-W. Luo, *J. Alloys Compd.* 622, 601–605 (2015).
- [180] Palmqvist, S. A method to determine the toughness of brittle materials, especially hard materials. *Jernkontorets Ann.* 1957, 141, 303–307.
- [181] Lawn, B. R.; Evans, A. G.; Marshall, D. B. Elastic/plastic indentation damage in ceramics: The median/radial crack system. *J. Am. Ceram. Soc.* 1980, 63, 574–581.

- [182] Anstis, G. R.; Chantikul, P.; Lawn, B. R.; Marshall, D. B. A critical evaluation of indentation techniques for measuring fracture toughness: I, Direct crack measurements. *J. Am. Ceram. Soc.* 1981, 64, 533–538.
- [183] Laugier, M. T. Palmqvist indentation toughness in WC-Co composites. *J. Mater. Sci. Lett.* 1987, 6, 897–900.
- [184] Dukino, R. D.; Swain, M. V. Comparative measurement of indentation fracture toughness with berkovich and Vickers indenters. *J. Am. Ceram. Soc.* 1992, 75, 3299–3304.
- [185] Ouchterlony, F. Stress intensity factors for the expansion loaded star crack. *Eng. Fract. Mech.* 1976, 8, 447–448.
- [186] Fischer-Cripps, A. C. Contact mechanics. In *Nanoindentation*; Springer: New York, 2011; pp 1–19.
- [187] Field, J. S.; Swain, M. V.; Dukino, R. D. Determination of fracture toughness from the extra penetration produced by indentation-induced pop-in. *J. Mater. Res.* 2003, 18, 1412–1419.
- [188] Lorenz, D.; Zeckzer, A.; Hilpert, U.; Grau, P.; Johansen, H.; Leipner, H. S. Pop-in effect as homogeneous nucleation of dislocations during nanoindentation. *Phys. Rev. B* 2003, 67, 172101.
- [189] Fischer-Cripps, A. C. Factors affecting nanoindentation test data. In *Nanoindentation*; Springer: New York, 2011; pp 77–104.
- [190] Volinsky, A. A.; Vella, J. B.; Gerberich, W. W. Fracture toughness, adhesion and mechanical properties of low-K dielectric thin films measured by nanoindentation. *Thin Solid Films* 2003, 429, 201–210.
- [191] Ritchie, R. O.; Dauskardt, R. H.; Yu, W. K.; Brendzel, A. M. Cyclic fatigue-crack propagation, stress-corrosion, and fracture-toughness behavior in pyrolytic carbon-coated graphite for prosthetic heart valve applications. *J. Biomed. Mater. Res.* 1990, 24, 189–206.
- [192] Sakai, M.; Bradt, R. C.; Fischbach, D. B. Fracture toughness anisotropy of a pyrolytic carbon. *J. Mater. Sci.* 1986, 21, 1491–1501.
- [193] Li, Y. Y.; Wang, G.; Zhu, X. G.; Liu, M. H.; Ye, C.; Chen, X.; Wang, Y. Y.; He, K.; Wang, L. L.; Ma, X. C. et al. Intrinsic topological insulator Bi₂Te₃ thin films on Si and their thickness limit. *Adv. Mater.* 2010, 22, 4002–4007.
- [194] Zhang, Y.; He, K.; Chang, C. Z.; Song, C. L.; Wang, L. L.; Chen, X.; Jia, J. F.; Fang, Z.; Dai, X.; Shan, W. Y. et al. Crossover of the three-dimensional topological insulator Bi₂Se₃ to the two-dimensional limit. *Nat. Phys.* 2010, 6, 584–588.
- [195] Liu, C. X.; Zhang, H. J.; Yan, B. H.; Qi, X. L.; Frauenheim, T.; Dai, X.; Fang, Z.; Zhang, S. C. Oscillatory crossover from two-dimensional to three-dimensional topological insulators. *Phys. Rev. B* 2010, 81, 041307(R).
- [196] Bansal, N.; Kim, Y. S.; Brahlek, M.; Edrey, E.; Oh, S. Thickness-independent transport channels in topological insulator Bi₂Se₃ thin films. *Phys. Rev. Lett.* 2012, 109, 116804.

- [197] Chiu, S. P.; Lin, J. J. Weak antilocalization in topological insulator Bi₂Te₃ microflakes. *Phys. Rev. B* 2013, 87, 035122.
- [198] W.C. Oliver, G.M. Pharr, An improved technique for determining hardness and elastic modulus using load and displacement sensing indentation experiments, *J. Mater. Res.* 7 (1992) 1564-1583.
- [199] W.C. Oliver, G.M. Pharr, Measurement of hardness and elastic modulus by instrumented indentation: Advances in understanding and refinements to methodology, *J. Mater. Res.* 19 (2004) 3-20.
- [200] J.J. Vlassak, M. Ciavarella, J.R. Barber, X. Wang, *J. Mech. Phys. Solids* 51 (2003) 1701–1721.
- [201] P. Giannozzi, S. Baroni, N. Bonini, M. Calandra, R. Car, C. Cavazzoni, D. Ceresoli, G.L. Chiarotti, M. Cococcioni, I. Dabo, A. Dal Corso, S. de Gironcoli, S. Fabris, G. Fratesi, R. Gebauer, U. Gerstmann, C. Gougoussis, A. Kokalj, L. Michele, L. Martin-Samos, N. Marzari, F. Mauri, R. Mazzarello, S. Paolini, A. Pasquarello, L. Paulatto, C. Sbraccia, S. Scandolo, G. Sclauzero, A.P. Seitsonen, A. Smogunov, P. Umari, R.M. Wentzcovitch, *J. Phys. Condens. Matter* 21 (2009) 395502.
- [202] J.P. Perdew, A. Zunger, *Phys. Rev. B* 23 (1981) 5048–5079.
- [203] J.P. Perdew, K. Burke, M. Ernzerhof, *Phys. Rev. Lett.* 77 (1996) 3865–3868.
- [204] S. Grimme, *J. Comput. Chem.* 27 (2006) 1787–1799.
- [205] H.J. Monkhorst, J.D. Pack, *Phys. Rev. B* 13 (1976) 5188–5192.
- [206] R.W.G. Wyckoff, *Crystal Structures*, Wiley and Sons, New York, 1964.
- [207] V. Chis, I.Y. Sklyadneva, K.A. Kokh, V.A. Volodin, O.E. Tereshchenko, E.V. Chulkov, *Phys. Rev. B* 86 (2012) 174304.
- [208] P.T. Jochym, K. Parlinski, M. Sternik, *Eur. Phys. J. B* 10 (1999) 9–13.
- [209] P.T. Jochym, K. Parlinski, *Eur. Phys. J. B* 15 (2000) 265–268.
- [210] J.J. Vlassak, W.D. Nix, *Philos. Mag. A* 67 (1993) 1045–1056.
- [211] J.J. Vlassak, W.D. Nix, *J. Mech. Phys. Solids* 42 (1994) 1223–1245.
- [212] J.R. Willis, *J. Mech. Phys. Solids* 14 (1966) 163–176.
- [213] J.O. Jenkins, J.A. Rayne, R.W. Ure, *Phys. Rev. B* 5 (1972) 3171–3184.
- [214] B.-L. Huang, M. Kaviani, *Phys. Rev. B* 77 (2008) 125209.
- [215] T.S. Gross, N. Timoshchuk, I.I. Tsukrov, R. Piat, B. Reznik, *Z. Angew. Math. Mech.* 93 (2013) 301–312.
- [216] M.W. Barsoum, A. Murugaiah, S.R. Kalidindi, T. Zhen, Y. Gogotsi, *Carbon* 42 (2004) 1435–1445.

- [217] T.S. Gross, N. Timoshchuk, I. Tsukrov, B. Reznik, *Carbon* 60 (2013) 273–279.
- [218] C. Lamuta, A. Cupolillo, A. Politano, Z.S. Aliev, M.B. Babanly, E.V. Chulkov, L. Pagnotta, Indentation fracture toughness of single-crystal Bi₂Te₃ topological insulators, *Nano Res.* (2016), 9(4): 1032–1042.
- [219] S.-R. Jian, C.-H. Tasi, S.-Y. Huang, C.-W. Luo, *J. Alloys Compd.* 622 (2015) 601–605.
- [220] Agarwal, A.; Patel, P. D.; Lakshminarayana, D. Single crystal growth of layered tin monoselenide semiconductor using a direct vapour transport technique. *J. Cryst. Growth* 1994, 142, 344-348.
- [221] T. Bjorkman *J. Chem. Phys.* 141 , 074708 (2014).
- [222] H. Rydberg, M. Dion, N. Jacobson, E. Schröder, P. Hyldgaard, S. I. Simak, D. C. Langreth, and B. I. Lundqvist *Phys. Rev. Lett.* 91, 126402.
- [223]] J.P. Perdew, K. Burke, and M. Ernzerhof. *Phys. Rev. Lett.*, 77, 3865, 1996.
- [224] S. Grimme, *J. Comput. Chem.* 2006, 27, 1787–1799. - Elsevier
- [225] A. Tkatchenko and M. Scheffler, *Phys. Rev. Lett.* 102, 073005 (2009).
- [226] M. Dion, H. Rydberg, E. Schroder, D.C. Langreth, and B. I. Lundqvist, *Physical Review Letters*, 92, 246401 (2004).
- [227] K. Lee, D. E. Murray, L. Kong, B. I. Lundqvist, and D. C. Langreth, *Physical Review B*, 82, 081101 (2010).
- [228]] V. R. Cooper, *Physical Review B*, 81, 161104(R) (2010).
- [229]] K. Berland and P. Hyldgaard, *Phys. Rev. B* 89, 035412 (2014).
- [230] J. Perdew and Y. Wang, *Physical Review B* 33, 8800 (1986).
- [231] I. Hamada, *Phys. Rev. B* 89 , 121103 (2014).
- [232] J. Klimes, D. R. Bowler, and A. Michaelides, *Journal of Physics: Condensed Matter*, 22, 022201 (2010).
- [233] R. Sabatini, T. Gorni, and S. de Gironcoli, *Phys. Rev. B* 87, 041108 (2013).
- [234] J.P. Perdew and A. Zunger. *Phys. Rev. B*, 23, 5048, (1981).
- [235] J.P. Perdew, A. Ruzsinszky, G.I. Csonka, O.A. Vydrov, G.E. Scuseria, L.A. Constantin, X. Zhou, K. Burke, *Phys. Rev. Lett.* 100, 136406 (2008).
- [236] David Vanderbilt, *Phys. Rev. B* 41 (Rapid Communications), 7892 (1990).
- [237] Zhu, W. N.; Yogeesh, M. N.; Yang, S. X.; Aldave, S. H.; Kim, J.-S.; Sonde, S.; Tao, L.; Lu, N. S.; Akinwande, D. Flexible black phosphorus ambipolar transistors, circuits and AM demodulator. *Nano Lett.* 2015, 15, 1883–1890.

- [238] Kim, K. S.; Zhao, Y.; Jang, H.; Lee, S. Y.; Kim, J. M.; Kim, K. S.; Ahn, J.-H.; Kim, P.; Choi, J.-Y.; Hong, B. H. Largescale pattern growth of graphene films for stretchable transparent electrodes. *Nature* 2009, 457, 706–710.
- [239] Chang, H.-Y.; Yogeesh, M. N.; Ghosh, R.; Rai, A.; Sanne, A.; Yang, S. X.; Lu, N. S.; Banerjee, S. K.; Akinwande, D. Large-area monolayer MoS₂ for flexible low-power RF nanoelectronics in the GHz regime. *Adv. Mater.*, in press, DOI: 10.1002/adma.201504309.

Annex

Some of the results reported in the present dissertation were published on peer-reviewed journals or presented at national and international conferences. A list of the publications produced during the three-years period of Ph.D. is reported below.

Book chapters

- Alfano M, Lamuta C, Chiarello G and Politano A, Elastic properties and electron-phonon coupling of graphene/metal interfaces probed by phonon dispersion, selected papers from GraphITA 2015, the Workshop on fundamentals and Applications of Graphene, Springer, Series Carbon Nanostructures (in press).

Journal papers

- Lamuta C, Campi D, Cupolillo A, Dasadia A, Politano A and Pagnotta L, Determination of the mechanical properties of SnSe, a novel superflexible material for nanomechanics (to be submitted).
- Lamuta C, Campi D, Cupolillo A, Politano A, Aliev ZV, Babanly MB, Chulkov EV, Pagnotta L, The anomalously low Young's modulus of Bi₂Se₃ topological insulator (to be submitted).
- A. Politano, C. Lamuta, and G. Chiarello, Cutting a Gordian knot: dispersion of plasmonic modes in Bi₂Se₃ topological insulator (in review).
- Sgambitterra E, Lamuta C, Candamano S, Pagnotta L, Brazilian Disk Test and Digital Image Correlation: a methodology for the mechanical characterization of brittle materials (in review).
- Lamuta C, Candamano S, Crea F, Pagnotta L, Direct piezoelectric effect in geopolymeric mortars, *Materials & Design* 107 (2016) 57–64.
- Lamuta C, Campi D, Cupolillo A, Politano A, Aliev ZV, Babanly MB, Chulkov EV, Pagnotta L, Mechanical properties of Bi₂Te₃ topological insulator investigated by density functional theory and nanoindentation, *Scripta Materialia* 121 (2016) 50–55.
- Lamuta C, Cupolillo A, Politano A, Aliev ZV, Babanly MB, Chulkov EV, Pagnotta L, Indentation fracture toughness of single-crystal Bi₂Te₃ topological insulator, *Nano Research* 9 (2016) 1032–1042.
- Lamuta C, Cupolillo A, Politano A, Aliev ZV, Babanly MB, Chulkov EV, Alfano M, Pagnotta L, Nanoindentation of single-crystal Bi₂Te₃ Topological Insulators grown with the Bridgman-Stockbarger method, *Phys. Status Solidi B* 253 (2016) 1082–1086.
- Lamuta C, Di Girolamo G, Pagnotta L, Microstructural, mechanical and tribological properties of nanostructured YSZ coatings produced with different APS process parameters, *Ceramics International* 41(2015) 8904–8914.

Conference papers

- Galloro A, Lamuta C, Comel L, Talerico A, Numerical analysis of a pressure vessel, reinforced by prs: static behaviour, 25th Annual International Conference on Composites or Nano Engineering (ICCE-25), 16-22-31 July 2017, Rome, Italy.
- Lamuta C, Candamano S, Crea F, Pagnotta L, Effetto piezoelettrico diretto in malte geopolimeriche, Giornate di studio sui Geopolimeri – IX edizione, Compositi geopolimerici, 26-27 Gennaio 2017, Napoli.
- Lamuta C, Bruno L, Candamano S, Pagnotta L, Piezoresistive characterization of graphene/metakaolin based geopolymeric mortar nanocomposites, XXV International Materials Research Congress, Cancun, Mexico, August 14-19, 2016.
- Sgambitterra E, Lamuta C, Candamano S, Pagnotta L, Determination of elastic constants of isotropic materials by means of Brazilian Disk Test and Digital Image Correlation, 44^o National Conference of the Italian Association for Stress Analysis (AIAS), September 2-5, 2015, Messina, Italy.
- Lamuta C, Di Girolamo G, Caliandro P, Pagnotta L, Microstructure and Mechanical Properties of nanostructured plasma sprayed YSZ coatings, 43^o National Conference of the Italian Association for Stress Analysis (AIAS), September 9-12, 2014, Rimini, Italy.
- Lamuta C, Di Girolamo G, Caliandro P, Pagnotta L, Influence of process parameters on the microstructural and mechanical properties of plasma sprayed nanostructured YSZ coatings, International Conference on Energy, Environment and Material Science (EEMAS), Saint Petersburg, Russia, September 22-26, 2014.

Acknowledgements

I would like to express my very great gratitude to my adviser, Professor Leonardo Pagnotta. He passed on to me the passion for research and the will to reach the highest results, which led me to truly love my job as a researcher. His useful critiques were perfectly balanced by his enthusiastic encouragement and were essential for my personal and professional growth. My affection and esteem for him will always remain unchanged. I wish to thank Professor Huseyin Sehitoglu, who gave me the possibility to work at the University of Illinois. Such experience changed my plans and my life forever. I would like to offer my special thanks to Emanuele, Giulia, Fabrizio, Piergiorgio, Giovanna, Carmine, Luigi, Marco, and Professor Franco Furgiuele. They made me feel part of a big family and gave me professional and moral support for the past three years. The collaboration with Giovanni Di Girolamo, Sebastiano Candamano, and Antonio Politano was really precious and I wish to thank them for the interesting exchange of ideas and their aid. I would like to thank Diego, Renato, and Ernesto for their valuable help and for making amusing the long time spent in the lab. I would sincerely thank University of Calabria. The friendly atmosphere and the kindness of people make Unical a great and unique place to work.

Thanks to my mom, Seruccia, and my father, Tonino. They always supported me with their advice and their unconditional love. Their example is more powerful than hundreds of spoken words. Thanks to Domenico, Daniela, and Antonio. They are for me family, friendship, constant point of reference and boundless sweetness. Thanks to my grandmothers Finita and Caterina for the pride that their eyes show when they talk to me. I wish to thank all my friends, which shared with me times of trouble and happy moments.

Finally, I would like to deeply thank Venanzio. My life has completely changed since the day I ran into him. I found true love, I found a friend, I found happiness. He teaches me to aim high, to never give up, and he believes in me more than I do. His positivity, his smile, and his love are my greatest strength. He completely changed my life plans and now “home” is for me wherever he is.